Universitat Autònoma de Barcelona

Tailoring the structural and electronic properties of graphene nanostructures by bottom-up methods

Michele Gastaldo

Tailoring the structural and electronic properties of graphene nanostructures by bottom-up methods

Michele Gastaldo

PHD THESIS

Supervised by

Aitor Mugarza

Gustavo Ceballos

Tutor

Jordi Pascual

November 2018

Programa de Doctorat en Fisica

Universitat Autònoma de Barcelona

Institut Català de Nanociència i Nanotecnologia

And the stars look very different today

D. Bowie - Space Oddity

Abstract

Graphene is a two dimensional material with extraordinary properties that can find applications in a wide variety of fields. In particular, its peculiar electronic properties, characterized by a high electron mobility and long spin relaxation length, make it a promising ground for the design of new devices for future electronics and spintronics. However, several important ingredients are missing in this material, crucial ones being the semiconducting electronic gap, and the capability to manipulate spins.

Nanostructuring graphene and interfacing with other materials can be an effective method towards tailoring the electronic and magnetic properties of graphene. At the nanoscale, these can dramatically depend on atomic scale variations in size and boundary structureThe possibility to fabricate real nano-devices from graphene such as graphene quantum dots then relies on the capability to control the structure of graphene at the atomic scale and to tune its properties for the desired applications.

In this work we study different bottom-up strategies to tailor the properties of graphene: (i) nanostructuring by the synthesis of graphene nanoislands with controlled shape, internal domain distribution and edge structure, (ii) proximity-induced tailoring of structural and electronic properties by metal intercalation, (iii) synthesis of lateral heterostructures. This is done by using chemical vapour deposition (CVD) to synthesize the nanostructures and metal beam epitaxy for the intercalation of metallic films, scanning tunneling microscopy (STM) and spectroscopy (STS) to study their atomic and electronic structures, and combining our experimental studies with ab-initio calculations.

The study follows previous work of the group on the synthesis of graphene nanois-

lands on Ni(111) by CVD. These results showed that the interaction with the substrate determines the edge termination and shape of graphene nanoislands: by selecting the post-annealing temperature, triangular islands with zigzag edges or hexagonal islands with alternated zigzag and reconstructed edges could be obtained. It was also shown that the strong interaction with the magnetic substrate transforms the Dirac cones into gapped spin polarized bands.

In this thesis, we gain a deeper insight in the structure and the growth mechanism of nanoislands on the surface of Ni(111). By high-resolution STM imaging, we access to a complete atomic scale characterization of the stacking symmetry and the edge structure. We also identify polycrystalline nanoislands and characterize both the stacking and orientation of graphene domains and the related boundary atomic structure. We report evidence of different continuous strained and topological defect boundaries.By comparing a statistical analysis of the rotated domains to grain-boundary formation energies, we conclude that the selection of rotational domains is determined by boundary rather than stacking energetics. However, the boundary structure, critical in defining transport properties across, seems to be defined by the substrate interaction. Finally, by analyzing the temperature evolution of the domains and shapes of nanoislands, we find a range of temperature where single-crystal shape-selected graphene nanostructures can be obtained.

Following the synthesis of graphene nanoislands with controlled shape and edge structure, Au intercalation is obtained by deposition and subsequent annealing. By combining both scanning tunneling microscopy and spectroscopy, we investigate the structural and electronic properties of the Au film and of the graphene nanoislands on it.

Regarding the Au film, we find a complex structural evolution, which involves alloying at the interface, the formation of a dislocation network in an overall compressed Au film, and the gradual strain-relief and formation of the herringbone reconstruction that corresponds to bulk Au(111) as we increase the thickness. We obtained this information by combining STM imaging of the surface structure with tunneling spectroscopy (STS) that probes the thickness evolution of field emission resonances and of the surface state.

At submonolayer coverage the intercalation is only possible by the Au alloying of the outermost Ni layer. At higher coverage, most graphene islands appear embed-

ded at the outermost Au layer, although a fraction can also be found on top. Some hexagonal islands are found with only zig-zag edges, implying that metal intercalation can also be used to induce structural modifications, such as a de-reconstruction of edges in this case.

The interaction of graphene with the substrate is monitored by tracking both the Shockley surface state of Au(111) and the Dirac states of graphene in spectroscopic measurements. By comparing the behaviour of the surface state under graphene at the Ni and Au/Ni surfaces, we evidence how such interaction is reduced after Au intercalation. An analysis of interference patterns in graphene leads to the conclusion that the Dirac band is recovered after Au intercalation. More interestingly, the decoupled nature of the graphene electronic properties is further confirmed by the detection of energy split localized peaks that are attributed to the predicted one dimensional spin-split edge states. The energy splitting we obtain is significantly larger than that measured in any other zigzag edge interacting with a metallic surface.

We also explore, at the end of this thesis, the synthesis of lateral graphene-hexagonal boron nitride (hBN) heterostructures on the Ni(111) surface, with the idea of exploiting the control on the edge structure of the graphene nanoislands. We find that heterostructures cannot be grown sequentially when starting with graphene nanoislands, due to the high temperatures required for the CVD growth of hBN, above the solubility onset of graphene. On the other hand, starting from hBN nanoisland leads to heterostructures with well-defined zigzag interfaces that could carry one dimensional electronic states.

Overall, the results of this thesis provide a deeper insight on the growth of two-dimensional nanostructures of graphene and hybrid layers and on the tuning of their structural and electronic properties by controlling the interfacial interaction with the underlying metal. These notions could be valuable for the realisation of shape-selected graphene quantum dots with tailored properties, which could find applications in optoelectronics and spintronics.

Contents

List of abbreviations

- **ARPES**: Angle Resolved Photoemission Spectroscopy
- **BZ**: Brillouin Zone
- **C.C.**: Constant Current
- **C.H.**: Constant Height
- **DFT**: Density Functional Theory
- **FER**: Field Emission Resonance
- **GNI**: Graphene Nanoisland
- **GNR**: Graphene Nanoribbon
  - aGNR/zzGNR: Armchair/zigzag -edged GNR
- **GQD**: Graphene Quantum Dot
- **hBN**: Hexagonal Boron Nitride
- **IFS**: Interface State
- **IPS**: Image Potential State
- **LT**: Low Temperature
- **QPI**: Quasi-Particle Interference
- **RT**: Room Temperature
- **SS**: Surface State

- **STM**: Scanning Tunneling Microscopy
- **STS**:Scanning Tunneling Spectroscopy

Chapter 1

Introduction

1.1 Graphene

Graphene is a one atom thick layer of carbon atoms, and is the first 2D material to be isolated. Although its peculiar electronic properties were theoretically predicted already in 1946 [1], its stability as a free-standing 2D structure was long quenstioned before being demonstrated in 2004 [2], a discovery worth the 2010 Nobel Prize. The unique properties of graphene have been ground for intense and broad research embracing all fields of science, leading the number of papers on graphene to increase from 4,000 in the year of its isolation to over 100,000 per year since 2014. Furthermore, the groundbreaking discovery of the stability of 2D materials has been the origin of a whole new branch of research, and many new single-layer materials with fascinating properties have been studied and isolated since [3, 4].

The extraordinary properties of graphene might need no introduction. It has unique electronic properties, among which the most relevant is maybe the ballistic transport of charge carriers behaving as massless relavistic particles [5]. Furthermore, it combines flexibility with exceptional mechanical strength [6] outstanding electronic and thermal conductivity, optical transparency, impermeability to all elements [7] and many other properties for which it was named "a miracle material" with possible applications in a wide variety of fields from the macro- to the nanoscale, from flexible electronics to biosensing, from photonics to material coating [8, 9]. Among them, it could serve to produce ultrafast, highly selective molecular sieves for water purification [10], gas separation [11, 12] or DNA sequencing [13, 14],

to fabricate ultrasensitive chemical sensors and biosensors [15, 16], or solar sails for space missions [17]. Though unlikely to replace silicon in electronics, it could improve silicon-based devices [18], and it seems now predictable that novel electronics at the nanoscale will be based on graphene and 2D materials combined [19–21].

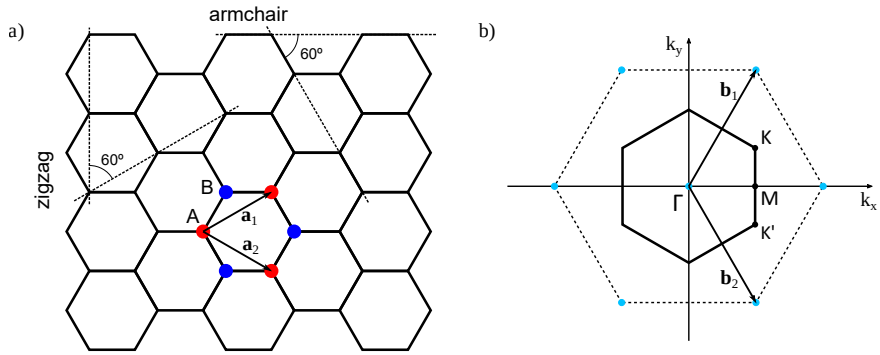

Figure 1.1: a) Graphene structure in real space, with indicated zigzag and armchair edge directions. A and B sublattices and the lattice vectors $|\mathbf{a}_1| = |\mathbf{a}_2| = 2.46$ Å are shown. b) Momentum space representation of the Brillouin zone of graphene, with primitive lattice vectors and high-symmetry points.

Structurally, graphene is a planar honeycomb lattice of carbon atoms organized in hexagonal (benzene) rings, with lattice vector a=2.46 Å and interatomic distance of 1.42 Å. The honeycomb pattern is in turn formed by two equivalent sublattices, A and B, with triangular symmetry, and is therefore a bipartite lattice (Fig. 1.1). These correspond, in momentum space, to two sets of unequivalent K and K' points at the corners of the hexagonal Brillouin zone (BZ), Fig. 1.1, which are the also called Dirac points. The reason of this naming can be understood from the electronic structure of graphene. As evidenced by the band dispersion, Fig. 1.2, at the K (K') point the valence and conduction bands of graphene meet in exactly one point, having a symmetrical conical dispersion in the vicinity of it. From this derives the semi-metal character of graphene, i.e. a metal with a density of states (DOS) equal to 0 at E_F. The conical dispersion close to the Dirac points is described by the relation [1]

$$E_{\pm}(\boldsymbol{q}) \simeq \pm v_F |\boldsymbol{q}| + O[(q/K^2)], \tag{1.1}$$

where $|\boldsymbol{q}| \ll |\mathbf{K}|$ is the momentum relative to the K (K') points, and v_F is the Fermi velocity, $v_F \simeq 10^6$ m/s, which is a constant. Interestingly, this linear dispersion is solution to a relativistic Dirac-like equation for massless particles [5]:

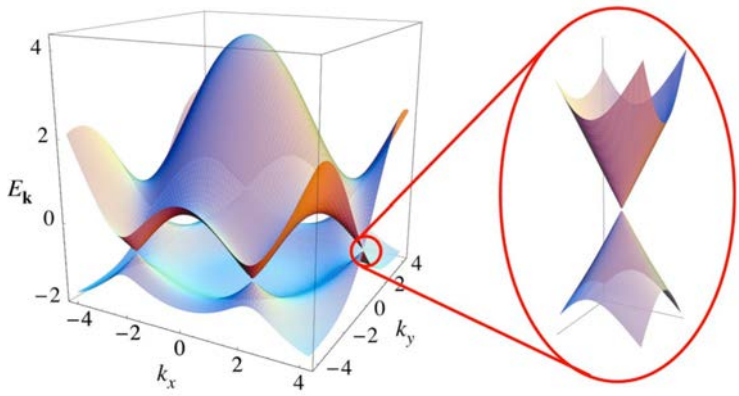

Figure 1.2: 3D rendering of the band structure of graphene in its Brillouin zone with a zoom on the conical dispersion centered in one of the six Dirac points. Reprinted with permission from [22]. Copyright 2009 by the American Physical Society.

$$-i\,v_F\boldsymbol{\sigma}\cdot\nabla\psi(\boldsymbol{r})=E\psi(\boldsymbol{r}), \tag{1.2}$$

where $\boldsymbol{\sigma}$ are Pauli matrices equivalent to those describing the spin. The eigenstates $\psi_{\boldsymbol{K}}(\boldsymbol{r})$ and $\psi_{\boldsymbol{K'}}(\boldsymbol{r})$ are defined in the vicinity of K and K' respectively.
From these equations, two of the main properties of graphene are derived: charge carriers in the vicinity of the Dirac points behave as massless Dirac quasiparticles, and they move at a constant relativistic Fermi velocity not depending on energy or momentum.

Moreover, the equation implies a pseudospin quantum number, formally equivalent to the spin, which is related to the sublattice exchange symmetry and has important consequences on the transport properties of graphene. It is also at the origin of unique effects: for instance, bandgap opening can arise upon breaking of its sublattice symmetry [23], and its coupling to electron spin can give rise to an unusual half-integer Quantum Hall Effect [24]. The projection of the pseudospin on the direction of momentum defines a helicity or chirality for the quasiparticles, given by the operator

$$\hat{h}=\frac{1}{2}\boldsymbol{\sigma}\cdot\frac{\boldsymbol{p}}{|\boldsymbol{p}|}, \tag{1.3}$$

and for which the eigenstates $\psi_{\boldsymbol{K}}(\boldsymbol{r})$ and $\psi_{\boldsymbol{K'}}(\boldsymbol{r})$ of Eq. (1.2) are also eigenstates

$$\hat{h}\psi_{\boldsymbol{K}}(\boldsymbol{r}) = \pm\frac{1}{2}\psi_{\boldsymbol{K}}(\boldsymbol{r}), \tag{1.4}$$

and similarly for K', with inverted sign. The pseudospin $\boldsymbol{\sigma}$ then has eigenvalues in the direction of the momentum or opposite to it, and a chirality is defined in the Dirac cones.

Spin manipulation in graphene is also a subject of research. Graphene has a very low spin-orbit coupling (SOC) giving rise to a predicted long spin relaxation length [22], which make it a promising spin channel material for applications in spintronics [25]. However, measured spin diffusion times remain several orders of magnitude below theoretical predictions, regardless of the quality of the graphene monolayer [26]. A recent study attributes such differences to the coupling of the spin with the pseudospin via spin-orbit coupling that could arise from adatom impurities, ripples in graphene, or substrate interactions [27]. This apparently negative result can be exploited to manipulate spins in graphene if one can control the source of SOC. Introducing a sizeable SOC in graphene would also allow the realization of quantum phenomena such as the Quantum Spin Hall Effect (QSHE) [28]. Many methods to induce spin-orbit coupling in graphene have been proposed, among which adatom adsorption [22] and proximity effect with high SOC substrates [29, 30].

1.2 Graphene nanostructures

A different but effective method to tailor the properties of graphene is the reduction of its size down to the nanometer scale. The two most evident consequences in doing that are the quantization of electronic states and the increasing relevance of boundary phenomena, sometimes even dominating the overall material's properties. Both effects are size-dependent and can therefore be tuned by controlling this parameter.

Electron quantization turns semimetal graphene into a semiconductor, with a gap that can be tuned with size [31, 32]. This has enabled the realization of field-effect (FET) transistors using graphene nanoribbons (GNR) [33, 34], or to track the transition from a single-electron transistor behaviour driven by Coulomb blockade to a true semiconductor behaviour as we reduced the size of a graphene quantum dot (GQD) [35]. The size-tunable optical properties of GQDs have also enable to

employ them as labels for bio-imaging, and for optical sensing and photovoltaics (see [36] and references therein).

Unlike conventional metal and semiconductors, the electronic and optical properties of graphene nanostructures will dramatically depend on the orientation of its boundaries, and hence their edge structure [37]. Whereas armchair nanoribbons (aGNRs) are semiconducting with a gap depending non-monotonically on the width [38, 39], zigzag nanoribbons (zzGNRs) exhibit metallic edge states that are spin-split when electron correlations are set on [40, 41]. The origin of the edge states lies in the bipartite nature of the honeycomb graphene lattice, and the fact that zigzag edge terminations consist only of one type of sublattice (a more thorough description of the magnetism in zigzag edges can be found in Chap. 4). Antiferomangnetic interactions between the two zzGNR edges exposing opposite sublattices result in a width-dependent spin splitting of the edge bands [38, 39]. The magnetic ground state of the edge states can be further manipulated externally: a transversal electric field can lead to half-metallicity (conduction of only one spin) [42], whereas doping can induce a semiconductor to metal transition that is related to a correlated antiferro- to ferromagnetic transition of the inter-edge coupling [43].

In GQDs, the magnetic configuration depends on the geometry of the dot, since edges can be formed of only one or both sublattice. The edges of triangular GCDs belong to a single sublattice, leading to an unbalance that results in uncompensated spins that couple ferromagnetically [44, 45]. On the other hand, adjacent edges in hexagonal GQDs are of opposite sublattices, leading to the antiferromagnetic coupling of ferromagnetic edges, similar to the case of zzGNRs [44].

Experimentally, split pairs of localized edge states have only been observed in zzGNRs [46–48]. Here the splitting was attributed to the π-orbital edge magnetism described above. The few trials in supported GQDs failed on detecting any fingerprint of edge states [49]. Their absence was attributed to a strong covalent interaction with the substrate that perturbed the pristine electronic states of the graphene edge by hybridization.

1.3 Chemical vapour deposition growth of graphene nanostructures

It is at this point evident that the structural properties of graphene at the nanoscale influence deeply its mechanical, electronic, magnetic and optical properties. While such tunability justifies the wide range of fields in which graphene might find applications, it requires the ability to nanostructure graphene with atomic precision in order to obtain the desired properties. The purity of graphene, its bulk crystallinity and its edge structure, the inclusion of foreign atoms or molecules at selected sites are all issues that need an unprecedented level of control in the synthesis and manipulation of this material.

To that end, the traditional, 'top-down' approach to nanostructuring, i.e. imposing a structure or pattern on a larger material to be processed [50], has technical or physical limitations that proved it insufficient or with very low yields, particularly when the edge structure is concerned. Electron beam and laser lithography, for instance, are intrinsically limited by the wavelength of the electrons or photons, and technically by the effective size of the beam, usually in the ~nm range, which is at least an order of magnitude larger than the resolution required for edge structuring. Other top-down techniques used in graphene nanostructuring include carbon nanotubes unzipping [51], plasma, hydrogen [52] or metal particle catalyzed [53] etching, sonochemical breaking, chemical oxidation cutting [54], all of them requiring high-level engineering at their phyisical limits to reach the necessary resolution.

A more promising approach relies on 'bottom-up' techniques, those that aim to guide the assembly of atomic and molecular building blocks into organized structures through intrinsic physical and chemical processes [50]. Such techniques are basically limited by the understanding of the processes inherent to the system to be manipulated and the ability to order and control them. Starting from molecular self-assembly on metal surfaces [55], this approach has gained more attention in the field of surface science.

The most common method for the bottom-up synthesis of carbon-based nanostructures is the use of polyaromatic precursors that transform into covalent nanostructures upon specific on-surface reaction steps - - usually involving at least polymerization and cyclodehydrogenation [56]. This technique has the great advantage that the molecular building blocks are designed in laboratory so that the desired

final chemical and structural properties can be obtained through predictable self-organization and chemical processes. Growth of highly precise structures has already been demonstrated, ranging from GNRs of different width [57], edge type [46, 56], and dopants [58, 59], to 2D porous networks [60–62].

Despite this impressive portfolio of atomically precise nanostructures, on-surface synthesis has severe limitations to build non-porous, compact graphene nanostructures beyond 1D chains, such as the GQDs we are interested in. This can be achieved by the more conventional CVD method, extensively used in the synthesis of standard graphene.

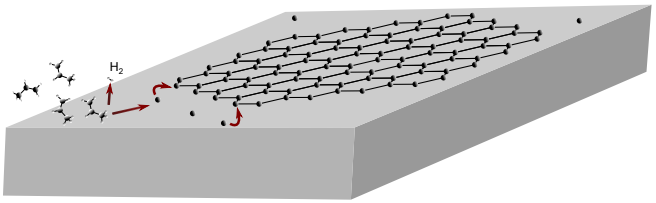

Figure 1.3: Schematics of the CVD growth of graphene: the gas precursor adsorbs on the surface. After catalytic dehydrogenation and decomposition of the molecule, hydrogen is mostly desorbed, while carbon atoms diffuse on the surface and form graphene structures.

Chemical Vapour Deposition (CVD) is a versatile method of growing thin films initially developed at the end of the 19th century [63]. In general terms, it can be described as the growth of thin films of solid material by dissociation and chemical reaction of reactants in the gas phase deposited on a surface in an activated environment. CVD is the established method to grow large-scale layer of graphene with high quality, together with epitaxial growth from SiC. The process of graphene growth by CVD involves the thermal decomposition of carbon-containing molecular precursors, either hydrocarbons (as propylene, ethylene, methane) or polymers, on a catalytic surface. The precursor dissociates through surface-assisted dehydrogenation, and the resulting carbon adatoms form graphene structures by nucleation and diffusion on the surface [64]. Depending on the substrate in use, more processes can be involved, such as dissolution in the bulk metal in Ni, explained in further detail in Chap. 2.

The growth process is essentially self-limited to one monolayer, since the catalytic effect of the surface is hindered by the presence of adsorbed graphene. However, further growth of following layers is technically achievable and desirable in

some cases [65].

As a consequence of this layer-by-layer catalytic growth, nanostructures can be obtained by limiting the feedstock of precursor on the surface. Technically, this is achieved by either limiting the exposure to hydrocarbons at growth temperatures or by depositing the precursor molecules on the surface at room temperature and then providing thermal energy to start the reaction, as explained in more detail in Chap. 2. Different energetics than those for extended graphene are in play at the nanoscale. In particular, at this reduced size, the competition between edge and bulk energetics can stabilize morphologies and stacking symmetries different from those stable in the extended case. While the stable shape for free-standing GNIs is hexagonal, as should correspond to the lattice symmetry, the shape of the grown structures is essentially dictated by the crystal symmetry of the surface and by the edge growth energetics and can take different forms, from triangular to rhombohedral [66]. Triangular and hexagonal nanoislands with preferential zigzag edges were grown on e.g. Co(0001) [67, 68], on Cu(111) [69] and Cu foil [70–72], on Pt [73] and on Ir(111) [74].

Nanoislands with selected triangular or hexagonal shape can also be grown on Ni [75]. Ni(111) is one of the first and most used substrate for growing extended graphene. As it provides an almost perfect lattice match to graphene and it displays a strong bonding to it, graphene mainly grows in 1x1 unrotated stacking, thus offering a great possibility to form large area graphene sheets with no domain rotation. Moreover, it provides a perfect template for nanoislands with purely zigzag edges. However, the electronic properties of free-standing graphene are disrupted by the strong hybridization of its bands with the metallic d bands of Ni(111). While such hybridization leads to an interesting lateral and vertical spin-filtering effect [76], which can be used for the construction of devices [77], a different substrate can be desirable in order to recover graphene pristine properties.

Our surface supported GNIs behave as GQDs in the sense that their characteristic x-y size in the nanometer range should induce electron quantization. The two expressions are equivalent, and hereafter we choose to use GNIs, a term that is more familiar to the surface science community where we belong.

1.4 Intercalation

The interaction of graphene with its substrate can be tuned after growth by intercalation of a different material underneath. This is technically achieved by depositing the intercalant on top of the grown graphene, and providing thermal energy for its diffusion under the it, so that the interacting metal is now the intercalated buffer film. Intercalation compounds of graphite have been studied since the 80's as a way to modify the electronic, magnetic and chemical properties of this material and particularly to obtain high conductivies [78]. In CVD growth of graphene, the intercalation method enables to decouple the catalytic and the proximity-induced tailoring role of the underlaying metal, by selecting the most suitable materials for the synthesis and intercalation respectively. In the most simple approach, graphene-metal interactions can be divided in weak and strong ones. The first ones generally preserve the band structure of graphene, particularly the linear dispersion near E_F, doping it and occasionally inducing a gap (usually small) at the Dirac point. Mostly noble metals belong to this group: Al, Ag, Au, Cu, Pt [79] and Ir [80] are the most notable examples. On the other hand, strongly interacting materials hybridize with the band structure of graphene, disrupting the Dirac cones. Example metals for such case are Ni, Co, Pd, Ti [81] or Ru [82]. While interesting applications can derive from such strong interaction, it is often interesting to recover the electronic properties of pristine graphene by intercalation. To this end, many different elements can be used. The first and more obvious is to intercalate weakly interacting metals, which has been demonstrated with e.g. Au [83, 84], Ag [85–88], Al [89], Cu [86, 90] on different substrates. Also some alkali metals are known to electronically decouple graphene, like Na [91] or Cs [92]. Other possibilities include semiconducting materials as Ge [93], and O [94–97] and H [96, 98] as oxidizing and reducing agents.

Electronic decoupling is not the only application, though. By intercalation, the morphology and interactions in graphene can be modulated [99, 100] and new artificial graphene/metal interfaces can be engineered [101]. Interesting for spintronics applications is the possibility to induce spin-orbit coupling [30, 102–104] or spin polarization [76, 105–107] in graphene. Recently, it was shown by Rybkin et al. [108] that the interplay between the structural modulation of an artificial metal/metal interface and the Rashba effect induced by the intercalant can cause complex spin textures. Also, graphene can be used as a protective layer for an intercalation system

with interesting magnetic properties [109].

Fewer studies are available for intercalation of graphene nanostructures, all grown on Ir(111) only: oxygen [110], Au [111, 112] and Ag [112] were used as intercalants. In such systems, the intercalation process can be different from the extended case, where the intercalant is deposited on top of graphene, and has the choice of either remaining on top of the inert graphene or binding to the more interacting substrate by intercalation. As a consequence, diffusion of the intercalant and coordination to the metal substrate is energetically favoured and is the guiding force of intercalation. Since graphene nanostructures do not cover the whole metal surface, a different mechanism can be in play. Moreover, the different interaction with the intercalated film can possibly lead to structural modification of the formed graphene structures.

1.5 Two-dimensional heterostructures

Many other two-dimensional materials have been predicted and isolated since the discovery of graphene, and many are yet to come. The first ones to be realized were atomic planes of layered materials such as hexagonal boron nitride (hBN) and transition metal dichalcogenides (TMDs) [3], but the creation of 2D allotropes of elements characterized by non-reducible 3D crystals was also demonstrated, as is the case for silicene [113]. New monolayer compounds such as C-B-N [114], or structures with non-stoichiometric relations can also be formed. By vertically stacking such 2D materials, new layered 3D composites can be engineered [115–118], while functionalized 2D structures can be obtained by combining them in lateral heterostructures [119–121]. This opens new perspectives in materials science. New structures and materials with selected physical properties can be synthesized, finding applications in a variety of fields, from plastics to fabrication of customizable devices for nanoelectronics and sensing [19, 122].

Lateral heterostructures have received increasing attention. Planar heterojunctions of different 2D materials can be the base for new devices for electronics and optoelectronics in reduced dimensionality, e.g. diodes and photodiodes, high-speed transistors, etc. Heterostructures of this kind have already been demonstrated, mostly comprising graphene, hBN and TMDs (Gr-hBN, Gr-MoS_2, hBN-MoS_2, WS_2-MoS_2, WSe_2-MoS_2, WS_2-WSe_2, MoS_2-$MoSe_2$ [120, 121, 123]). A regular interface is often

needed, and this is an issue especially when the two materials have different lattices and crystal structure.

Graphene and hexagonal boron nitride are a model system in this sense, as they share a honeycomb structure with a lattice mismatch of only 2%. Hexagonal boron nitride is thus structurally equivalent to graphene: it is formed by alternated boron and nitrogen atoms joined by ionic bonds in a sp^2 network with a lattice parameter of 2.51 Å. As graphene, it has outstanding structural properties as high in-plane mechanical strength [124], chemical stability and thermal conductivity [125]. The main difference from graphene is in its electronic properties: hBN has a wide, direct bandgap of ~5–6 eV [125–127]. Because of the structural equivalence to graphene, a perfect zigzag interface can form at the boundary between the two. Similarly to zzGNRs (Sec. 1.1), edge states were also predicted for zigzag BN nanoribbons [128–130], with a spin polarization that depends on the passivation of the edges [129]. At the Gr-hBN zigzag interface, a one dimensional metallic state polarized in spin develops [131–134]. Due to the hBN polarity and to charge screening at the interface, such state is half-semimetallic [135].

The interest in 2D hybrids of graphene and hBN is not only in the interface though. Several theoretical and experimental studies found that a heterostructure formed by domains of the two materials displays a bandgap with a size that depends on the structure of the domains and the relative abundance of each material, thus forming a tunable semiconductor [133, 134, 136–138]. Because of the discretization of the electronic states due to quantum confinement, quantum dots of graphene embedded in a hexagonal boron nitride layer can serve as e.g. light-emitting devices [139]. Furthermore, for triangular GQDs, hBN is predicted to preserve [137] or even enhance the magnetic moment of the edges [139]. Quantum dots of hBN in a graphene matrix can open and tune the bandgap of the latter similarly to an antidot lattice [138]. Hybrid layers composed of nanoribbons of the two materials have also been explored theoretically [133, 134, 140] and experimentally [141]. The wide tunability of the electronic and magnetic properties is the main interest of such 2D hybrid systems [142].

Experimental realization of lateral heterostructures was achieved by different approaches. Simulatenous bottom-up growth of the two materials by CVD, using a C containing precursor and a BN containing one, resulted in a hybrid layer with

mainly segregated domains of graphene and hBN, with a controllable concentration of C [136]. Substitutional doping of either material leads to intermixed layers of BNC [143, 144]. By using a patterned mask one can obtain a spatially controlled conversion of graphene into BNC and hBN [141]. A similar approach consists in templated etching of monolayer graphene and regrowth of hBN [145] or viceversa [146]. This method relies on the nucleated growth of the second material at the edges of the first. As a consequence, precise zigzag interfaces can be easily obtained, and this was demonstrated by STM for hBN flakes in Gr with irregular shapes on Rh(111) [147], and hexagonal shapes on Cu foils [148], where also hexagonal Gr flakes in hBN were demonstrated after hydrogen etching [149]. Irregular flakes of either material embedded in the other was shown on Ir(111) [150]. Sutter et al. [151] showed that on Ru(0001) depletion of residual carbon is necessary in order to avoid BNC formation at graphene flakes edges. On Ni(111), triangular hBN flakes with zigzag linking to graphene were demonstrated during the course of this thesis [152].

Intercalation can also be used in hybrid 2D materials grown on metals. For instance, Drost et al. [153] employed Au intercalation after heterostructure growth of graphene and hexagonal boron nitride on Ir(111) in order to observe the electronic properties of the pristine interface of the two by STS, finding signatures of a localized electronic state.

1.6 Motivation and outline of the thesis

In this thesis, we explored nanostructures of graphene on Ni(111) and tailored their structural and electronic properties by intercalation of Au thin films. We chose Ni(111) because the strong, epitaxial interaction of graphene with Ni can be used to control its geometry and edge structure, as was shown by previous results in our group using a modified CVD growth [75, 154]. Here we further explored the growth kinetics by analyzing the stacking and edge symmetries of the nanostructures. We investigated the domain and boundaries properties in order to understand their formation processes and gain control over the crystallinity, a requisite for functional graphene quantum dots. The experimental results are presented and discussed in Chap. 3.

The choice of Au as intercalant followed previous reports on the decoupling of extended graphene from Ni and the recovery of pristine graphene electronic properties. We studied the intercalation process as a whole, by investigating the kinetics

and final structure of the Au film and the intermixing of Ni, as well as the effects of intercalation on graphene nanostructures. The mechanism of intercalation under nanoislands, their topography on the surface and the atomic and edge restructuring induced by the modified interfacial interaction and the electronic properties of graphene and its edges on Au are the focus of the current research, resumed in Chap. 4.

Motivated by the promising applications of our graphene quantum dots embedditon in lateral heterostructures, we also explored the growth and characterization of hybrid 2D layers of graphene and hexagonal boron nitride. We first explored the growth of hexagonal boron nitride on Ni(111), and afterwards that of Gr-hBN heterostructures. We studied their morphology, with particular attention at the structure of the interface, and their electronic properties on Ni, and looked into the possibility of decoupling them by Au intercalation. This part of the work is resumed in Chap. 5.

Chapter 2

Experimental Methods

2.1 Growth

In this section, we present the experimental methods used for the preparation of the samples.

2.1.1 Chemical Vapour Deposition

Growing graphene by chemical vapour deposition (CVD) involves the decomposition and the chemical reaction of hydrocarbons - such as ethylene (C_2H_4), propylene (C_3H_6) or methane (CH_4), but also other precursors such as CO - on a catalytic surface. Heat is necessary to overcome the energy barrier for dissociation of carbon atoms from the molecule and their diffusion on the surface and nucleation of graphene [155].

Monolayer graphene is grown by exposing the surface of a metal to the precursor at the growth temperature. While industrial CVD at ambient or low pressure is mostly carried out in gas flux of the precursor together with hydrogen or inhert gases, CVD in vacuum occurs by introducing a partial pressure of precursor between E-8 and E-5 mbar for a certain amount of time. The amount of gas fed is measured as a dose, defined as the integral of the pressure over the exposure time:

$$D = \int_{t_0}^{t_f} P_{gas}(t)\mathrm{d}t, \tag{2.1}$$

which is measured in Langmuirs (L), where $1\,\mathrm{L} = 1 \cdot 10^{-6}\mathrm{torr} \cdot 1\mathrm{s} = 1.33\mathrm{mbar} \cdot 1\mathrm{s}$, corresponding to 1 ML of reference N_2 molecules adsorbed on the surface, according to gas theory - see Sec. 2.1.3 and in particular Eq. (2.3).

In the case of hydrocarbons, the precursors used in this work, after thermal dissociation of the molecule, hydrogen atoms tend to desorb as molecular H_2; carbon atoms instead diffuse on the surface and form graphene. This is the case for graphene growth on e.g. Cu [156] or Ir [157]. On Ni, a more complex process takes place, as carbon also dissolves into the bulk metal, in the near-surface region. Such carbon in the subsurface region either segregates at high temperature or precipitates to the surface upon cooling – the difference being that segregation is the process of elemental separation at the surface discontinuity at thermal equilibrium, whereas precipitation is a classical phase separation [156, 158, 159]. When precipitating, carbon forms a carbidic, quadrangular phase on the surface with the formula Ni_2C [160], which can form even under rotated graphene, decoupling it [161, 162]. Segregation can result in either graphene or Ni_2C formation depending on the growth conditions. Patera et al. [159] recently showed that on nickel three growth modes are available for graphene formation, depending on the amount of carbon dissolved in the subsurface region and on the growth temperature: for a clean subsurface, graphene either grows embedded in the surface layer by Ni replacement, or by a previous Ni_2C formation and conversion, in the high and low temperature ranges respectively. Contaminated subsurfaces rather favour epitaxial graphene formation on the Ni topmost layer.

On all substrates, continuous feeding of molecular precursor can lead to multilayer graphene formation [163], although the catalytic action of the substrate is highly hindered by the presence of monolayer graphene.

Our method for forming graphene nanostructures (nanoislands) is slightly different from classical CVD, and it is sometimes referred to as Temperature Programmed Growth (TPG) in the literature [64]: the surface is kept at room temperature when exposed to the gas precursor, and molecules adsorb on it. Heating is carried out subsequently, after the gas is evacuated and the base vacuum pressure is restored. The feedstock of carbon is therefore limited to the amount of precursor adsorbed on the surface and to the carbon segregating from bulk. The heating ramp must be steep, as molecules can desorb and Ni_2C can form at lower temperatures than graphene, -

i.e. it is important to reach the graphene growth temperature as fast as possible.

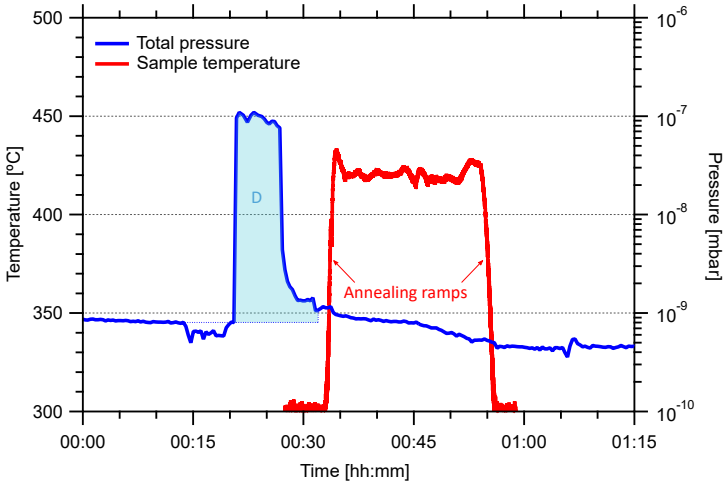

Figure 2.1: Sample graph of the total pressure in the preparation chamber and of the temperature measured on the sample surface by a pyrometer (see Sec. 2.3.3) during GNIs preparation. The shaded area corresponds to the dose D (measuring is usually interrupted before the pressure raises due to thermal annealing).

In this thesis, we used two molecular precursors in the gas phase: ethylene and propylene, with 99.9% purity. The gas bottles were mounted on stainless steel tubes of 6mm connected to the vacuum chamber through a leak valve. We measured the dose of gas by digitally integrating the partial pressure fed by the vacuum gauge over the time of exposure to the gas. A sample schematic of the pressure and temperatures is shown in Fig. 2.1. As a general rule, we employed doses of 2–50L, exposing the nickel surface to partial pressures of 1E-8 – 1E-7 mbar of either propylene or ethylene, for times varying between 20 s and a few minutes. Dosing was counted until recovery of the partial pressure in the chamber, ~3 min after closing the leak valve in our setups.

For the growth of hexagonal boron nitride (hBN) shown in Chap. 5, we employed borazine as a precursor. As a compound, borazine is a colourless, highly flammable liquid at room temperature with a vapour pressure of 170 mm Hg and a melting point of 217 K. Caution is necessary when handling it, as it reacts with moisture to form boric acid and ammonia, it reacts explosively with water and it decomposes at room temperature and under day light, polymerizing and forming $(BN)_6H_{10}$ and $(BN)_5H_8$, which appear as a solid white sediment [164, 165]. Moreover, it is highly

contaminant and its residuals are hard to remove. As a consequence, we mounted a new tube line on the system, especially dedicated to borazine, which we kept in a glass tube protected from light. The tube containing the molecule and the gas line were purged from impurities and degradation products by connecting them to a turbomolecular pump while the precursor was cooled to ~80 K in a liquid N_2 bath.This procedure was carried out every day before growth experiments.

Borazine ($B_3N_3H_6$) has a hexagonal ring structure composed of alternated boron and nitrogen atoms saturated by six hydrogen atoms. After dehydrogenation and decomposition on the surface of nickel, B and N diffuse on the surface, though it is not clear if in atomic form or in (sub)molecular units. Differently from carbon, their solubility in Ni is low, therefore dissolution to bulk does not take place. Nevertheless, recent DFT calculations show that a subsurface B diffusion pathway is only slightly more costly than surface diffusion, therefore the two processes might coexist, while N atoms diffuse on the surface only [166].

2.1.2 Thermal evaporation and intercalation of metals

In order to intercalate buffer layers of Au of variable thickness, we evaporated gold using two different methods: electron beam evaporation with a commercial Omicron EFMT/EFM3T evaporator, and evaporation through resistive heating in a homemade evaporator. Fig. 2.2 shows a schematic of the two methods.

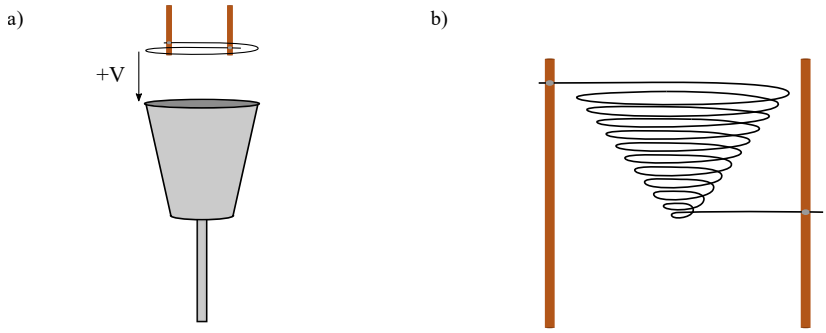

Figure 2.2: Schematic of the 2 evaporation methods: a) Electron beam evaporation: Au is heated by impinging electrons emitted by a filament and accelerated to the Au containing crucible through a voltage applied to this. b) Thermal evaporation: Au is placed inside a conical shaped filament and evaporated through resistive heating.

In the Omicron evaporator, Au pellets or wire with 99.9999% purity fill up a Mo

crucible connected to a high voltage V, in the range 500–800 V. A W filament emits electrons which hit the crucible with an energy $e \cdot V$, thus heating Au until it melts and evaporation starts. Thermal energy and inciding electrons result in ionisation of about 1% of the evaporated material: the metal ions accelerate to eV and leave the source together with the beam of evaporated neautral atoms [167]. The evaporated beam is collimated through a cylindrical tube, where an ion trap measures the current of impinging metal ions, which serves as a measure of the evaporation flux. By measuring the flux, we monitored the metal deposition rate on the sample surface, once a calibration (deposited material for a given flux and time) was obtained.

The homemade evaporator has a simpler design: the two terminals of a conical shaped W filament are connected to electrical bars. Au wire is placed inside the cone. A current of up to 5 A flows through the filament, heating Au which then evaporates. It is important to point out that Au, once melted, wets the filament rather than dropping off it. The filament is placed inside a cylinder made of Ta foil, with a hole in front of the filament acting as a collimator. The power applied to the filament is the parameter used to calibrate and control the deposition rate on the sample surface.

The first evaporation method gives a more precise control of deposition rate and final coverage. A feedback loop keeps the flux constant by controlling the voltage applied to the crucible, and thus a regular evaporation is obtained. The second method, on the contrary, is less systematic, as the deposition rate depends on the power, and the power depends on the resistance of the filament, which can change as the Au droplet/coating of the filament moves or changes shape - due to evaporation of Au or to thermal fluctuations in the heating/cooling phase.

On the other hand, the Au ions accelerated in the e-beam setup collide on the sample surface with a energy of up to 800 eV and therefore they can disrupt the structures on it – as it happens in the ion bombardment process used for surface sputtering –, they can implant in the surface or exchange atomic site [168].

2.1.3 Ultra High Vacuum

A clean environment is necessary for growing and studying atomically precise structures on solid surfaces. Minimizing interaction with foreign species assures a controlled interaction with the surface and neighbouring atoms during the growth, and avoids any unwanted perturbations in the properties of the pristine structures. In

particular, in order to reduce the presence of adsorbed contaminants in the gas phase, experiments are carried out in chambers where the ambient pressure is reduced to the maximum achievable by the current vacuum technology, the ultra-high vacuum regime. The pressure p determines the flux F of particles or molecules with mass m impinging on a surface in the unit of time and area through the relation

$$F = \frac{p}{\sqrt{2\pi m k_B T}}. \tag{2.2}$$

Assuming that a monolayer corresponds to $3 \cdot 10^{14} \frac{1}{\mathrm{cm}^2}$ adsorbed particles, and that all particles impinging on a surface stick to it (i.e. that the sticking coefficient $\theta = 1$), at 300 K a surface is fully covered by N_2 (molecular mass 28) in one second if $F = 3 \cdot 10^{14}$ cm^{-2} s^{-1} and therefore

$$p \simeq 10^{-6}\mathrm{Torr} = 1.33 \cdot 10^{-6}\mathrm{mbar}. \tag{2.3}$$

At 10^{-10} mbar then, a sample would be fully covered by impurities after 10^4 s (approximately 3 hours). In reality not all particles adsorb (i.e. the sticking coefficient $\theta < 1$), so that this is a lower limit. In order to assure a time span from hours up to a few days, the experiments in this thesis have been carried out in the $10^{-10} - 10^{-11}$ mBar range, within the Ultra High Vacuum (UHV) regime ($<10^{-9}$ mBar.

Details of the experimental setups including the equipment to maintain the UHV conditions are given in Sec. 2.3.

2.2 Characterization

2.2.1 Scanning Tunneling Microscopy

The Scanning Tunneling Microscope (STM) was the first instrument capable of obtaining three dimensional images of solid surfaces achieving atomic resolution. It was designed in 1981 at the IBM Research Laboratories in Zürich by Gerd Binnig and Herinrich Rohrer [169–172]. The STM, which exploits the tunnel effect and obtains a higher resolution, was successfully developed on the principle of the Topografiner, a field-emission scanner, which was invented in 1971 by Russel Young at the National Bureau of Standards in the USA [173].

The working principle is simple: a metallic tip, ideally with one atom protruding further than the others, scans a conductive surface at a distance of a few angstroms. According to quantum tunneling theory, for such small tip-sample preparations electrons have a certain probability of transmitting through the vacuum or air between the surface and the tip, and by applying a voltage V, a net current of electrons can be detected. Such a tunneling current depends on the tip-surface distance d as

$$I \propto \exp(-2\kappa d), \tag{2.4}$$

where κ is the decay constant of the wave function in the vacuum barrier and, when $\phi \gg V$, can be expressed as

$$\kappa = \hbar^{-1}\sqrt{2m\phi}, \tag{2.5}$$

where ϕ is the effective barrier height, equal to the work function in a first approximation [174]. This is the origin of the high resolution obtainable in STM, as it follows that for typical work functions of 4 eV, changing the distance by 1 Å results in a current change of one order of magnitude. This exponential behaviour also implies that most of the current tunnels through the last atom of the tip, which brings the lateral resolution to the atomic scale.

Based on the Bardeen theory of tunneling and its application to scanning tunnelling microscopy by Tersoff and Hamann [175, 176], the tunnelling current in the limit of low temperatures can be more correctly expressed as

$$I = \pm\frac{2e\pi}{\hbar}\int_{E_F}^{E_F+eV} \rho_T(E-eV)\rho_S(\vec{r}_0,E)\,T(\vec{r}_0,E,eV)\,\mathrm{d}E \tag{2.6}$$

where V is the voltage applied between tip and sample, $\rho_T(E-eV)$ is the density of states (DOS) associated with the tip, $\rho_S(\vec{r}_0,E)$ the DOS of the sample at the tip position $\vec{r}_0$, and $T(\vec{r}_0,E,eV)$ the transmission probability between tip and sample at the tip position.

This means that the tunnelling current is actually a convolution of the DOS of both the sample and the tip. Therefore, a metallic tip with a constant DOS around E_F is often desirable, in order to minimize tip effects. In metals, the main limitation are the d states, which show highly structured DOS. An alloy of Pt/Ir is often used,

though sharper tips can be etched from W wires. In such case, a constant DOS can then be obtained by e.g. dipping the tip in the surface of a noble metal sample (Au, Ag), for which the d states lie at high binding energies [177].

A direct consequence of Eq. (2.6) is that the resulting image has to be interpreted, as it does not necessarily represent a topographic map of the surface: the *apparent height* depends on the local density of states (LDOS) under the tip. For instance, metal atoms will often appear higher than molecules which topographically have the same height, and adsorbates with significantly lower DOS than the surrounding surface can appear even with lower apparent heigth than the surface.

The STM operates by scanning the surface line by line and registering either the tip height z over the surface while keeping the current at a fixed value through a feedback loop or registering the current at a fixed z, with the feedback open. These are known as constant current (C.C.) and constant height (C.H.) mode, respectively. C.C. mode is generally preferred, while C.H. mode is limited by the roughness of an area and is more used in spectroscopic measurements.

The line-by-line scanning is relatively slow: for instance, in our STM systems (Sec. 2.3), typical image acquisition times vary between ~20s for flat, low-area scans ($\leq$ 10x10 nm^2) to a few minutes for large areas. These are typical timescales for STM scanning, although recent techniques allow frame rates of up to 60 Hz [178, 179]. Thermal drift, i.e. the deformation due to the thermal fluctuations and the relative expansion/compression of the different materials, can therefore be an issue, and often a correction of the images is necessary. A different cause of deformation to care for is the piezoelectrics creep, i.e. their time-dependent response, possibly resulting in non-linear deformations.

The full potential of Scanning Tunneling Microscopy is available when scanning at low temperatures. Low temperatures are usually kept by contact to a cold reservoir of either liquid N_2, at ~77 K, or liquid H_2, at ~4 K, which also minimizes thermal fluctuations. As the temperature is lowered, the thermal energy falls below diffusion barriers and vibrational excitations, therefore single molecules and atoms become stable. Furthermore thermal drift is minimized, as the thermal expansion coefficients and their differences between materials are reduced. These effects are important for STM imaging but also for Scanning Tunneling Spectroscopy, introduced in the following.

2.2.2 Scanning Tunneling Spectroscopy

Since the tunneling current is directly related to the density of states of the sample in a controllable energy range, the Scanning Tunneling Microscope allows spectroscopic measurements. These consists of a series of techniques which go under the name of Scanning Tunnelling Spectroscopy (STS).

From Eq. (2.6), it derives that for a constant tip DOS ρ_T,

$$\frac{dI}{dV} \propto \rho_S(\vec{r}_0, E) \tag{2.7}$$

which implies that the derivative of the current gives direct access to the sample DOS at the selected energy, corresponding to the applied bias voltage. The tip DOS is not always constant: in such cases, when even *in situ* tip preparation methods are not sufficient to achieve a constant tip DOS, it is necessary to carefully analyse spectra of known structures and surfaces to determine the origin of the features in spectroscopy and subtract the background. This will be shown in Sec. 4.4.

2.2.2.1 Lock-in technique

A STS spectrum can be recorded by placing the tip at a fixed point and registering the current variation while sweeping the bias voltage in a selected energy range. As the signal-to-noise ratio is usually very low due to electrical and mechanical noise coupling to the current signal, a lock-in amplifier is often convenient [180]. The lock-in superimposes a small sinusoidal signal at a reference frequency ω_{ref} to the constant bias voltage V_{DC}, so that $V_b = V_{DC} + V_{mod}\sin(\omega_{ref} t)$, where V_{mod} is the amplitude of the sinusoidal modulation. Assuming a linear I(V) relation in the small $2V_{mod}$ range, the tunnelling current is proportional to the slope of the I(V) curve and thus to the derivative dI/dV, and will then contain a sinusoidal component with the same frequency as the bias, $I \propto dI/dV \sin(\omega_{ref} t + \phi_{sig})$, see schematics in Fig. 2.3. Here ϕ_{sig} is the phase of the current signal. This signal is converted to a voltage by the pre-amplifier of the STM, and the resulting total current signal is then

$$V_I(t) = V_{DC}^I + V_{sig}^I \sin(\omega_{ref} t + \phi_{sig}) + V_{noise}^I(t), \tag{2.8}$$

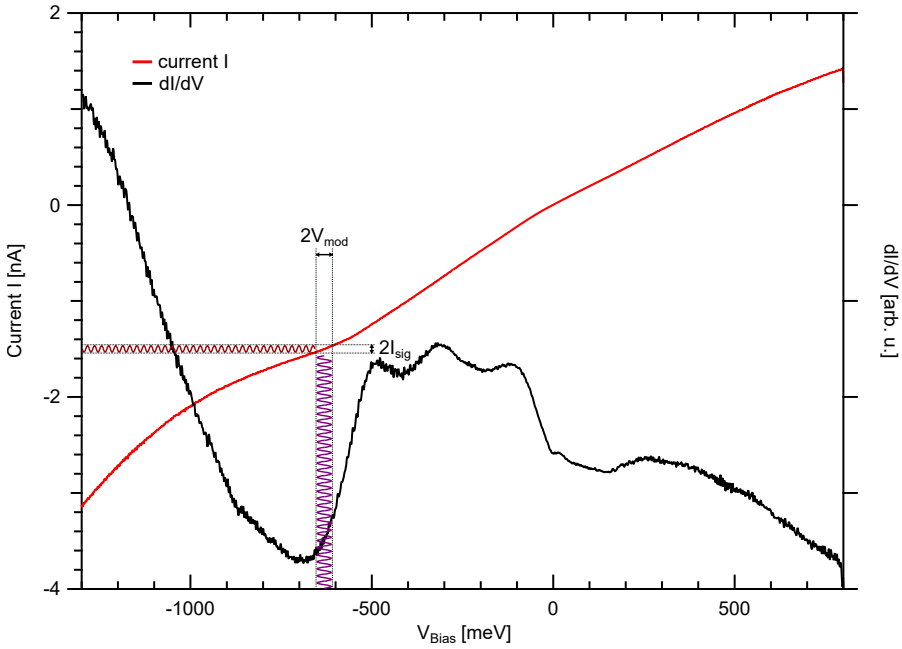

Figure 2.3: Schematics of the lock-in technique. A sinusoidal signal is added to the bias voltage during an I-V ramp. The amplitude of the resulting modulation in the current signal is proportional to the slope of the I(V) curve, i.e. to the dI/dV derivative.

where V^I_{DC} is the DC component of the current, V^I_{sig} is the signal containing the dI/dV, proportional to V_{mod}, and $V^I_{noise}(t)$ the noise in the system. This is multiplied by the lock-in with a reference signal at the same frequency $V_L(t) = V_{ref}\sin(\omega_{ref}t + \phi_{ref})$, thus the resulting signal contains the product of two sine waves:

$$\begin{aligned} V_{psd} &= V_I \cdot V_L = V^I_{DC} \cdot V_L(t) + V^I_{noise}(t) \cdot V_L(t) + \\ &\quad V_{ref}\sin(\omega_{ref}t + \phi_{ref}) \cdot V^I_{sig}\sin(\omega_L t + \phi_{sig}) \\ &= V^I_{DC} \cdot V_L(t) + V^I_{noise}(t) \cdot V_L(t) + \\ &\quad + \frac{1}{2} V_{ref} V^I_{sig} \cos(2\omega_{ref}t + \phi_{sig} + \phi_{ref}) + \\ &\quad + \frac{1}{2} V_{ref} V^I_{sig} \cos(\phi_{sig} - \phi_{ref}). \end{aligned} \tag{2.9}$$

The last term is constant, i.e. a DC signal. Then by applying a low-pass filter, i.e. integrating the signal over a time τ, all the AC components are sorted out and the

remaining signal is

$$V_{psd} = \frac{1}{2} V_{ref} V^I_{sig} \cos(\phi_{sig} - \phi_{ref}) + V^{psd}_{noise}, \tag{2.10}$$

where V^{psd}_{noise} is the component of the current noise with frequency equal (near) to ω_{ref} resulting from the $V^I_{noise}(t) \cdot V_L(t)$ term of Eq. (2.9). Then, by choosing a ω_{ref} frequency containing low mechanical and electrical noise, and by setting a reference phase so that $\phi_{ref} = \phi_{sig}$, the dI/dV signal V^I_{sig} can be maximized and the noise sorted out.

In our experiments, we used modulation frequencies of 2500–3200 Hz, the lowest frequency range where our STM provides a clean reproducible tunneling current. Though with the typical gain of 10^9 the pre-amplifier has a 1000 Hz bandwidth, the cut-off slope is small enough to allow us working in such range. We set the reference phase ϕ_{ref} so that the reference signal is perpendicular to the capacitive noise in the STM circuitry, i.e. to the current signal detected out of tunneling.

The time constant τ determines the low-pass filter bandwidth: a higher integrating time results in a lower bandwidth, thus a higher signal-to-noise ratio. On the other hand, it also determines the minimum acquisition (sampling) time, so that a compromise is often needed. In our experiments, we typically used time constants of 0.3–10 ms and sampling time of 5–8$\cdot\tau$.

The intensity of the recorded dI/dV signal is proportional to the amplitude of the reference signal V_{mod}, but increasing V_{mod} means at the same time reducing the energy resolution. A good compromise can be achieved by e.g. setting a V_{mod} that allows the desired resolution for the measurement, and approaching the tip to the sample so to increase the current signal as much as possible. Depending on the resolution needed, V_{mod} was usually in the range 0.1–50 mV.

The other main limitations to the energy resolution are given by the uncertainty principle and the finite temperature. From the uncertainty principle $\Delta x \Delta k \geq 1/2$, it follows that for a metallic surface [181]

$$\Delta E \geq 0.47 \frac{E_F - E_0}{r\, k_F}, \tag{2.11}$$

where 0.47 is the relative intensity of the tip-induced local states, E_0 the bottom of the valence band and r the lateral resolution of the tip. For instance, when atomic resolution is achieved $r \leq 2$Å, and the maximum energy resolution is 0.2 eV.
The temperature also limits the energy resolution, as $\Delta E \approx 4k_B T$, which means that at room temperature $\Delta E \approx 0.1$eV. Since at the Helium boiling point of 4.2 K, $\Delta E \approx 0.0015$eV, it is evident that cryogenic temperatures are necessary for millivolt resolution.

2.2.2.2 Data acquisition modes

As in topographic imaging, also in STS two different acquisition modes are available, yielding different information on the electronic properties of the surface.

The example used in the previous section, where the tip height is fixed and the feedback loop open, is the constant height (C.H.) mode. It is used to locally investigate the full DOS of selected features of the surface. As the tip is kept in position by the piezos, special care must be taken in order to stabilize the scanner and avoid drift in the z direction. Drift compensation is also possible in our systems.

The other available mode is the constant current (C.C.) mode. Here, the feedback loop is closed and the tip z is adjusted in order to keep it constant while sweeping the bias voltage. As a consequence, the explored energy range cannot cross 0, in order to avoid tip crashes. This is mainly used to access the field emission resonance (FER) states confined in the vacuum between the tip and the surface, which is explained in more detail in Sec. 4.4.

In both modes, it might be useful to acquire lines or grids of point spectra (the latter is also known as current-imaging-tunnelling spectroscopy, CITS [182]). The setpoint bias and current are used while moving the tip in x and y direction along the selected line/grid of points, and a spectrum is then acquired at each point. In this way, a spatial study of the full DOS in 1 or 2 dimensions can be made. For instance, we acquired lines of C.H. spectra across an interface to determine the existence and spatial distribution of 1D states. Care must be taken as the tip height can vary from point to point.

Once the DOS is known, a dI/dV map can be acquired by registering the dI/dV signal while scanning an image at selected bias V_b, either in C.H. or C.C. mode. The resulting image is a map of the spatial variations in the LDOS at energy $E = E_F +$

eV, which can give information on the extension and the spatial modulation of an electronic state on a surface. This technique was used in this work to study how scattering at surface defects determines the spatial distribution of electronic states by creating quantum interference patterns.

2.2.2.3 Quasi particle interference mapping

Quasi particule interference (QPI) patterns are due to the scattering and consequent formation of standing waves of electrons or quasi-particles of a 2-dimensional electron gas (2DEG), such as those occupying surface states or belonging to 2D materials like graphene. Reflection can take place at defects, impurities, edges and boundaries on the surface. Thus, one can obtain information on the interaction of adsorbates and nanostructures with a known surface [183], but most importantly on the nature of the 2D electronic state itself. For instance, the scattering amplitude depends on the spatial distribution of the scattered electrons wavefunction, and from the standing waves wavelength the dispersion relation of the state can be extracted. In fact, the wavelength λ of the resulting standing waves corresponds to a scattering wave vector $\vec{q} = \vec{k}_i - \vec{k}_f$. 2D Fourier analysis of the dI/dV maps allows direct visualization and measurement of the scattering wave vector. This is usually done by looking at 2D Fast Fourier Transformation (FFT) maps, where the periodic features of the real space image appear as maxima in reciprocal space. For instance, in the simple case of backscattering of an electron belonging to a parabolic surface state centred in Γ, such as that of Cu(111), Fig. 2.4, since $\vec{k}_f = -\vec{k}_i$, the FFT will show a ring centred in Γ with radius $q = 2k$ and therefore the state wave vector at energy E is $k(E) = q/2$. By recording dI/dV maps at different bias voltages, the full dispersion relation $k(E)$ of the state can be constructed.

However, $k(E)$ can not always be directly extracted, since FFT maps only represent the dispersion of the scattering vector $q(E)$. On the Au(111) surface, for instance, where Rashba spin-orbit coupling gives rise to two split parabolic bands with a non trivial spin texture [184], FFT maps of the surface state show only one ring centred in Γ, since the Rashba splitting is symmetric with respect to Γ: as is clear from the scheme in Fig. 2.4, q will have the same value for backscattering electrons in each of the two parabolas, and the absolute $k(E)$ relation can be exctrated from the $q(E)$ dispersion only by considering some assumptions on the band structure of Au(111).

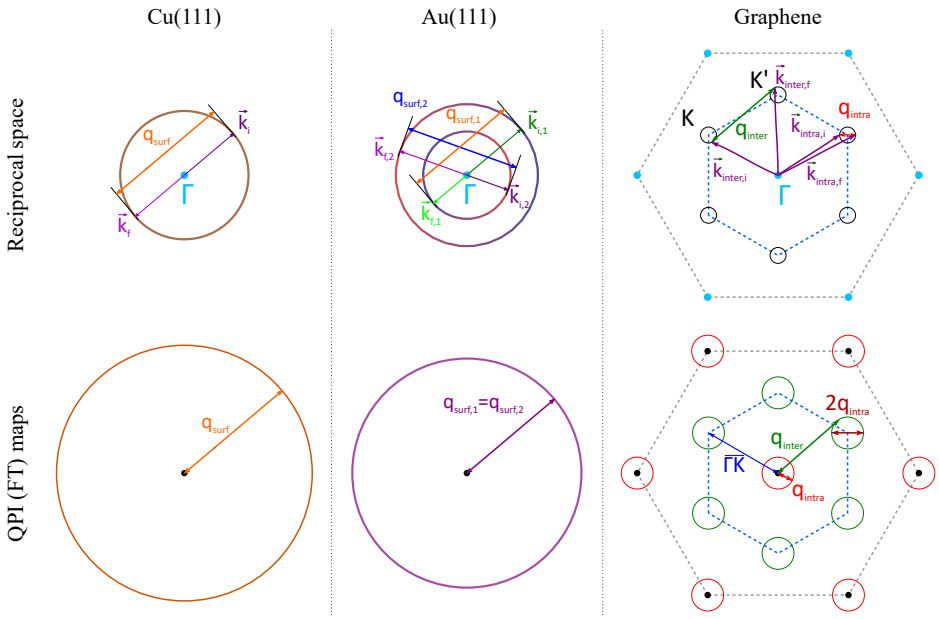

Figure 2.4: The scattering vectors in reciprocal space and the corresponding QPI (FFT) maps obtained are represented for Cu(111) as the most simple case, for Au(111) and graphene. In Au(111), FFT maps show only one parabola due to the symmetry of the Rashba-split surface state respect to Γ. In graphene, pseudo-spin is neglected. Both intra- and intervalley scattering vectors are indicated.

Fig. 2.4 also shows a schematic of the scattering vectors in free-standing graphene. As the scheme represents a section of the energy bands at $E \neq 0$, circles centred in the K (K') points represent sections of the Dirac cones. Charge carriers in the conical bands have two possible scattering routes: intra-valley scattering refers to backscattering inside the same cone (valley); inter-valley scattering is the scattering between neighbouring cones. The scattering vectors associated with the two processes are q_{intra} and q_{inter} . Neglecting pseudo-spin conservation in a first approximation, intravalley scattering results in rings with radius q_{intra} centered in the (0,0) point of the FFT and in higher order spots, while FFT of intervalley scattering will result in a hexagonal construction of circles, each centred at a distance $|\vec{K} - \vec{K}'| = \overline{\Gamma K}$ from the (0,0) point. The radius of the circle will still be q_{intra} , since $\vec{k}_{i,f} = \vec{K} - \vec{q}_{intra}/2$ [185]. Pseudo-spin conservation hinders the backscattering processes, and thus intravalley scattering is quenched in monolayer graphene, while different intensities characterize the rings found at $\overline{\Gamma K}$ from (0,0) [186]. Thus, it is in principle possible to probe the intrinsic electronic properties of graphene by QPI

mapping. Also, it has been shown that the properties of the susbstrate can be revealed by complex QPI patterns [187].

2.3 Experimental setups

We performed the experiments detailed in this thesis in two different systems: a chamber equipped with an Aarhus 150 Variable Temperature STM (VT-STM), able to operate between 77 K and 400 K, and a second one equipped with a Createc Low Temperature STM (LT-STM) which operates between 4 K and 300 K. We used the first system mainly for characterizing the growth and the structural properties of the samples at RT, as preparation of the sample and analysis are much faster and versatile in its chamber. The LT-STM setup was mainly employed for electronic characterization through STS measurements.

2.3.1 Variable temperature system

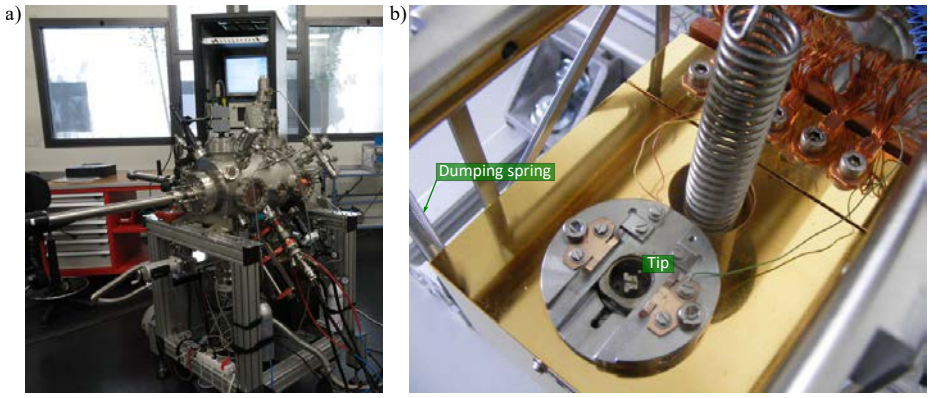

Figure 2.5: (a) The VT-STM system in its laboratory and (b) the head of the microscope

The VT-STM is mounted in a UHV chamber pumped by a turbomolecular and an ionic pump which maintain a base pressure $\leq 3 \cdot 10^{-10}$ mbar. A titanium sublimation pump is also available. The system is shown in Fig. 2.5. Though not relevant for the present thesis, it should be noted that the chamber is mounted on a aluminium structure equipped with wheels, allowing the whole system to be moved and connected to other systems: this was done to combine STM and synchrotron light (XMCD) measurements at the ALBA Synchrotron facility. Heating of the sam-

ples is performed in an electron beam heating stage in the same chamber. A pyrometer pointed on the sample surface or on the sample holder (see Sec. 2.3.3) monitors the temperature at each stage of preparation. The STM is mounted on a heavy copper block offering mechanical and thermal stability, the latter enhanced by the gold capping. Three springs hold the copper block, isolating from mechanical vibrations. The stiffness of the parts and the vibration-isolating system of the microscope allow it to be operated it while all pumps are running. However, even in such conditions, atomic resolution is easily achievable.

2.3.2 Low temperature system

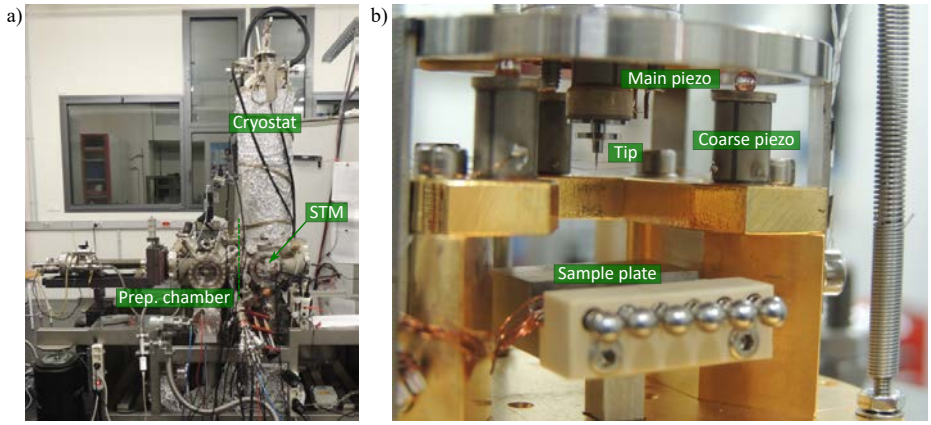

Figure 2.6: (a) The Createc LT-STM system and (b) the head of the microscope

The LT-STM is mounted in a second UHV system equipped with two separate chambers, one for sample preparation and one for low temperature STM characterization. Each chamber is equipped with an ion pump and a Titanium sublimation pump, and a turbomolecular pump is connected to the preparation chamber. A separate loadlock chamber for sample insertion is available. The whole system is mounted on four air-pressured legs for isolating from vibrations. The heating system of the sample is integrated in the sample holder itself: a Mo-covered resistive oven holding the sample is mounted on a heavy metal holder. Contacts for a thermocouple attached to the oven itself are provided in the back of the holder. The same thermocouple and oven contacts are used to carry bias voltage in the STM. The microscope is mounted inside a double shield: in normal operation, the inner

shield is kept at 4–5 K by a cryostat filled with liquid Helium. At this temperature, even light gases such as H_2 are completely adsorbed on the cryostat walls. The pressure at the sample surface in the shield is consequently $\sim 10^{-11}$mbar, which is the lower limit for ion gauge measurement. The outer shield, connected to an external crysotat concentric to the first, serves as a buffer layer and is kept at 77K by liquid nitrogen.

2.3.3 Temperature measurements

The growth of graphene nanostructures by CVD is highly sensitive to the characteristics of the annealing process: a precise and reproducible control of heating ramp, annealing temperature and cooling rate is necessary for reproducible preparations of nanoislands. Measuring temperatures in UHV systems is usually done by either K type (Ni/NiCr) thermocouples attached in the proximity of the sample on the annealing system, or by pyrometers pointed to the sample surface or its vicinity. In our VT-STM system, there is no thermocouple installed on the annealing stage, and a pyrometer is used instead. In the LT-STM system, a thermocouple, usually spot-welded to the heating element of the sample holder, a few mm away from the sample, is available. The geometry of the preparation chamber also provides optical acces for pyrometer measurements though.

Two different pyrometers from IMPAC are available: one has a PbSe sensor measuring in the spectral range of 3–5 μm , sensitive to temperatures ranging from 50 to 1200°C, while the second one has a InGaAs sensor measuring in the 1.45-1.8 μm range of wavelengths and in the 300–1300°C temperature range. As the usual glass (Kodial) windows for UHV systems have a transmission coefficient $< 50\%$ for wavelengths above ~ 2.5 μm, one sapphire window is available in each of the two systems to allow measurements with the low range (LR) pyrometer. The high range (HR) pyrometer can in principle measure through any of the two types of windows.

It was evident during the course of the experiments, that the preparation recipe for graphene nanoislands could not be directly transferred between different UHV systems, but needed to be adapted in each case. The reason for this is that the heating/cooling ramps can differ depending on the annealing system available and one cannot rely on the absolute temperature measurement, even when using the same measuring method. Thus, a careful calibration is needed. For instance, the read-

ing of the pyrometer depends on the lighting conditions, on the emissivity of the sample surface (which in turn depends on the sample material, the polishing of the surface, the facet exposed, the flatness, etc.), and on the angle of measurement, etc. Consequently, the measurement can vary across different setups. Moreover, the two pyrometers usually differ in output in the same conditions on the same sample.

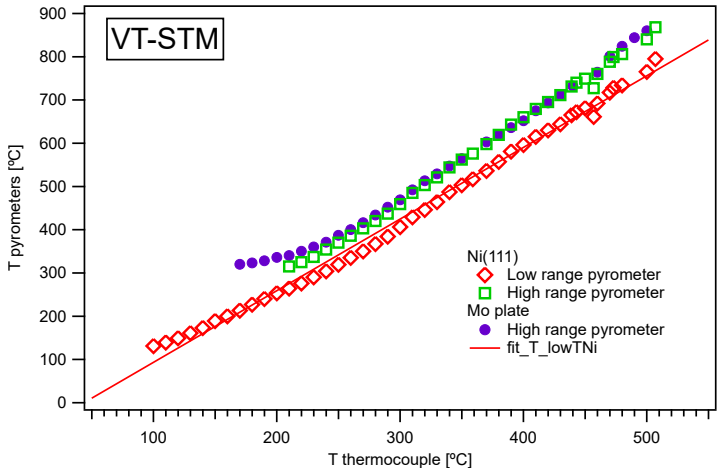

Figure 2.7: Graph of the temperatures measured in the VT-STM on the Ni(111) surface with the two pyrometers and on the Mo sample plate with the high temperature pyrometer as a function of the temperature measured with a thermocouple placed on the surface of the crystal

Fig. 2.7 shows the temperature measurements carried out during various heating ramps on the Ni(111) sample in the VT-STM system. For this calibration, a thermocouple was especially installed on the annealing stage and held on the sample surface by a Ta foil. The temperature measured with the two pyrometers on the sample surface and with the HR pyrometer on the Mo sample holder was registered as a function of the thermocouple reading. The first evident result is that the temperature measured by the pyrometers is approximately linear to the thermocouple reading, with a slope of ~ 1.6, indicating that the pyrometers can measure up to 300°C higher than the thermocouple in the considered range. Also, the two pyrometers differ in output between each other by 50-70°C. The notable result is that measuring on the Mo plate or on the Ni(111) surface is equivalent: this is relevant because the measurement on the Mo plate can be repeated and calibrated with any sample mounted.

A similar graph is shown in Fig. 2.8 for measurements in the LT-STM system.

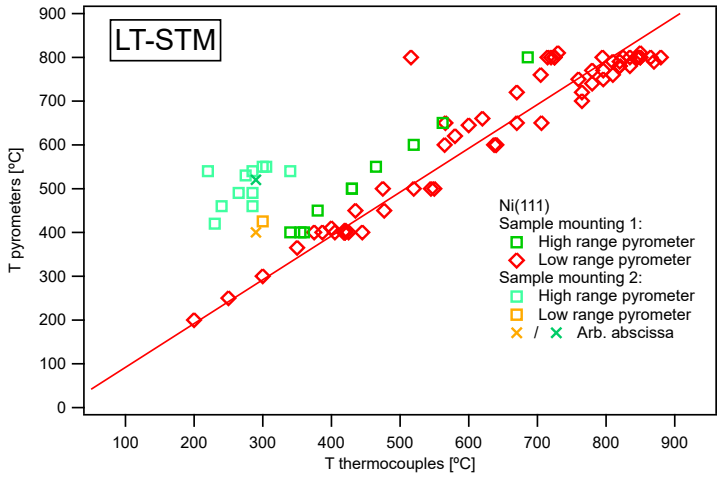

Figure 2.8: Graph of the temperatures measured in the LT-STM on the Ni(111) surface with the two pyrometers as a function of the temperature measured with a thermocouple spot weld on the oven. Two series of measurements are shown, for two distinct mountings of the sample and the thermocouple on the sample holder. Each point in series 1 corresponds to a single annealing, with the thermocouple temperature as reference. In series 2, points where both measurements are available were recorded during the same annealing procedure. The crosses indicate a single annealing where no thermocouple measurement is available. The red line is a linear fit of the red squares, with a fixed coefficient of 1 (y=x+b), as a guide to the eye.

Here, two different series of data are shown, as the measurements were repeated with a different mounting of the thermocouple. In the first series, the LR pyrometer measured nearly the same temperature as the thermocouple, thus the points fit a line with slope fixed to 1, which then intersects the Y axis at -8°C. The HR pyrometer measures 20-100°C higher than the LR one.
The second series has only two points where both pyrometers readings are available. In contrast to the first series, the points were measured during the same preparation, while keeping the surface at nearly constant temperature. As can be observed, the temperature differences are 120 and 125°C.
The difference between the two series evidences how crucial is the positioning and the contact of the thermocouple on the sample holder, which is not always easily reproducible.

In the VT-STM system, using the temperatures measured with the HR pyrometer generally yields the expected results: after annealing to 600–800°C, the sputtered Ni surface results in flat terraces; after exposure to carbon precursor, only nickel carbide is formed when annealing $\lesssim$ 450°C [160, 188]; both graphene and carbide are

found at higher temperatures [161, 189], and finally high or complete carbon dilution to the Ni bulk is achieved around 650°C [189–191]. Therefore, the measurement from the HR pyrometer in the VT-STM system has been taken as an absolute reference, and the other measures are reported to this through the available calibration curves.

A true and complete calibration in the LT-STM system was not found. Using the high temperature pyrometer, already above 550°C the coverage of graphene was usually very low, as expected when carbon dilution is thermally activated, and no preparation above 600°C showed graphene. As a consequence, we consider that an offset of 50°C is to be considered, compared to the VT-STM system, when using this pyrometer: this is the reference used for the current thesis. All temperatures reported for preparations in the LT-STM system with the high temperature pyrometer correspond to actual measurements which are 50°C lower. The other pyrometer and the thermocouple measurement are converted to this through calibration. However, the difference in annealing ramp, and possibly other details of the system, did not allow to completely reproduce in the LT-STM preparations from the VT-STM system (lower coverages and more disordered shapes of graphene nanoislands were generally found). Thus, we are not fully confident of the temperature readings in this second setup. In any case, all structural studies related to the synthesis and reaction temperatures were performed in the VT-STM.

Chapter 3

Growth and characterization of graphene nanoislands on Ni(111)

Nickel is one of the most employed substrates for the growth of graphene. The study of the growth of graphitic carbon layers on nickel dates longs before the isolation of graphene [192]. As a consequence of the good lattice match and the strong chemical bonding, graphene grows epitaxially on this surface: having a face-centered-cubic lattice structure with a lattice constant of 3.52 Å, its (111) facet has a triangular unit cell with lattice constant of 2.49 Å, differing by only 1.4% from the lattice constant of graphene (2.46 Å). The unstrained 1x1 stacking can lead to the growth of high quality, large-area single crystal graphene layers.

However, the chemical and geometrical advantages contrast with the difficulties arising from the complex growth mechanism, where different concurrent processes lead to different structures [159]. As a consequence of the high carbon solubility in Ni, graphene formation originates from both hydrocarbon decomposition at the surface and carbon segregation from the bulk [193]. This often leads, in ambient CVD growth processes, to multi-layer graphene structures [194–198], due to formation of graphene layers by carbon segregation under the grown layer, upon cooling of the samples [196, 197]. Recently, multi-layer formation has been demonstrated also after growth in UHV conditions, either attributed to bilayer [199] or to nickel carbide [161, 162, 200] formation originating from segregation of C under graphene, especially in weakly coupled rotated areas. The growth of the carbidic Ni_2C phase is another complication of the growth process, and has been subject of intense inves-

tigation. Its formation can compete with graphene growth [188], but Ni_2C can also transform into graphene [159, 189, 201], or decouple graphene from the substrate [159, 161] .

The above mentioned features and issues have been studied for the growth of extended graphene on Ni(111). Here, the edges do not play a role. In the case of graphene nanostructures, instead, edge energetics have to be taken into account, as they can be determinant. Previous work from our group has shown that the strong interaction of graphene with the catalytic Ni(111) surface leads to a temperature-dependent edge stabilization mechanism, by which graphene nanoislands (GNIs) with selected geometry and edge morphology can be obtained [75, 202]. The nanostructures thus grown reveal a particular interest because of the stabilization of graphene quantum dots with zigzag edges, for which electronic and magnetic effects have been predicted [40–42, 44] and observed [47, 76, 203].

During the course of this thesis, we have continued characterizing nanoislands obtained by the above mentioned method. By high-resolution STM imaging we identified and correlated the lattices of graphene and the underlying Ni, accessing to information related to the stacking, the edge structure, and the domain and boundary structures within the GNIs. This analysis has enabled a deeper insight on the growth mechanism of GNIs on Ni, resulting in important discoveries such as GNIs with non-equilbrium stacking symmetries, the coexistence of transparent and reflective domain boundaries, or the determination of the atomic structure of edge reconstructions.

This chapter presents such results. First, in Sec. 3.1, we will introduce the growth of GNIs on Ni(111), following the method developed in our group and the contributions brought to it. Sec. 3.2 is dedicated to the morphology of nanoislands: the stacking configurations, the morphologies of the edges, the energetics of these and their relation to the nanoislands shape. Next, in Sec. 3.3, we present the newly observed polycristalline nanoislands, the structure of the domain boundaries that we found and their properties. Finally, the effect of temperature on the stacking, the crystallinity and the shape of GNIs, entailing a controlled growth of graphene quantum dots, is discussed in Sec. 3.4.

The work in this chapter has been carried out in collaboration with Dr. Sofia Parreiras and Dr. Roberto Paniago from Universidade Federal de Minas Gerais (Belo

Horizonte, Brasil), and Dr. Maximiliano D. Martins from Laboratório de Nanoscopia, Centro de Desenvolvimento da Tecnologia Nuclear (CDTN) (Belo Horizonte, Brazil).

3.1 Growth by chemical vapour deposition

3.1.1 Ni(111) preparation

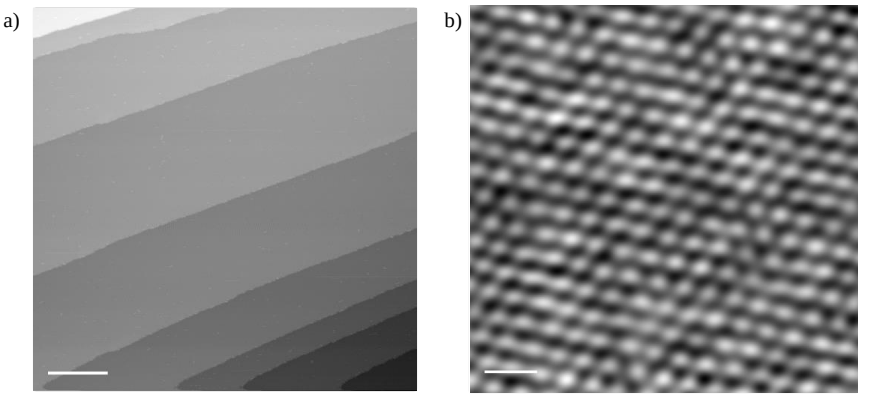

Figure 3.1: a) Typical STM topographic image of Ni(111) after a series of preparations. V_b=0.67 V, I_t=0.3 nA. Scale bar 30 nm. b) Atomic resolution of the Ni(111) surface. V_b=10 mV, I_t=3.25 nA. Scale bar is 0.5 nm.

For the experiments of this and the following chapters, we used as substrates two commercial Nickel single crystal with 99.9999% purity exposing the (111) surface. The two substrates were equivalent, with negligible differences in purity and surface order, so they will be referred to as "the substrate" with no differentiation. The crystal surface was cleaned by repeated cycles of sputtering-annealing. Ar^+ sputtering was performed at energies of 1-1.5 kV for 10-15 minutes at Ar pressures of ~10^{-6}mbar. Annealing was carried out at temperatures between 700 and 800°C for times varying between 10 seconds and 2 minutes. Sputtering energies and times, as well as annealing temperatures and times, were progressively diminished as the surface conditions improved. A typical image of the Ni(111) surface after such cleaning process is shown in Fig. 3.1a. Terraces have an average width of 35 nm, although flat planes of up to 200 nm are seldom found. Atomic resolution of the hexagonal lattice of the surface is shown in Fig. 3.1b.

Surface purity was ensured by controlling the abundance of adsorbed molecules as well as by the coverage of surface carbides. Carbon dilutes in Ni bulk at high

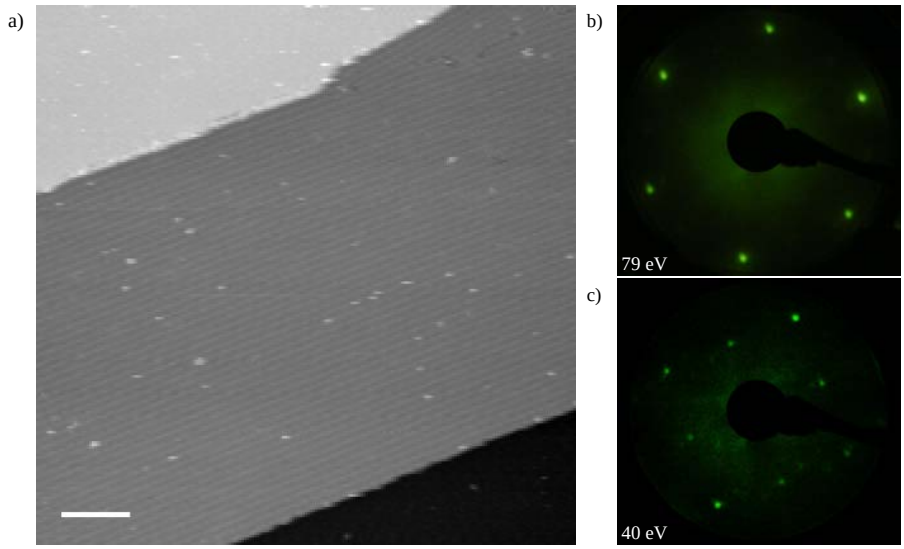

Figure 3.2: a) STM topographic image of Ni after few cleaning cycles with a base pressure of $2 \cdot 10^{-9}$ mbar, showing a part of a very large carbide domain, covering a whole Ni terrace. The presence of carbide is recognizable by the parallel lines, spaced 16 Å. The bright spots are residual impurities. Scale bar 10 nm. b-c) LEED of a Ni surface after few cleaning cycles, showing in b) an hexagonal pattern corresponding to the Ni(111) surface (beam energy: 79eV) and in c) the two quadrangular patterns of Ni_2C [161] (beam energy: 40eV).

temperatures and segregates to the surface upon cooling, bounding to the atoms of the surface to form monolayer Ni_2C structures [204]. These form domains preferentially at step edges and are recognized in STM by parallel stripes spaced 16 Å apart, given by their rectangular structure [160], as showed in Fig. 3.2a for a carbide domain found on the surface after few cleaning cycles. In LEED, they appear as two rectangular structures which are observed at low energy (~40 eV), as shown in Fig. 3.2c. As the abundance and size of such domains depends on the C doping of the bulk crystal, and especially the sub-surface region, sputtering-annealing cycles are repeated until few domains of relatively small size (<20 nm in longitudinal direction, as a rule of thumb) are found on the surface. This can take up to 30 cycles for monolayer graphene preparations [161], where carbon is continuously fed to the crystal at a high temperature. The history of a Ni substrate highly influences the amount of C diluted in bulk, and long and careful cleaning processes might be necessary on different crystals.In the experiments of this thesis, 4 to 10 cycles were generally enough to obtain the desired surface purity.

3.1.2 Growth of nanoislands

Previous work from our group has shown that it is possible to grow graphene nanoislands with selected geometry and edge structure on a Ni(111) surface by a modified Chemical Vapour Deposition (CVD) process - introduced in Chap. 2 [75, 154, 202]. The original preparation process consists of three steps:

1. Exposition of the Ni(111) surface to a dose D of molecular precursor (propene) at room temperature
2. Decomposition of propene and formation of irregular graphene nanoislands at reaction temperature $400°C \leq T_R \leq 500°C$
3. Post-annealing of graphene nanoislands at temperatures $500°C \leq T_{PA} \leq 650°C$ to select edge morphology and shape

The scheme of Fig. 3.3 illustrates the process graphically, with the necessary parameters. Ethylene has also been employed as a molecular precursor: though a systematic study of growth was not carried out, no difference in the resulting nanoislands was found, except that growth at temperatures ≤500°C was not possible.

The dose of molecular precursor fed to the surface affects the final yield of graphene nanoislands. For a $T_R = 500°C$, the final graphene coverage rises linearly with the dose until a saturation limit at around $D = 5\ L$ [154]. The saturation limit can be different at different temperatures, though. Also, the slower resistive annealing systems might require higher initial doses in order to obtain the same final graphene coverage, to compensate for the material loss in desorbtion and carbide formation. Doses of $2-50$ L were generally used.

Fig. 3.4a shows typical STM topographic images of the surface after preparation of the nanoislands at 400°C, while Fig. 3.4b-d show the effect of the post-annealing process at different temperatures. At 500°C the favoured shape is triangular, Fig. 3.4b. As the temperature raises the triangles evolve into hexagonal shapes: at 550°C, triangles with truncated edges (or, equivalently, irregular hexagons with alternated long and short edges) are preferred, Fig. 3.4c. At temperatures ≥ 620°C, hexagonal islands are stable, Fig. 3.4d. The reason of this evolution is the edge energetics at different temperatures. The equilibrium shape of free-standing graphene nanoislands is hexagonal, since the stable orientation for graphene edges is zigzag [49, 68, 205]. The

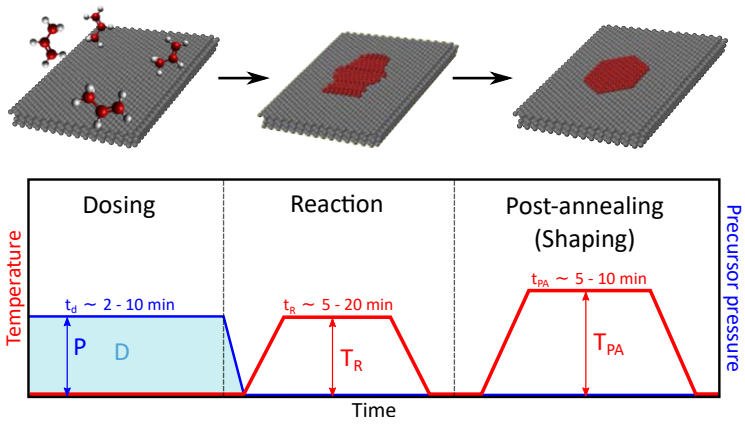

Figure 3.3: Scheme illustrating the graphene nanoislands growth process. The precursor pressure is the partial pressure of propene/ethylene. Once the dose is complete the sample is heated to a reaction temperature T_R during a time t_R. The surface reaction results in the formation of irregular graphene nanoislands. Post-annealing at a temperature T_{PA} during a time t_{PA} induces changes of the size and shape of the irregular graphene nanoislands.

stacking symmetry of graphene with Ni(111), though, groups the edges in three stable zz_h edges (i.e. zigzag edges having the outermost C atom in hollow adsorption site) and three unfavourable zz_t edges (where t indicates a top site). Edge structures differing from symmetric zigzag are favoured along the latter: the nature of these is discussed in Sec. 3.2. However, since graphene flakes grow by carbon attachment to the edges [154, 179], at low temperatures growth in zz_t direction appears to be kinetically limited as edges in this direction grow shorter than zz_h edges, giving the islands a triangular shape in the corresponding temperature regime. At temperatures ≥620°C, instead, the growth rate for zz_h edges and edges in the zz_t direction is similar and equilibrium hexagonal shapes are formed. We therefore call the temperature range between 500°C and 600°C a regime of kinetically limited growth, and that above 620°C the equilibrium growth regime. Above ≃ 600°C, though, diffusion of C to Ni bulk is active and competes with nanoislands growth, and above 650°C all surface carbon structures dissolve as carbon impurities into bulk Ni.

Along the latter, a reconstruction is energetically favoured, but is associated to an energy barrier.

Graphene nanoislands often display point-like features or zones of a higher apparent height. Profiles taken over these zones reveal a height of 2.1 Å, coinciding with the height of Ni steps on the surface (2.1 ± 0.3 Å in our measurements), and

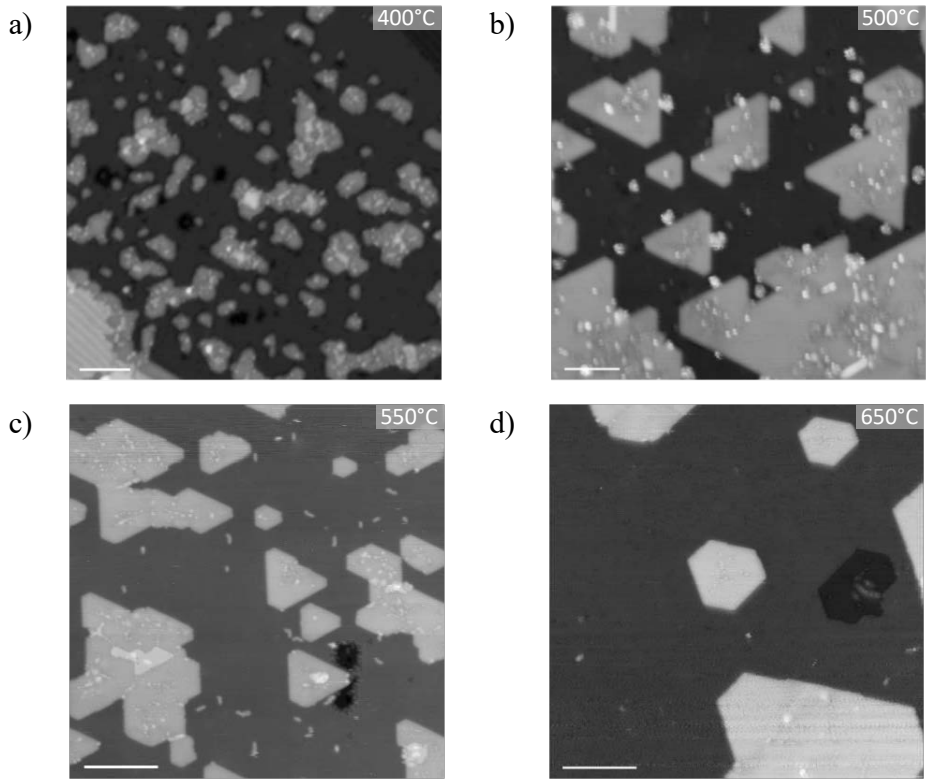

Figure 3.4: STM topographic images of graphene nanoislands after (a) preparation at 400°C and (b-d) post-annealing at 500°C, 550°C and 650°C, respectively. The scale bar is 10 nm.

spectroscopic measurements display the features *d* orbitals of Ni [76]. Moreover, recent work by Patera et al. [179] showed that, at growth temperature, Ni atoms from the topmost layer can diffuse and bond to the graphene edges, where they catalyse the growth. It is probable then that a part of such atoms is trapped during growth and remains in the final graphene structures.

In the growth process, many different variables affect the final result. In the annealing process, not only the final temperatures T_R and T_{PA} count, but also the heating and cooling rates. The heating process should be as fast as possible from RT to the final temperature, as different temperatures correspond to different growth regimes which can affect the final morphology of graphene nanoislands. Precursor molecules adsorbed by dissociation of only one hydrogen atom [206] can desorb from the surface below reaction temperatures, during the first growth step. Also, the

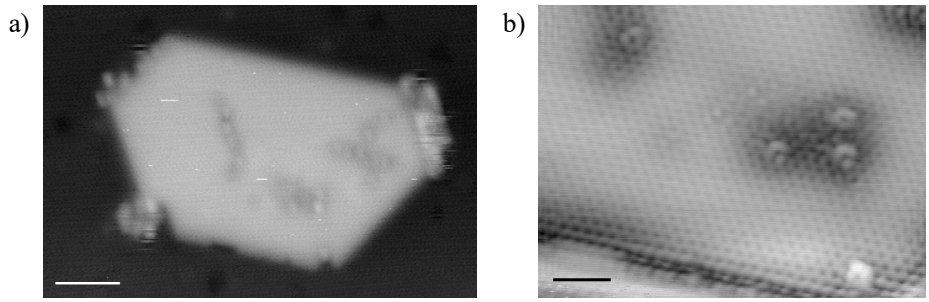

Figure 3.5: a) STM topographic image of a graphene nanoisland containing various Ni impurities, visualized as spot-protrusions. Scale bar 3 nm. b) Zoom on the bottom right edge of the island in (a), evidencing the presence of Ni impurities in the graphene bulk as well as at the edge. Scale bar 1 nm.

carbide phase forming during Ni(111) preparation can form also during the graphene growth process, especially as it is the only stable carbon structure at temperatures < 450°C. The formation of carbide competes with nanoislands growth, although carbide can be converted into graphene over long time scales at reaction temperature [159, 188, 201]. Cooling should also be fast, for similar reasons. In electron beam heating systems, the requisites of fast annealing ramps are easily satisfied, and heating/cooling rates of 12°C/s and 2°C/s are usually employed Resistive annealing systems are generally characterized by a higher thermal inertia, resulting in slower rates. In the LT-STM, the heating and cooling rate are both 1.5–2°C/s. Thus, it is evident how adapting growth to different systems can be difficult, as also discussed in Chap. 2.

3.1.2.1 Single annealing growth

The growth process described above is composed by two heating stages: one for nucleation and growth of nanoislands, and a second one dedicated to shaping. This step-by-step method allows control of each process and the possibility to correct the results by e.g. repeating some of the steps. This is especially necessary when pursuing hexagonal islands, as these grow in a temperature regime where concurrent dissolution of C into bulk Ni occurs, resulting in a final coverage lower than that obtained after growth of nanoislands. A coverage >30% before the shaping step is often desirable in order to ensure a final coverage of hexagonal GNIs ≥ 15%.

However, this multisequential method is highly time consuming, and a simpler procedure is desirable. The growth and nanostructuring steps are not really differ-

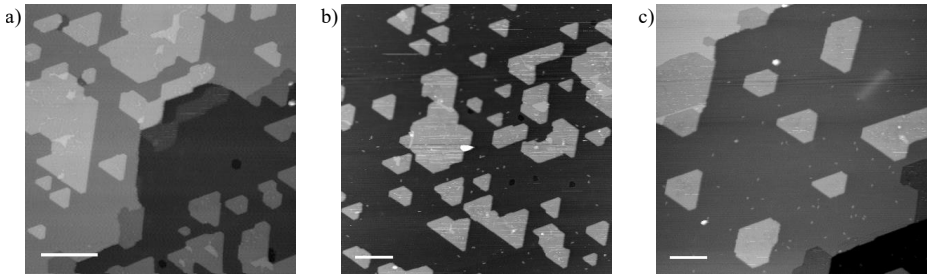

Figure 3.6: a) STM topographic image of GNIs grown on Ni(111) using D=25L of ethylene at a reaction temperature of 600°C, displaying triangular shapes with corner truncation in few cases. The coverage of graphene islands on the sample is 47% of the surface area. b) Another preparation of GNIs using ethylene with D=25L and T=625°C, where the same triangular and truncated shapes are visible. A number of islands with irregular shapes can be recognized as smaller triangular islands joined together. The coverage on the sample is 25%. c) STM topographic image of the same surface of (b) after annealing to 650°C for 10 minutes. The coverage is now 20%. The stabilization of the zz_t edge direction is recognizable. Scale bars (a-c) 20 nm.

ent processes, since the graphene nanoislands grow also during the shaping step. Therefore, in principle the two annealing steps can be merged in a single one. Although a full, systematic study of growth of nanoislands with one annealing step has not been carried out, this has been tested in more than 25 experiments, using annealing temperatures of 600°C $\leq T \leq$ 650°C.

In general, we observe structures similar to those grown with the 3-steps method. However, the absence of a previous reaction step has to be compensated with longer annealing times. This is seen for instance from Fig. 3.6a-b, where growth at 600°C and 625°C for 2 minutes, respectively, yields triangular and truncated nanoislands rather than hexagonal. After post-annealing to 650°C for 10 minutes, the triangular nanoislands of Fig. 3.6b evolve in hexagonal nanoislands (Fig. 3.6c), but the coverage is reduced from 30% to 20%. Therefore, for short annealing times triangular nanostructures might persist, but for long annealing times C might dissolve into the bulk of Ni.

A single-step annealing can be interesting not only for speeding up and simplifying the method, but also to avoid the formation of multiple domains at intermediate temperatures, as will be discussed in Sec. 3.3. However, the growth of hexagonal islands usually still requires (or benefits from) an intermediate reaction step where irregular or triangular GNIs are formed in order to avoid excessive diffusion to bulk. Since growth of graphene flakes happens preferentially by bonding of C atoms to

clusters or between clusters [155], the presence on the surface of large clusters, i.e. graphene nanoislands, can ensure a higher final coverage.

3.2 Stacking and edge morphology

The exact stacking of graphene on Ni(111) has been investigated for long time, and many structures have been proposed: top-fcc, top-hcp, fcc-hcp, bridge-top, bridge-fcc, etc [207–210]. For graphene monolayer the most abundant and therefore most stable stacking was found to be top-fcc, followed by bridge-top and top-hcp [209, 211], although bridge-top was not identified until recently [207, 208]. For graphene nanoislands, top-fcc and top-hcp stackings were identified [75], with top-fcc as the most stable, as confirmed by DFT calculations [202].

In the following we present a comprehensive study of the stacking configuration of GNIs. By simultaneously resolving the graphene and Ni lattices, we determine several coexisting configurations and discuss their correlation with the particular island shape. First, we present the 1x1 stacking family, which can be grouped in two sets: i) the top-hollow stackings, namely top-fcc and top-hcp, which are the ones where edge energetics enables their shape selection. ii) bridge-top stackings, where pairs of atoms from the two sublattices bridge the Ni atoms of the top layer. Here we find non-equilibrium shapes related to an unconventional growth mechanism. We then describe rotational domains that lead to stacking configurations beyond the simple 1x1 configuration.

A precise determination of the stacking of the islands was only possible after correction of thermal drift, fitting the atomically resolved graphene and Ni lattices into rigid hexagonal models and examining their stacking relation. This was done by applying a compression in the slow-scan (y) direction together with a shift of one pixel in the fast-scan (x) direction at each n^{th} line. The level of compression and the interval n have been adjusted carefully to match the Ni atoms in the resulting image with a Ni hexagonal lattice model. This same method has been applied also in the following sections of this chapter.

3.2.1 1x1 stacking

Fig. 3.7 shows three triangular graphene nanoislands on Ni(111), after growth at 470°C and post-annealing to 560–575°C. The three represent unrotated 1x1 stack-

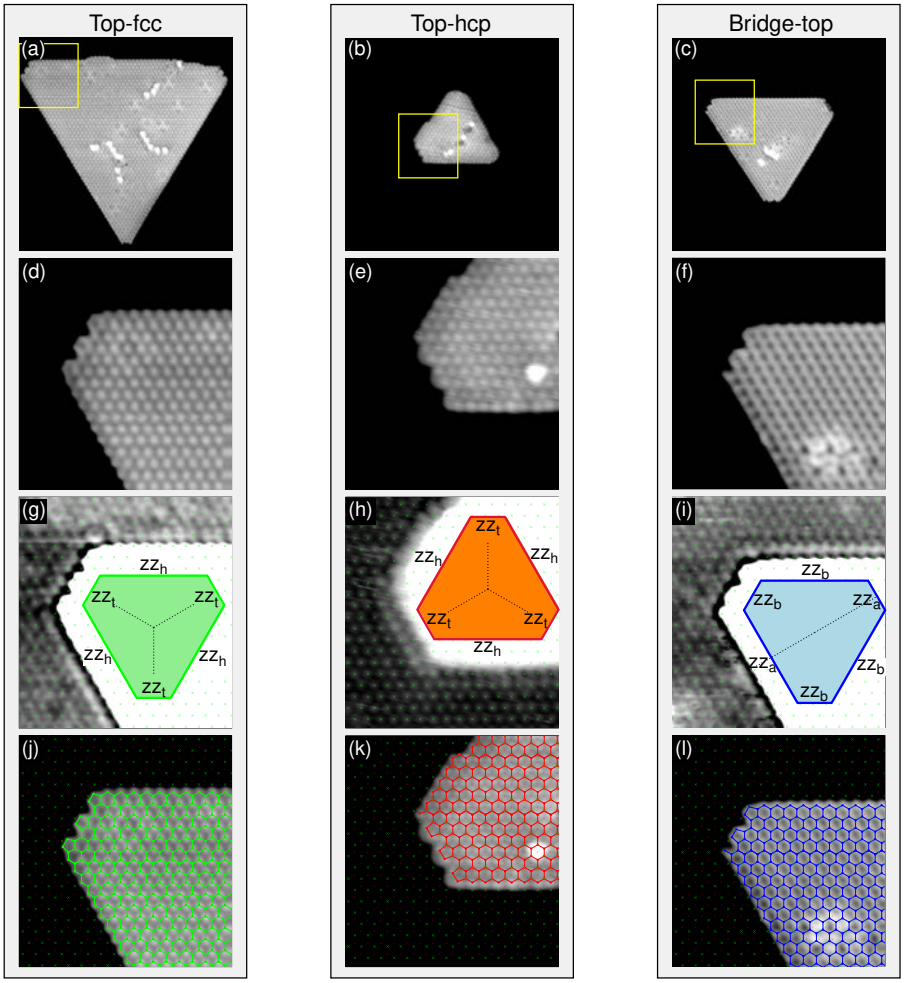

Figure 3.7: Graphene islands of top-fcc (a), top-hcp (b), and bridge-top (c) stacking. By adjusting brightness and contrast we image either the graphene structures (d-f) or the underling Ni atoms (g-i), which correspond to the zoomed areas indicated in (a-c). The triangular shapes of top-fcc and top-hcp configurations, with 60° of relative rotation, follow the three-fold symmetry of their zigzag edge stackings - see labels schematics in (g) and (h). In contrast, the triangular shape of the bridge-top island is not consistent with the two-fold symmetry of the corresponding edge stacking (i) for this configuration In (j-l) we superimpose the Ni and graphene lattices. Green (red) marks represent the Ni top (fcc) sites. Image size: 16×16 nm^2 and 5×5 nm^2 for large and zoomed images respectively. Post-annealing temperature and tunneling conditions, grouped as (T, I_t, V_b): a) 575°C, 16 nA, 83 mV, b) 560°C, 10 nA, 24 mV, c) 575°C, 15 nA, 83 mV.

ing configurations that will be described in the following. A schematic of the main stacking symmetries is shown in Fig. 3.8. We will start discussing top-fcc and top-hcp stacked nanoislands, while the discussion of bridge-top stacking will be given in Sec. 3.2.1.3.

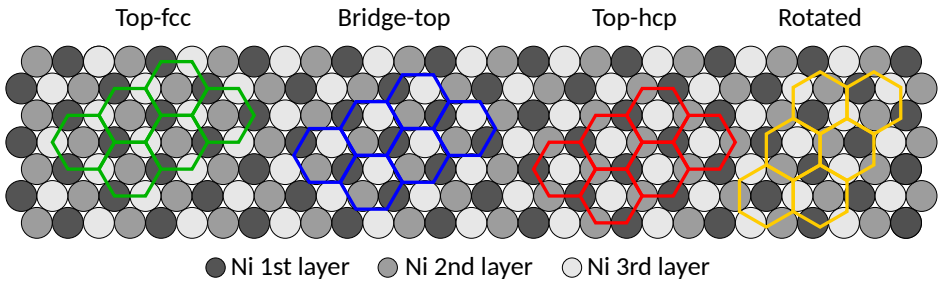

Figure 3.8: Scheme showing the stacking configurations observed for graphene on Ni(111). For the rotated stacking, an angle of 30° has been used as an example, because it is the most frequent – as discussed in Sec. 3.3.2.2

3.2.1.1 Top-hollow stacking

For top-fcc and top-hcp stackings, one sublattice of graphene sits on top of Ni atoms, while the other sits in hollow fcc or hcp positions, i.e. on top of Ni atoms of the 3rd or 2nd topmost layer, respectively. Top-fcc stacking is reported in both theoretical and experimental studies as the most favourable stacking geometry for graphene on Ni(111) [202, 207–209, 211, 212], while top-hcp stacking is found to have a slightly higher energy [202, 207, 211]. This is in agreement with the much lower abundance of domains or single islands in this stacking, as found by STM (see also Fig. 3.23). All top-hcp domains and single islands imaged by STM are small, below 15 nm^2, which can be explained by the increase of total energy difference with the number of carbon atoms between this and the top-fcc ground state.

The appearance in STM of the two stacking symmetries is similar: in top-hollow configurations, because of the different coordination of atoms adsorbed on top sites from those in hollow positions, the sublattice sitting in hollow position is imaged as bright protrusions, while the top sublattice is imaged with lower apparent height and the Ni from the 2^{nd} or 3^{rd} level appears as a dark pit in the center of the hexagon [202, 211, 213]. The difference between top-fcc and top-hcp stacking in STM is only given by the 60° difference of the two.

As noted from Fig. 3.7a-c, triangular nanoislands are defined and characterized by three long zigzag edges, and three shorter reconstructed edges corresponding to the corners (details on the atomic structure of the reconstruction will be discussed later in this chapter). For a given substrate orientation, top-hollow stacked islands in this shape are oriented the same way. Top-fcc nanoislands all point to the $[11\bar{2}]$ or equivalent direction in the plane. Top-hcp islands, instead, point to the opposite direction. This is a direct consequence of the stacking energetics of the edges in each case. As noted in Sec. 3.1.2, the most stable edge configuration for free-standing graphene is zigzag, but top-hollow stacking with Ni(111) separates the six zigzag directions in groups of three zz_h and three zz_t edges, with 60° rotation between edges in each group (see Fig. 3.10 for schematics of the edge configurations). The former ones are the directions of minimum energy (see Fig. 3.9 and [202] for edge energetics calculations), from which the triangular shapes. The orientation of the most stable zz_h edges between top-fcc and top-hcp stacking is rotated by 60°, which results in a relative rotation of the same angle of the islands between the two stackings.

3.2.1.2 Effect of edge energetics on shape selection

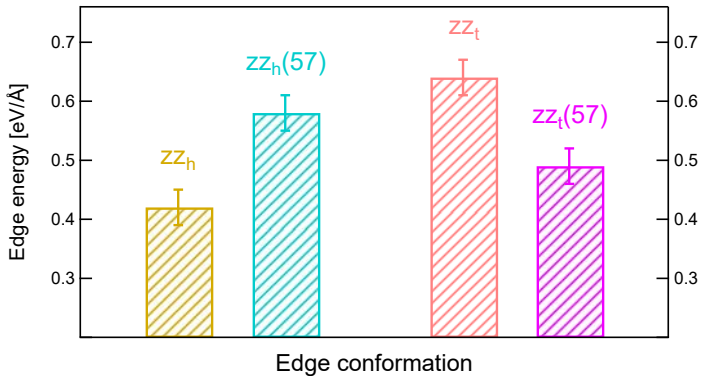

Figure 3.9: Edge energies per unit length for different edge configurations as calculated by DFT [202], evidencing the high energy cost of zz_t edges compared to zz_h , and compared to the pentagon-heptagon reconstruction $zz_t(57)$

The shape selection mechanism is determined by the edge energetics and the growth kinetics at the temperature of annealing (equally in the reaction or post-annealing step). Fig. 3.9 shows a graph of the edge energies formation per unit of length for different edge configurations explained in the following. In the most sim-

ple scenario, considering equilibrium growth and the absence of residual hydrogen, the triangular and hexagonal shapes observed at different temperatures can be explained in grounds of a 57 reconstruction of the zz_t edges, the most stable in this direction in the absence of H, and the energy barrier for their formation. If the thermal energy is below this barrier, the zz_h and zz_t energy difference is large enough to inhibit the growth of the latter. Then, zz_h grow long and triangular shapes result from the stacking symmetry, as discussed previously. Above this thermal threshold, zz_t edges reconstruct into $zz_t(57)$. The energy is considerably reduced, and the equilibrium ratio between the two edges increases: this gives rise to the hexagonal shapes obtained for temperatures >620°C.

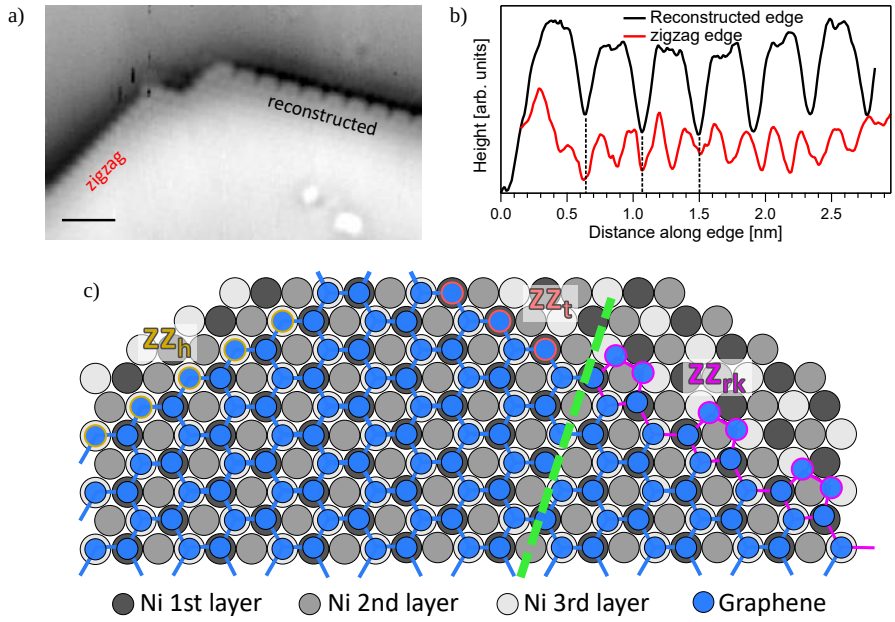

Figure 3.10: a) STM topographic image of a zigzag hollow and a reconstructed edges in a hexagonal island. V_b=23 mV, I_t=1 nA, scale bar 1 nm. b) Profiles along the two edges (not displayed in (a) for sake of clarity) evidencing the double periodicity of the reconstructed edge respect to the zigzag edge. c) Scheme displaying zz_h, zz_t and reconstructed zz_{rk} edges for a graphene flake in top-fcc stacking. Edge atoms are marked with a coloured border. The position of the atoms in the zz_{rk} is approximated to DFT calculations [214].

But a more complex scenario has been recently proposed, where hydrogen passivation can determine different reconstructions at the growth and imaging temperatures [214]. In this study, graphene edges are imaged in-situ at high T, showing that at the growth temperature zz_t edges reconstruct as 1x1 Klein (zz_k) edges, i.e.

zigzag edges with an extra C atom bonded to each outermost edge atom, and not as 57, the most stable at T=0 K according to DFT [202]. The authors do not find any T-dependent transition of the edge structure that could be correlated to the shape selection of islands we observe. In this case, the transition from triangular to hexagonal shape would be driven by kinetic arguments, rather than related to equilibrium structures. The RT images of Africh et al. do show, however, a 2x2 reconstruction of zz_t edges when imaging at RT. They attribute it to H-passivation of zz_k edges pairing Klein edges into pentagons, that are labelled as reconstructed Klein rk. A STM topographic image of the reconstructed edge and the proposed zz_{rk} structure are shown in Fig. 3.10

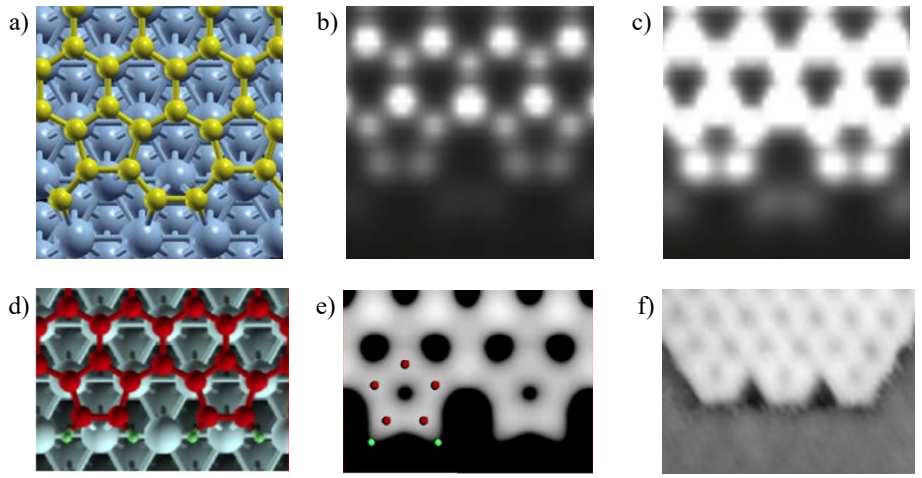

Figure 3.11: a) DFT-optimized structure for the 57 edge structure in top-fcc stacking symmetry. b-c) Constant LDOS maps at a distance of 0.95Å from the bulk atoms of graphene of the structure in (a). Two different limit LDOS are considered: in (b) the lowest LDOS at which the bulk C atoms are not saturated, while in (c) the value is the minimum for saturation of the atoms of the "5". d) DFT-optimized structure for the rk edge structure. e) DFT-simulated STM image of the rk edge structure. f)STM topographic image of a reconstructed edge, from an island post-annealed at 575°C. (d-e) adapted with permission from [214]. Copyright 2014 American Chemical Society.

The discrimination of the two RT reconstruction configurations is a difficult task, since the STM appearance is very similar in both cases, Fig. 3.11. According to DFT simulations, in the 57 reconstruction only the pentagon remains in the graphene plane, the heptagon being bent towards the Ni surface in order to saturate the uncoordinated C bonds. We still believe that the most likely structure is the H-passivated rk for two reasons: i) The heptagon could still be resolved slightly above the Ni plane

at high enough setpoint currents, but we do not see any hint of it in our best images, Fig. 3.11d. ii) the zz_h edges provide an indirect proof. There is a large difference in the height of the outermost atoms depending whether they are H or Ni passivated, the latter again being much closer to the Ni plane. From the fact that our images show zz_h edge atoms at the graphene plane, we conclude they must be hydrogenated, and correspondingly that the rk reconstruction is the most likely for the zz_t edges.

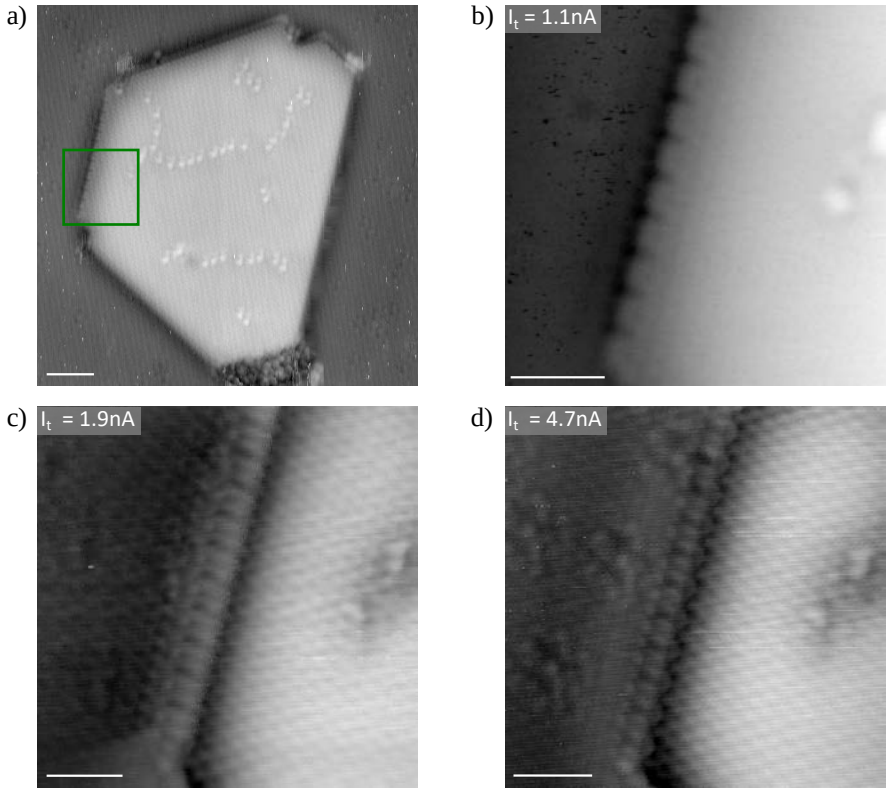

Figure 3.12: a) STM image of a hexagonal island with alternated zigzag and reconstructed edges. The effect of a double tip apex in diagonal direction is clearly recognizable at the top edge of the island. A green square highlights the zone where the following scans are taken. V_b=0.11 V, I_t=0.4 nA, scale bar 2 nm. b) Zoom of the zone highlighted in (a). A double periodicity is here recognized. V_b=0.023 V, I_t=1.1 nA c) At a closer tip-sample distance, the edge is nearly indistinguishable from a zigzag edge. V_b=0.023 V, I_t=1.9 nA. d) When the tip is approached even more, the edge shows point protrusions with double periodicity, resembling a Klein edge.V_b=0.028 V, I_t=4.7 nA. Scale bar for (b-d) is 1 nm.

Finally, it is interesting to note the critical role of the tip conditions and scan-

ning parameters in the determination of atomically resolved structures, such as the reconstructed edges. Fig. 3.12a shows a quasi-hexagonal island where the two type of edges should coexist. A zoom in Fig. 3.12b-d shows atomic resolution images of an edge where the 2x2 reconstruction is clearly visible. However, after an unintentional modification of the tip apex occurring during a scan with high setpoint current, the appearance of the reconstruction is drastically changed: the island termination appears as a 1x1 zigzag, and a much weaker 2x2 features appear close to the surface apparent height. The 2x2 periodicity at the graphene plane can be recovered by increasing the setpoint current from 1.9 to 4 nA, but now it appears as single points instead of pentagons. This series of images are a good example of the care one has to take when determining atomic structures with STM.

3.2.1.3 Bridge-top stacking

Graphene in bridge-top stacking appears different in STM from top-hollow stacking: images display bright stripes along a single Ni(111) close-packed, as a consequence of a reduced stacking symmetry. Dark dots are imaged in what is recognized as the geometric center of the benzene rings [211]. As noted from Fig. 3.8, bridge-top stacking is so that top Ni atoms are in bridge position with respect to the overlaying graphene atoms; alternatively, it can be visualized as pairs of carbon atoms bridging the Ni atoms.

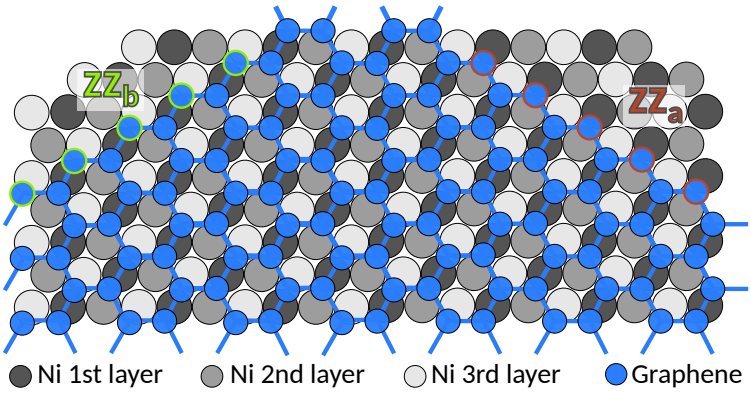

Figure 3.13: Schematic of the zz_a and zz_b edges for the bridge-top stacking configuration.

This stacking configuration is quasi-degenerate with top-fcc, according to recent DFT calculations [209], and is indeed the second most abundant stacking configu-

ration found for extended graphene [211] and that we find as well, though much less abundant than top-fcc (see Fig. 3.23). Some of the triangular single crystal GNIs we found are in bridge-top stacking, as the one that was showed in Fig. 3.7c. The observation is surprising, as this is not compatible with the two-fold symmetry of this stacking configuration. Bridge-top islands with zigzag termination exhibit one pair of opposing *a*-type (zz_a), and two pairs of opposing *b*-type (zz_b) edges, or viceversa. The difference between them is that zz_b edges can be seen as C-pairs bridging the Ni atom, whereas in zz_a edges one atom of the pair is missing, as seen in Fig. 3.13. This should give rise to uniaxially elongated hexagonal (truncated rhombic) shapes, because the different edge structures are expected to have different stability and growth rates. This statement, solely based on symmetric arguments and applicable both in the kinetically limited and equilibrium growth regimes, is however in stark contrast to the experimentally observed triangles. We attribute the origin of this non-equilibrium morphology to substantial differences in the stacking energetics at growth and low temperatures. The triangular shape and orientation of the bridge-top nanoislands we find (Fig. 3.7c is one example), together with the 2x2 reconstruction of the truncated edges (Fig. 3.7f), which are not expected in this stacking geometry, suggest that the stacking configuration at the growth temperature is top-fcc, and hence must have been shifted to bridge-top during cooling. This scenario is supported by the DFT calculations, that reveal an isoenergetic path connecting top-fcc and bridge-top configurations by a 0.7 Å translation along the armchair direction [209]. A shift of an entire island from top-fcc to bridge-top with such a translation is depicted in Fig. 3.14, revealing a change from three- to two-fold stacking symmetry.

The truncated edge structure of bridge-top islands might provide relevant information about the sequential order of the processes occurring during the growth of GNIs. As discussed in Sec. 3.2.1.2, zz_t edges reconstruct as $zz(57)$ or zz_{rk} , depending on the hydrogenation of the edges. In both cases, both (i) the reconstruction (either 57 formation or pairing of the Klein edge atoms in pentagons) and (ii) the stacking shift from top-fcc to bridge-top take place at an intermediate temperature between growth T and RT. In the case of $zz(57)$ edges, the energetically unfavourable stacking of the outer C atoms on top of Ni is avoided by formation of heptagons which bring two outer C atoms to a symmetric configuration respect to the Ni atoms underneath, forming stable sp^2 bonds to them. Such symmetry is lost in bridge-top

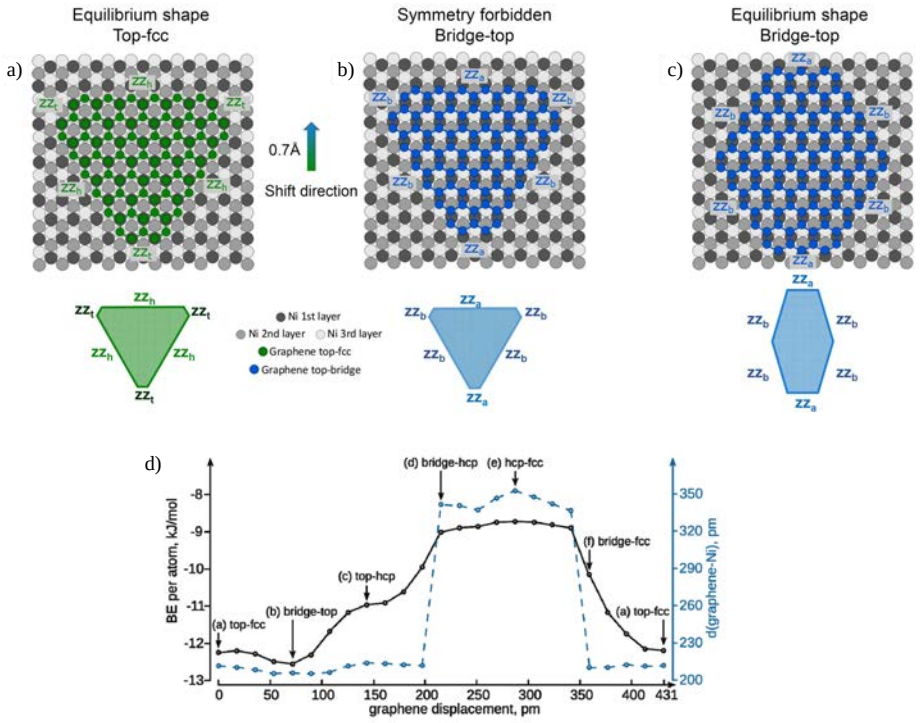

Figure 3.14: Schematic representation of the atomic stacking of top-fcc (a) and bridge-top (b) triangular islands. The two are connected by a translation of 0.7 Å perpendicular to a zigzag edge. According to the stacking symmetry of edges, this morphology can only correspond to top-fcc islands. c) Equilibrium morphology of bridge-top islands, for the case of zz_b being more stable than zz_a. d) DFT-calculated potential energy surface and distance to substrate for stacking configuration of graphene on Ni(111). Adapted with permission from [209]. Copyright 2011 American Chemical Society.

stacking for zz_b edges, the 57 reconstruction would unlikely take place after the shift has occurred, and as a consequence the order of processes must be (i) followed by (ii). In the case of zz_{rk} , instead, determining the order is not as direct, since Klein edges grown at high T are stabilized by pairing of the protruding C atoms and the dangling sp^2 bonds are saturated by H. Although the stacking symmetry argument for zz_b edges still applies, it cannot be excluded that the rk reconstruction is more favourable than the Klein edges also in this stacking.

Nanoislands can also shift from top-hcp stacking to bridge-top stacking; also, the shift can take place for domains only, in mainly top-hollow stacking. This is shown in Fig. 3.19 and discussed in the appropriate section, together with the corresponding domain boundaries.

3.2.2 Stacking superstructures in rotational domains

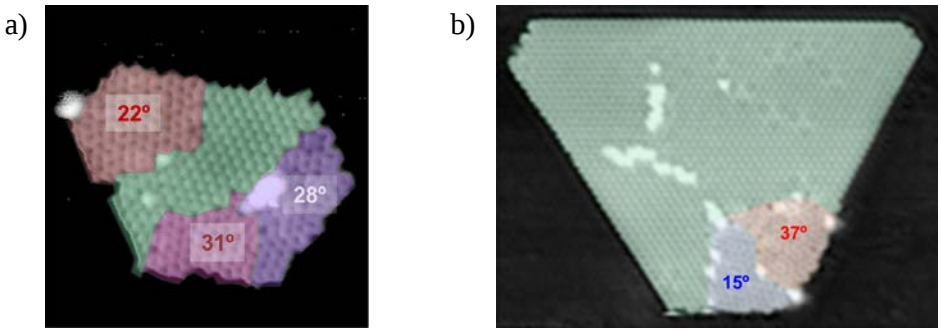

Figure 3.15: a) STM topographic image of a graphene nanoisland after preparation at 500°C, with a domain in top-fcc stacking and three rotational domains. b) STM topographic image of a graphene nanoisland after post-annealing to 575°C mainly in top-fcc stacking with two rotated domains.

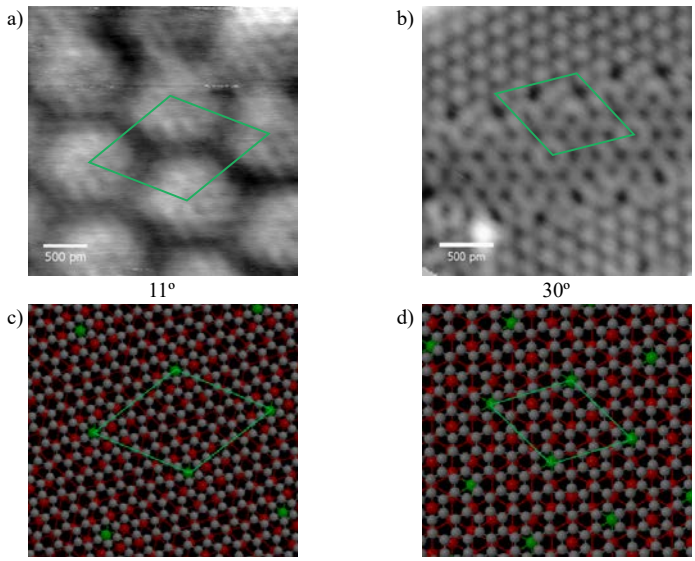

Figure 3.16: a,b) STM topographic images for different rotated domains found in Gr islands on Ni, and c,d) corresponding ball-and-stick models. The unit cell and repetition of the Moirè patterns resulting are indicated in green, to guide the eye. The angle here is the rotation of graphene relative to the Ni(111) substrate.

Although graphene on Ni(111) mainly grows in 1x1 unrotated stacking, a number of rotated domains are found. Fig. 3.15 shows two examples of nanoislands where 1x1 and rotated domains are seen. As it is noticed, these domains are generally small in size, and they always appear interfaced to other domains, never as isolated is-

lands on the surface, thus evidencing their instability on the substrate. In general, in these areas 1x1 commensurability that breaks sublattice symmetry in graphene is lost, so that the full honeycomb is imaged. Yet, as can be observed in large enough domains, graphene keeps commensurate with the substrate with large stacking superstructures giving rise to different Moiré patterns. This is shown in Fig. 3.16, where two different rotated domains observed in STM are compared to the corresponding stick-and-ball model, highlighting the supercell periodicity.

The rotation angles observed and their stability is discussed in Sec. 3.3, as they are related to domain boundaries found in polycristalline islands.

3.3 Domains and boundaries in polycrystalline nanoislands

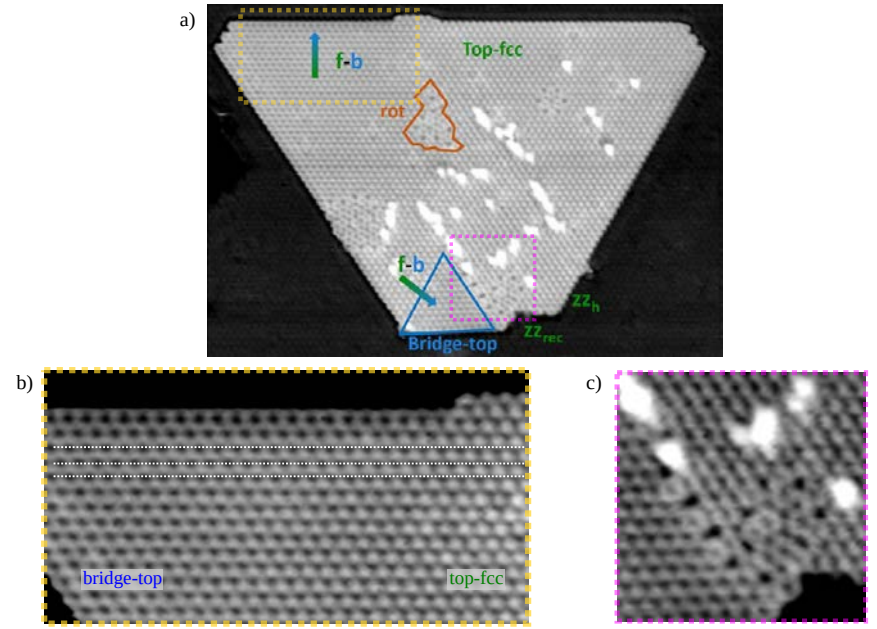

Figure 3.17: a) STM topographic image of an island after growth at 500°C, showing mainly one 1x1 stacking and few areas with Moirè and different appearance. Scan size 11×11 nm^2. b) Magnification of the area highlighted in yellow in (a). Here a continuous stacking shift is recognized by following the white lines from left, where they are aligned to the hollow sites of the bridge-top domain, to the right, where they find no exact correspondence. c) Manification of the area highlighted in purple, displaying topological defect boundaries between differently 1x1 and rotated stacked domains near the edge of the nanoisland.

The relevance of domain boundaries in polycrystalline graphene is well known, since they can determine electron transport by the scattering of carriers [215] or by

hosting 1D states [207, 216] and they also affect the mechanical stability of graphene, with a dependency on the relative rotation of adjacent domains [217, 218]. The coexistance of different stacking domains and the correspoding boundaries have been reported for extended graphene on Ni(111) [207, 211, 219], but these do not necessarily have to be the preferred ones in our GNIs, where the different growth method and their nanometer scale can impose a different energy landscape and kinetics.

With the aid of a stable and very sharp STM tip, we imaged for the first time polycristalline nanoislands with regular shapes, which were so far thought to be monocrystalline. Simultaneous atomic resolution of nanoislands and the Ni substrate, after drift correction was applied, also allowed recognition of bridge-top domains.

Fig. 3.17a is a good example of a polycrystalline island. Though the overall truncated triangular shape is determined by the dominating top-fcc matrix, the island contains several other small domains. Some of them are delimited by a continuous transition where the lattice is not interrupted by defects, such as the one shown in the zoom in of Fig. 3.17b. In the absence of a clear boundary, the stacking transition can be yet directly followed by a gradual change in the STM contrast. Other domains show clear topological defect boundaries, such as the ones shown in Fig. 3.17c. We note that the Ni impurities that appear as saturated bright protrusions tend to aggregate in defect boundaries. As discussed in Sec. 3.1.2, these impurities seem to play an important role in the growth of the islands.

In the following we describe each of the stacking domain and corresponding boundaries one by one.

3.3.1 Continuous boundaries

Continuous boundaries, always separating top-fcc and bridge-top domains, are often found at the periphery of large islands. Fig. 3.18 shows one example found in a hexagonal nanoisland. From our analysis, we find that graphene shifts continuously from top-fcc stacking to bridge-top through a region of strained graphene with undefined stacking, Fig. 3.18b. DFT calculations of Fig. 3.14 indicate that there is an energetic plateau of intermediate states between these two quasidegenerate stacking configurations. A possible reason for the formation of these boundaries is that the system prefers to relax the strain arising from the small Gr and Ni lattice mis-

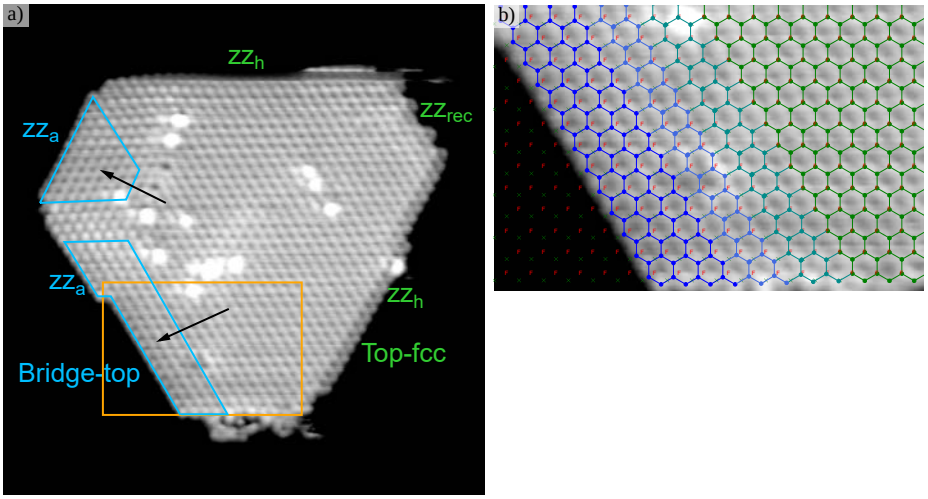

Figure 3.18: a) A continuous strained boundary is displayed between a top-fcc and a bridge-top stacked domain in a hexagonal island. The different stackings can be recognized by the different appearance both for the atoms in the 2D bulk of graphene as well as by the different contrast of the edges (zz_h edges appear combed). b) Zoom in on the continuous boundary, where the lattice of graphene and the top (green crosses) and fcc (red F) Ni sites are superimposed.

match by forming this low energy cost boundaries at the periphery of the islands, as found in our experiments.. The orientation of the strain boundaries is slightly different than those reported in [211] for monolayer graphene. They can explain their boundary by a transversal distortion, whereas we find a uniaxial elongation perpendicular to the boundary, Fig. 3.18b.

It is important to note that continuous boundaries are only related to a strained graphene and do not break its crystallinity.

3.3.2 Topological defect boundaries

3.3.2.1 558 defects

The two triangular islands joined in a rhomboidal nanostructure of Fig. 3.19a show a complicated boundary structure: on the left side, a stripe of rotated domain 'bridges' the two islands by the corresponding topological boundaries. These will be discussed later. On the right side, the two islands are directly connected by a topological line defect. The unit cell of this kind of boundary is composed of a heptagon and a pair of pentagons (558). These have already been observed in graphene on

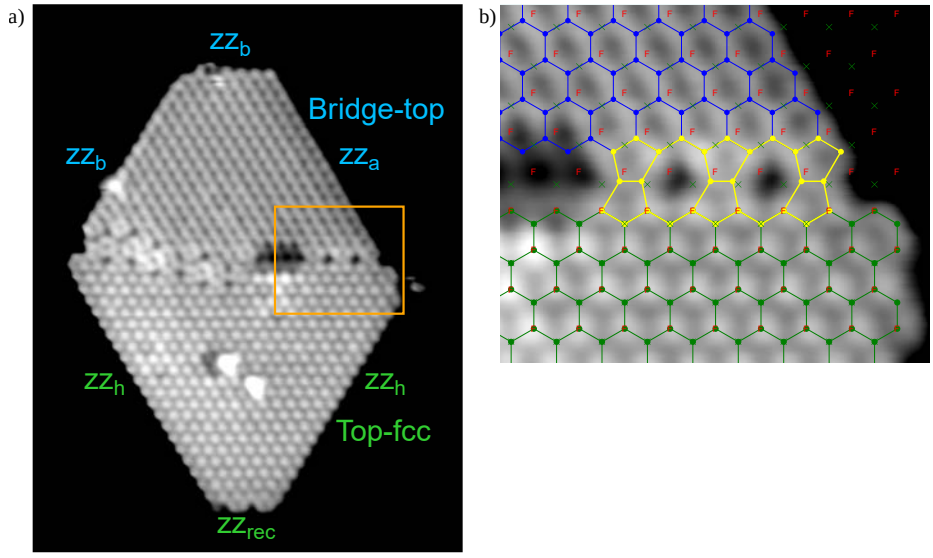

Figure 3.19: a) A bridge-top stacked island is joined to a top-fcc stacked nanoisland. The topological 558 boundary formed at the junction on the right side is displayed in a magnified image with superimposed lattice in (b). On the left side, an elongated rotated domain has formed between the two islands.

Ni, at the boundary between top-fcc and top-hcp domains [207] as well as between bridge-top and top-hcp [211].

In Fig. 3.19a, the bottom island is in top-fcc stacking, while the top island seems to have grown in top-hcp stacking, given the triangular edge symmetry, and later shifted to bridge-top upon cooling. This is consistent with the observations of 558 defects between top-fcc and top-hcp domains in monolayer graphene [207, 211] and with the stacking shift previously discussed. The shift results in a distorted structure of the boundary, thus evidencing the formation of such boundary at growth temperature, and the shear strain applied to it due to the shift.

The 558 defect boundaries are interesting because they can host 1D metallic states [207], but we observed them only few times in our experiments.

3.3.2.2 57 boundaries in rotated domains

As opposed to non-rotated stacking domains, domains with relative rotation can only be interfaced by topological defect boundaries. The minimum energy ones have been described in theoretical studies by periodic arrays of pentagon-heptagon

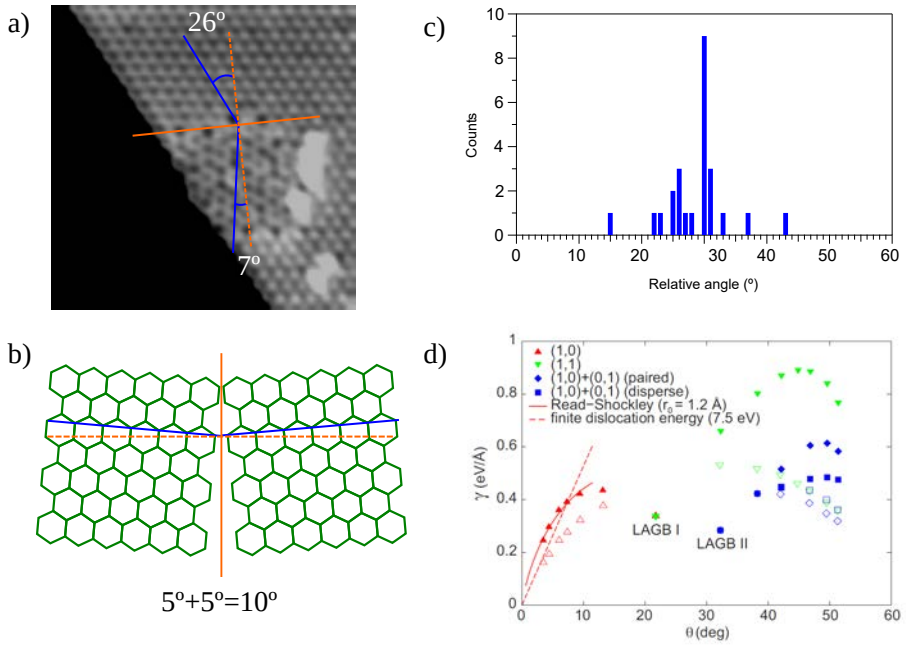

Figure 3.20: a) Example of angle analysis for a rotated domains at the edge of a mainly top-fcc nanoisland. An orange solid line marks the direction of the boundary, the dashed line its normal. b) Schematic of the analysis of boundaries tilt angles, evidencing the angle measurement between zigzag directions. A simple measurement of angle difference would result in a 30° symmetry. c) Histogram of the analysed domain boundaries with respect to the tilt angle. d) Calculated topological defect boundaries energies as a function of the angle for different defects morphologies. LAGBII corresponds to a continuous straight line of 57 defects. Reprinted figure with permission from [220]. Copyright 2010 by the American Physical Society.

(57) pairs in different configurations [221–224]. The calculated angle-dependent energetics predicts a metastable plateau spanning around 20-35 °with a particular pronounced minimum around 28-32,° related to C-C bond relaxation around the topological defect.

We compared the experimental results to the above predictions by analysing the relative angle between the lattices of rotated and top-fcc domains. This has been done using the atomic resolution of real space images. Figure 3.20a shows an example of such analysis, where the angle is taken as the sum of the angles of rotations of the domains relative to the boundary, as in Ref. [220] (Fig. 3.20b shows schematically the measuring method). The resulting statistics of the angular distribution is shown in Fig. 3.20c. Interestingly, all observed domains fall within the calculated

metastable region, Fig. 3.20d [221, 223, 224]. We never observed small-angle rotation domains (<15)°, as have been found for instance in extended CVD graphene on Cu foils [225]. The inhibition of small-angle domains could reflect the strong interaction of Ni(111), where the preference for non-rotated stacking could shift them into the top-fcc matrix.

At intermediate angles, however, boundary energetics seems to dominate over stacking energetics, according to the coincidence of the statistical distribution with the free standing calculations. The pronounced maximum at 30° agrees very well with the local energy minimum predicted around this angle for boundaries in free standing graphene, as reported in the graph of Fig. 3.20d.

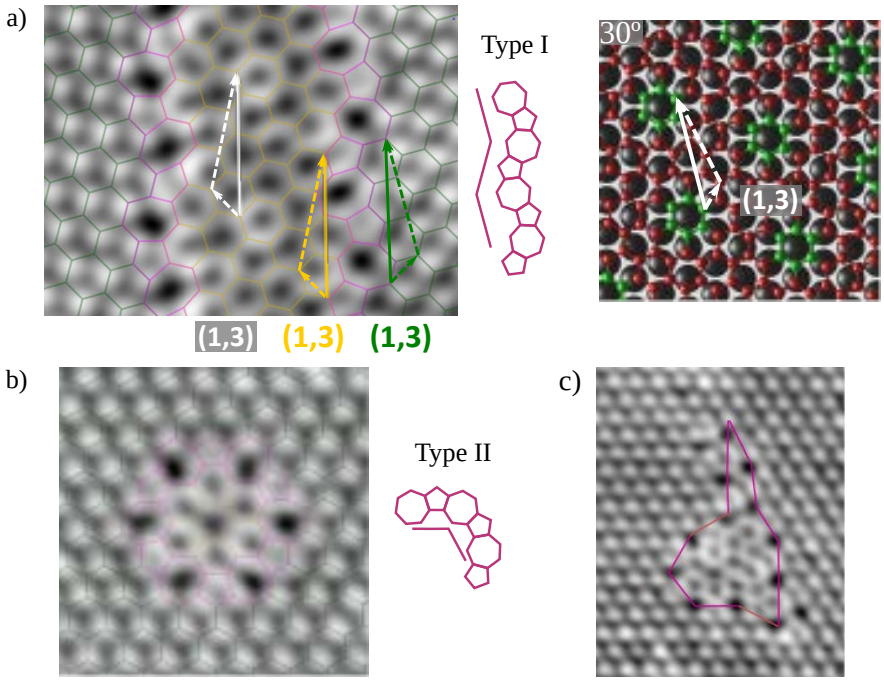

Figure 3.21: a) A 30° rotated domain with Type I boundary. Yellow and green arrows define the boundary repetition unit on the two sides, white arrows mark the Moirè periodicity for the rotated domain. The atomic model of the domain has been reproduced in aside for a graphene sheet rotated 30° respect to Nickel. Green hexagons are intended as guide to the eye. b) A 30° rotated domain enclosed by Type II boundaries; forming a quantum dot. c) Irregular rotated domain mixing Type I and II boundaries.

Several arrangements of 57 units have been proposed for this angle, all of them showing a local minimum in the angle dependence [221–224]. Our measurements

can help us discriminate which ones are stable in our Gr/Ni system. Atomically resolved images as the ones displayed in Fig. 3.21 are representative images of the boundaries found in our experiments, always made of continuous 57 arrays. Here, we divided them according to the direction of repetition of the 57 unit. Type I boundaries (Fig. 3.21a) are linear and define ribbons of the rotated stacking domain, whereas the type II structure (Fig. 3.21b) forms quantum dots. Most domains, however, are limited by less symmetric boundaries that combine both types, as in Fig. 3.21c.

Type I has already been studied theoreticaly, classified as a stable linear boundary [221, 223, 224]. The symmetric configuration of the two domains results in identical (1,3) translation vectors of its periodicity using the two different honeycomb lattice orientations at each side of the boundary. This has important consequences for the electron transport across the boundary, as described in the following.

Translation vectors are also important because they allow to determine the transport properties of the boundaries. These depend not only on the relative rotation of the adjacent graphene domains - i.e. by the coincidence, in k—space, of the Dirac bands in the rotated Brillouin zones, but also on the boundary periodicity. This folds the Dirac bands in the corresponding 1D Brillouin Zone defined by the boundary, allowing for new matching conditions that open transmission channels [221, 226]. In other words, certain superlattice wavevectors can connect Dirac cones at the two sides of the boundary allowing electron hopping between them by momentum transfer at the boundary. The matching conditions can be obtained by using the translation vectors of the boundary respect to left (n_L, m_L) and right (n_R, m_R) domains, which account for both the relative rotation of the grains and the periodicity of the boundary. Using the notations of [221], we can distinguish three cases. When the relation between translation vector is (a) $n-m=3q$ or (b) $n-m\neq 3q$ (where q is an integer) for both L and R domain, the Dirac cones of the two domains overlap and transmission through the boundary is allowed: these are labelled class Ia,b boundaries. Such is the case for Type I boundaries, for instance, which fall in the second case.
In the third case, where $n-m=3q$ applies to only one of the two domains, no matching occurs and a gap opens at the boundary.

A clear assignement to either class of boundaries is not possible for Type II boundaries using the model of Yazyev and Louie [221], since here the boundary conditions

are circular and the superlattice vector has no specific direction in reciprocal space. However, similar quantum dots found in graphene grown on SiC indicate the presence of confined resonances [227].

3.4 Thermal evolution of domains

The temperature not only determines the edge stabilization and the shape of nanoislands. Fig. 3.22 shows images of two nanoislands after annealing at 500° and 650°, respectively. As it is clear from the two representative images, the abundance of rotated domains tends to diminish with the temperature: if for the special case of the nanoisland of Fig. 3.22a rotated domains represent about 75% of the nanostructure, at 650° the rotated domains represents only about 5% of the graphene flake. Healing of defects by thermal annealing was already observed for extended graphene [64, 219, 228], but few studies investigated crystallinity [229].

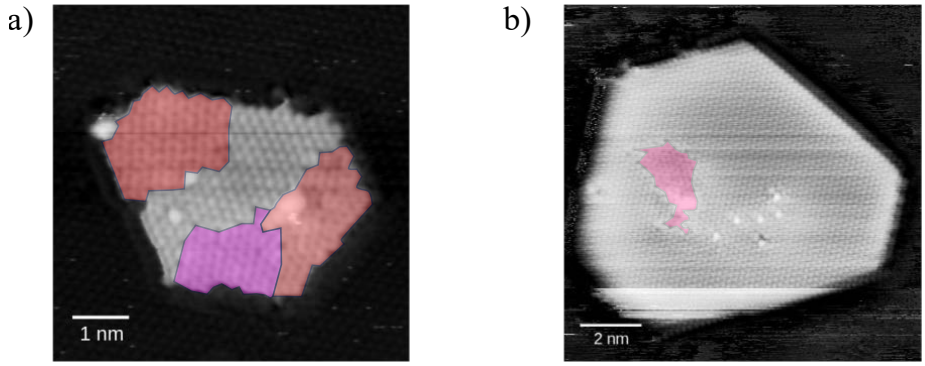

Figure 3.22: a) Atomic resolution STM topographic image of a polycristalline island grown at 500°C. Rotated domains with angles 22°, 30° and 21° are highlighted in colours. b) Atomic resolution of an island grown at 650° with hexagonal shape. A single 30° rotated domain is highlighted in pink.

We conducted a statystical analysis of the evolution of the stacking domains at increasing temperatures, in the range 500–620°C. The graphs in Fig. 3.22a represent, respectively, the average area and relative abundance of each domain type. At the low annealing temperature of 500°C, all domains are similarly small, and their relative abundance is of 45% (top-fcc), 25% (bridge-top), 5% (top-hcp), and 25% (rotated). As the temperature is raised the only domains that increase both in size and relative abundance are the top-fcc. Bridge-top domains appear to be inhibited as

they grow in size for increasing temperature. On the other hand, the small top-hcp and rotated domains decrease in relative abundance as the temperature is raised.

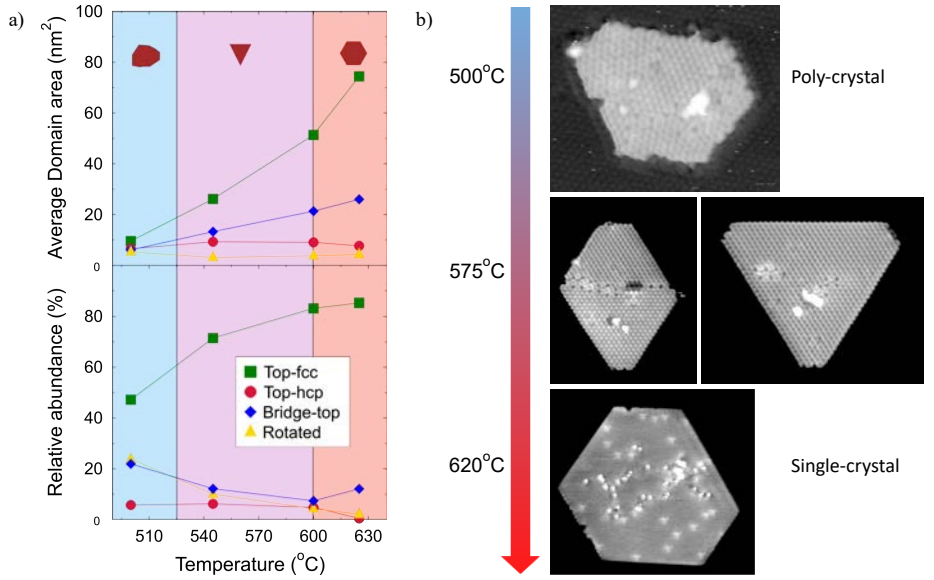

Figure 3.23: a) Average domain area and relative abundance of the stacking domains as a function of the annealing temperature. The temperature ranges for growth of irregular/triangular/hexagonal GNIs is indicated by the background colour. b) Representation of the evolution from polycristalline to single-crystal nanoislands.

The top-fcc to bridge-top ratio is at all temperatures higher than the 60/40 found in extended graphene [209, 230] and does not reflect the quasidegeneracy found by DFT either [209]. This can be related to the differences between our nanoscale islands and monolayer graphene. The top-bridge domains we find here are either small single domain islands or pheripheral domains in larger islands, both presumably formed by a stacking shift during the cooling. The presence of bridge-top domains in monolayer graphene, totally surrounded by the top-fcc matrix [211], can be related to a different growth mechanism.

The significant presence of rotated domains found at low temperature, critical for the crystallinity of the islands due to their topological boundaries, can be annealed out to 5-7% at the regime where triangular islands are grown, and down to 2-3% in the regime of hexagonal islands. This agrees nicely with the observations on extended graphene [219], suggesting that their non-equilibrium nucleation is related to the high migration rate of sp^2 carbon clusters in the initial stages of growth

at mild temperatures [155].

The combined morphological and structural evolution, summarized in Fig. 3.23b, goes from ill-defined, polycrystalline islands for T<525°C, to triangular islands where the average number of domains gradually reduces to 1.5 (T=525–575°C), and finally to single crystal hexagonal islands (T>600°C). The most important conclusion that can be grasped from the thermal evolution analysis is therefore that there is a temperature regime where both triangular and hexagonal well-defined single crystals can be formed. These represent ~90% of the graphene nanostructures in such regime, since bridge-top domains, as noted, are predominantly interfaced by continuous strained boundaries.

3.5 Summary

The growth of graphene nanoislands on Ni(111) has been investigated. Based on the preparation method described in [75, 154], the stacking domains, boundaries structures and energetics, edge morphology and the crystallinity of these nanostructures has been disclosed by high resolution STM images.

Graphene nanoislands grow on Ni(111) by a three-steps method, where the last annealing ensures control of the edge structure and shape of nanoislands. Stable top-fcc stacked domains dominate, followed in order of abundance by bridge-top, top-hcp and rotated domains. This is in agreement with the calculated energetics for bulk stacking. Nanostructures with forbidden symmetries in bridge-top stacking allowed to identify a multi-step growth mechanism for which nanoislands grow in 1x1 (top-fcc or top-hcp) stacking and isoenergetically shift to bridge-top after growth, at a lower temperature. Combined STM images and DFT calculations confirm a Klein reconstruction for edges in zz_t direction and the related hydrogen coordination of the nanoislands dangling bonds, also during cooling. From our analysis, we cannot determine in which order these two processes - stacking shift and edge reconstruction - take place.

Polycrystalline nanoislands identified by atomic resolution STM images were investigated. Domains in 1x1 stacking with Ni(111) and rotational domains are identified in the same nanostructures, and their boundaries analysed. A stacking shift where graphene is strained but structurally perfect is found to be also possible between top-hollow and bridge-top stacked domains. 558 topological defect bound-

aries are sometimes found at the frontier between unrotated nanoislands grown together to form a single nanostructure.

Small areas of rotated domains are found with small areas, and a variety of rotational angles. Such domains are always interfaced by 57 topological defects to unrotated domains. By analysing rotational domains and their angle to commensurate domains, we identify the role of topological defect boundaries energetics in the selection of rotational domains. Stacking and boundaries energetics concur to determine transparent, linear topological defect boundaries interfacing 30°-rotated domains with top-fcc stacked domains. Circular repetitions of the 57 unit lead to the formation of perfect quantum dots embedded in 1x1 graphene matrix.

Finally, we analyse the area and abundance of stacking domains at different temperatures. We find a route leading from poli-crystal nanoislands in the lowest temperature regime to predominant single-crystal nanoislands at temperatures $\geq$600°C. Thus, thermal annealing allows to tune the nanoislands shape, univocally correlated to the edge structure, and crystallinity, and to obtain single-crystal graphene quantum dots with either triangular or hexagonal shapes.

Chapter 4

Structural and electronic properties of the intercalation system

The interaction with the underlying substrate is an effective way to tailor the electronic and magnetic properties of graphene. The interfacial interaction can dope Dirac cones and induce band gaps [81], spin polarization [76, 77, 105–107] or spin-orbit coupling [29, 104, 231–233]. The same interaction also controls the growth morphology and edge atomic structure, as seen in Chap. 3. There, we have shown that the interaction with the Ni(111) substrate determines the edge termination and shape of graphene nanoislands, and that such interaction can be controlled by selecting post-annealing temperature. Electronically, the linear dispersion of pristine graphene bands is disrupted by hybridization with the Ni *d* bands. Instead, gapped spin polarized bands are induced in graphene [76]. Lateral, spin- and edge-dependent electron scattering was also demonstrated by combining STS and DFT calculations. These properties can be used to engineer e.g. a vertical spin-filtering effect [77].

The pristine electronic properties of graphene can be restored by intercalation at the graphene-Ni(111) interface. In extended graphene, many intercalants have been employed for this purpose: Cs [92, 234], K [235], Na [91] among the alkali metals, O_2 [97, 236], Al [89], Ge [93], transition metals like Cu [86, 90], Ag [85] and Au [83, 84, 237, 238]. In particular, ARPES measurements show that Au intercalation restores the linear dispersion of electrons around E_F in graphene with a very small *p* doping and no gap opening [84]. Marchenko et al. [103] reported a giant Rashba-type spin-orbit

splitting of 100 meV induced in the π bands of graphene due to hybridization with the d bands of Au. This is especially interesting because it fullfills the requirement of inducing a sizeable spin-orbit coupling in graphene while preserving the Dirac bands for applications in spintronics devices, such as spin filters [239]. However, recent calculations combined with STM measurements attribute this effect to intercalation of Au clusters under limited areas of the graphene monolayer [240], thus resembling a proximity effect as induced by adatom adsorption [22, 241].

At the nanoscale, the decoupling effect of Au is interesting in order to investigate the electronic properties of graphene nanostructures and their edges. However, the structural properties of these can be modified upon intercalation, and the dynamics of this can behave differently from the case of extended graphene. Fewer studies are available for intercalation of graphene nanostructures, all grown on Ir(111) only: O_2 [110], Au [111, 112] and Ag [112] were used as intercalants. Leicht et al. [112] showed by STM that quasi-freestanding graphene nanoflakes are obtained by Au intercalation, displaying signatures of the edge state predicted for zigzag edges. By QPI mapping, they showed a doping of 240 meV [242]. By the same method, they were also able to observe the Rashba splitting of the surface state of Au in GNRs [187]. Morgenstern et al. [111] also showed the recovery of the edge state by Au intercalation on Ir using STM topographic imaging. The nature and properties of the edge state on Au are a matter of discussion: while few STS studies showed a spin-split edge state on this substrate [43, 47], Wang et al. [203] showed that such splitting is observed in zigzag graphene nanoribbons only when transferring them from Au to NaCl monolayers.

In this chapter, we will discuss the results on the intercalation of Au under the graphene nanostructures grown on Ni(111). The experimental methods will be discussed in Sec. 4.1. As a complex metal surface results from the interaction of Au with the Ni(111) substrate, the structure of this will be discussed in Sec. 4.2. Then, the morphological and structural properties of the graphene nanoislands after intercalation of Au will be introduced in Sec. 4.3. Here, a mechanism of intercalation in the system will also be discussed. Finally, the electronic properties of the system as investigated by STS methods are discussed in Sec. 4.4.

4.1 Sample preparation

We pursued the characterization of the system of graphene nanoislands grown on Ni(111) after intercalation of Au films of different thicknesses. We prepared graphene nanoislands on Ni(111) following the recipe of Chap. 3. Though different preparations were used, we mainly aimed at hexagonal graphene nanoislands, because these provide the perfect environment to characterize the system of intercalated nanostructures and in particular the properties of the edges.

After GNIs growth, Au was deposited on the sample at room temperature. In order to determine the Au coverage, Au evaporation was calibrated by depositing submonolayer amounts of Au on the clean Ni(111) surface, which was then investigated by STM. A relation between deposition time and Au coverage was thus extrapolated and employed to deposit thicker Au films. This procedure was done for each experimental run, to ensure repeatable measurements. The deposition rates employed could vary, depending on the evaporator employed and the system in use, between 0.5 and 0.125 ML/min.

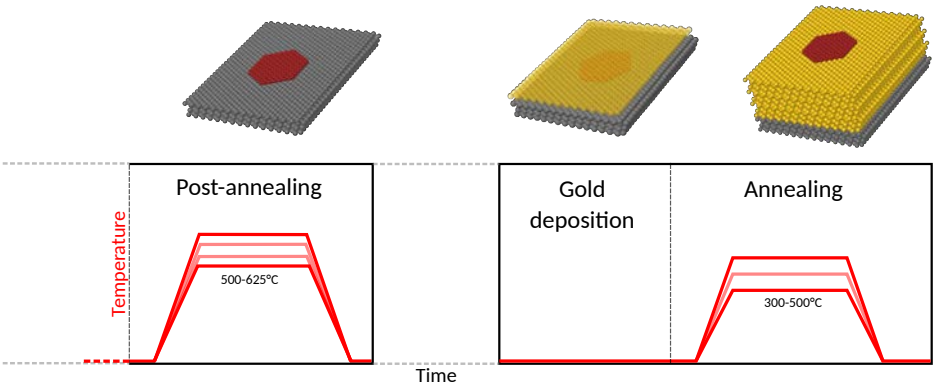

Figure 4.1: Scheme of the intercalation process: after graphene nanoislands preparation and shaping, gold is deposited on the surface at room temperature. By annealing, Au intercalates under graphene. The temperature range indicated is the one explored during the experiments.

For the intercalation of Au in the GNI/Ni systems, Au was first deposited on the surface. Amounts varying between ~0.9 ML and 10 ML of gold were deposited in the first place. Intercalation was then achieved by annealing the sample at temperatures in the range 380–500°C for few minutes. Depending on the temperature and the amount of Au deposited, we explored annealing times ranging from few seconds

to 30 minutes. In order to obtain thicker films of intercalated Au, the deposition-annealing process was repeated on the same samples: this is the case for the samples of >10ML in the following of the chapter.

At temperatures <350°C, a uniform Au layer is not formed. This is in line with experiments reported in literature for extended graphene [83, 84, 86, 103, 243]. Though the solubility of Au and Ni is very low, a metastable solid alloy is formed at temperatures ≥500°C [244]. A surface alloy is however formed already at room temperature, upon deposition of Au. This will be discussed in further detail in Sec. 4.2.

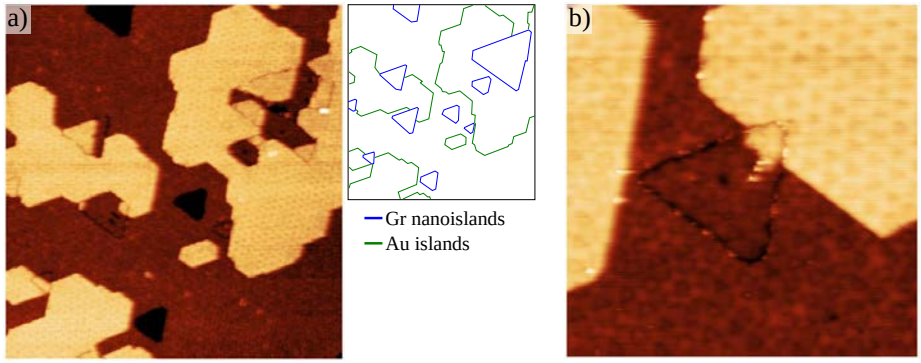

Figure 4.2: a) STM topographic image of a system of triangular graphene nanoislands grown on Ni after intercalation of Au. A scheme evidences the Gr nanoislands and Au islands recognizable in the area. Scan size: 100x100nm^2 b) Topographic image of a triangular graphene nanoisland on the same surface, at the edge of an Au island. The pattern of the Au surface layer continues under the island, evidencing the intercalation process. Scan size: 30x30 nm^2

Fig. 4.2 shows as an example a sample surface after growth of triangular graphene nanoislands on Ni(111) and intercalation of ~1.5 ML of Au. Triangular shapes are recognized all over the imaged area, with different apparent heights, as indicated in the inset of Fig. 4.2. These are triangular graphene nanoislands after the intercalation process. A corrugation appears in most parts of the surface: this is due to a misfit dislocation network forming at the Au/Ni interface, proving the presence of Au. A zoom on one of them is shown in Fig. 4.2b: as observed, the dislocation network appears also under such triangular areas, thus confirming succesfull intercalation.

We will start discussing the structural properties of the system from the morphology of the Au film. The morphologies and the structure of the nanoislands will be discussed in Sec. 4.3.

4.2 Structure and properties of the Au film

The structure and properties of the Au film are first presented, since the complex evolution of Au on the Ni substrate is fundamental for characterizing the electronic properties of graphene.

4.2.1 Dislocation network in the thin film regime

As observed in Fig. 4.2, a pattern of corrugations forms on the surface of the samples after the intercalation process. As seen in better detail in Fig. 4.3, this pattern actually consists of a network of triangles. Such triangles are known to form on the Ni surface upon deposition of Au already at RT [245]. They are lines of vacancy misfit dislocations, forming as a consequence of Ni atoms of the top layer shifting from fcc to hcp sites (inside the triangles), in order to increase the coordination number of Au atoms from 1 to 3. Ni atoms are squeezed out of the topmost Ni layer and alloy in the first Au layer. They can be recognized as bright protrusions in the first Au layer, Fig. 4.3b. The following layers have little or no Ni alloyed. As observed in the atomically resolved topographic image of Fig. 4.3b, the size of the triangles is variable, with a length of the vacancy lines of 3–8 Au atoms. We measure the average unit vector of this network 2.36 ± 0.2 nm, 9.5 times the lattice constant of Ni(111), in line with the 9.7×9.7 superlattice reported[245]). This network is important for graphene, as it is can induce an exchange field giving rise to a giant gap at K (K') points shown by [108].

4.2.2 Thickness evolution of the Au surface

The corrugation due to the triangular misfit dislocations is repeated in the following Au layers, as was observed in Fig. 4.3b for an Au island on top of an Au layer. With a corrugation of ~20 pm in the first Au layer, dislocations are smoothed out at each subsequent monolayer. Fig. 4.4 shows the appearance of the surface for increasing thicknesses of the Au layer. After intercalation of 5 ML of Au, Fig. 4.4b, the dislocation network is still recognizable. While a decreased corrugation is to be expected (10 pm according to [245]), we were not able to measure this behaviour, as it requires a careful measurement in repeatable conditions which was out of the scope of this work. The dislocation network is visible up to a film thickness of approximately 10 ML: Fig. 4.4c shows the sample surface after intercalation of 11±1 ML. The 2D pattern of

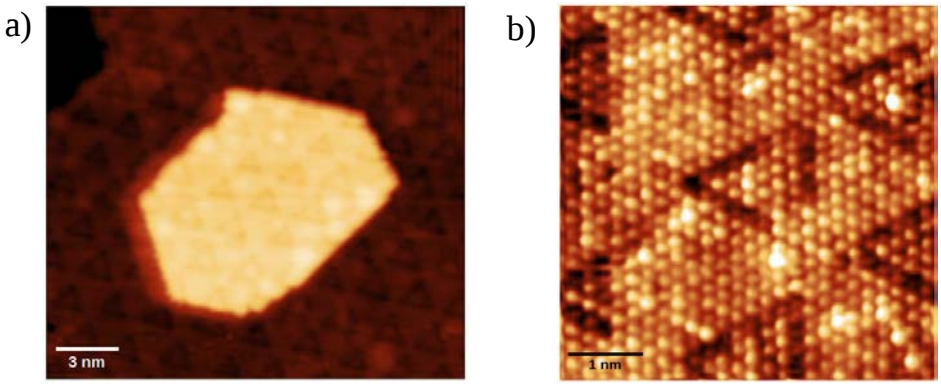

Figure 4.3: a) An Au island on top of the first Au layer on Ni. The network of triangular dislocations is seen on both surfaces. A double tip effect at the edge of the island is seen. b) Atomic resolution of the the dislocation network. The triangles from the dislocation pattern have different sizes: of 3, 5, 6 atoms per side

dislocations is not recognizable any longer. The surface displays a disordered corrugation, which might be due to a lack of crystallinity in the film.

Increasing further the film thickness is expected to lead to a Au(111) surface. Fig. 4.4d shows a sample after intercalation of 22±1 ML. Here, terraces still show a corrugation of few pm, though no 2D order can be identified. However, pairs of ridges are recognized on the surface. Fig. 4.4c-d show examples of them. These are the domain boundaries between fcc and hcp regions characteristic of the Au(111) surface, where they appear as a herringbone pattern [246]. As can be appreciated in Fig. 4.4d, in our experiments a true "herringbone" reconstruction was not observed: the pairs of lines displayed irregular shapes and variable direction. No long-range order can be recognized. This observation and the persistent corrugation point to a crystalline disorder in the Au film. Nevertheless, the presence of ridges proves the formation of bulk Au with (111) orientation and a considerable purity over the Ni(111) surface. This conclusion is confirmed by spectroscopic measurements, showed later in this chapter, which also confirm that, at this thickness of the Au film, the effect of the underlying Ni(111) is negligible.

4.3 Au intercalation

In this section, the morphology of the surface and the nanoislands after the intercalation process is first presented, in order to introduce the necessary concepts for the

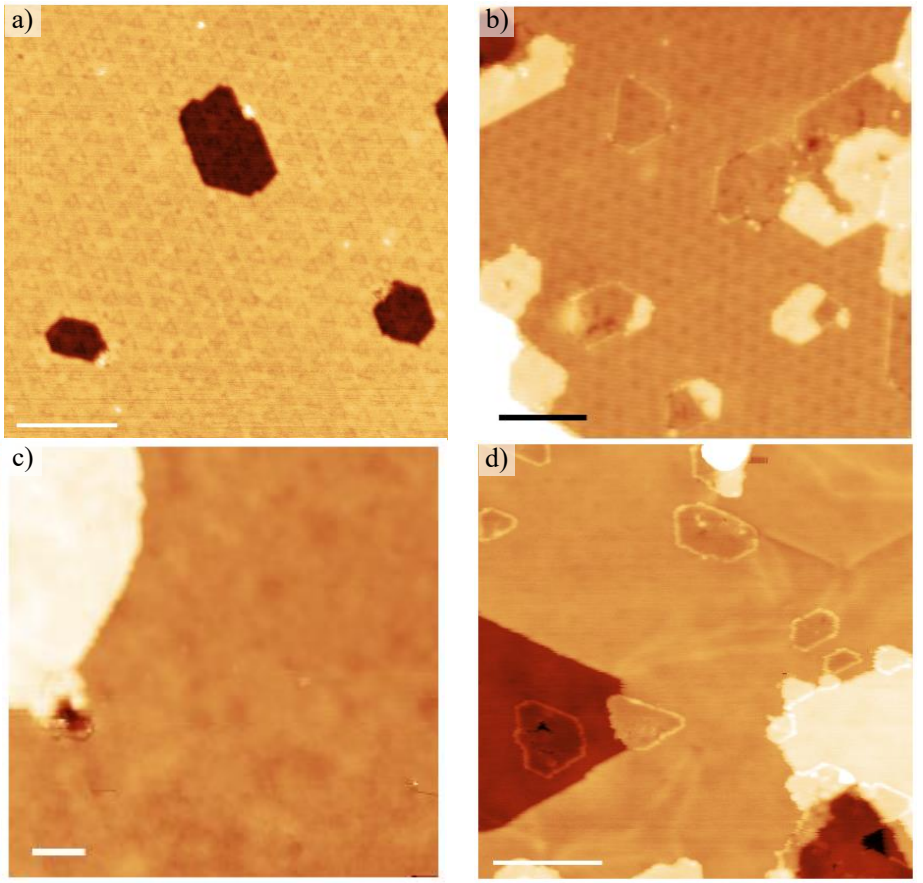

Figure 4.4: STM topographic images of the Gr/Au/Ni system with different thicknesses of Au film. a) Au film of ~0.9 ML, where the dislocation network is seen all over the surface, with an average corrugation of 20 pm. b) After intercalation of ~5 ML of Au, dislocations are still visible. c) At 11±1 ML, the dislocations disappear, and the surface displays a corrugation with no 2D order. d) At 22±1 ML, though a slight corrugation of the surface persists, the ridges of the Au(111) reconstruction are seldom observed. Scale bar is 10 nm.

following of the chapter. Next, a proposal for the mechanism of intercalation under nanoislands is explained. Finally, the atomic structure of the nanoislands and of their edges is investigated.

4.3.1 Intercalation morphology

As was observed in Fig. 4.2, after Au deposition over GNI/Ni(111) and annealing, the graphene nanoislands are recognizable by their shapes and sizes. Different apparent

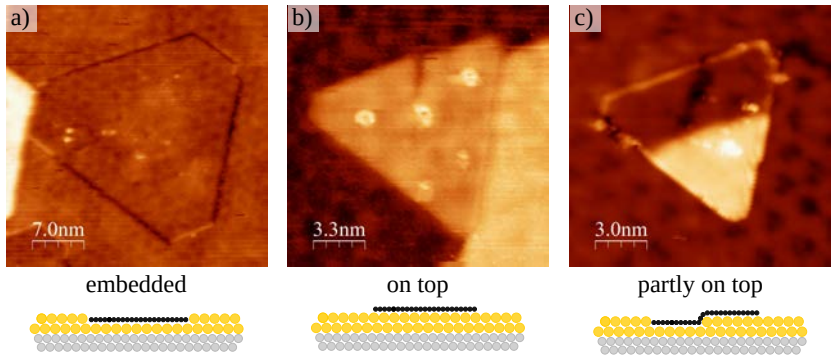

Figure 4.5: Representative STM images of graphene nanoislands after intercalation of 1.5 ML of Au in a) embedded b) on top and c) partly on top configuration. Schemes representing each configuration are included (2 ML of Au are here used for clarity).

heights are displayed by the nanoislands, though. While some islands display the same height as the Au surface layer, others appear higher or lower, and many display different heights. This is a consequence of the different configurations in which the nanoislands can be found after the intercalation process is carried out. It was found that GNIs can have three different configurations, shown in Fig. 4.5:

- *Embedded*: GNIs can be entirely embedded in the Au film, i.e. being surrounded by Au, either in the topmost layer or in a lower one, when a multilayer Au film was deposited, Fig. 4.5a. They appear as areas of the surface delimited by hollow or high borders, displaying a height difference of only 0.2 ± 0.1 Å to it.

- *On top*: GNIs can be found on top of the Au surface or Au islands, Fig. 4.5b. They can have a lateral interface to Au islands or step edges, and can also extend across steps. Their apparent height is 2.1±0.2 Å Å

- *Partly on top*: finally, GNIs extending over more than one Au ML can be partly in on top configuration and partly embedded, as in Fig. 4.5c.

The origin of these configurations stems from the intercalation mechanism which, at a first glance, seems to start from the edges of the nanoislands towards the bulk. This will be discussed later in more detail in Sec. 4.3.

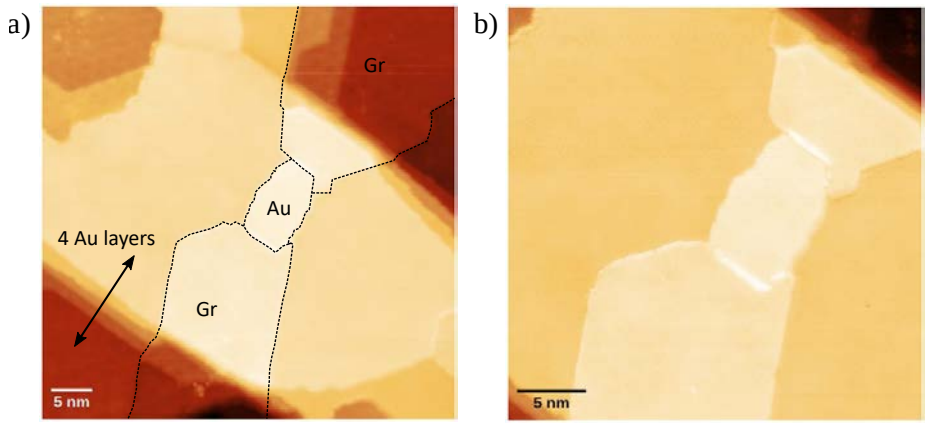

Figure 4.6: a) Two large graphene flakes extending over the edge of an Au island composed of 4 monolayers and joined by an Au island, demonstrating the weak vertical bonding of graphene to Au. b) A magnification of the top of the Au island, where the graphene flakes and the Au island bond together.

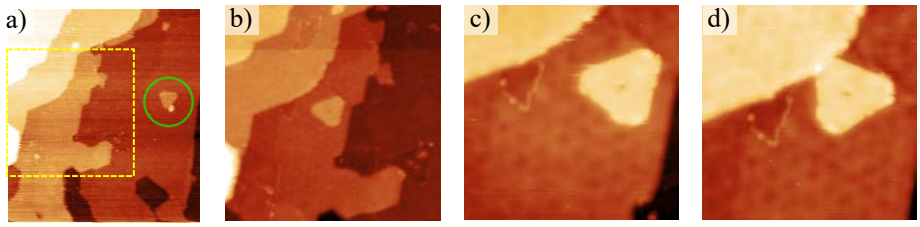

Figure 4.7: Series of subsequent STM topographic images showing the tip-induced diffusion of a hexagonal graphene on top nanoisland over a step edge and its rotation on a terrace. a) Initial scan, where the nanoisland (circled in green) is observed on a wide terrace. b) Zoom of the yellow square marked in (a). The nanoisland is now on the adjacent, higher terrace. c) After zooming on the island, this in a subsequent scan (d) rotates again and diffuses near the next step edge. Scan parameters: a) V_b=0.69 V, I_t=0.46 nA, b) V_b=0.33 V, I_t=0.2 nA, c) V_b=0.12 V, I_t=0.3 nA, d) V_b=0.12 V, I_t=0.2 nA

In all of the configurations, nanoislands can extend over steps. This is a first proof of the weak interaction of the Au surface, and of the weak coupling of the nanoislands to it. A particular case is shown in Fig. 4.6: two large graphene nanoflakes extend from an Au terrace to the top of an Au island formed by 4 Au monolayers and join together through an Au island, as in an inverted transistor configuration. A second proof is given by the possibility to displace on top GNIs over the surface while scanning at RT. Fig. 4.7 shows a series of STM scans representing a graphene nanoisland displaced over a terrace step and rotated. The diffusion of the island is solely driven by the interaction with the tip. The fact that islands can diffuse on the

surface is not surprising by itself, as we could seldom observe a similar effect for GNIs on Ni(111) at high setpoint currents and low bias voltages. A strongly interacting tip was also necessary, as in the present case on Au. However, the possibility to do this at "mild" tunneling conditions ($0.1 < V_b < 1$ V and $I_t < 1$ nA) and the fact that nanoislands can displace across step edges demonstrate a weak physisorption and therefore a notable chemical decoupling after intercalation of Au. This effect has also been observed for graphene nanoribbons and large nanoflakes on Au [112], and is consequence of a nearly superlubric contact [247].

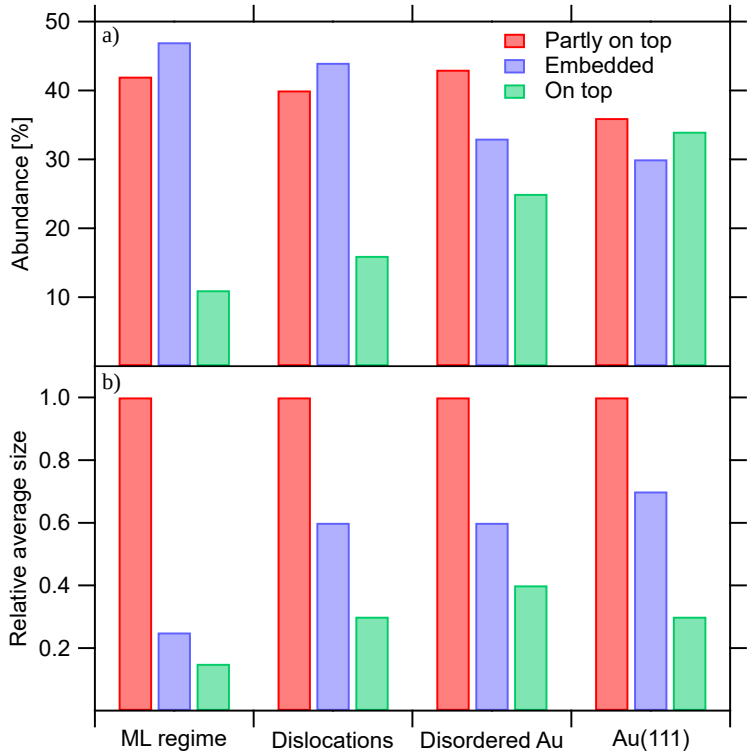

Figure 4.8: Statistical analysis of more than 250 GNIs at different Au thickness regimes, for intercalation temperatures of 380–500°C. a) Abundance of the nanoislands configurations for each regime. b) Relative average size of the nanoislands, as a fraction of the highest value for each regime (see text), for each thickness regime.

In order to better understand the intercalation system, a statistical analysis on the configuration of the nanoislands has been carried out. The abundance and average size of nanoislands in each configuration have been measured for different Au film thicknesses and annealing temperatures. The results are reported in Fig. 4.8.

Four thickness regimes have been defined, according to the evolution of the Au film described in Sec. 4.2.2: a *monolayer regime* for Au film thicknesses 1 ML≤ Θ<2 ML; a *dislocations regime* for thicknesses Θ<10 ML, where dislocations are recognized on the surface; a *disordered Au regime*, for Au films of Θ>10 ML, where a corrugated Au surface with no 2D order is observed; and a *Au(111)* regime, for samples where the ridges of the herringbone reconstruction are observed.

Fig. 4.8a reports the relative abundance of the three configurations, counted as the relative number of nanoislands found in each of them. A clear evolution can be observed. For thicknesses of Au up to 10 ML, the vast majority of nanoislands are found in partly on top or embedded configurations (about 40% each), while only 10–15% on top nanoislands are found. As the thickness increases, though, the abundance of on top islands also increases, until in the Au(111) regime the three configurations are equally represented on the sample surface (36%, 30% and 34% for partly on top, embedded and on top nanoislands respectively). A tendency favouring on top nanoislands and reducing embedded ones with increasing Au film thicknesses is therefore clear. The effect on partly on top nanoislands, instead, is less pronounced.

We also analysed the average size of nanoislands in each configuration. Since the absolute size of the nanostructures highly depends on the specific preparation on Ni(111) – partly on top islands, for instance, have average sizes varying from 58 to 1066 nm^2 –, we considered for each thickness regime the size relative to the nanoislands configuration displaying the greatest absolute value. As observed in the graph of Fig. 4.8b, partly on top nanoislands are always the largest flakes on the surface. At all Au film thicknesses, also, embedded nanoislands are the following in size, though a great difference in the monolayer regime respect to the others. On top nanoislands are the smallest at all points.

Before discussing the physical meaning of such analysis, the limits of the definitions have to be noted: on top nanoislands, in fact, have been defined as nanoislands with either all of the edges "free-standing" (i.e. not having any recognizable lateral contact with Au), or those having a part embedded, but laying on a single terrace; while partly on top nanoislands must both have a part embedded, and lay on multiple Au layers. The definition of on top nanoislands then embraces nanoislands in contact to step edges or Au islands, but also those which are partly embedded at the step edges. For instance, as Au grows layer-by-layer until the first ML is com-

pleted, fewer nanoislands can be found embedded at step edges when intercalation is completed, which can explain the low availability of on top nanoislands in the monolayer regime.

Most importantly, the choice of definition helps explaining the behaviour of the sizes of nanoislands, as it is quite obvious that larger nanoislands have a higher probability of "meeting" in lateral contact an Au island or step edge, and at the same time are more hardly intercaleted uniformly (especially when considering samples where the average size of nanoislands in partly on top configuration is >1000 nm^2). Furthermore, as will be discussed in more detail in Sec. 4.3.2, intercalation most likely proceeds from the edges or from defects and vacancies of the graphene nanoflakes. A uniform intercalation is therefore less probable for larger nanoflakes, which are then more often found laying on different Au layers. These two considerations explain why partly on top and embedded nanoislands display larger sizes. As a result, smaller nanoislands are the ones with the highest probability of being on top.

The most interesting result, however, is the increasing abundance on top nanoislands with the Au film thickness. Part of the explanation could reside in the decreasing concentration of Ni alloyed in the Au layer, leading to a different interaction of the edges and the bulk of graphene with the substrate. However, the concentration of alloyed Ni is expected to be negligible already in the 2^{nd} Au ML, and therefore this alone cannot explain the observed behaviour.

4.3.2 Intercalation mechanism

The intercalation process is widely studied for extended graphene on transition metals [83, 90, 235]. It is well established that in this system, the intercalant is first deposited on the graphene layer and then, upon annealing, intercalates under it through vacancies, defects and grain boundaries [248–250], though also a mechanism of intercalant-aided vacancy formation in the graphene layer and healing after intercalation has been proposed[251, 252]. The process is driven by the energy gain in adsorbing over the metal surface rather than over graphene [251]. When growing graphene nanostructures, however, the metal surface is available, and therefore different results and mechanisms might be expected for metal intercalation under these. Edges must also be taken into account, as these can be an intercalation channel, but an energy barrier is associated to unbinding of them from the substrate [94]

A series of experiments of Au intercalation with thicknesses in the submonolayer and monolayer range (0.9–1.6 ML) under graphene nanoislands on Ni(111) clarified the mechanism of intercalation in this system.

The main features are shown in Fig. 4.9. Fig. 4.9a shows the surface of Ni(111) after growth of graphene nanoislands. The nanoislands display different shapes with straight edges in the zigzag direction, and have an average size of 122 nm^2. Fig. 4.9b shows the same surface after depositing 1.6 ML of Au and annealing. Dislocations cover the whole area of the terraces observed, as well as the islands on top of it, which are recognized as Au islands. Hollow zones of different sizes and apparent regular shapes are also observed. These display different heights in their inside. The magnified STM topographic image of one of them is shown in Fig. 4.9c. As observed, dislocations are visible in the surrounding Au layer, but not anywhere in the inside of the hole. The deepest part of the island looks flat, except for a number of protrusions, either point-like or irregularly shaped and distributed ("bubbles"). Two areas are imaged high, and otherwise have the same appearance of the bottom part of the island. Magnified scans displaying these features are shown in Fig. 4.9d-e. From these last images, taken with atomic resolution, it is also possible to appreciate the hexagonal lattice both in the bottom area (Fig. 4.9d) and on the high parts, whether in the "bubbles" or in the high flat area, where electronic interference gives rise to different patterns (to the right of the area in Fig. 4.9e and less clearly on its other edges too). The atomic lattice corresponds to that of graphene, and the electronic interference is due to electron scattering, as will be discussed in more detail in Sec. 4.4. Therefore, the hole doubtless corresponds to one of the graphene nanoislands grown on Ni(111).

Fig. 4.9f-g show profiles evidencing the apparent heights of all of the presented features respect to the Au/Ni surface. As observed, the bubbles display an apparent height of 1.2±0.1 Å with respect to the bottom of the nanoisland, similar to the Au surface surrounding. The higher, flat areas display instead a height difference of 2.1±0.1 Å to the bottom. Such height could in principle correspond to that of Gr on Au (2.1±0.2 Å), but the height difference to the surrounding Au/Ni surface of 0.8 Å has no simple explanation.

The absence of dislocations in the whole of the nanoisland suggests that a different process is ongoing respect to the rest of the surface. As seen previously in

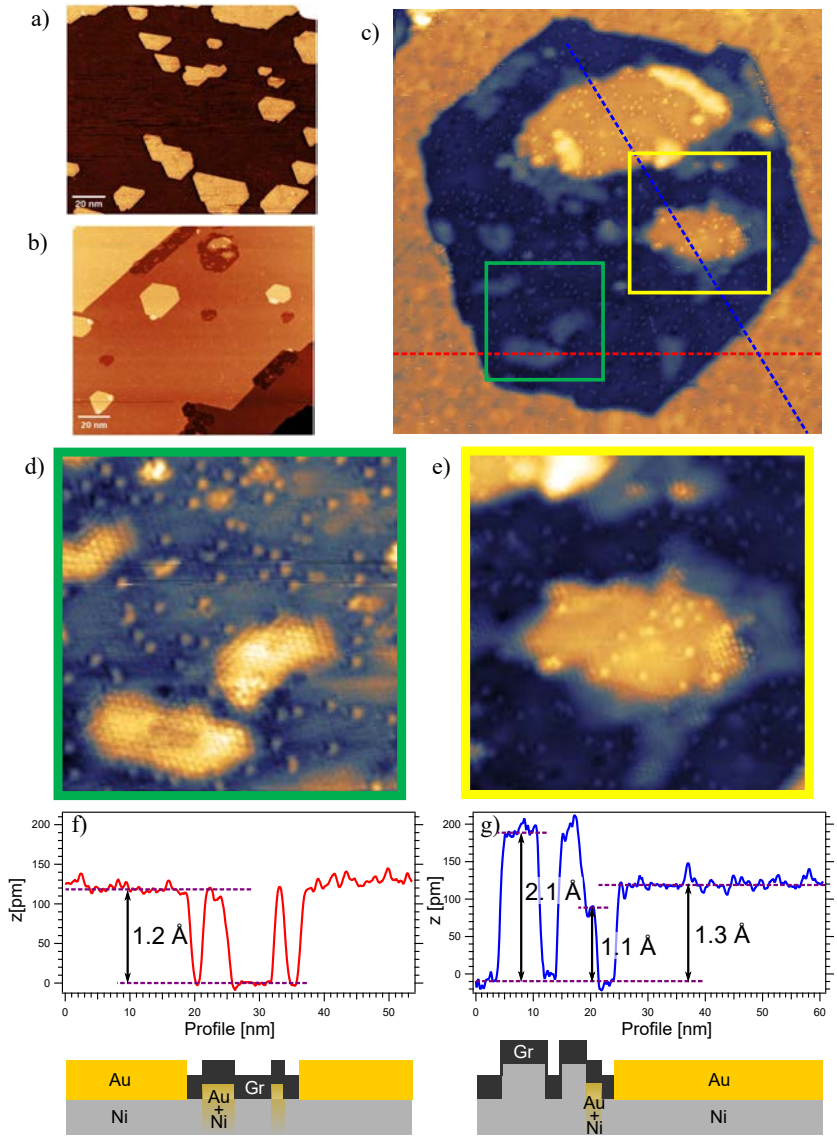

Figure 4.9: a) STM scan of a GNI/Ni preparation (T_R=500°C and T_{PA}=650°C); the coverage of graphene is 17% of the surface area. b) STM scan of the same surface after deposition of 1.2ML of Au and annealing. c) Magnification of a Gr nanoisland seen in the top of (b), embedded in the Au overlayer. Point defects and raised areas are seen in its interior. d-e) Magnifications of the areas highlighted in (c). In (d) graphene is partly raised from the substrate, displaying atomic resolution. Its height is similar to the Au/Ni surface as displayed in the profile in (f). In (e) an area is displayed where the bottom (blue) parts of the GNI have the same appeareance as on top of an island (yellow), with raised parts both on the bottom - at the sides of the intercalated island - and at the sides and on top of the island. g) The height of the island is greater than the surrounding Au/Ni and measures 2.1 ± 0.2 Å as a Ni step.

the figures presented along this chapter, dislocations are observed under graphene nanoislands after successful intercalation of Au. Moreover, intercalated nanoislands in embedded configuration show a height difference of 0.2±0.1 Å to the surrounding surface, very different from the 1.2 Å measured for these nanoislands.

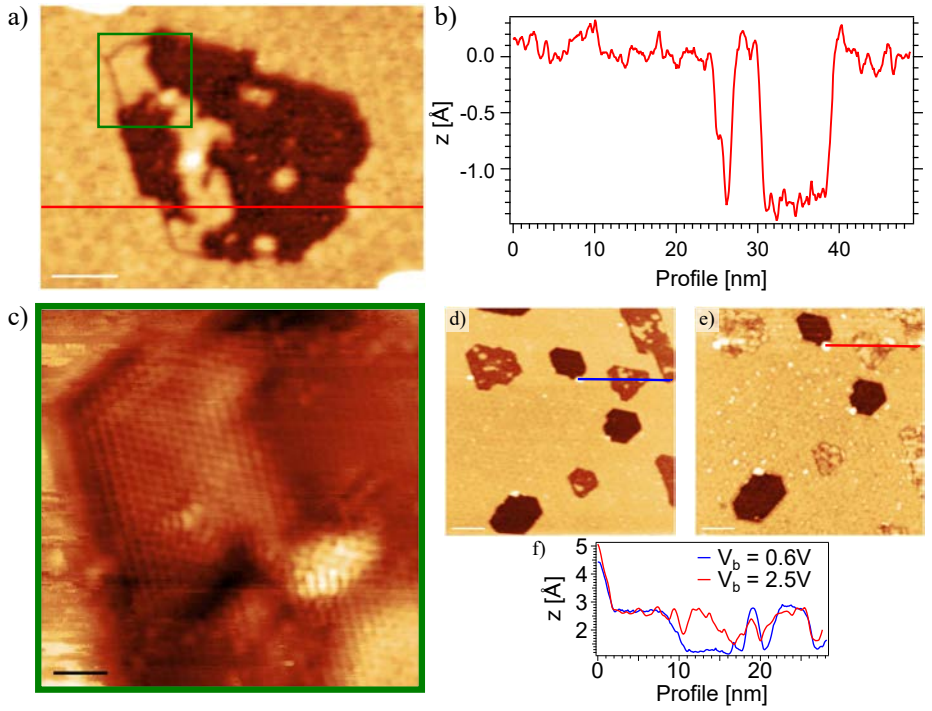

Figure 4.10: a) STM topographic image of a GNI after deposition of 0.9 ML of Au and annealing. The island is embedded in the Au overlayer. V_b=0.83 V, I_t=0.5 nA, scale bar 5 nm. b) Height distribution of the scan of (a). The surface of Au/Ni is normalized at 0. Only another peak is recognized at -1.3 Å. c) Magnification with atomic resolution of the squared area in (a). The lattice of graphene is resolved on the raised parts of the island and displays some scattering effects near the defects. V_b=5 mV, I_t=13 nA, scale bar 1 nm. d) Scan of an area on the sample, where some graphene nanoislands and some holes in the Au overlayer are recognized. V_b=0.6 V, I_t=0.2 nA. e) The same area with V_b=2.5 V, I_t=0.2 nA. f) Profiles across the two lines shown in (d-f). The island looking low and embedded in (d), shows a corrugated profile in (f), with an average height similar to the Au surface.

Another example for a similar preparation is shown in Fig. 4.10. Fig. 4.10a shows a graphene nanoisland surrounded by Au and 1.3 Å lower than it, except for some zones which display the same height of Au, as evidenced in the profile reported in Fig. 4.10b. Fig. 4.10c shows a zoom on one of such raised areas with atomic resolution: once more, the lattice of graphene is resolved and scattering effects are observed. A larger scan area is displayed in Fig. 4.10d-e, at V_b=0.6 V and 2.5 V respec-

tively. A starking contrast difference is observed in the bottom part of the nanoislands: graphene now seems to be raised, as eivdenced by the profiles reported in Fig. 4.10f.

This is the same effect observed for graphene nanoislands grown on Ni(111), due to the onset of an interface state (IFS) at E=2.45 V arising from the shift of the surface state of Ni under graphene[76]. Furthermore, the apparent height of graphene on Ni(111) is 1.4±0.1 Å, and since an Au island on Ni(111) measures 2.5±0.1 Å, the observed depth of 1.2±0.1 Å for the nanoislands of Fig. 4.9 and Fig. 4.10 is fully compatible with the height difference of an Au ML on Ni(111) and a GNI/Ni(111). Therefore, the bottom of GNIs is laying on Ni(111), and this part is consequently not intercalated.

We next discuss the nature of the parts of nanoislands which are raised. As previously observed, the large flat areas displaying a height of 2.1±0.1 Å (Fig. 4.9c and e) respect to the GNI/Ni(111) parts, have also the same appearance as the bottom parts of the nanoislands adsorbed on Ni(111). Since the height difference of 2.1 Å is that of a Ni step, these parts are recognized as Ni islands under the graphene nanoislands.

Finally, the "bubble" areas, raised by 1.2±0.1 Å and showing scattering effects, has to be explained. The observation of scattering effects at the bias voltages employed for these images (V_b<10 mV for the STM topographies with atomic resolution) can be related to a decoupled graphene, as discussed below in Sec. 4.4. Such electronic decoupling could derive from a wrinkling of graphene due to strain, as in Gr/Pt(111) [253]. But it is observed that such bubbles are here found always in the vicinity of either a nanoisland edge or a vacancy defect, which are the preferential sites for metal intercalation [94]. Therefore, we associate such scattering effect to intercalation of Au.

Furthermore, an alloying-dealloying mechanism for Au on Ni(110) was reported [254]. At low concentrations, Au is alloyed in the topmost Ni layer, and the "squeezed out" Ni atoms form 2D islands on the surface. Only at higher concentrations (>0.5 ML), Au islands and patches start to form on top of the Ni surface.

The explanation of the whole appearance of the nanoisland of Fig. 4.9 is represented in Fig. 4.11 and could be as follows: Au atoms can intercalate under graphene nanoislands only through vacancy defects or from the edges. As an energy barrier is associated to intercalation through edges and the metal surface surrounding is an

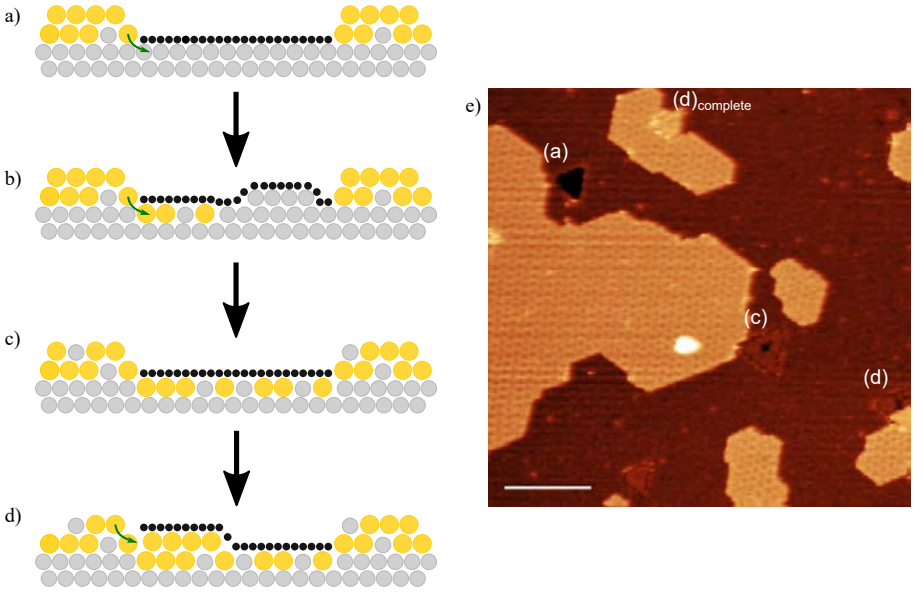

Figure 4.11: Proposed intercalation mechanism. a) Au atoms penetrate through the edges or defects under GNIs. b) For low intercalated Au coverages, they are alloyed in the topmost Ni layer, and Ni atoms squeezed out of it form 2D islands under Gr. c) Intercalation continues until completion. The Ni atoms of the 2D islands diffuse and alloy in the Au overlayer. d) After completion of the first Au layer, more Au layers can intercalate under Gr. e) STM topography showing the intercalation evolution in one frame: an island adsorbed on Ni, two nanoislands intercalated by 1 Au ML (only one is indicated), a nanoisland where the second Au layer is intercalating and one where this process is completed. 1.5 ML Au was deposited. Scale bar 20 nm.

energetically favourable site of adsorption, this process is determined by kinetics, and few atoms or clusters of Au are allowed to intercalate. These atoms alloy into the topmost Ni layer, while Ni 2D islands form under graphene, Fig. 4.11b. The fact that the total area covered by "bubbles" (120 nm^2) and intercalated Ni islands (100 nm^2) is very similar seems to confirm this scenario. Intercalation then continues until completion, Fig. 4.11c. The Ni atoms squeezed out likely alloy in the Au layer, either under GNIs or in the surface around them, where a Au/Ni alloy is already present. Intercalation can then continue for more layers, as more Au is available at the edges of Gr, Fig. 4.11d. A frozen frame displaying the process is shown in Fig. 4.11e (see also Fig. 4.2 for another example).

One could think that at sufficient high coverage of intercalated Au, the alloying process does not take place, as it happens with the Au deposited on the bare Ni surface around the nanoislands. This, however, was not verified in our experi-

ments. This can be attributed to the different energetic landscape given by the presence of Gr on top of Ni and/or to the intercalation routes (edges/defects) limiting the Au availability under Gr. The effect would be similar to the "colander effect" proposed for Co intercalation under Gr/Ir(111), where Gr limits the intercalated Co cluster sizes, resulting in alloying-mediated stretched Co/Ir film, different from bare Co/Ir(111) [255, 256].

4.3.3 Atomic structure of the graphene islands

Intercalation is an effective method of controllably modifying the electronic properties of graphene and realizing graphene/metal interfaces not possible by direct growth on the intercalant or entirely novel, as is the case of Gr/Ni/Ir [101]. By CVD growth, we can grow selected GNIs controllably on Ni(111); by intercalation of Au, recovery of the pristine graphene electronic properties is expected [84], as will be discussed in Sec. 4.4. However, as the structural properties of graphene depend on the chemical and stacking interaction with its substrate, intercalation can lead to structural modification of the as-grown graphene nanoislands. The strong interaction with Ni(111) induces a slight strain (by 1.2%) in the atomic lattice of graphene, in order to provide a perfect match of its relaxed structure (lattice constant a_{Gr}=2.46 Å) to the almost coincident structure of the surface (lattice constant a_{Ni}=2.46 Å). A different interaction with the weakly-interacting Au ($a_{Au(111)}$=2.88 Å) is to be expected.

Fig. 4.12 shows STM topographies with atomic resolution of two lateral interfaces of Gr to Au for embedded islands. In the two cases, the atomic lattice of both Gr and Au are contemporarily resolved. As observed, the two lattices are completely aligned, along the high symmetry directions of the Ni(111) substrate . After calibration, we measure a_{Gr}=2.43 Å and a_{Au}=2.82 Å from Fig. 4.12a, which is taken in the VT-STM system, and a_{Gr}=2.46 Å and a_{Au}=2.86 Å from Fig. 4.12b, which was taken in the LT-STM system. Both images are taken on Au thin films in the dislocation regime, where the lattice constant of Au is reduced compared to Au(111) [245]. The corresponding lattice mismatch is 13.8% and 13.9%, respectively..

The lateral interface shows also the commensurability of graphene to the substrate. As seen from the coincidence lattice superimposed on Fig. 4.12a, commensurability between Gr and Au lattices is found for Gr 8x8 cells to Au 7x7 cells. Marchenko et al. [103] report a 8x8 superstructure together with a 9x9 supestructure forming for

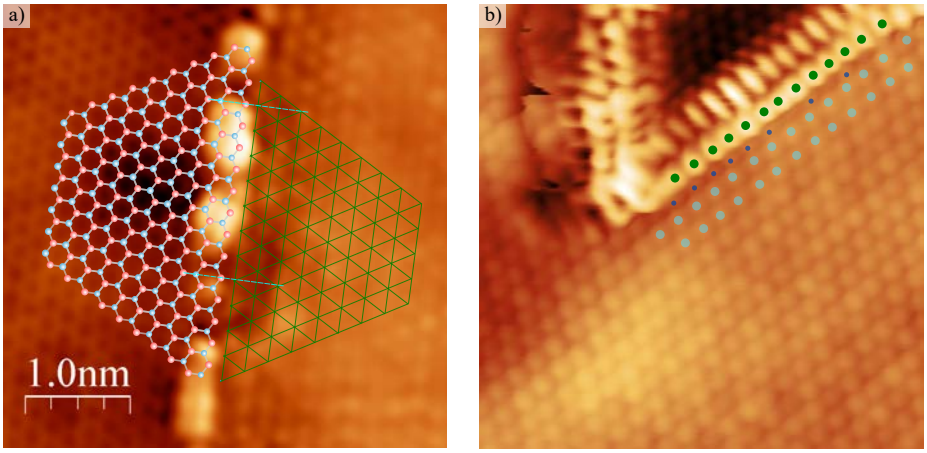

Figure 4.12: a) STM topographic of the interface between the embedded GNI of Fig. 4.5a and the Au surface. The atomic networks have been superimposed. Though the direction of the Gr edge suggests a zigzag perfect structure, the exact structure of it is not clearly resolved due to a strong interaction of the tip. Nevertheless, the commensurability with Au can be extrapolated. b) STM topographic image of a different embedded GNI and its interface to the Au overlayer.

low amounts of Au deposited and which, instead, we did not observe.
The long range commensurability does not induce a Moirè pattern on graphene, which is indicative of the weak interaction with the Au substrate. Instead, for Au film thicknesses in the dislocation regime, the dislocation lattice is repeated under graphene, as observed in Fig. 4.2b in the beginning of this chapter and along the following figures.

4.3.3.1 Edge structure

As discussed in Sec. 3.2.1.2, on Ni(111) zz_t edges reconstruct because of energetically unfavourable stacking of the outer edge atoms to top Ni atoms, and thus hexagonal nanoislands are characterized by alternated zz and reconstructed (zz_{rk}) edges. After intercalation of Au, though, the stacking and energetics of the edges are completely modified. Since the chemical interaction of graphene with Au is reduced respect to Ni, it is interesting to investigate the behaviour of reconstructed edges upon intercalation and the possibility for them to recover the zz symmetry corresponding to free-standing graphene. We also expect different edge coordinations for embedded or on top edges, which might induce different behaviours also for the reconstructed edges.

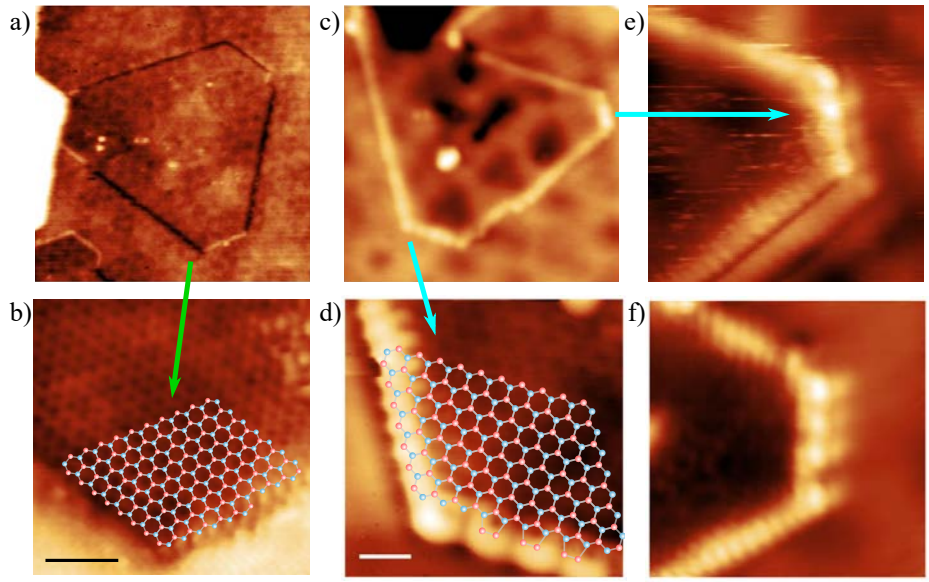

Figure 4.13: a) STM topographic images of a hexagonal nanoisland embedded in the Au topmost layer. b) Magnification of the bottom part of nanoisland in (a). Atomic resolution is displayed on the edges, and the atomic lattice is superimposed on the STM topography. Two zigzag edges are recognized, where the one to the right also displays a kink. V_b=6 mV, I_t=1.1 nA, scale bar is 1 nm. c) STM topography of the termination of a larger graphene nanoflake, formed by the cohalescence of the hexagonal island represented and another nanoisland not shown in the scan. d) Atomic resolution on the edges shows a zigzag edge on the left and a curly structure with a periodicity double that of zigzag, identifying its structure as a reconstructed edge. V_b=0.3 V, I_t=1.0 nA, scale bar is 1 nm. e) With a different tip, another short edge displays regularly spaced protrusions. f) displays the same structure on a different GNI with higher resolution.

Fig. 4.13 shows STM topographic images of the edges of two hexagonal nanoislands embedded in the Au layer with their corresponding edge structures, as extrapolated from the images with atomic resolution (Fig. 4.13b,d). Both nanoislands display three long and straight edges, and two short edges – while the last edge is in contact to a saturated step edge in (a), and the nanoisland in (c) is coalesced to a larger graphene nanoflake. The corresponding surfaces are, in both cases, Au thin films in the dislocation regime. The temperature of intercalation was 500°C for the nanoisland of Fig. 4.13a and 380°C for the one of Fig. 4.13c. As it is observed, two different cases are represented. Fig. 4.13b shows a magnfied topographic scan of the bottom edges of nanoisland (a). Atomic resolution reveala the honeycomb structure of graphene, ending in a straight line to the left of the nanoisland. The edge to the right/bottom, instead, displays straight lines of point protrusions at the two sides

of a kink. As evidenced by the superimposed lattice of graphene, such protrusions have the periodicity of one benzene ring and thus a zigzag symmetry.

Fig. 4.13d shows a different behaviour. Here, both edges have an apparent height greater than both graphene and Au – the appearance of the edges will be addressed in Sec. 4.4. The edge to the left displays a line of protrusions with the spacing of a zigzag edge. The bottom edge, instead, displays larger protrusions. We observed this appearance in many islands, at the short edges where reconstruction is expected on the Ni surface, and measured an average periodicity of 5.2±0.3 Å. This is compatible with the 2x2 reconstruction observed for GNIs on Ni(111) (see Sec. 3.2.1.1).

Fig. 4.14 shows a series of STM topographic images of on top hexagonal GNIs and the termination of the edges where reconstruction is expected to take place on Ni(111), after intercalation of Au at 380–390°C. The three nanoislands represented are all found in the proximity of a step edge: Fig. 4.14a has a part embedded in the higher terrace. We note that, by our definition, this is considered on top. Fig. 4.14d is actually a partly on top nanoisland, with a part embedded in the higher terrace and a smaller portion extending over it, across the step edge; Fig. 4.14g is a nanoisland with two edges in contact to a step edge. STM topographies with atomic resolution of their bottom edges are shown in Fig. 4.14b,e,h (in h the full atomic lattice is not resolved, but the protrusions of the edges are visible), and the corresponding profiles are reported in Fig. 4.14c,f,i together with profiles of their zigzag edges, for comparison.

The three terminations show different behaviours. Edge 1 of Fig. 4.14b displays a series of protrusions with the same zigzag periodicity of edge 2, as seen in the profiles. In the other two nanoislands, a clear periodicity is not recognized. The edge of Fig. 4.14e displays a curvy shape, with point protrusions of different appearance and oddly spaced. In Fig. 4.14h, the edge has a curly appearance, and though a periodic structure is not recognized, comparison to the zigzag profile of edge 2 shows a near-to-double coincidence. The spacing of these protrusions measures 0.52 Å, 0.40 Å and 0.32 Å. The exact structure, however, could not be resolved.

In conclusion, the edges grown in zz_t direction in Ni(111) appear with diverse structures after the intercalation process, and a unique final structure was not observed. Perfect zigzag edges were observed in two cases along the short edges of hexagonal islands; protrusions with different spacings were observed in others. These

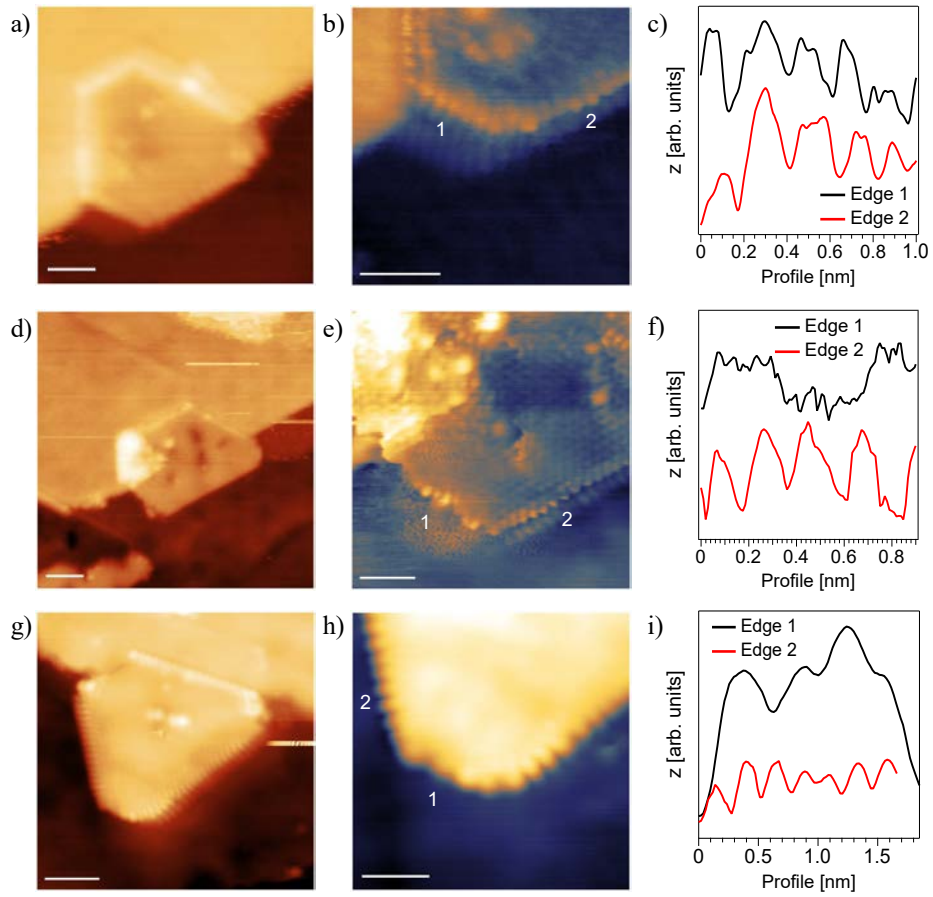

Figure 4.14: Left column (a,d,g): STM topographic images of on top hexagonal nanoislands after intercalation at 380–390°C. Central column (b,e,h): magnification of the bottom edges of the nanoislands, with atomic resolution. Right column (c,f,i): Profiles along the two edges indicated in the images of (b,e,h). a) V_b=0.4 V, I_t=0.83 nA, scale bar 1 nm b) V_b=-50 mV, I_t=7 nA, scale bar 1 nm d) V_b=0.67 V, I_t=1 nA, scale bar 2 nm e) V_b=10 mV, I_t=8 nA, scale bar 1 nm g) V_b=284 V, I_t=1 nA, scale bar 2 nm h) V_b=210 mV, I_t=2 nA, scale bar 1 nm.

are mostly compatible with the spacing expected for well-formed zz_{rk} edges.

It has to be noted that, on Ni(111), nanoislands can grow embedded in the Ni layer, as also shown for extended graphene in [159]. Here, zigzag edges also in zz_t direction have been observed, and therefore one of the possible reasons of the observation of zigzag edges after intercalation is that the nanoislands grew embedded in the Ni substrate. As the abundance of embedded nanoislands in Ni(111) is usually low, though, and these often display irregular shapes, this is unlike to be the

main mechanism through with fully zigzag GNIs are obtained.Furthermore, given the intercalation mechanism previously explained, it seems unlikely that nanoislands growing embedded in Ni would be on top in Au.

Overall, the presence after intercalation of edges displaying reconstruction, disordered structures and zigzag suggests that a recovery of the regular zigzag edges is indeed the equilibrium situation, but that the process is hindered. Though the equilibrium structure is zigzag, in fact, an energy barrier has to be overcome in order for the carbon atoms of the edge to reorganize. The thermal energy provided during the intercalation process in the range of temperatures allowed, might not be sufficient to overcome such barrier. The observation of zigzag edges in the reconstruction direction after intercalation at 500°C does point to an energy barrier limitation. Furthermore, either a carbon source or a loss of 1 carbon atom per unit cell from the edges are necessary in order to transform the pentagons of the zz_{rk} edge into hexagonal benzene rings.. "Dereconstruction" of the reconstructed edges into zigzag symmetry is then not a straightforward process, and a full control might not be possible in the Gr/Au/Ni system due to the phase diagram of the two metals.

4.4 Electronic properties

As discussed in Chap. 2, the electronic properties of a surface can be probed with spatial resolution by STS methods. In this section, we explore the electronic properties of the Gr/Au/Ni system and compare them with Gr/Ni from different perspectives. i) With field emission resonances (FERs) we access to work function variations that can be used as chemical probe. ii) By studying surface states of Au we study the effect of graphene on the underlying Au, which gives information on the relative interaction. iii) The study of QPIs gives information on the scattering properties of the lateral Gr/Au interface, another indirect way to probe the Gr/Au interaction. iv) The final part is the direct study of the Gr electronic properties. Here we find difficulties to access to bulk Gr properties, due to the fact that surface states are the preferred tunneling channel. We do, however, detect states localized at the edges.

4.4.1 Chemical identification by field emission resonances

When an electron is placed in front of a conductive surface, an image-charge arises in the substrate. This image-charge defines a potential in which a set of hydrogen-

like (Rydberg) states known as image-potential state (IPS) arise. IPS can also be viewed from the phase accumulation model proposed by Echenique and Pendry [257]. In this model, bound states in the quantum well defined by the crystal band gap and vacuum potential are obtained from the phase shifts at each boundary, whenever the accumulated phase gives rise to constructive interference. The condition for this can be written $\phi_B + \phi_C = 2\pi n$, where ϕ_C is related to the crystal band structure, and ϕ_B to the vacuum barrier. In particular, image states arise from phase changes in the reflection at the vacuum boundary (changes in ϕ_B), , and are therefore related to details in the vacuum potential. For that reason, they carry important information on the work function and any other surface property that shape the vacuum potential. We will see in Sec. 4.4.2 that states originated from phase shifts in ϕ_C are called intrinsic surface states and are more related to the crystal band structure.

In STS, image states can be accessed when the bias approximates the work function, $V_b \gtrsim \phi$, i.e. in the field-emission (FE) regime. The vacuum potential is therefore strongly distorted by the electric field of the tip, hence in this regime the IPS are Stark-shifted and become field-emission resonances (FERs) [180, 258–260]. Although the absolute relation between the original IPS and FER energies cannot be extracted, the relative changes in IPS energies due to local work function changes, lateral confinement, etc. are reflected in FERs. In general, the lowest lying FER is most sensititve to the details in the shape of the original image potential, whereas the higher lying FERs feel more the region of the potential barrier distorted by the tip [259, 261]. The width of the FERs additionally carries information on the lifetime, dominated by their coupling to bulk states above the surface projected gap [262]. Because of the relevant information on the properties of a surface, the investigation of IPS/FERs has been widely used in graphene/metal systems [263] to e.g. explore different interaction regimes [243], local variations in the Gr/metal interaction [100], interfacial coupling and graphene thickness [264] or lateral confinement in GNIs [265].

During the course of this thesis, we exploited FERs as chemical probes, identifying the different species or structures on the surface. We also studied their evolution with the thickness of the Au film and used them as an indipendent thickness calibration, as will be discussed in the next subsection. Spectra were acquired in the C.C. mode due to the high energies to be accesed (up to 10 V above the Fermi level). This way the tip retracts as the voltage increases, thus reducing current and electric

field induced processes.

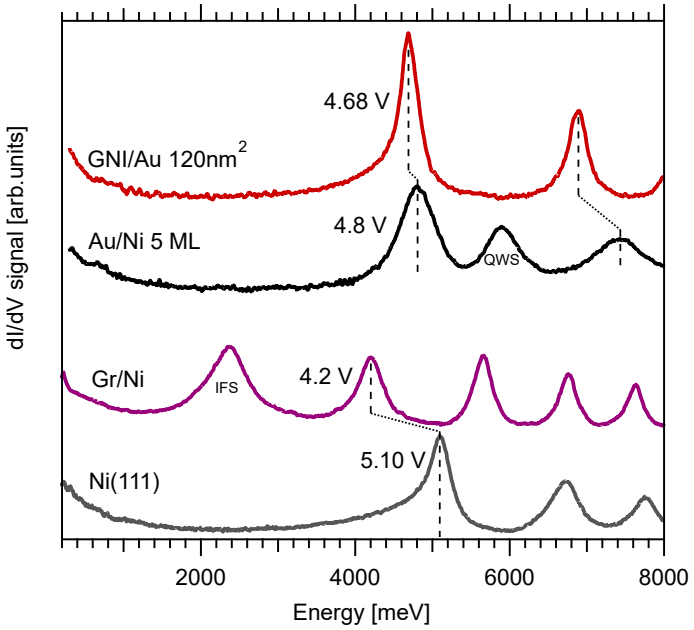

Figure 4.15: Constant current dI/dV spectra of graphene nanoislands on Au/Ni and on the surface of Ni(111) and of the corresponding surfaces. The spectrum of Au is the one corresponding to the surface where the graphene nanoisland of the Gr/Au spectrum was measured.

Fig. 4.15 shows C.C. spectra acquired on graphene nanoislands adsorbed on Ni(111) and on Au films, and the corresponding spectra on the bare metals. As can be observed, the spectrum of Ni(111) shows its first peak at an energy of 5.10 eV, identified as the $n = 1$ FER. The spectrum of graphene on this surface shows its first peak at an energy of 2.4 eV. This peak is not related to the $n = 1$ resonance, actually, but rather to the onset of an interface state (IFS), which will be further discussed in Sec. 4.4.2. The first resonance appears at 4.2 eV, thus at an energy difference of 0.9 eV from the Ni one. This identification is verified by combined calculations and by observing the continuous energy shift when going from Ni to Gr in a line of C.C. spectra as in [76].

As a consequence of the very different spectra, identifying Gr on Ni is straightforward. In fact, this can be done easily even in topographic images. When the bias

voltage exceeds ~2.3 eV, tunneling in the IFS over graphene flakes results in a much enhanced apparent height compared to Ni, which displays a flat DOS at this bias. A similar effect can in principle be obtained for bias voltages around the first Gr FER at 4.2 eV, where the DOS of Ni is still much lower. In practice, the first method is generally preferred.

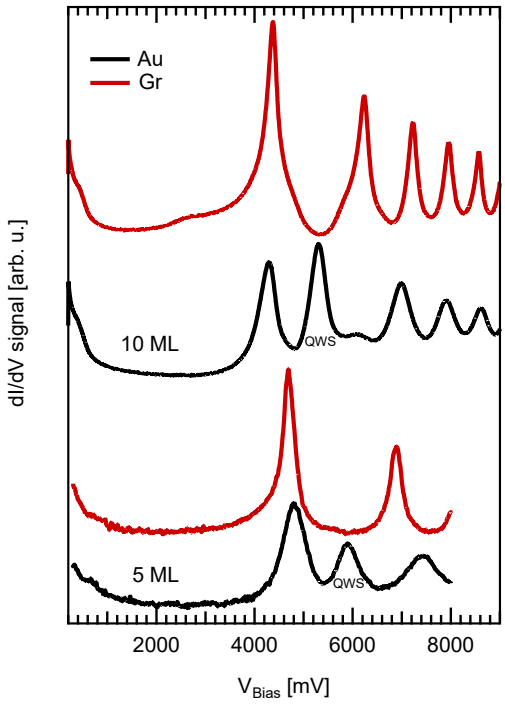

Figure 4.16: Constant current dI/dV spectra on the Au surface and on Gr for two different Au film thicknesses, evidencing how the QWS peak marked in the Au spectra is not detected under Gr. The different width of the peaks in Au and Gr is also noticed.

After intercalation of Au, differentiating graphene and Au is less direct. The spectrum of the Au surface for a film thickness of 5 ML shows the $n = 1$ FER at an energy of 4.8 eV. On Gr, such FER appears at 4.68 eV. Different energies can be found for different nanoislands, with a negative shift in the range of 0.1–0.2 eV respect to Au. However, in order to identify the materials, we further note that the peaks width is considerably reduced from Au to Gr. This implies an enhanced lifetime of the FERs [261], which we relate to the increased distance of the image states from the surface due to presence of the graphene spacer. The graphene-induced energy shift

of the n=2 FER is larger, of 0.6 eV. It has been shown that FERs for n>1 are better suited to estimate work function changes due to the localization of the n=1 deep in the potential well [266]. We can therefore attribute a work function reduction of 0.6 eV to the presence of the GNI on Au, a value smaller than the ~1 eV measured for extended graphene on Au/Ni by inverse photoemission [243]. We note that qualitatively this effect seems more pronounced than for Gr/Ni, consistent with the reduced coupling.

The peak located between the n=1 and n=2 FERs on Au, labelled as QWS, does not have its shifted counterpart on Gr. This is due to the fact that it is related to the quantization of bulk Au states, which cannot be accessed when the tip is on top of the graphene. This provides a more direct chemical fingerprint than the relatively small energy shifts of the FERs. Fig. 4.16 shows spectra acquired on samples with two different thicknesses, where the presence of QWS only on the Au spectra is clear. The energy of QWS depends naturally on the film thickness, and can be used as a calibration pattern, as shown in the following.

4.4.1.1 Thickness evolution

In metallic thin films, the reduced size of the system leads to the formation of quantum well states (QWS) in the direction normal to the surface. Vertical electron confinement leads to quantization of the bulk bands [267], which leads to a subtle perturbation of the image potential in the vacuum outside the surface. Such small modifications are hard to be detected by the FERs. However, more important perturbations arise from the interaction between QWS and FERs and the resulting hybridization [268]. Furthermore, structural changes that evolve with thickness provide another source of perturbation that can be explored by FERs and used to identify the thickness of a given film.

We collected C.C. dI/dV spectra on the surface of Au at different film thicknesses, Fig. 4.17. Au was evaporated using the home made evaporator (see Chap. 2) and keeping a constant power. The estimated deposition rate was 0.45 ML/min, with an error of ~10%, as calibrated by imaging surfaces with submonolayer coverage. As an example, after evaporation for 12'30" the estimated coverage is 5.6±0.6 ML. The representative spectra on this surface is indicated as 5 ML. We note that the spectrum corresponding to 7 ML was also acquired on this surface, on a large Au

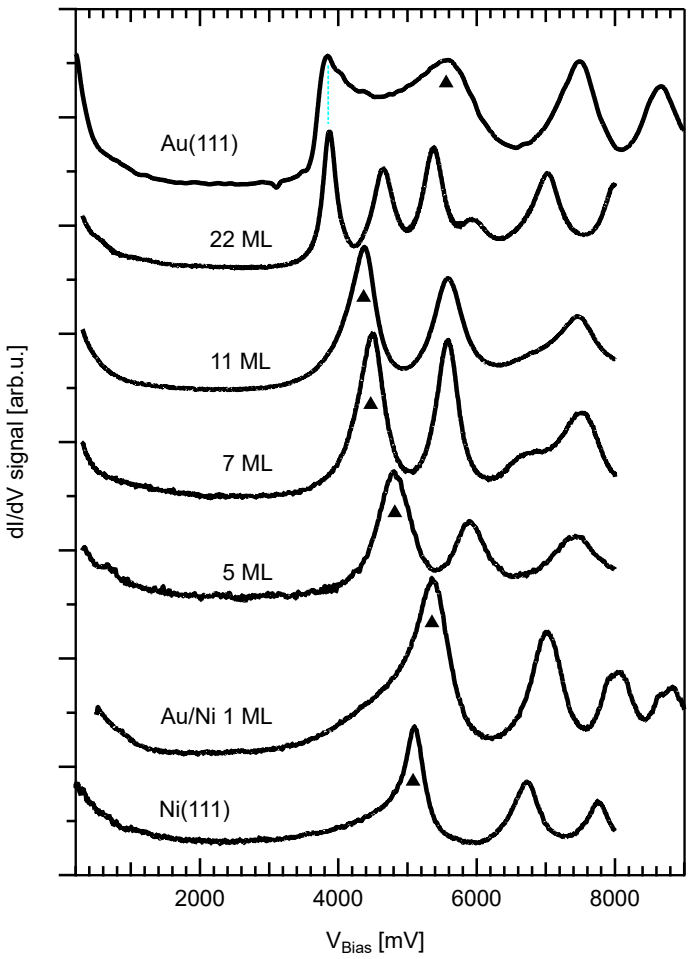

Figure 4.17: dI/dV spectra at constant current acquired on the surface of Au films of different thickness and on the surface of a Au(111) crystal, showing the evolution of FERs with thickness. The first FER, when identified, is marked with a black triangle. A blue dashed line marks the Au(111) bulk band edge.

island of 2 layers. We used a sample where graphene nanoislands were grown, and intercalated increasing amounts of Au by repeating the deposition-annealing process, for a total of 3 depositions (two of 12'30" and one of double time). Only the point corresponding to ~1 ML belongs to a sample without graphene nanoislands and where no annealing was carried out, so that Au/Ni intermixing is minimized.

A monotonic decreasing behaviour is observed for the lowest lying peak for in-

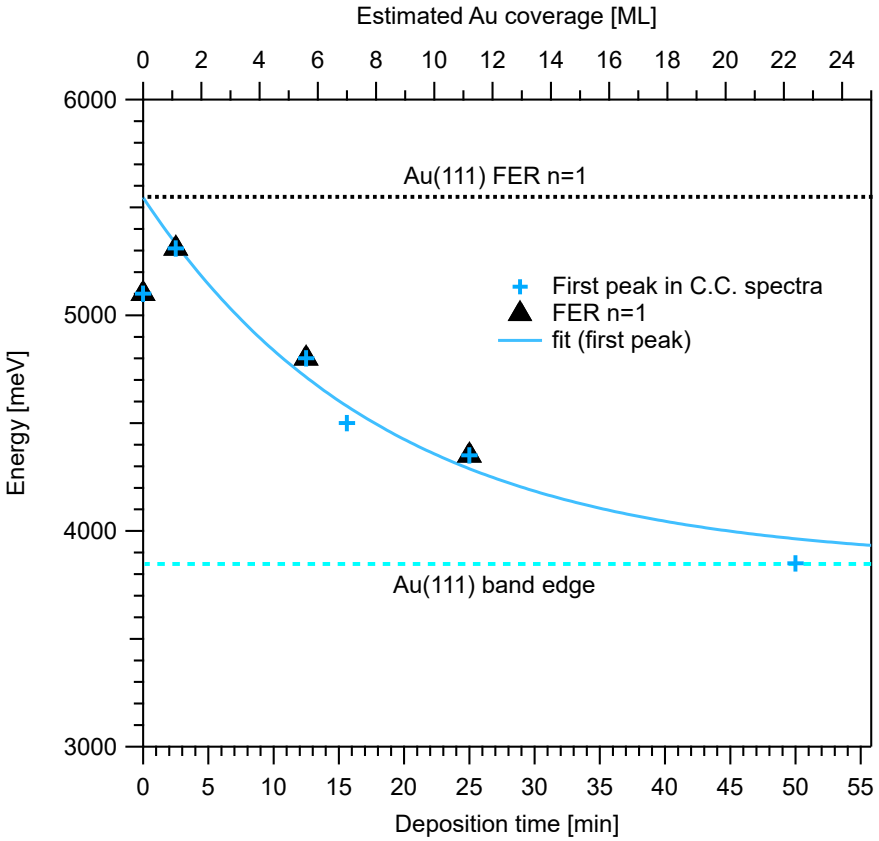

Figure 4.18: Evolution of the lowest lying peak in the C.C. spectra of Au with film thickness. The data have been fitted to an exponential $E = E_0 + A \cdot \exp(-\tau x)$, where y0 has been fixed to the asymptote corresponding to Au(111), indicated with a blue line at 3850 mV in the figure. The peaks recognized as the $n = 1$ FER are marked with a triangle, and the energy of this in Au(111) is indicated by a black line at 5550 mV.

creasing film thickness. At a film thickness of 22±1 ML, it appears at an energy of 3.85 eV, which is already the energy found for bulk Au(111). In Fig. 4.18 we plot the energy of such peak as a function of Au thickness. The data fit quite nicely an exponential curve of the type $E(x) = E_0 + A \cdot \exp(-\tau x)$, where E_0 was fixed to 3.85 eV. By using this curve, we could consistently cross check the Au film thickness on different samples and independently confirm the evaporation rate.

Regarding the physical interpretation of the nature of the tracked peak, we note that this cannot be identified as the $n = 1$ FER for two reasons: the first is that a decrease in energy of around 1.3 eV when going from Ni to thick Au films would

not be consistent with the ~0.3-0.4 eV increase expected from the corresponding work function difference [243]. Secondly, we know from previous work that the C.C. spectra on Au(111) shows a sharp onset at 4 eV that is not related to FERs, but to the upper boundary of the projected band gap and the onset of bulk states above this energy. According to this, the second peak in the Au(111) spectra, at 5.6 eV, would correspond to the n=1 FER. A 0.5 eV shift with respect to Ni would indeed be in agrement with the work function differences. That means that at some point there is a crossover between the n=1 FERs, i.e. the lowest peak for thin Au films, and the Au QWS, which converges to the lowest lying peak in bulk Au(111). By comparing spectra with and without graphene, we have identified the n=1 peak for thicknesses where data was available (marked as triangles in Fig. 4.17 and Fig. 4.18), and we can locate the threshold for the crossover somewhere above 11 ML.

We attribute the initial energy reduction and final recovery of the n=1 FER to the presence of a substantial strain in the thin Au films that is gradually released as we increase the thickness. This scenario will be further corroborated with the thickness evolution behavior of surface states, as described in the next section.

4.4.2 Monitoring substrate interactions by surface states

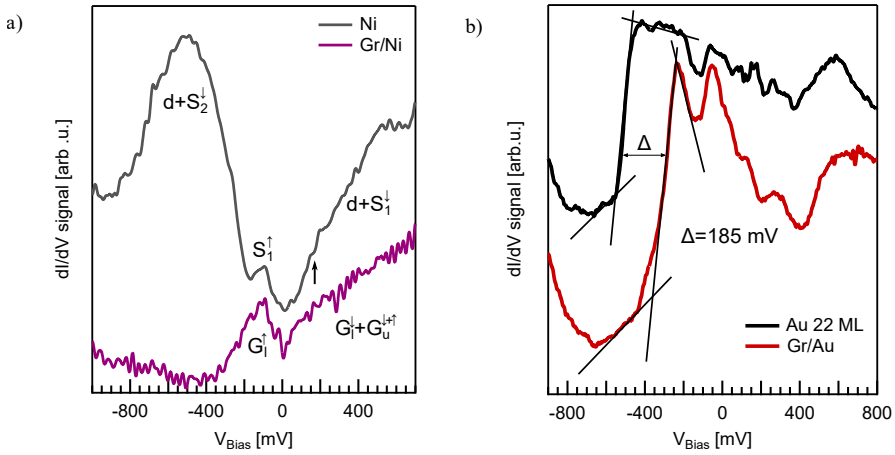

Figure 4.19: Typical dI/dV spectra at constant height of a) Ni(111) and GNI/Ni(111), V_{mod}=10 mV, ν=3.5 kHz. b) Au thin films on Ni(111) (22 ML) and GNI/Au/Ni on the same surface. Onsets: -505 mV and -320 mV for Au and Gr respectively. V_{mod}=10 mV, ν=3.3 kHz.

In the phase accumulation model previously introduced, surface states (SS) can

be seen as the $n = 0$ (image) states. As explained before, they are originated from phase shifts at the crystal boundary (ϕ_C), which is closely related to the crystal band structure. Their wave function is mostly confined close to the surface plane, making it sensitive to the presence of defects, impurities or adsorbates including adsorbed layers. In the case of the nanoislands relevant to our case, if the interaction is not strong enough to quench the surface state, it will only shift its energy at the interface due to the new boundary conditions imposed by the island. This shift can be measured directly in dI/dV spectra, where the onset of the SS band is seen as a step-like increase of the (momentum integrated) density of states. A more accurate determination of the shift can be carried out by momentum-resolved band structure information. This can be obtained via another consequence of the interaction of SS with the adsorbed material: the scattering. The interference patterns arising from the scattering of the surface state at the two sides of the boundary of the nanoisland can be used to obtain the momentum of the scattered waves and map the band structure. Fitting the latter with parabolic bands, as should correspond to nearly free electrons, can allow an accurate determination of the band onset if the data point density at the low k region is large enough to follow the maxium curvature.

In noble metals, the Gr-metal interaction is weak enough to induce only relatively small energy shifts, and energy shifts have been obtained from the onset analysis in dI/dV spectra [269, 270] and quasiparticle interference anaylsis [242, 269, 270]. We will use both methods to analyze the effect of graphene on the surface states of Ni(111) and Au(111).

Fig. 4.19 shows comparative dI/dV constant height spectra of graphene-covered Ni and Au/Ni and of the respective metal surfaces. The spectrum of Ni shows a prominent peak at bias about -500 mV, a weaker peak at negative bias near E_F and a broad peak at positive bias. The first one is coming from majority bulk d bands, convoluted with the minority band of a hole-like dispersing surface state labelled as S_2 in previous studies [76, 271]. The next feature, at around -100 mV, is related to the majority band of a electron-like dispersing surface state labelled as S_1. At positive bias, the minority S_1 and bulk d bands overlap resulting in a broad peak with onset at around 150 mV. These values are in qualitative agreement with other STS measurements: Krönlein et al. [272] found the onset of majority S_1 at -165 mV, and Garcia-Lekue et al. [76] at -110 mV, while Braun and Rieder [273] measured the bottom of majority and minority S_1 at -225 mV and -165 mV respectively.

A double peak structure around E_F is also shown in the spectrum of graphene on Ni(111). Ab-initio calculations assign these features to the π bands of graphene, which are those forming the Dirac cone around the Fermi energy. The interaction with the Ni d bands opens a gap around the Dirac point and spin polarizes these π bands into $G_{u/l}^{\uparrow/\downarrow}$ bands [76]. This results in a spin-dependent alignment of the graphene π and the Ni d peak that could explain the strong spin filtering effect observed at this interface [77]. The coincidence of graphene π states at the energy of the Ni surface states makes it difficult to conclude if the latter still remain at this energy region. To check for surface state fingerprints we look at the interference patterns that they should produce in spectroscopic maps. An example of such dI/dV map, acquired at -100 mV, is shown in Fig. 4.20. The map shows clear inteference patterns outside the GNI. In contrast, we find no features inside the GNI, indicating the abscence of any SS at the GNI/Ni interface in this energy region. It is possible to understand what happened by looking back to the C.C. dI/dV of Fig. 4.15. According to the theory, the peak there identified as IFS at around 2.4 eV can be assigned to an interface state derived from the Ni(111) S_1 state [76]. The strong energy shift is another indication of a substantial Gr-Ni interaction, in line with the perturbation of the graphene Dirac cone described above.

After intercalation of Au, the situation is radically changed. Fig. 4.19b shows the spectra acquired on a 22 ML Au film and a GNI found on top of it. In both cases a pronounced step-like signal increase is the dominant feature. This is usually related to the onset of a 2D nearly free electron band, in this case a surface state. In Au the onset lies at -505 mV, which is the value corresponding to the Au(111) surface state [274]. For the GNI the onset is shifted to -320 mV. This shift of 185 mV is larger than the 90 mV measured for graphene flakes on intercalated Au films on Ir(111) [242]. Yet, the magnitude of the shift is much lower than that found for Ni, indicating a weaker interaction with Au.

The energy evolution of the quasiparticle interferences (introduced in Chap. 2) and the band dispersion obtained from it is an alternative way to analyze the surface states. Fig. 4.21 shows an example of such analysis, using dI/dV maps at different energies and the corresponding FFT images. Due to the small size of the GNIs, not much larger than the QPI periodicities, obtaining clear signal in the FFT images is challenging. We chose an area with many GNIs, in order to maximize the signal from the small flakes. The resulting FFTs display a ring and a star-like feature in the center,

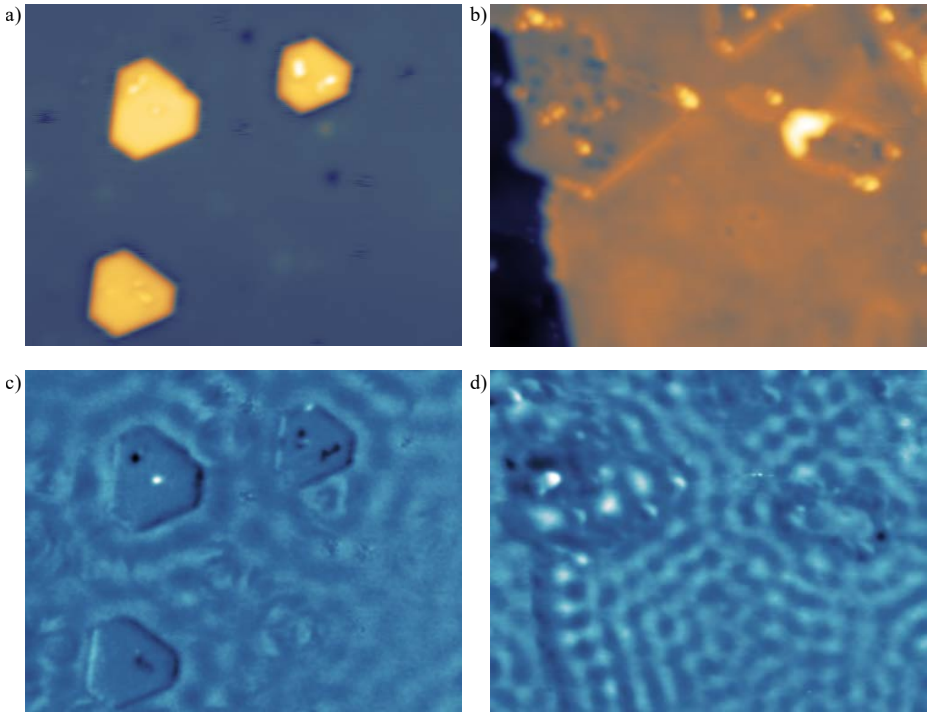

Figure 4.20: STM topographic image of GNIs on a) Ni(111) and b) Au (22 ML) on Ni after intercalation. c) dI/dV map of the area in (a) at V_b=-100mV, showing the standing waves of the S_1 surface state of Ni reflecting at GNIs edges. d) dI/dV map corresponding to (a) at V_b=-150mV: in Au, the standing waves propagate also under GNIs. Size (a-d): 37x29 nm^2. (a) and (c) adapted with permission from [76]. Copyright 2014 by the American Physical Society.

which give maxima in the profiles as in Fig. 4.21d. We interpreted the ring as related to the standing waves on the Au surface, while the star-like feature as resulting from scattering at GNIs edges, displaying dominant triangular symmetry. To cross-check such interpretation, we decoupled the two contributions by differentiating the Au and the GNIs in separate images, as shown in Fig. 4.21e-f. The scattering vectors were then obtained as the radius of the ring and the distance of the star's vertices from the center. We measured them in the comprehensive FFTs (Fig. 4.21c-d) and checked that such measurements would be equivalent to those in differential FFTs within an error of 8%, which is lower than the standard deviation.

Fig. 4.22 shows the resulting band dispersions. The graph also reports the curves obtained by [112] for Au intercalated at the graphene nanoflakes/Ir(111) interface using a similar method. Our data points were fitted to parabolas of the type $E =$

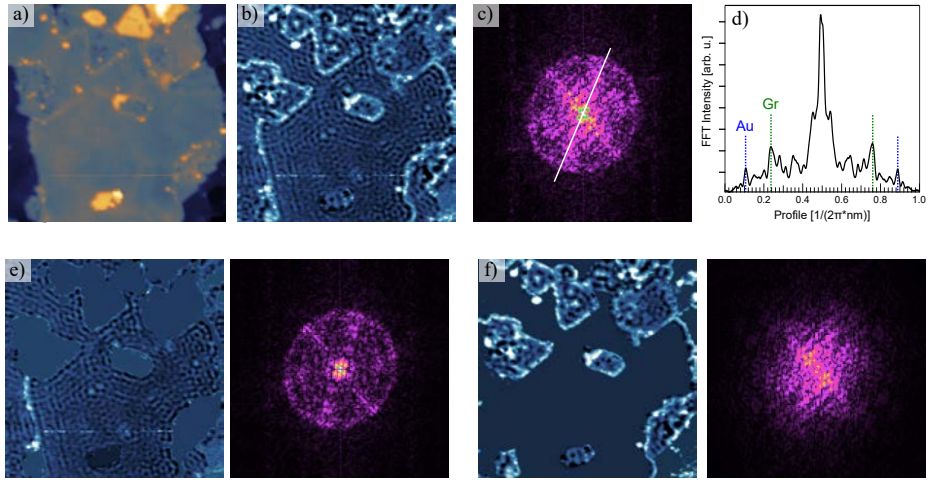

Figure 4.21: a) STM topographic image of the area where QPI mapping was carried out. V_b=450 mV, I_t=1.2 nA, size 100x100 nm^2. b) Corresponding dI/dV map (V_{mod}= 10 mV). c) FFT of the dI/dV map. A star-like feature results from scattering in Gr due to the islands symmetry. This is concentric to a ring resulting from the standing waves on Au. d) Profile along the white line in (c) displaying the features related to Au and Gr. e) The same as (b,c), showing only Au signal and its FFT after GNIs subtraction and f) complementary map and FFT image of GNIs after Au subtraction.

$E_0 + G/m_{\text{eff}}q^2$, where G is a constant $G = \hbar^2/(2m_0)$ with m_0 the electron rest mass. The parameters E_0 and m_{eff} represent the band onset and the effective mass factor of the electrons, $m^* = m_{\text{eff}}m_0$, respectively. Each set of data was fitted with both free parameters and setting E_0 to the value found by dI/dV spectra analysis. The results are shown in Table 4.1 together with those of [112].

	Band onset E_0	**Effective mass $m_{eff}=m^*/m_0$**	**Ref.**
Au	-505 mV (fixed)	0.21	This work
	-393 mV	0.25	*ibi*
	-390 mV	0.26	[112]
Gr	-320 mV (fixed)	0.09	This work
	-92 mV	0.12	*ibi*
	-300 mV	0.26	[112]

Table 4.1: Parameters from the fits shown in Fig. 4.22. Here m^* represents the effective mass factor, $m_{\text{eff}} = m^* m_0$, where m_0 is the electron rest mass.

We found that the free curve interpolates quite well the Au data, with an offset of -393 mV which is quite different from the -505 mV found by dI/dV spectra analysis but in excellent agreement with that found by Leicht et al. [112]. The effective

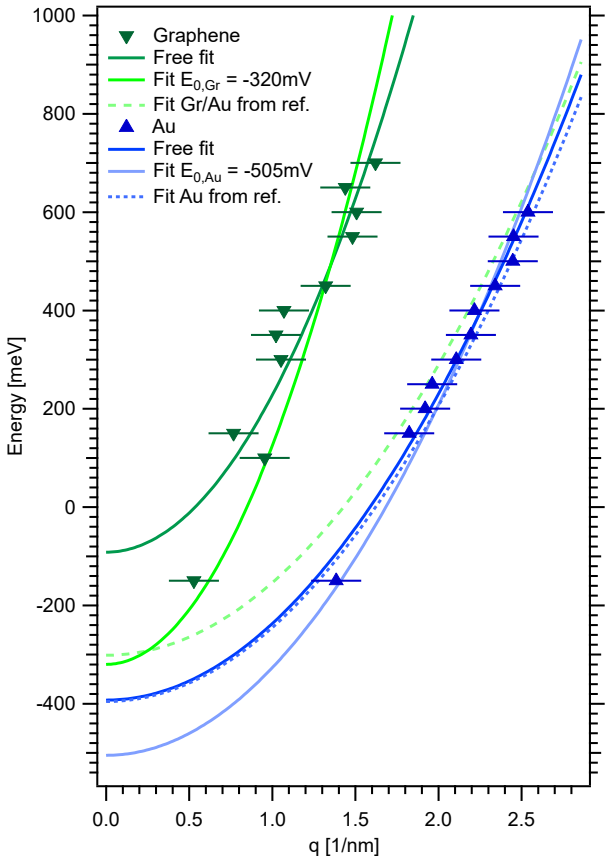

Figure 4.22: Band dispersion for Au and GNI/Au 22 ML as found from QPI mapping at different energies. Free parabolic fits and fits where the onset at Γ has been fixed at the energy found from dI/dV spectra analysis are plotted in light and dark colour respectively. For comparison, the dispersion relations found for Au/Ir(111) and Gr nanoflakes on it in [112] are shown as dashed lines. The error bars represent the highest standard deviation, found for energy -200 mV in graphene, 0.15 1/nm.

masses of the free fits also agree quite well, and both are in the range 0.25–0.28 found on Au(111) by STS and/or photoemission measurements [275–278]. Lowering the band onset also lowers the effective mass by ~20%. However, in the case of graphene, the results are very different. Free fitting results in a band onset at -92 mV, very different from the -300 mV found by [112]. Though this is near the -320 mV we found by spectra analysis, they find an effective mass similar to that on Au, while our m^* are smaller by more than 50%. A weaker interaction with the substrate of our small GNIs is to be supposed, compared to the rather big graphene nanoflakes (400x160 nm^2 in the case of the relevant measurements) of [112]. It should be noted that al-

though a tip interaction can not be completely excluded, such effect alone seems unlikely to justify such a shift, particularly considering the consistency of it at all energies (while the setpoint was adjusted to mantain a sufficient dI/dV signal).

4.4.2.1 Thickness evolution

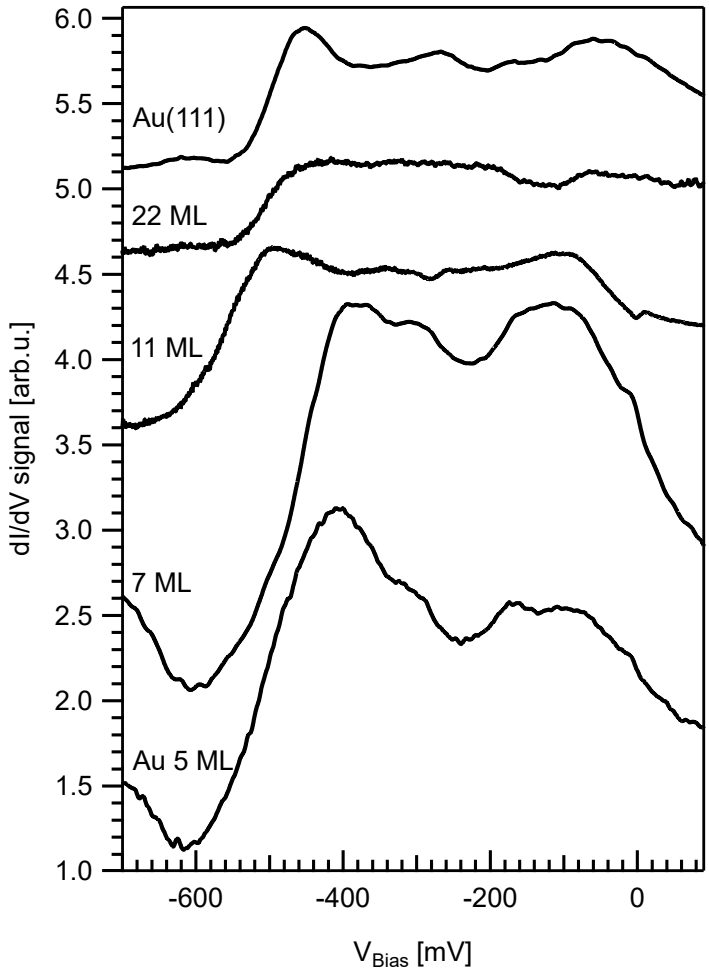

Figure 4.23: dI/dV spectra at constant height on the surface of Au films of different thickness on Ni and on Au(111), showing a non-monotonic shift of the onset of the surface state.

The surface states are also affected by the particular conditions of a thin film. If the thickness of the film is smaller than the intrinsic decay length of the surface state

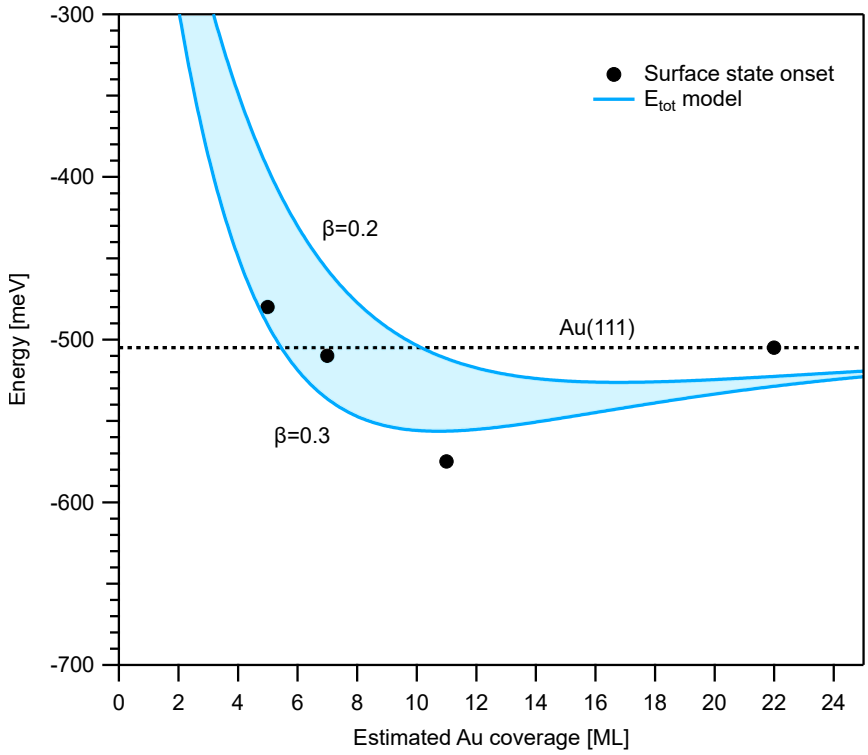

Figure 4.24: Evolution of the onset of the Au Shockley surface state for different Au film thicknesses. The dashed line indicates the Au(111) asymptotic value of -495 meV, as measured on the corresponding crystal surface in our system. A coloured area is delimited by two model E_{tot} curves for limit β values.

in the semi-infinite crystal, the presence of the interface and the penetration of the wave function into the bulk material (in our case the Ni) modifies the boundary conditions and shifts the energy [279–281]. The lattice structure of the film might also differ from the bulk due to strain and the presence of difference surface reconstructions that release this strain. For Au/Ni, this differences from the nominal Au(111) surface are very explicit, with the abscence of the herringbone reconstruction and the presence of a dislocation network. The evolution of this structure and its consequences on the surface state can be used to monitor the film thickness.

We measured the onset of the surface state of Au on different film thicknesses by acquiring dI/dV spectra at constant height. The data are plotted in Fig. 4.23, where a clear shift can be observed. It should be noted that, differently from FER analysis, we do not have reliable data for 1 ML and therefore omitted it.

The onset energy is plotted against the film thickness in Fig. 4.24. A non monotonic behaviour is observed. This cannot be explained by only considering the crystal potential variation across the interface, but one has to consider the chemical and structural evolution of the film and the interface.

The presence of the Ni crystal potential below the interface itself cannot account for the observed downshift of the SS onset below the values of the bulk Au(111) crystal (dashed horizontal line in Fig. 4.24). A chemically pure (unmixed) heteroepitaxial system that could be described with the crystal potentials of the two components with a smooth transition at the interface (see [282]), would lead to SS energies in between those of the corresponding components. In our case that would correspond to a value between the S_1 onset on Ni(111) discussed in the beginning of this section, around -100 meV and +150 meV for the majority and the minority band respectively,and that of the Au Shockley state at -505 meV. The crossing of the SS energy below the bulk value cannot be explained by the effect of the dislocation network either, since this would contribute with a small upwards shift due to the superlattice potential they provide [282]. Therefore, by exclusion, we temptatively attributed the downwards shift to the strain of the film, that would compete with the contributions originated by the presence of the Ni interface and the dislocation network.

In order to check such assumption, we constructed a model for the system in the following way. The final energy of the surface state will be between that of the Au film and that of Ni, the exact value depending on the extension of the SS wave function across each crystal potential (i.e. on the "weight" of the crystal potential on the SS). It is then modeled as $E_{\mathrm{tot}} = E_{\mathrm{Au}} \cdot f_{\mathrm{Au}} + E_{\mathrm{Ni}} \cdot f_{\mathrm{Ni}}$, where the weights $f_{\mathrm{Au,Ni}}(x)$ are the amplitudes of the SS wave function in each crystal potential. Since the SS wave function decays exponentially away from the surface, we can write it as $\psi(x) = Ae^{-\beta x}$, where A is the amplitude at the surface and β is the (inverse) decay length in bulk. For an Au thickness x, the weigths can then be written $f_{\mathrm{Ni}}(x) = e^{-\beta x}$ and $f_{\mathrm{Au}}(x) = 1 - e^{-\beta x}$. As for the decay parameter β, Kevan and Gaylord [275] found a value of β=0.20 by ARPES measurements on Au(111), which is in agreement with the similar values that can be derived from the surface state energy evolution measured on Au films on Ag(111) [281]. An upper limit of β=0.33 can be obtained from the two-band approximation within the nearly free electron model (Eq. 4.11 in [283]).

The contribution of strain is contained in the definition of $E_{\mathrm{A}u}$. An epitaxial

growth of Au on Ni would imply a compression of 10%, but after relaxing by the formation of dislocations the Au lattice is compressed by about 3% (2.80 vs 2.88Å) [245]. A temperature-dependent study of the Au SS shift indicates that lattice compression leads to a downwards shift as a result of the downwards shifting of the projected bulk band edge [284]. A compression of about 2% (500 K range of study, thermal expansion coefficient of Au $1.42 \cdot 10^{-6}$ K^{-1}) leads to a shift of about 0.1 eV. Then a 3% of compression would lead to a shift of about 0.15 eV, to an energy of -650 meV. We therefore modeled E_{Au} as $E_{Au}(x) = E^0_{Au} - 150 \cdot e^{-(x-1)/\tau}$. Here the parameter τ is a strain constant or a strained film thickness, i.e. the thickness for which the potential in the strained film is the same as Au(111), and thus tunes the "speed" of approximation to the asymptotic value in the graph of Fig. 4.24. Since we found that for a 10 ML film the Au surface displays no dislocations, resembling the relaxed Au lattice, and considering that each subsequent layer not only decreases the average strain but also relaxes the strain in underlying Au layers, we tentatively assigned this thickness to the relaxed potential of Au, setting $\tau = 10$.

For Ni, we considered the S_1 surface state as the one contributing to the final surface state in the Au/Ni crystal, and used the average of the spin-split bands onsets (-100 mV and +150 mV, see previous section) as the energy for this crystal, E_{Ni} = 25 mV.

As observed from the graph in Fig. 4.24, such model approximates quite well the behaviour of the energies found experimentally. We find that a decay length β=0.3 could better approximate the real value in the Au/Ni crystal. We note, more in general, that the contribution of strain in the Au film due to the lattice mismatch with Ni can explain the observed behaviour for the energies.

4.4.3 Electronic properties of graphene nanoislands

Previous ARPES and STM studies showed that intercalation of 1 ML of Au under graphene/Ni(111) yields a quasi-free standing graphene sheet where the linear dispersion of carriers characteristic of graphene is completely recovered. The effect of the metal is to slightly p-dope graphene by shifting the Dirac point 100-200 meV above the Fermi energy [112, 233]. The abscence of strongly interating d states near the Fermi level in Au therefore results in a weaker interaction as compared to the Ni(111) surface, where the strong $\pi - d$ hybridization opens a gap and spin polar-

izes the Dirac cone, as shown in Fig. 4.19a.

In the previous section we showed how the Au intercalation affects dramatically the interfacial interaction between graphene and the underlying metal by tracking its effects on the electronic properties of the metallic surface. In this section we will show how the electronic properties of the graphene nanoislands are affected.

4.4.3.1 Quasi Particle Interference in nanoislands

Contrary to the pronounced maxima giving rise to dI/dV peaks at the edges of the Ni-induced gaps in the spectra of Gr on Ni Fig. 4.19a, the smooth, linear DOS variation in graphene Dirac bands together with its reduction down to zero at the Dirac point makes the direct detection of graphene states in dI/dV spectra challenging. The difficulties are added by the fact that states far away from the Γ point are difficult to access by STM. A final difficulty comes from the fact the larger decay length into the vacuum of the underlying metallic surface states makes them the primary tunneling channel [285]. A sizeable contribution of Gr states is only achieved at reduced tip-sample distances, where clean metallic tips interact strongly with Gr.

Due to all the above difficulties we did not succeed on having direct spectroscopic proofs of the graphene Dirac cone. However, we were able to capture evidences from the QPI patterns (see Chap. 2) arising in the topography itself. For small enough bias voltages the tunneling current, i.e. the integral of the DOS from the Fermi level to the bias voltage energy, can be approximated to the DOS at the Fermi level, making topographic images similar to dI/dV maps at this energy [186]. Fig. 4.25 shows one of this "topographic" maps obtained at RT with a bias voltage of 25 mV. The atomic resolution of the graphene lattice is clearly distinguishable, in particular far away from edges and point deffects, where electron scattering gives rise to interference patterns. Both the atomic lattice and interference paterns can be identified in reciprocal space by performing a FFT transform to the topo image (Fig. 4.25c).

The FFT shows two hexagonal patterns, rotated 30° respect to each other: one (blue circles in Fig. 4.25c) is made of sharp intense points, with a distance of $k = 4.76$ nm^{-1} from the origin of the 2D-FT, corresponding to a real-space periodicity of 0.243 nm. This pattern therefore fits with the reciprocal representation of the atomic lattice of graphene; the other one, (green circles in Fig. 4.25c), is composed

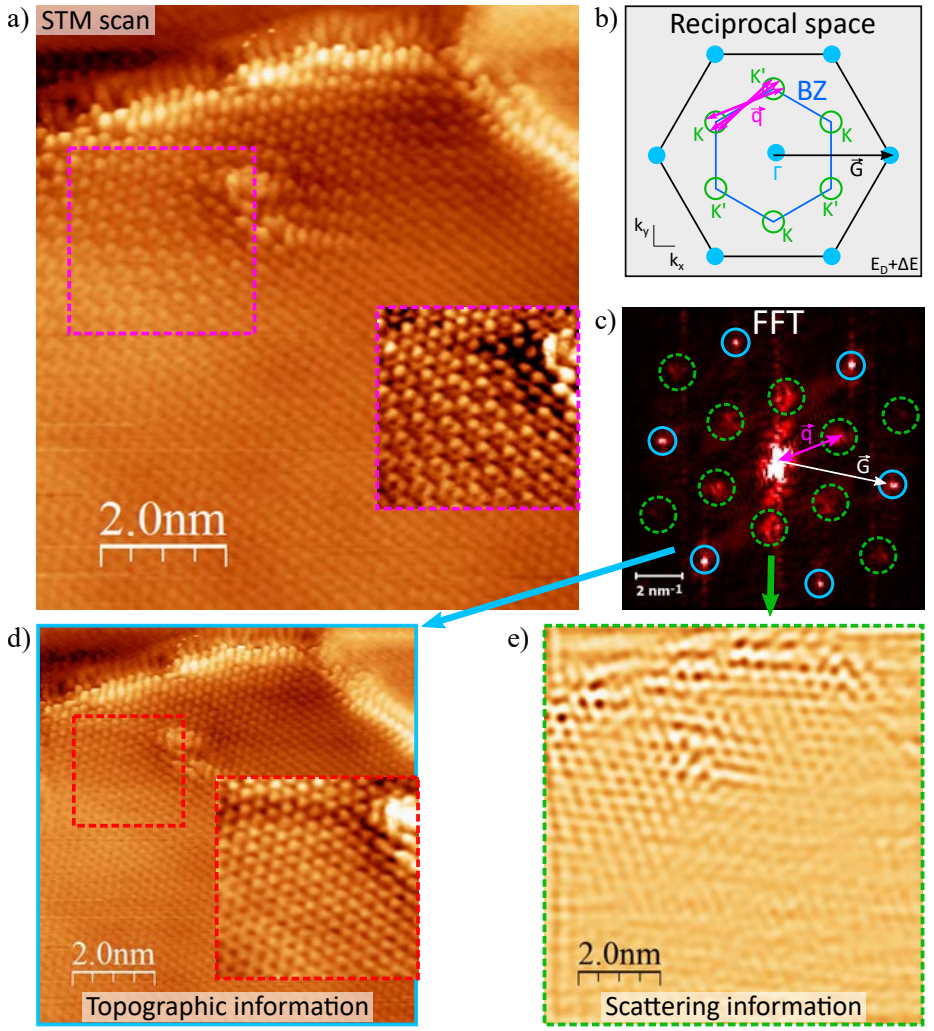

Figure 4.25: a) STM scan of the edge and bulk of a graphene nanoflake - the one shown in Fig. 4.6. The atomic lattice of graphene is distorted by electron scattering near the edges, while far from the edges (at the bottom) it is regularly imaged as a three fold structure. The inset shows a zoom of the highlighted area. b) Representation of a cut in reciprocal space at energy E_D+ΔE, where the Dirac cones appear as circles centered in K (K'). Possible q_{inter} vectors are indicated. c) FFT map of the scan in (a). The features circles in green have been filtered into d), where the modulations due to scattering at the edges and the defect are seen as the only areas with amplitude. e) Inverse FFT after filtering out the scattering information in (d). Now the whole atomic structure of graphene is visible, even in the areas where scattering was observed, as shown in the inset.

of broader features, with an average distance from the origin of $k = 2.66$ nm^{-1}, i.e. 0.434 nm in real-space. This corresponds, within a 3% error, to a $(\sqrt{3} \times \sqrt{3})$R30° lat-

tice respect to the first one (in k-space $(1/\sqrt{3} \times 1/\sqrt{3})$),and can be attributed to intervalley scattering vectors of graphene (see Fig. 4.25b and recall Fig. 2.4) [185, 186]. The origin of each pattern can be checked by applying specific filters to the FFT image and inverting it back into a real space image. By filtering in only the first pattern (blue circles), one obtains an image of an homogeneous atomic lattice of graphene (Fig. 4.25d). On the other hand, filtering in the second pattern (green circles), the inverted real space image shows only features close to the graphene edge and the point defect nearby, which can be attributed to interfefrences (Fig. 4.25e).

The dominance of intervalley scattering processes has been confirmed in more accurate studies, acquiring real dI/dV spectroscopic maps on extended Gr films where large area maps increase the k resolution in the FFT images. The abscence of first order intravalley scattering patterns around the center of the (0,0) vector of the FFT image has been attributed to pseudospin conservation, a quantum number that is related to the sublattice symmetry of graphene and resembles the spin quantum number [185, 186]. Another consequence of pseudospin conservation is the suppression of certain intervalley processes. This turns the rings that would arise from scattering in the abscence of pseudospin to a highly anisotropic pattern with nodes separating asymmetric sections of the rings [185–187]. Indeed, our FFT image does show the presence of half sections around the R30°xR30° points. This confirms the role of pseudospin in the scattering in our GNIs, but it is also a proof of a sizeable doping of the graphene islands (scattering between K and K' Dirac points should give rise to a single point centered at R30°xR30° points). We can estimate the radius of the ring section to be around 0.4 nm^{-1}, which for the same Fermi velocity as that found in graphene flakes and monolayers would result in a shift of the Dirac point of 150 meV comparable to that found by ARPES [233], and slightly smaller than that found by STM [242]. Our single point analysis is however far from ideal, and cannot be used for conclusions further than saying that the Au intercalation modifies the electronic properties of GNIs in a similar way as that found for larger flakes and monolayer graphene, giving rise to the recovery of slightly doped Dirac bands.

4.4.3.2 Edge states

The graphene honeycomb structure is a bipartite lattice that consists of two intertwined hexagonal sublattices. This leads to intriguing bulk properties such as the existence of the sublattice pseudospin coupled to momentum, as mentioned in the

prevoius section, but also to particular edge properties that are related to magnetism.

According to Lieb's theorem [286], uncompensated bipartite lattices exhibit a finite total spin S=1/2(N_A-N_B), N_A and N_B being the number of atoms in each sublattice. This can be understood by the fact that sublattice uncompensation leaves N_A-N_B nonbonding states at the Fermi level, localized at the uncompensated sites. When switching electron correlations, the spins at these sites align ferromagnetically obeying Hund's rule, and a spin gap is opened in the energy spectrum.

Interestingly, zigzag terminated graphene nanostructures may show uncompensated sublattices at the edges depending on the geometry. In particular, triangular islands are terminated by a single sublattice and can therefore develop ferromagnetism localized at the edges [44, 45, 287]. Hexagonal islands, on the other hand, present edges with the two type of sublattices and therefore should exhibit a zero magnetic moment. Yet, the overall nonmagnetic solution can be satisfied by polarized edge states of each sublattice that are coupled antiferromagnetically. According to theory such antiferromagnetic configuration can be stabilized above a critical size, when the exchange interactions overcomes the sublattice mixing between adjacent edges [44]. A similar scenario can be found in zzGNRs, where the edge-to-edge distance can be tuned by increasing the width. Here it is shown that spin-polarized solutions become stable above a critical width where exchange interactions take over, and above that value the antiferromagnetic coupling between edges brings further stabilization [288]. As we increase the width further, the inter-edge interaction decreases, and so does the stabilization effect as well as the total energy difference between the FM and AFM configurations, reaching to negligible values when the width turns larger than the decay length of the edge states [288, 289].

Experimentally, edge states have been detected in graphite zz edges [290], patterned graphene stripes [291], zz sections of irregular graphene sheets [292], zzGNRs [46–48], and termination of AGNRs [203], but not yet in graphene nanoislands. One difficulty for the latter is that the reactivity required to grow GNIs by CVD can result in excessive interactions that quench the edge magnetism, as shown by STS measurements on GNIs grown on Ni(111) [76], and a recent work of hexagonal GNIs grown on Ir(111) [49]. This interaction could be minimized by the intercalation of more inert metals such as Au. Thus the GNIs described in this chapter, with well-

defined zz edges and separated from the reative Ni by a Au film, seem to be promising structures to explore edge magnetism.

Fingerprints of the presence of edge states can already be found in topographic images of embeded islands, where edges can appear as bright protrusions for particular tunneling conditions. Fig. 4.26 shows a truncated triangular GNI embedded after intercalation of 5.5 ML of Au, displaying bright edges 45±5 pm higher than the Au surface around it. In spite of point defects observed at the edges, one can clearly distinguish the three long edges corresponding to the favorable zig zag directions during the GNI growth. The edges show contrast variations with a periodicity of 2.46 Å. On the other hand, the short edges are more irregular, and only one of them shows regular protusions with a periodicity about twice that of the long zigzag edges, a reminiscence of the edge reconstruction ocurring during the nanoisland growth. Knowing the atomic structure of the other two short edges is not possible from this image. Yet, we note that the brigth appearance of the edges is independent on their structure or orientation.

To discard any purely topographic effect that could give rise to an edge contrast, such as a structural distortion of the edges, spectroscopic measurements are necessary. In the same GNI, two series of point dI/dV spectra at constant height have been recorded along and perpendicular to the zigzag edge at the bottom of the island, which seems the most perfect according to the STM appearance.The full series of spectra are plotted in Fig. 4.26c-f as a function of the bias voltage (c-d) and as a 2D color plot of the dI/dV signal as a function of bias voltage and position along the lines (e-f). The main features are evidenced in Fig. 4.26b where the average of the spectra recorded along the edge is plotted together with representative examples of spectra acquired on the Au surface and the inner region of the GNI. Two prominent peaks that are exclusive to the graphene edge can be clearly observed, at energies of -800 mV and +380 mV. The two peaks are absent in the Gr and Au spectra, where the main feature is the SS state, shifted upwards in energy in the case of graphene as described in Sec. 4.4.2.

Both peaks are actually localized at different distances perpendicular to the edge line, as evidenced by the plots of Fig. 4.26c and e: the intensity maximum of the unoccupied state appears 4.0±0.1 Å inwards the graphene with respect to the occupied one. The intensity of the two peaks, measured as $(I_1 - I_0)/I_0$, where I_1 is the ampli-

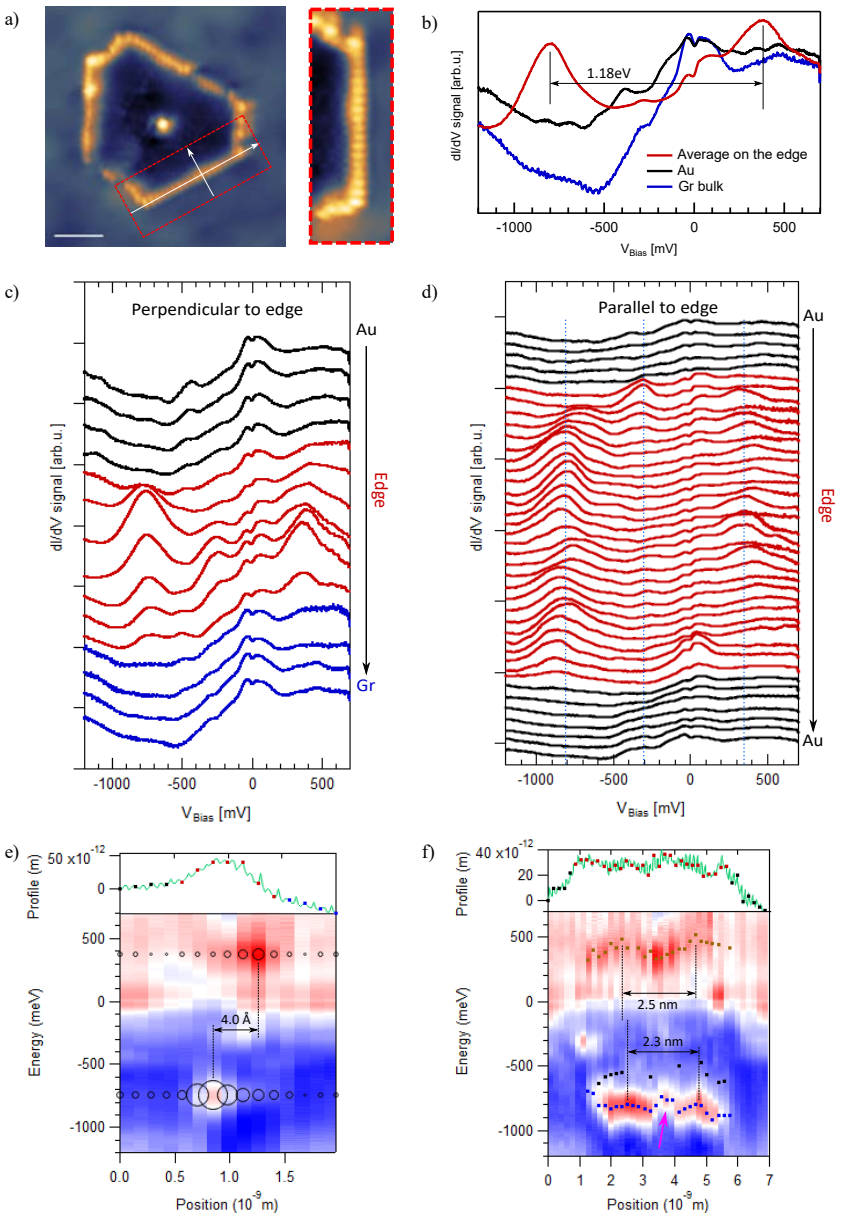

Figure 4.26: a) STM topographic image of a hexagonal GNI embedded in 5 ML Au, and (inset) zoom on the rectangular area marked in red. The arrows indicate the direction of line STS spectra taken along and across the zz edge. V_b=0.2 V, I_t=1.0 nA, scale bar 2 nm. b) Representative dI/dV spectra of the average spectra on the Au surface, in Gr bulk and on the zz edge. c) Series of point dI/dV spectra perpendicular to the zz edge of the GNI in (a). d) Series of point dI/dV spectra parallel to the edge. Blue dashed lines evidence the energies of the dI/dV maps represented in Fig. 4.27. e-f) Edge profiles (top graph) and colour plot of the spectra (bottom) represented in (c,d) respectively. The circles in (e) represent the intensity of the peaks, the dots in (f) represent the fitted peak energies. An arrow marks the defect along the edge in (f). The setpoint for the two line STS was V_b=0.7 V, I_t=0.11 nA.

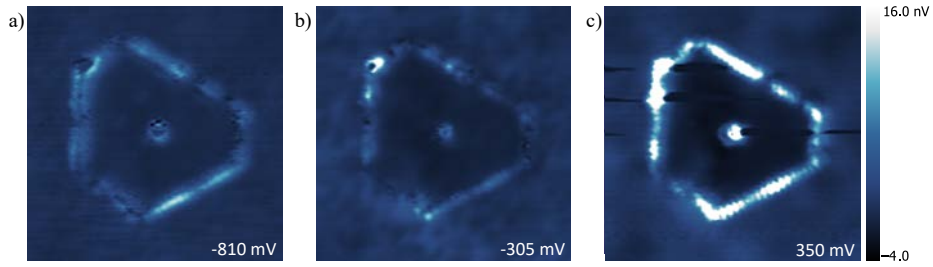

Figure 4.27: dI/dV maps at constant height of the embedded GNI of Fig. 4.26 at energies a) -0.81 V, in correspondence of the occupied state, b) -0.305 V, in the gap and c) 0.35 V, in correspondence of the unoccupied state. The colour scale is reported in units of the recorded signal and is the same for the three images, where the same point on Au has been set as the 0. Setpoint V_b=-0.305 V, I_t=0.22 nA.

tude of the dI/dV signal at the energy of the peak and I_0 the background signal on Au, is represented as the size of the dots overlaid to the color plot for a better visualization of the maxima.

From the spectral plots of Fig. 4.26d and f, it is evidenced that the energies of the peaks are not constant along the edge. An oscillatory behaviour is observed, with the energy of the occupied state varying between -887 and -716 meV and that of the unoccupied one between 326 and 520 meV. An abrupt energy shift is observed at the position of the protrusion, which we attribute to a point defect. Disregarding this local deviation, the modulation of energy shows a wave-like behaviour with wavelength of 2.4±0.1 nm. As this is equal to the superlattice constant for the dislocation network, the modulation is assigned to a periodic interaction with the underlying dislocation network. Unfortunately, a complete spectroscopic study on a low defect density edge was only carried out in this edge, and the tip conditions here did not allow for a direct identification of dislocations on the nearby Au, so we were unable to correlate the energy maxima/minima with any specific point of the dislocation network.

The edge states can also be detected in constant height dI/dV maps, as shown in Fig. 4.27 for the same GNI studied in Fig. 4.26. Here the different setpoint parameters makes the intensity of the unoccupied state significantly larger, but the edge contrast can be found at both peak energies. At the energy region between the two peaks, the edge contrast dissappears except at some points that can be assigned to defects or impurities, which are either protruding from the graphene plane or exhibit higher conductivity at this energy region Fig. 4.27b.

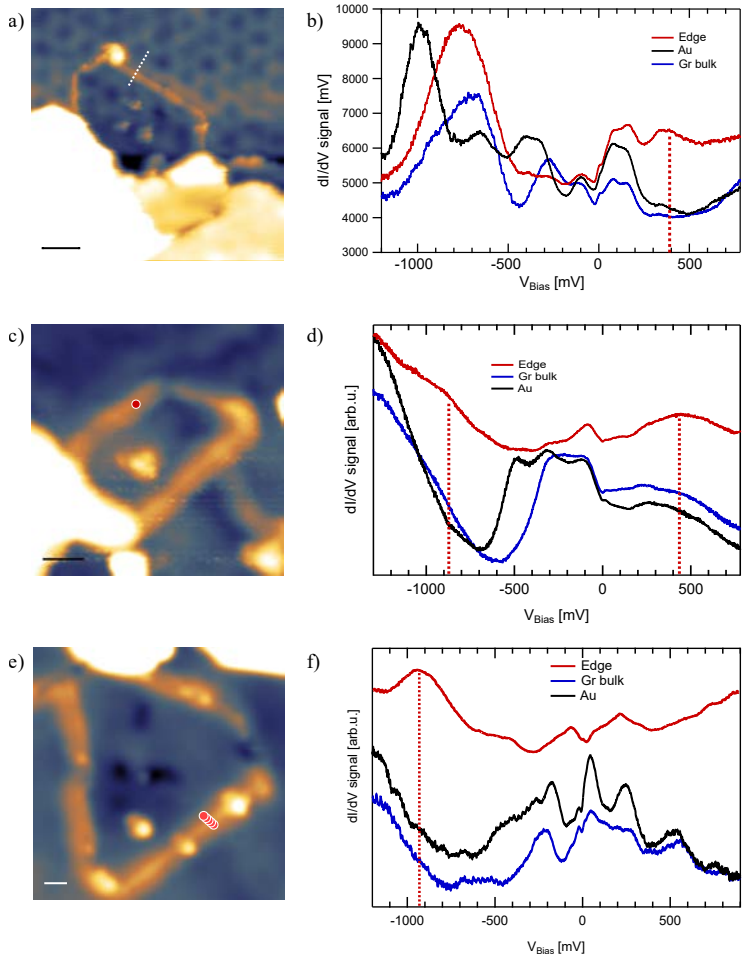

Figure 4.28: a) Embedded GNI on 5 ML Au surface showing dislocations. Scale bar 3 nm. b) Average of the dI/dV spectra along the line shown in (a). A peak at energy 340 meV is seen both on Au and on the edge, where also a second peak is observed at 380 meV. Setpoint V_b=800 mV, I_t=0.11 nA. c) Trapezoidal GNI embedded on the topmost of 11 ML of Au, at a step edge. Scale bar 2 nm. d) The averaged spectra recorded on the zigzag edge, at the point indicated in (a), and on Gr and Au. Both the unoccupied and occupied state on the edge are convoluted in larger peaks belonging to tip states. Setpoint V_b=0.8 V, I_t=0.3 nA, approaching 0.5 Å. e) Triangular GNI embedded on the topmost of 22 ML of Au. Scale bar 1 nm. f) Average of the spectra recorded at the tip positions indicated in colour in (a) for the edge, and for Gr and Au. Setpoint V_b=1.2 V, I_t=3.6 nA. Spectra in (d) and (f) have been vertically displaced for clarity.

Fig. 4.28 shows examples of other embeded GNIs where edge states have been detected. One clear thing to note is that the peak intensity is very different in each case. This can be an effect of the particular tip electronic structure in each case, which could give rise to variations in the edge-to-surface state contrast, similar to that found in extended graphene on Cu(111) [285]. Yet, any intrinsic relation between peak intensity and the particular local edge configuration cannot be excluded. Strong resonances in the tip electronic structure can also hinder in some cases the edge state signal. This is the case for the unoccupied state in Fig. 4.28f.

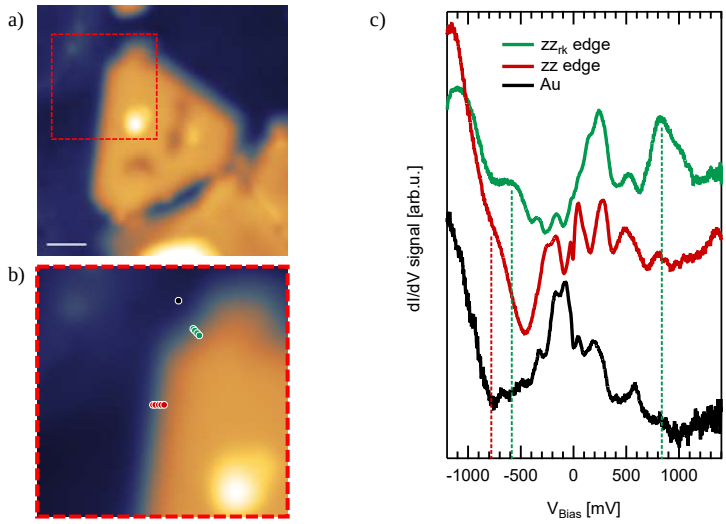

Figure 4.29: a) STM topographic image of a truncated GNI on top of 22 ML of Au (scale bar 2 nm) and b) zoom in the area marked in red, at the corner between a zigzag and a short edge. The coloured dots indicate the positions where the spectra were recorded. c) Average of the dI/dV spectra recorded on the zigzag and short (reconstructed) edges of (b), and that of Au as reference. Setpoint V_b=1.4 V, I_t=4.0 nA.

On top GNIs have also been explored, although with less statistics due to their lower abundance. The majority exhibit edge states, as shown by the representative case displayed in Fig. 4.29. In this example the presence of edge states is more evident in the short edges of the truncated triangular island, but seems to be present in both.

Table 4.2 summarizes a statistical analysis of the peak energies and the corresponding splitting for different type of edges, and both the embedded and on top configurations. We can say that, despite all energy and intensity variations, the vast majority of studied GNIs show at least a clear occupied edge state (in one case only

Edge type	Occupied (meV)	Unoccupied (meV)	Gap avg.(eV)	[N,o/u,g]
Embedded: zz	-920 – -740	300–455	1.32±0.20	23,21,4
Embedded: zz_{rk}	-860 – -680	-	-	3,2,0
Top: zz	-925, -800, -745	-	-	4,3,0
Top: zz_{rk}	-600	815	1.42	2,1,1

Table 4.2: Energies of the states and average size of the gap found for different configurations of the edge. The vecor [N,u/o,g] indicates the number of samples measured (N), where only one of the states could be seen (o/u) and where both were resolved (g). The short edges are indicated as zz_{rk} for simplicity, though the tip conditions never allowed to confirm the structure at the time of spectra acquisition.

the unoccupied state was observed). We attribute the difficulties on finding the unoccupied one to the presence of the Au surface states at this energy region, which does not only contribute by increasing the dI/dV background, but could also affect the edge state itself by hybridization, resulting in a broader, weaker resonance as compared to the decoupled unoccupied peak. This selective hybridization could also explain the different spatial localization of the two peaks, as shown in Fig. 4.26c and e.

Several main conclusion can be obtained from the above analysis. The first observation is that the values of the energy splitting of the peaks measured in our GNIs, ranging from 1.10 to 1.39 eV, is considerably larger than those below 0.3 eV found for zzGNRs on Au(111) [43, 47]. An energy splitting close to the 1.7 eV obtained by GW for free-standing GNRs was only obtained by intercalating a NaCl film between the GNR and the substrate to minimize screening and hybridization with the metal electrons [46]. We note that hereafter we will compare our values to the maximum splitting of the theoretical edge bands (Δ_1 in [38, 39, 46]), located at the BZ boundary. This is a value that does not depend on edge-to-edge interactions due to the short decay length of edge states at this k value. In contrast, the minimum splitting (Δ_1 in [38, 39, 46]), occurring at 2/3 of the BZ, where edge states are much more extended into the ribbon, gradually goes to zero for increasing GNR width [38, 39]. In our analysis we do not observe any size effects, as shown by the uncorrelated dispersion of peak energy and splitting values plotted as a function of edge size and island area in Fig. 4.30. Hence, we conclude that our splitting is related to that of the BZ boundary.

Differences in the energy splitting can be directly attributed to the critical role of the interaction with the substrate in the edge magnetism. For zzGNR, a decrease in the C-Au distance as small as 0.2 Å can lead to a two-fold decrease in the magnetic moments of edge atoms according to DFT [293]. The quenching of the magnetic

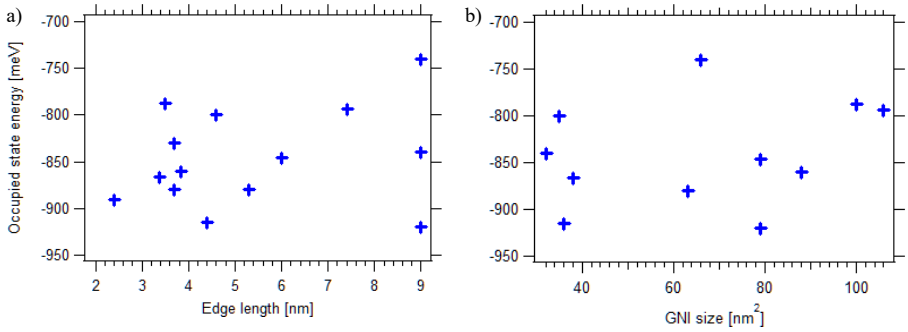

Figure 4.30: Graphs of the energy of the occupied state as measured on different GNIs embedded in Au as a function of a) the length of the edge where the spectra were measured, and b) the GNIs surface area.

moment, correlated to a decrease in the energy splitting, is attributed to screening and hybridization effects by the substrate. In reality, the distance to the substrate of a given nanographene can critically depend on its size and the particular atomic structure. For instance, the emergence of edge states on zzGNR on Au(111) has been attributed to minute adsorption configuration differences induced by functionalizing the edges by indene groups [46, 293]. In our case, a more decoupled adsorption configuration of GNIs as compared to zzGNRs could therefore account for the larger splitting observed in the former. This could be related to the intrinsic geometry of the GNIs, but also to the particular, corrugated structure of the Au films on Ni, which could lead to a more efficient decoupling. The lack of any size and shape effect on the observed energy positions and splitting of edge states suggest a dominant role of the surface structure.

A different possible contribution of our particular substrate on the observed enhancement lies in the screening reduction that could result from the vertical quantization of Au states in the film. Such thin film to bulk transition in the screening behaviour has been observed of Ag films on Ni(111) by tracking the plasmonic response [294]. One would expect a similar transition in Au films but, in contrast, we observed similar values of the splitting in the range of 5–22 ML, as shown by the examples of Fig. 4.28. Thus we discard any film thickness effect on the screening of edge states.

Another clear conclusion of our analysis is that edge states are very robust, in the sense that different embedded and on top configurations, as well as edge length and atomic structure do not seem to affect dramatically the peak energies and splitting .

On the one hand, this striking result implies again a dominating role of the surface structure in the interaction, minimizing the effect of different edge structure and coordination configurations. We note that intrinsic magnetic edge states have already been predicted for different type of reconstructed edges, including Klein and $zz57$ ones [295, 296]. Secondly, assuming that the edge states are related to magnetic π-bands implies that C edge atoms in embedded and on top configurations have both the same sp^2 coordination. This can be achieved by either Au or H passivation. However, recent calculations show that the strong hybridization with Au states quench the edge magnetism of zzGNRs upon metal coordination [297]. Based on that, and on the assumption that the edges of the original Gr islands on Ni(111) are passivated with H during cooling (see Sec. 3.2.1.2 and [214]), we conclude that both embedded and on top GNIs on Au remain H-passivated. This could explain the presence of similar edge states in both configurations.

4.5 Summary

In this chapter, we investigated the morphological, structural and electronic properties of the GNIs on Ni(111) after intercalation of Au films of different thicknesses.

We first discussed the structure of the Au film, showing that a network of triangular dislocations forms at the Au/Ni interface due to the interfacial interaction and the lattice mismatch of the two metals. The resulting corrugation is repeated and smoothed out in the following layers, until a flat surface is achieved. Here, ridges corresponding to the Au(111) herringbone reconstruction are observed.

We then turned to graphene nanoislands on this surface after Au intercalation, finding that they display different topographic configurations respect to the Au layer, with island mostly found embedded in the Au layer, and a fraction on top of it. By a statistical analysis, we showed how the final configuration of nanoislands could depend on their size and on the thickness of the Au film. In particular, on top nanoislands are found to be small, and their abundance increases with the film thickness. At submonolayer coverage of Au, GNIs are mostly embedded, and the observation of Ni islands under them lead us to conclude that at this coverage intercalation is mediated by Au alloying to the topmost Ni layer. We then analised the atomic and edge structure of GNIs on Au, finding that the edges reconstructing on Ni show a tendency to recover a zigzag structure after Au intercalation. This is related to the

reduced interaction with Au.

We then explored the electronic properties of the Gr/Au/Ni system by STS, and compare them with those of Gr/Ni. We showed how field emission resonances measured in dI/dV spectra can reveal variations of the work function that can be used as chemical probes, and how the behaviour of the Ni and Au/Ni surface state under graphene can evidence the reduced interaction after intercalation. The latter was studied by measuring the onset energy of the surface state band in the tunneling spectra, but also by mapping the quasiparticle interferences to obtain direct information of the band dispersion. We further studied the complex thickness evolution of both FERs and SS, finding that this can be explained by a gradual strain relief in the Au film with increasing thickness. In graphene nanoislands, by analyzing the interference patterns we find signature of intrinsic intervalley scattering in the Dirac cones, deducing recovery of the pristine graphene bands with a slight doping. At the edges, we consistently detected energy-split peaks, with a large energy separation independent of the size and the structure of the edges. We relate this observation to the predicted spin-split edge states of graphene.

Chapter 5

Lateral heterostructures of graphene and hexagonal boron nitride

Since the isolation of graphene, two-dimensional materials have attracted increasing attention, both for their physical properties and for applications in future electronics. Their applicability relies on the capacity to form lateral and vertical heterostructures with controlled final properties for technology applications in e.g. transistors, light and gas sensors, quantum emitters, etc. [4, 19–21, 298].

Among the 2D materials, single layer hexagonal boron nitride (hBN) was brought to the spotlight for being structurally equivalent to graphene but with very different electronic properties. It shares with graphene the layered honeycomb structure, with a lattice parameter of 2.51 Å differing by only 2% from that of graphene, entailing high in-plane mechanical strength [124], chemical stability and thermal conductivity [125]. It is formed by alternated boron and nitrogen atoms in a sp^2 network, the polar bond between the two species being the main difference from the purely covalent C-network of graphene. Electronically, hBN is an insulator with a very wide bandgap of ~6 eV [127]. Due to this and to the morphological similarity, it has been explored as a substrate for graphene for e.g. vertical metal-insulator heterostructures [300–303]. Lateral heterostructures of graphene and hexagonal boron nitride (GBN) are interesting for applications in future electronics and optics due to the predicted unique electronic properties as the controllable bandgap size [133, 137, 138, 298, 304–306] and the predicted magnetic effects [137, 139, 307–309].

Particularly interesting are the electronic properties of the interfaces. One dimensional electronic states are predicted at the zigzag interface between 2D honeycomb materials independently of the conductive properties of these [310]. More in general, the interface between polar materials has interesting electronic and magnetic properties [311, 312]. At the lateral zigzag interface of graphene and boron nitride, a one dimensional electronic state is predicted, with a spin polarization [132, 133] originating from charge accumulation at the boundary rather than to the intrisic chemical composition of the interface [135]. This state might be at the origin of the 100% spin-polarized current in layer of Gr and hBN nanoribbons [309], which, together with other predicted magnetic effects [139], make these hybrid materials interesting for applications in spintronics.

Heterostructures composed of boron nitride and graphene have been produced by top-down patterning and re-growth [53, 145], but precise interfaces were hardly obtained. Sequential growth, occasionally including an etching step, is preferred. This was demonstrated on e.g. Cu foil [149, 313, 314], Ir(111) [150], Ni(111) [152], Ru(0001) [151], Rh(111) [147].Signatures of a localized electronic state on such interface have been observed by STM/STS on Cu [314] and on Au/Ir [153], though the magnetic properties could not be unravelled with this technique.

With the acquired knowledge on the growth of graphene nanoislands with precise edges on Ni(111), we investigated the growth and electronic properties of 2D heterostructures of graphene and hexagonal boron nitride. In this chapter, Sec. 5.1, we first describe the growth of boron nitride on Ni(111). In Sec. 5.2 we discuss heterostructures growth, first by seeding hBN from graphene nanoislands, and viceversa afterwards.We then discuss the electronic properties of the 2D materials interface to Ni(111) and of the 1D interface of the planar heterostructure, Sec. 5.3.

Part of the experiments were conducted at the Materials Physics Center (Donostia/San Sebastian, Spain), under the supervision of Prof. Enrique Ortega and in collaboration with Dr. Jorge Lobo Checa, Dr. Jens Brede and Dr. Mikel Abadia.

5.1 Growth of hexagonal boron nitride on Ni(111)

Hexagonal boron nitride was grown on Ni(111) from purified borazine ($B_3N_3H_6$) as described in Sec. 2.1.1. After Ni(111) preparation (see Sec. 3.1.1), the surface was brought to the growth temperature, in the range 600–750°CWe used doses of bo-

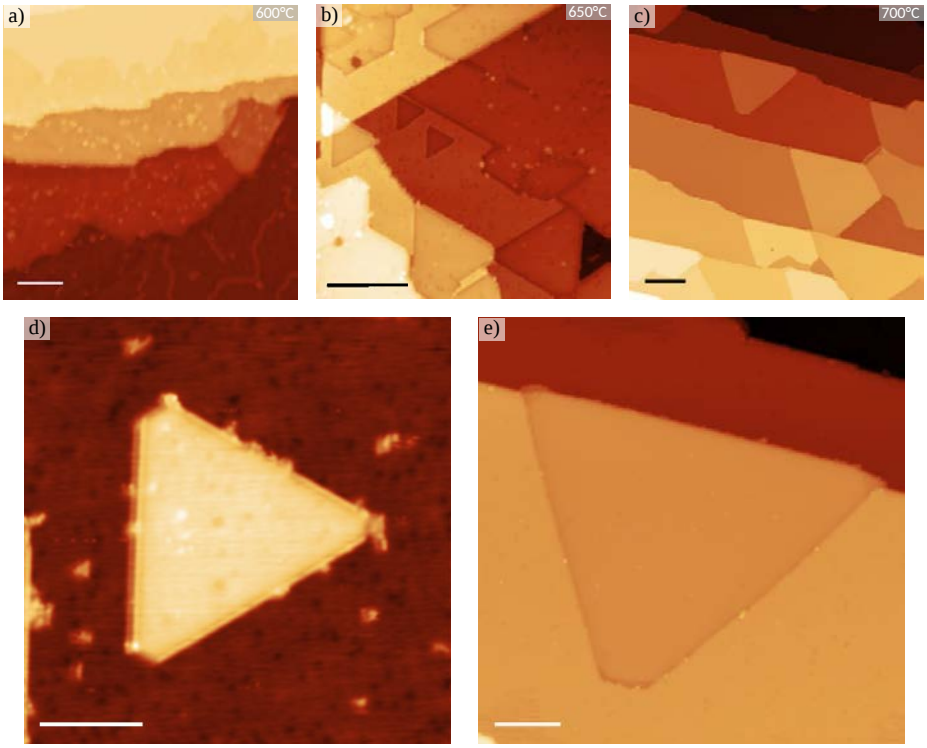

Figure 5.1: a-c) STM topographic images of hBN after growth at different temperatures a) 600°C, b) 650°C, c) 700°C. Scale bars 20 nm. d-e) Topographic images of triangular hBN nanoislands on Ni(111) d) on top of the surface and e) embedded at a step edge. Scale bars (d) 0.5 nm, (e) 20 nm.

razine of 1–30 L, resulting in hBN coverages from 0.3 to the self-limiting coverage of 1 ML.

Fig. 5.1 shows an overview of the grown structures at different temperatures. As the growth temperature increases, fewer defects are observed in the hBN. At all temperatures, hBN grows mainly embedded in the Ni layer or at step edges: a substitutional growth mode displacing Ni atoms has been proposed [152], similar to that observed for graphene on the same substrate [159]. It must be noted that due to the low solubility of B and N in Ni, here the mechanism of dilution to Ni bulk and segregation/precipitation to the surface typical of C atoms can be excluded [166, 315]. Triangular structures are favoured, with the edges aligned to the close-packed directions of the surface, as evidenced by the alignment to the step edges, similarly to what observed for GNIs in the kinetically limited regime (Sec. 3.1.2). As observed,

Fig. 5.1d, truncated edges are seldom observed. These are always short, and we observe them only at the lateral interface with Ni (or graphene, see Sec. 5.2).

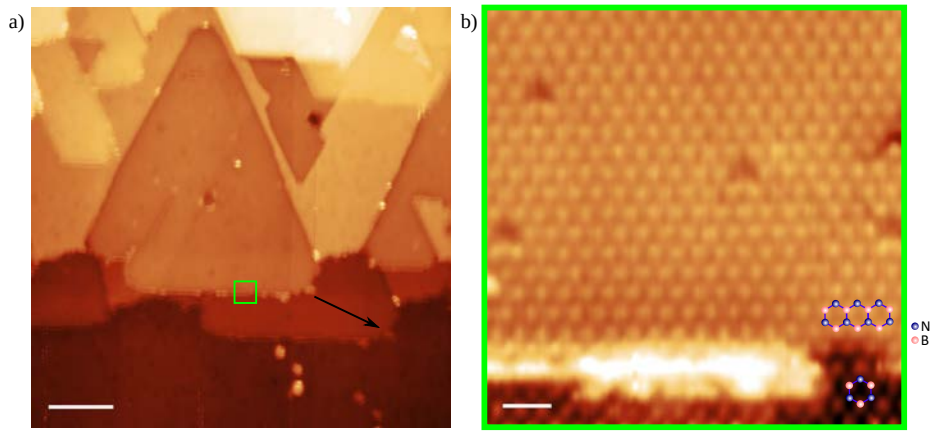

Figure 5.2: a) Topographic image displaying a hBN triangular island embedded at a step edge. Scale bar 10 nm. An arrow indicates the effect of a second tip apex several nanometers away from the main one. The effect of it is minimal at close tip-sample distances. b) Zoom in with atomic resolution on the area highlighted in (a). The zigzag alignment of the edge is evidenced, though impurities (saturated) impede resolution along the whole of it. The proposed atomic structure assigning high-imaged atoms to B in hollow position and low-imaged atoms to N is also drawn. Vacancies are all of one kind, corresponding to B vacancies for the proposed structure. Scale bar 0.5 nm.

We could not acquire topographic images with simultaneous atomic resolution of the hBN layer and the Ni(111) and cannot therefore determine the exact stacking. However, the similarities in imaging in our STM topographies between hBN and 1x1 graphene, Fig. 5.1b, where one sublattice of atoms is imaged as point protrusions while the other is imaged lower, suggests that a top-hollow stacking is favoured. This is supported by the matching with the graphene lattice in heterostructures, as will be discussed in Sec. 5.2. The most stable stacking configuration according to DFT calculations [316–318] and combined XPD/STM analysis [319, 320] is a 1x1 structure with N atoms on top of Ni atoms and B atoms in hollow fcc sites, (N,B)=(top,fcp), with a small energy gain respect to the other stable configuration, (N,B)=(top,hcp). As a consequence, triangular hBN nanoislands must point preferentially to one direction, similarly to triangular GNIs on Ni(111) (see Sec. 3.2.1.1) which is confirmed by our experiments. The same was observed on this surface by Auwärter et al. [320] and on Co(0001) by Orofeo et al. [321].

From Fig. 5.2b, we note that the zigzag edges of hBN islands are terminated by

the atoms imaged high. Due to the triangular symmetry, only one species composes the zigzag edges termination, and the stability of either termination is determined by the chemical environment, which in turn depends on the concentration of B and N on the surface [152, 299, 322]. The assignment of either N or B atoms to the terminations and to the atomic positions revealed by STM is a subject of discussion. Simulated LDOS maps in the Tersoff-Haman approximation suggest that on this surface the main contribution to the current comes from top N atoms [316], and combined XPD and STM analysis found that triangular islands on Ni(111) are terminated by these [320]. In principle, this is in agreement with the higher stability of N-terminated zigzag edges found by DFT calculations [152, 299] and observed by transmission electron microscopy [323] for free-standing hBN. The same termination was assumed for triangular hBN nanoislands on Cu foils [324].

However, on Ni(111) different energetics might apply: recent DFT calculations show that on this surface N-terminated edges are stable only in N-rich chemical environment [152, 322], and that B terminations are favoured otherwise. We tentatively assign this configuration to the observed hBN nanoislands, i.e. (N,B)=(top,fcc) with the latter imaged high and B-terminated zigzag edges. Further motivation for this will be discussed in Sec. 5.2.

We note from the atomically resolved STM topographies that only one type of vacancy forms in the hBN structures. This is in agreement with previous observations on exfoliated hBN, though the assignment to either species is not univocal [323, 325].

5.1.1 Tubular corrugations

A peculiar feature found in the hBN layer is shown in Fig. 5.3. These are long lines mainly aligned to the three-fold symmetry in chain direction of the substrate, appearing higher than the hBN layer. We observe them in nanoislands with side-length of >50 nm, and never in smaller ones, and thus relate their formation to a critical size of the hBN flakes. They display a width of 2.5 nm, corresponding to 10 unit cells of the layer, while their apparent height depend on the bias voltage: it is 40 pm at 0.3 V, and 60 pm at -0.3 V. At bias >1.85 V, they appear lower than the hBN layer, as a consequence of the electronic properties of hBN/Ni(111), which will be discussed in Sec. 5.3.

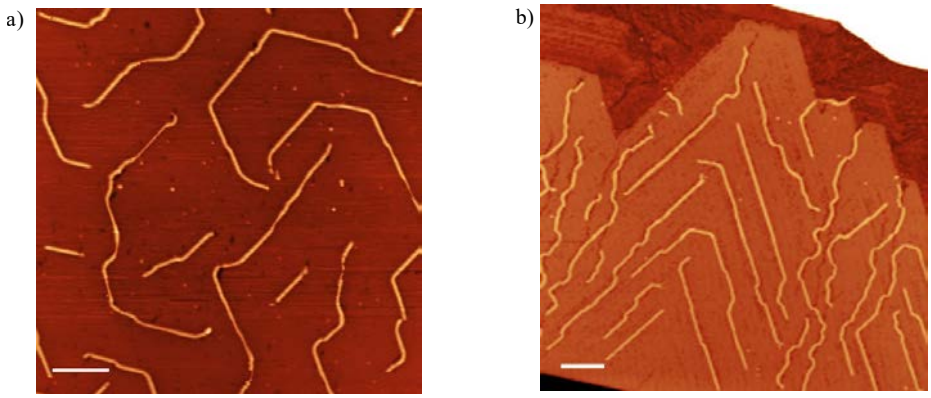

Figure 5.3: a) Tubular folds in a hBN ML sheet and b) in a hBN nanoisland. Here, graphene was grown at the sides, see Sec. 5.2. Scale bars (a-b) 20 nm.

We relate these structures to tubular corrugations of the hBN layer. Fig. 5.2 shows their structure with atomic resolution. They display an hexagonal lattice with the same unit cell as that of hBN. We compared the stacking configuration of hBN at the two sides of them, Fig. 5.2b: as observed, this doesn't seem to change. However, it must be noted that the stacking could not be resolved directly, so that we needed to filter by FFT only the frequencies resulting in hexagonal patterns. Such method is not safe from artefacts. We note that near the corner of a tubular fold, its lattice displays a rotational angle of 2±1° respect to plane hBN. For a width of 10 unit cells, this results in a shift of 0.9 Å in the armchair direction. Top-fcc and top-hcp stackings are shifted by 1.44 Å, corresponding to 3.3° rotation, which falls within the error of measurement. However, since the folds do not define closed domains, and we didn't find indications of topological defects in the vicinity of them, we cannot relate them to stacking domain boundaries, and we propose that they instead result from a stress release due to the small mismatch between hBN and Ni lattice. This is supported by the fact that they are often distributed parallel to each other, with a spacing of between 20–30 nm.

We occasionally observed a displacement of these folds in consecutive STM topographic scans, and we were able to controllably manipulate them by applying voltage pulses through the STM tip. In Fig. 5.5 two examples of this are shown. The series of Fig. 5.5a-c shows the effect of manipulation through a voltage ramp from 0.7 to 1.2 V at constant height. After the mild voltage pulse, a flat hBN layer appears

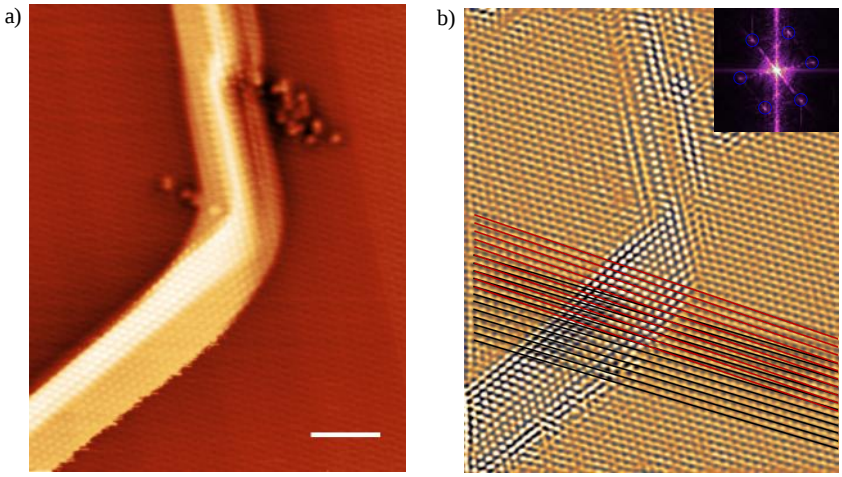

Figure 5.4: a) Topographic STM image of the corner of a tubular fold. V_b=32 mV, I_t=2.9 nA, scale bar 2 nm. b) The same image after FFT filtering of the dominant hexagonal pattern (highlighted in the inset FFT). Black lines follow the lattice of flat hBN, red lines that of the tubular fold, displaying a 2° tilt direction.

in the subsequent STM scan, but the fold appears again before the end of it. As seen from Fig. 5.5c, the tubular corrugation is here restored to its original position. This is not always the case, as seen in the series of Fig. 5.5d-f. Here, a constant voltage of 5 V under the tip for 20 s was necessary for the manipulation. In the following STM scan, the fold appears broken apart in smaller units, Fig. 5.5e. In a later scan, some of these are joined again. The fragmentation of the folds does not help to reduce the overall stress and consequently coalesce again.

One further hint not to associate this folds with domain boundaries is the fact that occasionally they are displaced far from the scanning area rather than flattened out.

5.2 Heterostructures growth

Knowing the growth properties of graphene and hexagonal boron nitride, lateral heterostructures can be grown. While graphene nanostructures embedded in hBN are in principle more interesting for applications in electronics [133, 137, 139, 308], the constructrion of a hybrid 2D material with e.g. controllable gap size can rely on hBN nanostructures in a graphene matrix [306, 326–328], thus the two heterostructures are to be investigated. Furthermore, zigzag interfaces can be obtained by se-

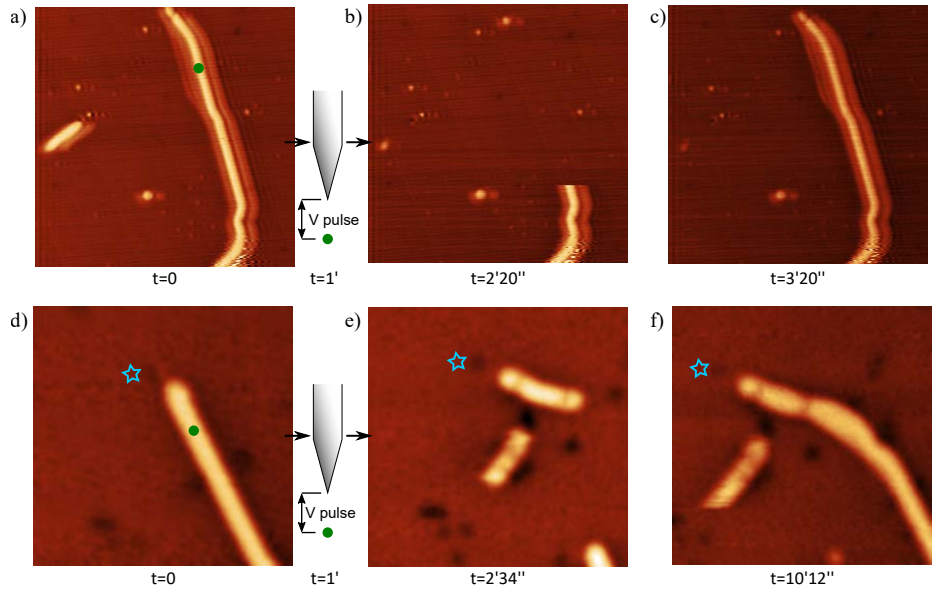

Figure 5.5: Two examples of folds manipulation with STM tip: a-c) After a moderate voltage pulse at constant height (V_{ramp}=0.7–1.2 V, t=7 s, I_{set}=0.5 nA), the hBN flattens out, but the corrugation is formed in the same position (reappearing while scanning image (b)). d-f) The termination of a fold is disrupted by a tip pulse (V=5 V, t=20 s, I_{set}=0.5 nA). Smaller corrugations form (e), which are "ironed" together by the tip (f). A star marks a defect in hBN serving as a placeholder.

quential growth, taking advantage of the edge-seeding growth of one material from the previously grown nanostructures of the other [145, 148, 149]. We therefore grew heterostructures with both orders of growth, and report the results in this section.

5.2.1 Embedding graphene nanoislands in hBN

We first tried growing graphene nanoislands and afterwards hBN on the same surface. This is a challenging task, because of the reduced stability of graphene at the hBN growth temperatures. This is especially important when considering that the reported growth temperatures of ≥800°C for hBN on Ni are far above the limit of 650°C of graphene nanostructures stability [315, 319, 329], and at least a temperature of 700°C seemed to be necessary for complete dehydrogenation of borazine [125]. As reported, we could partially grow hBN on Ni(111) at 600°C and above, though only from ~650°C a sufficient purity was obtained.

We carried out three different experiments of hBN growth at the sides of GNIs,

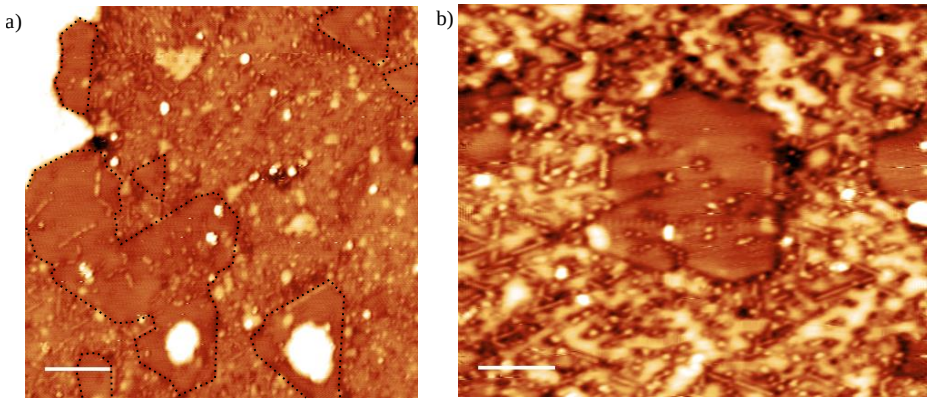

Figure 5.6: a) STM topographic image of disordered hBN grown on Ni(111) at 550°C from the edges of GNIs. The graphene islands are evidenced for clarity. Scale bar 10 nm. b) STM topography of a GNI surrounded by disordered hBN with Ni impurities and presumably C. Scale bar 5 nm.

which were grown on Ni(111) following the method exposed in Chap. 3. After nanoislands growth, the preparation quality was checked with the STM. We later grew hBN by exposing the GNI/Ni(111) surface to borazine during the heating ramp of the sample to growth temperature. This was done in an intent to stabilize the graphene nanostructures, since we expected that the graphene edges would be a reactive site for borazine bonding and reaction, while being passivated by it. Three different temperatures were used: 700, 650 and 550°C. Only in the latter experiment we could observe graphene nanoislands after preparation. Preparations at higher temperatures revealed a hBN layer with similar properties, where GNIs could not be found though.

Fig. 5.6 shows STM topographic images of the GNI+hBN surface. As noted, GNIs are found embedded in a disordered layer. We note that a general preservation of the shape of GNIs is maintained after the hBN growth process. Point protrusions following the 3-fold symmetry directions of Ni(111) are found ubiquitously around the graphene. We attribute such protrusions to Ni impurities because of their appearance similar to those in graphene, Fig. 5.6b. Although a phase separation between B-N and C-C bonds is energetically favoured [131, 330, 331], the diffusion of C atoms from either the edges of graphene or the bulk of Ni in the hBN layer cannot be excluded. While from STM analysis we cannot identify the chemical composition of the layer, we speculate that the surface layer is formed by a mixture of C, B, N

atoms with Ni impurities, due to the high mobility of C and Ni atoms at the growth temperature. This is consistent with the substitutional doping of C in hBN layers on Ru(0001) originating from unreacted C on the metal surface [151]. The authors prove that removal of such residual C results in undoped hBN structures. However, due to the constant presence of C in the bulk and sub-surface Ni, depletion of carbon from this surface is a far more complex process.

In order to obtain the desired heterostructures of hBN and graphene with zigzag interfaces we inverted the growth order, since the growth temperatures on Ni(111) favour this method. We show this in the next section. Nevertheless, we note that we still do not hold sufficient experimental evidence to exclude that hBN seeding at GNIs edges can form an ordered heterostructure with a careful optimization of the method.

As a final note, we report that a different growth method for Gr seeding at hBN edges was also tried, by creating holes in monolayer hBN by Ar^+ sputtering. The surface was then annealed in order to recover order in the hBN layer, before growing graphene. Also in this case a GBN layer with segregated GNIs was obtained, although these had irregular shapes and edge structures as a consequence of the amorphous holes sputtered in hBN. We suggest that further effort in this method and in particular in the production of hBN holes with precise edges, though out of the scope of this thesis, could provide an effective method to obtain regular GNIs embedded in a hBN lattice with zigzag interfaces.

5.2.2 Embedding hBN nanoislands in graphene

As noted from Sec. 5.1, triangular hBN nanoislands with zigzag edges can be readily grown on Ni(111) in a similar way to GNIs. In order to obtain regular Gr-hBN interfaces, we grew hBN islands at 700°C and graphene at 550–580°C after these. Fig. 5.7 shows some examples of the results. As noted, after growth the surface looks flat and generally regular. The triangular shapes of hBN nanoislands are preserved, and can be recognized as embedded structures in the graphene layer - see Sec. 5.3 for the identification of the phases using the electronic structure.. A height difference of only 30 pm is measured between graphene and hBN. As noted from Fig. 5.7b, the interface between hBN nanoislands and the Gr layer displays an enhanced apparent height. We could only observe this at the edges of few nanoislands, while mostly

they present a flat or sunken interface (as discussed in the following). As noted from Fig. 5.1, this is a feature related to hBN edges rather than to Gr-hBN interfaces. We do not hold sufficient evidence to state the origin.

During the course of the experiments, the work published by Drost et al. [152] showed that perfect zigzag hBN-Gr interfaces can be grown on Ni(111), using a similar method. In the following, we discuss the structure of the hBN-Gr interface we obtained.

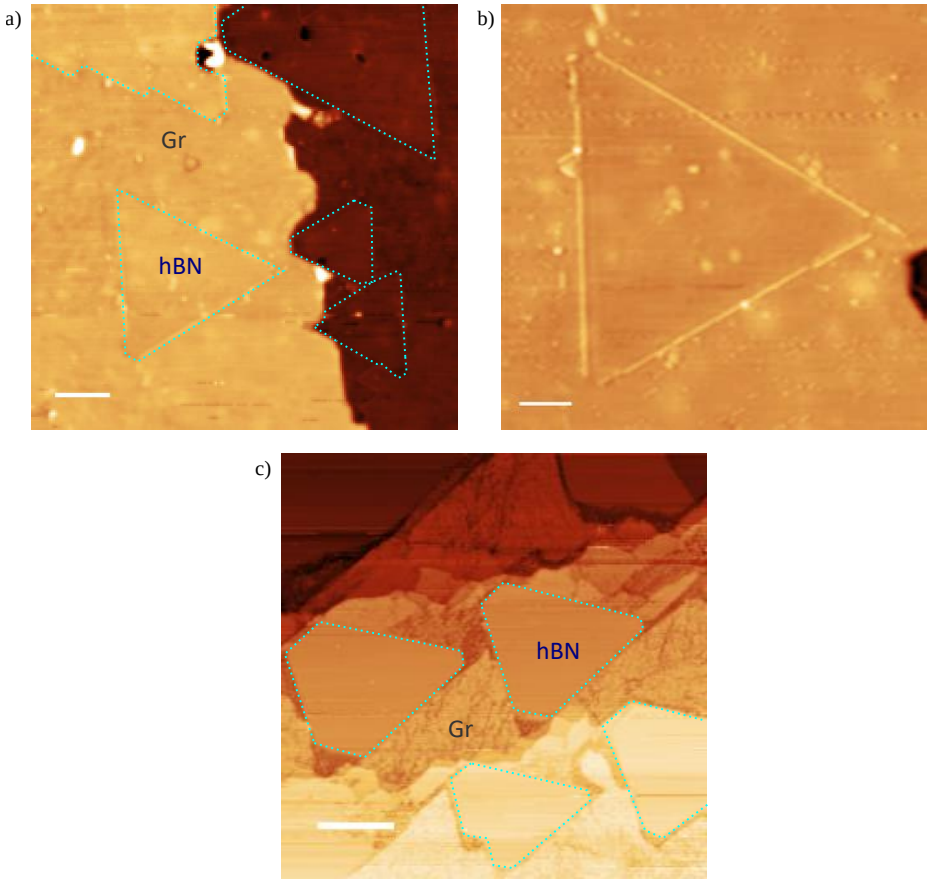

Figure 5.7: a) STM topographic image of (highlighted) triangular hBN islands embedded in a Gr matrix. Scale bar 10 nm. b) Zoom in of a hBN island with enhanced apparent height at the edges, surrounded by Gr. c) STM topographic image of a different preparation of hBN truncated nanoislands embedded in defective graphene. The scan is taken at V_b=2.5 V, where the contrast between hBN and Gr is enhanced (see Sec. 5.3.1)

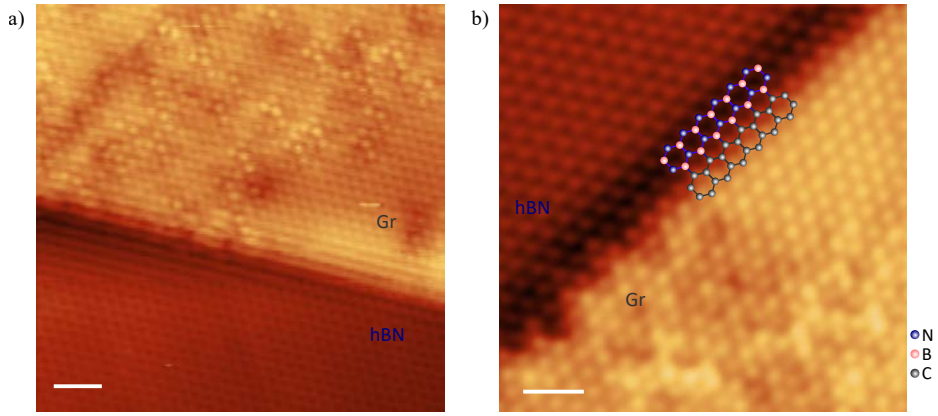

Figure 5.8: Two STM topographic images of the zigzag interface between hBN nanoislands and defect rich Gr. In (a) interference patterns parallel to the edge prevent full resolution of the edge, though the zigzag direction is clearly deduced. V_b=15 mV, I_t=3.1 nA. b) The Gr-hBN interface is fully resolved, showing a zigzag morphology with one defect (bottom). The proposed atomic structure is indicated. V_b=10 mV, I_t=1.0 nA. Scale bars (a,b) 1 nm.

Fig. 5.8 shows two examples of the interface between zigzag hBN edges (the long sides of the triangular nanoislands) and defect rich graphene grown at the side. The presence of Ni impurities and defects is attributed here to the growth temperature employed for graphene, since a healing effect of temperature is known for both GNIs, as discussed in Chap. 3, and for monolayer graphene [219, 228, 229]. . As observed, the zigzag symmetry of hBN edges is preserved upon formation of graphene, which grows continuously from the side of hBN islands. While intermixing of B and N in the graphene layer might still take place due to unreacted borazine or local etching of the edges, the growth at different temperatures [332] seems to provide an atomically sharp interface with a high degree of purity. Fig. 5.8b shows the interface with atomic resolution. As noted, the interface appears dumped, with a height difference of 10 pm to hBN. The interface shows few vacancies and a wider kink, likely related to intermixing at the edge or single vacancies, which are energetically stable and near the energy of a perfect zigzag interface [333].

We note that the atoms imaged high form a continuous hexagonal lattice across the interface, thus confirming a top-hollow stacking for hBN because of the matching with graphene. This also corroborates the top-fcc preferential stacking predicted by calculations for hBN seems, as a consequence of the graphene stacking energetics favouring this configuration. Furthermore, the identification of the hollow (fcc or

hcp) stacked atoms of graphene as protrusions implies the same in hBN. This identifies the high-imaged atoms as B in hollow sites according to stacking energetics.

The proposed atomic structure of the interface is also drawn in Fig. 5.8b. The assumption of (N,B)=(top,fcc) stacking configuration for hBN implies a B-C interface at the boundary with graphene. This is in agreement with DFT calculations for GBN on Ni, showing that N-C interfaces are energetically stable only in N-rich conditions, and otherwise a reconstruction would be favoured [152]. Similarly, Drost et al. [153] found that on intercalated Au/Ir the GBN interface is composed of B-C bonds. We conclude that C-B interfaces form at the graphene-hBN boundary, in agreement with the B terminations assigned in Sec. 5.1 to the hBN zigzag edges on Ni(111).

The observation of zigzag edges is also important because a reconstruction is often expected at the interface between polar and non polar materials due to charge accumulation and screening, an effect known as 'polar catastrophe' [334–336]. Furthermore, misfit dislocations were observed on Ru(0001), and related to relaxation of the strain due to the 2% mismatch between graphene and hBN [337]. This might be the origin of the defects we observe at the hBN-Gr interface, Fig. 5.8. On the other hand, the lack of periodicity points to a local intermixing of B, N and C at the interface, with the strong interaction and the lattice match to Ni(111) stabilizing a zigzag morphology.

5.3 Electronic properties of the heterostructure

5.3.1 Chemical identification by field emission resonances

Image potential states, the related field emission resonances in STS and their utility in chemical identification of the materials on a surface were introduced in Sec. 4.4.1. This method provided especially useful in the identification of hBN and Gr on Ni(111), since just using the topographic information is not enough due to the similar morphology and the absence of Moirè superstructures deriving from the lattice match of the materials.

Fig. 5.9 shows a line of C.C. spectra acquired across the interface between a hBN island and graphene. The first peak appears in hBN at ~1.8 eV and on Gr at ~2.4 eV. A transition zone is observed at the interface, where the two peaks appear with differ-

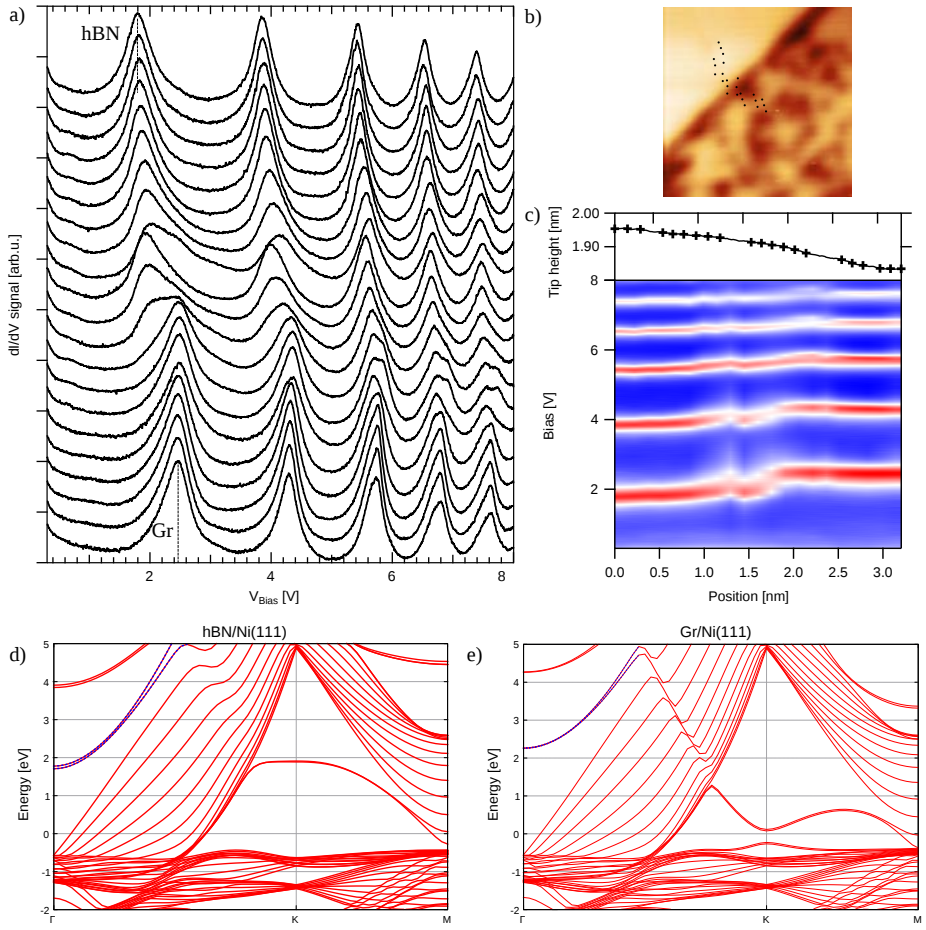

Figure 5.9: a) Constant current dI/dV spectra along a line from hBN/Ni to Gr/Ni. Setpoint V_b=0.3 V, I_t=0.5 nA b) STM topography with the tip position for the spectra of (a). c) Profile and colour plot of the spectra represented in (a). d-e) DFT calculated spin majority band dispersion of (d) hBN/Ni and (e) Gr/Ni. The IFS, marked in blue, have their onset at Γ at (d) 1.70 eV and (e) 2.24 eV. Graphs (d) and (e) courtesy of Aran Garcia-Lekue.

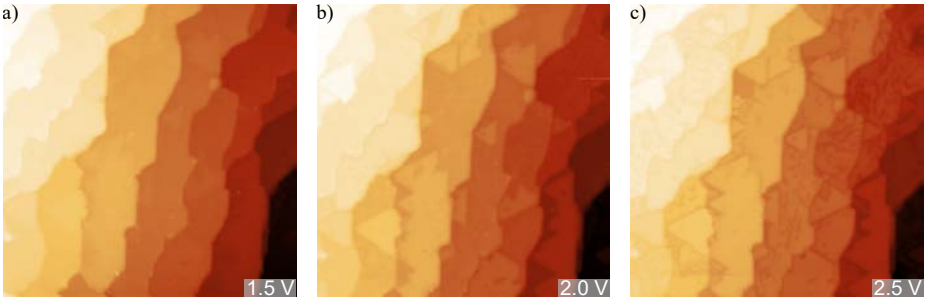

Figure 5.10: STM topographies at different bias voltages on the same 100x100 nm^2 area of hBN- and Gr-covered Ni(111) surface, showing a) flat terraces when the bias is lower than the IFS energies, b) higher contrast for hBN islands for $V_b \geq 1.8$ eV, c) both hbN and Gr appearing high for $V_b \geq 2.4$ eV, with enhanced contrast at their interface.

ent relative intensities. As discussed in Sec. 4.4.1, the peak there observed in graphene at ~2.45 eV is related to the evolution of the surface state of Ni into an interface state (IFS) between the Ni surface and the Gr layer, as a result of the strong electronic interaction of the two materials [76]. The same effect is at the origin of the peak observed in hBN. This is evidenced by the calculated band structures of hBN/Ni(111) and Gr/Ni(111) of Fig. 5.9d and e, both displaying a band with parabolic dispersion and surface character having energy onset at 1.70 eV and 2.24 eV, respectively. This is in agreement with our experimental STS measurements, and similar values were found in the same system by STS [152] and DFT calculations [316]. The interface state predicted for the hBN/Ni(111) layer is not to be confused with the hBN interlayer state defined between hBN planes in multilayer crystals [338, 339].

In STM topography, scanning at $V_b \geq 2.4$ eV results in an enhanced apparent height of the graphene areas, with a dendritic appearance [76]. A similar effect can be observed for hBN when $V_b \geq 1.8$ eV. Fig. 5.10 shows how the two effects can serve for rapid chemical identification. The areas covered by hBN are enhanced in STM by scanning the surface with $1.8 \leq V_b \leq 2.4$ eV (the actual range might be slightly lower, since the IFS has a finite energy width due to the modification of the vacuum potential with the bias voltage [174, 260]) and can thus be unequivocally identified. At $V_b \geq 2.4$ eV, both Gr and hBN appear higher, Fig. 5.10c, with an enhanced contrast at the interface.

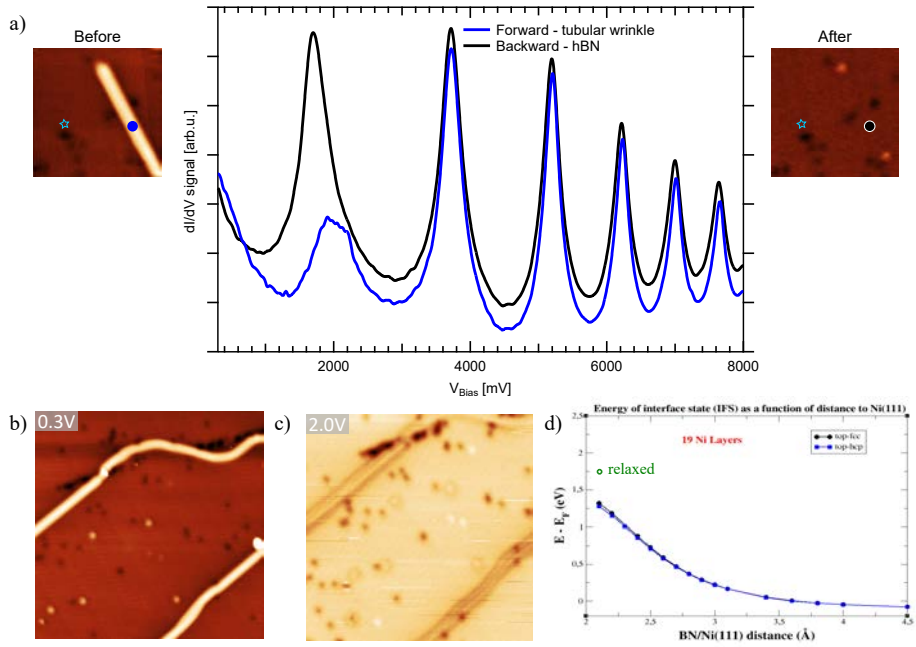

Figure 5.11: a) Forward and backward C.C. spectra acquired on top of a tubular corrugation which is flattened out at high voltage (see Sec. 5.1.1), as demonstrated by the corresponding topographic images taken just before and after the acquisition, appearing as insets. The indicated defect in the hBN layer is used as a place marker. Setpoint: V_b=0.3 V, I_t=0.5 nA b-c) STM topographic image displaying two tubular folds on hBN appearing b) high at V_b=0.3 V, and c) with inverted contrast for V_b=2.0 V, above the onset of the hBN/Ni IFS. d) DFT calculations displaying the energy of the interface state as a function of the distance to Ni(111) for unrelaxed hBN in top-fcc and top-hcp stacking. The value for the relaxed structure at the equilibrium distance is also shown. (d) courtesy of Aran Garcia-Lekue.

5.3.2 Tubular corrugations

With the same method of the previous section, some information can be grasped on the tubular corrugations we found in the hBN layer. Fig. 5.11 shows C.C. the forward and backward spectra acquired with the tip placed on top of one such corrugation in the hBN layer. The difference between the two spectra is given by the manipulation operated by the tip at high voltage, as discussed in Sec. 5.1.1, resulting in (i) acquisition of the STS spectrum of the tubular fold in the forward scan, (ii) manipulation (displacement) of the fold, (iii) acquisition of the backward spectrum on flat hBN. As it is evident from Fig. 5.11a, the first peak on tubular folds appears at a higher energy (~1.90 eV) and is characterized by different width and DOS respect to the IFS of hBN/Ni. The shift to higher energy is in apparent contrast with a rippling of hBN,

as an increase of hBN-Ni distance would result in a lower energy of the IFS state, as also shown by calculations reported in Fig. 5.11d and [340]. However, little is known so far about the coupling to hBN states of the electronic states in such tubular folds. The width of the peak suggests a shorter lifetime of the state observed, and thus possibly a hybridization with bulk states [262] or with local states.

5.3.3 Graphene-hexagonal boron nitride interface

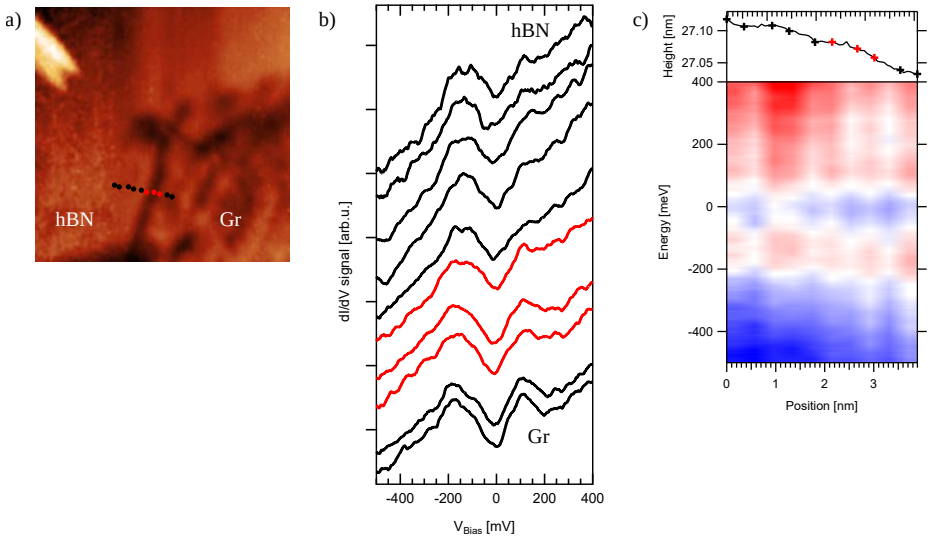

Figure 5.12: a,d) STM topography of hBN-Gr zigzag interfaces. b,e) C.H. dI/dV spectra at the positions marked in the topographic image. c,f) Edge profiles along the lines and colour plots of the spectra represented. Setpoints for the STS measurements: (a-c)V_b=-0.5 V, I_t=0.5 nA, (d-f) V_b=-1 V, I_t=2.1 nA.

A localized 1D state is predicted [131] at the zigzag interface between hBN and Gr, and it was observed by STM/STS on weakly interacting substrates such as Cu [314] and intercalated Au [153]. We therefore investigated such interface by STS on the strongly interacting Ni surface, in view of Au intercalation experiments.

We were able to only collect few sample spectra in this system. Fig. 5.12 shows a line of C.H. STS spectra taken across a hBN-Gr zigzag interface. The series shows no features peculiar to the interface. Only the characteristic features of Gr/Ni (see Sec. 4.4) and peak at -200 mV related either to the tip or to Ni *d* states are recognized. Similarly featureless spectra were registered in at least one other case. An enhanced intensity of the dI/dV signal is observed on the hBN side at positive bias voltages .

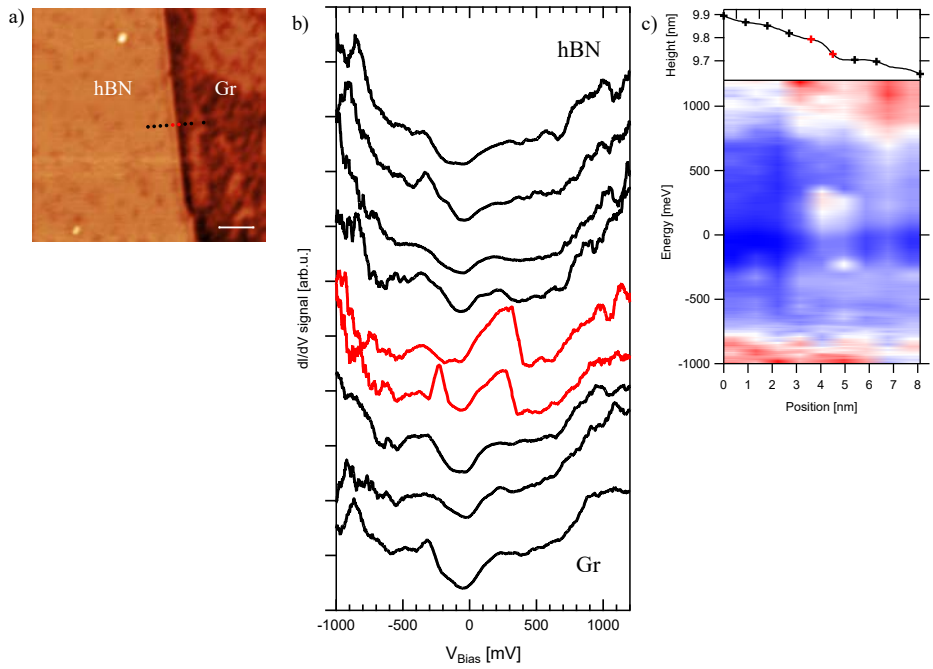

Figure 5.13: a) Topographic image and b) C.H. line STS across a hBN (left) to Gr (right) interface, at the points indicated. Here, a (double) feature around E_F appears on the spectra around the interface. c) Profile along the line and colour plot of the spectra of (b). Scale bar in (a) is 5 nm. Setpoint for STS: V_b=-0.5 V, I_t=0.5 nA.

Fig. 5.13 shows a different example. Here, a series of spectra are acquired across a hBN edge imaged high and its interface to Gr. The series clearly shows a double feature around E_F, displayed as a broad peak at +300 mV and a sharper peak at −210 mV. The spatial resolution for this series doesn't allow to determine if peaks are localized on the hBN edge or on the interface. However, dI/dV spectra on the high-imaged hBN edge alone didn't reveal such features.

These features are very unlikely to be due to the predicted interface state [131] around E_F and to a spin splitting of it [135, 299]. As noted in Sec. 4.4.2 for graphene, the interaction of both hBN and Gr with the Ni substrate is very strong, so that the band dispersion calculated for pristine graphene/hexagonal boron nitride nanoribbons [130, 132] is heavily modified and hybridized with the *d* states of Ni. Understanding the origin of these depends on the identification of the nature of the enhanced height at the border, which we could not determine in our experiments.

5.4 Summary

We investigated the growth and morphology of lateral 2D heterostructures of graphene and hexagonal boron nitride on Ni(111), and showed preliminar results on their electronic properties and on Au intercalation.

Submonolayer growth of hexagonal boron nitride was carried out at different temperatures, showing increasing purity for higher temperatures. The energetically favourable (N,B)=(top,fcc) stacking leads to preferential growth of triangular nanostructures with zigzag edges, as for GNIs. We find that stress-induced tubular corrugations form in the hBN layer, and that they can be manipulated with the tip.

Seeding of hexagonal boron nitride from graphene nanoislands is found to be challenging: GNIs are dissolved at high temperatures, and the hBN layer is highly defectuous in the whole growth range. Purging C from the surface and sub-surface of Ni or sputtering of antidots in the hBN layer are indicated as possible routes to obtain GNIs embedded in hBN.

Oppositely, graphene is successfully grown on the hBN nanoislands precovered Ni surface. Nearly perfect zigzag interfaces are obtained. Though the chemical composition of the terminations cannot be resolved, we compared STM topographic images of hBN to calculated LDOS, and the appearance of the laterally matched Gr and hBN layer. We propose that zigzag edges of hBN nanostructures on Ni(111) are B-terminated, contrary to the preferential N-terminations predicted for free-standing hBN, and that C-B bonds form at the heterostructure zigzag interface.

Electronically, we identify an interface state between the Ni surface and hBN, similar to that found for Gr/Ni(111), and we show how they can be used for chemical identification. A different FER spectrum is found on tubular corrugations. Finally, we investigated the zigzag interface of Gr and hBN, showing the absence of a confined electronic state on the surface of Ni(111).

Chapter 6

Conclusions and outlook

The challenge behind the experiments in this thesis was double. From one side, this work is inscribed in the effort of current research to find methods and strategies to synthetize nanostructures, particularly of graphene, with control over the atomic and edge structure of them, and to simultaneously manipulate their electronic properties. This is an essential condition for the realization of devices at the nanoscale. From another side, we pursued the accomplishment of this goal by using exclusively bottom-up methods, which take advantage of the intrinsic interactions of matter at the atomic level to drive the formation of nanostructures with the desired properties, bringing unprecedented levels of control on fundamental, natural processes.

We combined STM and STS methods, because they are surface-sensitive techniques which allow the structural as well as electronic characterization of nanostructures on a surface with atomic resolution. The whole growth and characterization process was carried out in UHV conditions in order to maximize the purity of the grown structures and of the system to be analyzed, additionally running selected experiments at low temperature to perform atomically resolved spectroscopic measurements that probe the fundamental properties of the system.

For the achievement of our goal, we used three bottom-up methods: i) CVD growth of graphene nanostructures, with control of the edge structure and shapes ii) intercalation of metal films at the graphene/metal interface to control the final properties of the graphene/metal system and iii) interfacing graphene with other 2D materials in lateral heterostructures. The first two methods rely on the control

of the interfacial interaction with the substrate, while the third one includes the in-plain combination of two-dimensional materials with differing properties.

Growth of the nanostructures was conducted on a nickel substrate because it provides a reactive growth surface with an epitaxial match to graphene, which allows unstrained growth of it. By an adapted CVD process shape-selected nanostructures can be produced with an exquisite control over the edge structure.

Gold was chosen as the metal intercalant, because the reduced interaction entails the possibility of inducing structural changes to graphene by the modified substrate coordination and of decoupling graphene to recover its quasi-freestanding properties.

We further tried to produce atomic layers with controlled electronic properties by producing heterostructures of graphene and two-dimensional hexagonal boron nitride. The latter was chosen because of its structural homogeneity to graphene combined to the electronic properties of a wide gap insulator, meaning that planar layers with tunable bandgaps could be obtained, with interesting interfacial properties. With the knowledge acquired from the growth of graphene, we hoped to obtain a precise control on the growth of boron nitride nanostructures on Ni, and to combine these and graphene nanostructures in hybrid layers.

We have shown that the intrinsic complexity of the processes involved in the growth of graphene on nickel challenges the assumed simple picture of the formation of perfectly epitaxial graphene (nano)structures. We found that, depending on the growth parameters used, the internal structure of regularly shaped nanoislands can be far less than perfect when observed with atomic resolution. However, characterizing precisely the stacking symmetries and domain boundaries of the grown nanostructures led us to identify strategies for the formation of quantum dots with controlled crystallinity, shape and size by controlling the growth.

Throughout our experiments, intercalation of Au on such Gr/Ni system was shown to be an effective way to tailor both the structural and electronic properties of the as-grown graphene quantum dots. While we could not track changes in the internal structure, we found that, by intercalation, the edge structure of the graphene can be modified, recovering purely zigzag structure. Thus, the interfacial interaction with the underlying metal, first Ni and then the intercalated Au, can be used as a method to finely control the edges of graphene nanoislands. Furthermore, the effect of such

interaction on the electronic properties was shown to be detrimental: while on Ni a strong interaction leads to the opening of gaps, and induction of spin polarization of the former Dirac cone, we showed by STS that on Au the freestanding properties of graphene are recovered. Interestingly, we found that our graphene nanoislands display a different interaction with Au than that previously observed for other graphene nanostructures. Not only a reduced interaction with Au is measured, but also we find solid, reproducible signatures of a pair of occupied and unoccupied states confined at the zigzag edges, which we attribute to the spin split π bands. This finding, combined to our control on the structure of nanographenes, could lead to the realization of triangular graphene quantum dots on Au that, due to the entanglement between their unbalanced bipartite lattice and the spin alignment on their edges, would have ferromagnetic properties.

From the growth of 2D heterostructures of Gr and hBN, we learned that the complexity of a system does not always allow the realization of the desired structures (sometimes 1+1 does not sum 2!), although new materials with interesting properties can be obtained. While the graphene quantum dots can not be embedded in an insulating hBN lattice due to the different growth and stability temperatures on Ni, we could fabricate planar heterostructures by embedding hBN triangles in graphene, obtaining precise zigzag interfaces. We propose that Au intercalation could lead to the observation of electronic states localized on such interfaces.

Outlook

The greatest teaching of a thesis is that research might have a clear beginning but knows nothing about the ending. However, if research was a line (or an entanglement of crossing lines), a PhD thesis would be only the part visible through a high-resolution lens. The points that follow are unknown, but a few suggestions can be made. However, each PhD does need to end, hopefully providing suggestions for another beginning.

The most relevant result of this thesis is doubtlessly the observation of energy-split edge states in graphene quantum dots, and the consequent possibility to realize magnetic GQDs. Probably the following step with highest importance would then be to magnetically investigate such quantum dots, in particular those showing lattice imbalance (triangular GNIs). The first and most obvious thought is towards scan-

ning probe microscopy (STM/AFM) measurements with spin sensitivity (SP-SPM), to assess the presence of spin-polarized states on their edges and the magnetic alignment between them.

The quantum dots could be transferred to a different substrate, especially an insulating one, as it is currently done in many laboratories – including ours – for nanoribbons grown on Au surfaces. However, the general preference of the nanoislands for the (partly) embedded configuration might pose a limitation to such method. Our statistical analysis suggests that thick Au films could maximize islands on top, and this could provide a way to overcome such limitation.

Finally, though in this thesis the intrinsic band structure and the opening of a gap in graphene quantum dots could not be unraveled, we expect that a sizeable gap (0.2 eV for 3 nm wide GNIs) could be found in these GQDs, thus displaying photoluminescence in the infrared spectrum, thus making them interesting for applications in optoelectronics.

Acknowledgements

A Thesis is a very important part of life. It's the road connecting who I was in the moment of starting this project, and the person I am now. It is the result of all the people who participated in its completion, both in the hard work of physics and in the life behind it. Few people in life face the challenge of resuming five years in a manuscript, not easier is it to thank all the people that contributed. Each and everybody had their role, it will not be possible to have them all in a few pages... Especially for people like me, who can get stepped and apologize for placing my foot underneath, and thank for the great excuse to clean the shoes!

The first thanks goes to my directors, Aitor and Gustavo, as for tradition but not only. If I learned how fun it can be to make research, it's mostly thanks to them. They have been not only an invaluable help, but also a great inspiration, scientifically as much as personally.

To Aitor for the contagious enthusiasm, the constant source of motivation and inspiration, the unbreakable optimism and the eruption of ideas. And, not least, for the personal support, maybe not so visible but solid. Permiso?

To Gustavo, a patient suggestion for everybody, a magician in many ways, especially creating a story where I could only see atoms on top of more atoms. I lack the words to better define that sort of mute patience I could sense from you, for my limits. But I do thank for it.

I'm quite sure I wouldn't have completed a PhD with different supervisors. You named yourselves "fathers", and no doubt you are.

I want to thank each and everyone of the people who have passed from the group, and those who I have worked with. All of them had their role and importance in this

work.
First, a great thanks to Sofia. She posed the first stone and consequently held the main responsibility on the analysis of nanoislands on nickel. And taught me how to work, probably.
A thanks to Markos, for your constant dose of motivation, and your great expertise in life-lessons and perspectives, your encouragement(s), jokes and chocolates. And for the help with measurements! The spiritual mentor for me, and I believe also for the rest of the group. It's as rare to meet a person with so much sensitivity in the field of science as to find a cat in the middle of the ocean. As for me to find a good metaphor. But I hope you appreciate the intention.
To Marc GC, for our almost working language exchange, for the constant cotilleos - ops, now it's written! -, for standing my questions and doubts every time without everever getting upset or showing (showing..) boredom.
To Cesar, for transmitting strength and determination, always and with no excuse, no exception, no doubt. For the amount of suggestions, for his guidance, for sharing helpful experiences and for his example. And also for not killing me when deserved!
To Sylvie, for all the hard work done together. And for the good company and discussions. And for one of the best mottos I could know: "The better is enemy of the good". I wish I could make it truly mine.
To Miguel, for all the coffees we promised to have: hectares of coffee plants were saved thanks to our procrastination. And for not smoking with me so many times.
To Marc M., for introducing me to the catalan world.
And also thanks to Stefano, Mirco, Maria, Mercedes, Jeremy, Amina, Alex and Sergi for their scientific and human contributions.

Great thanks to all the people in San Sebastian: firstly Enrique for receiving me. Thanks to Jens, Mikkel and Jorge for their collaboration in the lab (and out..). And to all the people at CFM for their always warm welcome.

I must give great thanks to many people from the institute: to Christina and to the italians, Caterininaina, Anna, Francesco and Lorenzo for somehow standing me and my boring and demotivated "moments" (in the timescale of the universe at least). Really, thanks!

I also must thank Pau, Raul, Rafa, Ainhoa, Sandra saint Sandra standing my questions!, Federico, all the smokers and the non-smokers passing by.

A special thanks to Mariangeles :) , Laura, Marta and Jose from the dark. I survived thanks to you, really.

I must also thank many people that, along this period, had a fundamental role in my life, and often helped me to make it through.

First my family, a constant support, a constant understanding - for a person that needs a lot of understanding!

To try shortening this never ending list, I've chosen one or two reasons each, in rigorous disorder:

To Michaela, the dearest of all, I cannot choose one. Thanks for aaaargh.
To Delphine, for producing happiness just by nature, appearing out of nowhere.
To Ale, for the teachings on butchery of crocodiles and for cozze friday night after the lab. Un-for-get-ta-ble.
To Manfredin, for the constant support, the special moments... Thanks.
To Sara and Curi, for being my abroad parents. And to Aleix for stealing them from me.
To Robi, because I still laugh of the ebook reader reading pdf's in loud voice.
To Michelone, for your great sentencing: "The sea without sun is only salty water" (and a definition of the thesis I'll let you write elsewhere)

A great thanks to La Miranda for being my second home, and all the people composing the family giving life to it.

More thanks to Fabio, Chiarucci, Alessia & Nicola, Farah, Albert.

On behalf of Lorenzo, thanks to the INFN Laboratories at Gran Sasso.

To Carmine, the greatest thanks, the greatest wishes. No matter what Lola thinks about this.

For a Teorema, thanks to Terence Stamp. Anyways.

And to those I forgot, thanks for not getting too upset with me.

List of publications

S. O. Parreiras, M. Gastaldo, C. Moreno, M. D. Martins, A. Garcia-Lekue, G. Ceballos, R. Paniago, and A. Mugarza, *Symmetry forbidden morphologies and domain boundaries in nanoscale graphene islands*, 2D Materials **4**, 025104 (2017).

A. Lerch, L. Fernandez, M. Ilyn, M. Gastaldo, M. Paradinas, M. A. Valbuena, A. Mugarza, A. B. M. Ibrahim, J. Sundermeyer, U. Höfer, and F. Schiller, *Electronic Structure of Titanylphthalocyanine Layers on Ag(111)*, The Journal of Physical Chemistry C **121**, 25353 (2017).

M. Ormaza, L. Fernández, M. Ilyn, A. Magaña, B. Xu, M. J. Verstraete, M. Gastaldo, M. A. Valbuena, P. Gargiani, A. Mugarza, A. Ayuela, L. Vitali, M. Blanco-Rey, F. Schiller, and J. E. Ortega, *High Temperature Ferromagnetism in a $GdAg_2$ Monolayer*, Nano Letters **16**, 4230 (2016).

M. Gastaldo, A. Garcia-Lekue, G. Ceballos, A. Mugarza, *Spin-polarized edge states at graphene quantum dots*, in preparation.

M. Gastaldo, G. Ceballos, A. Mugarza, *Tailoring structural and electronic properties of graphene nanoislands by metal intercalation*, in preparation.

M. Gastaldo, G. Ceballos, A. Mugarza, *Thickness evolution of image and surface states in Au films on Ni(111)*, in preparation.

Bibliography

[1] P. Wallace, *The Band Theory of Graphite*, Physical Review **71**, 622–634 (1947).

[2] K. S. Novoselov, A. K. Geim, et al., *Electric Field Effect in Atomically Thin Carbon Films*, Science **306**, 666–669 (2004).

[3] K. S. Novoselov, D. Jiang, et al., *Two-dimensional atomic crystals*, Proceedings of the National Academy of Sciences **102**, 10451–10453 (2005).

[4] K. S. Novoselov, A. Mishchenko, A. Carvalho, and A. H. Castro Neto, *2D materials and van der Waals heterostructures*, Science **353**, aac9439–aac9439 (2016).

[5] A. H. C. Neto, F. Guinea, N. M. R. Peres, K. S. Novoselov, and A. K. Geim, *The electronic properties of graphene*, Reviews of Modern Physics **81**, 109–162 (2007).

[6] C. Lee, X. Wei, J. W. Kysar, and J. Hone, *Measurement of the Elastic Properties and Intrinsic Strength of Monolayer Graphene*, Science **321**, 385–388 (2008).

[7] A. K. Geim and K. S. Novoselov, *The rise of graphene.*, Nature Materials **6**, 183–191 (2007).

[8] K. S. Novoselov, V. I. Fal'ko, et al., *A roadmap for graphene*, Nature **490**, 192–200 (2012).

[9] F. Bonaccorso, Z. Sun, T. Hasan, and A. C. Ferrari, *Graphene photonics and optoelectronics*, Nature Photonics **4**, 611–622 (2010).

[10] D. Cohen-Tanugi and J. C. Grossman, *Water Desalination across Nanoporous Graphene*, Nano Letters **12**, 3602–3608 (2012).

[11] D.-e. Jiang, V. R. Cooper, and S. Dai, *Porous Graphene as the Ultimate Membrane for Gas Separation*, Nano Letters **9**, 4019–4024 (2009).

[12] S. P. Koenig, L. Wang, J. Pellegrino, and J. S. Bunch, *Selective molecular sieving through porous graphene*, Nature Nanotechnology **7**, 728–732 (2012).

[13] S. Garaj, W. Hubbard, et al., *Graphene as a subnanometre trans-electrode membrane*, Nature **467**, 190–193 (2010).

[14] B. M. Venkatesan and R. Bashir, *Nanopore sensors for nucleic acid analysis*, Nature Nanotechnology **6**, 615–624 (2011).

[15] A. N. Grigorenko, M. Polini, and K. S. Novoselov, *Graphene plasmonics*, Nature Photonics **6**, 749–758 (2012).

[16] D. Rodrigo, O. Limaj, et al., *Mid-infrared plasmonic biosensing with graphene*, Science **349**, 165–168 (2015).

[17] A. M. Hein, K. F. Long, et al., *The Andromeda Study: A Femto-Spacecraft Mission to Alpha Centauri*, (2017).

[18] K. Kim, J.-Y. Choi, T. Kim, S.-H. Cho, and H.-J. Chung, *A role for graphene in silicon-based semiconductor devices*, Nature **479**, 338–344 (2011).

[19] G. Fiori, F. Bonaccorso, et al., *Electronics based on two-dimensional materials*, Nature Nanotechnology **9**, 768–779 (2014).

[20] G. Iannaccone, F. Bonaccorso, L. Colombo, and G. Fiori, *Quantum engineering of transistors based on 2D materials heterostructures*, Nature Nanotechnology **13**, 183–191 (2018).

[21] W. Zhang, Q. Wang, Y. Chen, Z. Wang, and A. T. S. Wee, *Van der Waals stacked 2D layered materials for optoelectronics*, 2D Materials **3**, 022001 (2016).

[22] A. Castro Neto and F. Guinea, *Impurity-Induced Spin-Orbit Coupling in Graphene*, Physical Review Letters **103**, 026804 (2009).

[23] S. Y. Zhou, G.-H. Gweon, et al., *Substrate-induced bandgap opening in epitaxial graphene.*, Nature materials **6**, 770–5 (2007).

[24] Y. Zhang, Y.-W. Tan, H. L. Stormer, and P. Kim, *Experimental observation of the quantum Hall effect and Berry's phase in graphene.*, Nature **438**, 201–204 (2005).

[25] W. Han, R. K. Kawakami, M. Gmitra, and J. Fabian, *Graphene spintronics.*, Nature nanotechnology **9**, 794–807 (2014).

[26] S. Roche and S. O. Valenzuela, *Graphene spintronics: puzzling controversies and challenges for spin manipulation*, Journal of Physics D: Applied Physics **47**, 094011 (2014).

[27] D. V. Tuan, F. Ortmann, D. Soriano, S. O. Valenzuela, and S. Roche, *Pseudospin-driven spin relaxation mechanism in graphene*, Nature Physics **advance on** (2014) 10.1038/nphys3083.

[28] C. L. Kane and E. J. Mele, *Quantum Spin Hall Effect in Graphene*, Physical Review Letters **95**, 226801 (2005).

[29] A. Avsar, J. Y. Tan, et al., *Spin-orbit proximity effect in graphene.*, en, Nature communications **5**, 4875 (2014).

[30] M. M. Otrokov, I. Klimovskikh, et al., *Evidence of large spin-orbit coupling effects in quasi-free-standing graphene on Pb/Ir(111)*, 2D Materials **110**, 428–433 (2018).

[31] N. Merino-Díez, A. Garcia-Lekue, et al., *Width-Dependent Band Gap in Armchair Graphene Nanoribbons Reveals Fermi Level Pinning on Au(111)*, ACS Nano **11**, 11661–11668 (2017).

[32] S. Zhu, Y. Song, et al., *Photoluminescence mechanism in graphene quantum dots: Quantum confinement effect and surface/edge state*, Nano Today **13**, 10–14 (2017).

[33] X. Li, X. Wang, L. Zhang, S. Lee, and H. Dai, *Chemically Derived, Ultrasmooth Graphene Nanoribbon Semiconductors*, Science **319**, 1229–1232 (2008).

[34] P. B. Bennett, Z. Pedramrazi, et al., *Bottom-up graphene nanoribbon field-effect transistors*, Applied Physics Letters **103**, 1–5 (2013).

[35] L. A. Ponomarenko, F. Schedin, et al., *Chaotic Dirac Billiard in Graphene Quantum Dots*, Science **320**, 356–358 (2008).

[36] M. Bacon, S. J. Bradley, and T. Nann, *Graphene quantum dots*, Particle and Particle Systems Characterization **31**, 415–428 (2014).

[37] X. Zhang, J. Xin, and F. Ding, *The edges of graphene*, Nanoscale **5**, 2556–2569 (2013).

[38] L. Yang, C. H. Park, Y. W. Son, M. L. Cohen, and S. G. Louie, *Quasiparticle energies and band gaps in graphene nanoribbons*, Physical Review Letters **99**, 6–9 (2007).

[39] Y.-W. Son, M. L. Cohen, and S. G. Louie, *Energy Gaps in Graphene Nanoribbons*, Physical Review Letters **97**, 216803 (2006).

[40] K. Nakada, M. Fujita, G. Dresselhaus, and M. Dresselhaus, *Edge state in graphene ribbons: Nanometer size effect and edge shape dependence*, Dec. 1996.

[41] M. Fujita, K. Wakabayashi, K. Nakada, and K. Kusakabe, *Peculiar Localized State at Zigzag Graphite Edge*, Journal of the Physical Society of Japan **65**, 1920–1923 (1996).

[42] Y.-W. Son, M. L. Cohen, and S. G. Louie, *Half-metallic graphene nanoribbons.*, Nature **444**, 347–9 (2006).

[43] G. Z. Magda, X. Jin, et al., *Room-temperature magnetic order on zigzag edges of narrow graphene nanoribbons*, en, Nature **514**, 608–611 (2014).

[44] J. Fernández-Rossier and J. J. Palacios, *Magnetism in graphene nanoislands*, Physical Review Letters **99**, 177204 (2007).

[45] W. L. Wang, S. Meng, and E. Kaxiras, *Graphene NanoFlakes with large spin*, Nano Letters **8**, 244–245 (2008).

[46] P. Ruffieux, S. Wang, et al., *On-surface synthesis of graphene nanoribbons with zigzag edge topology*, Nature **531**, 489–492 (2016).

[47] C. Tao, L. Jiao, et al., *Spatially resolving edge states of chiral graphene nanoribbons*, Nature Physics **7**, 616–620 (2011).

[48] M. Pan, E. Costa Girao, et al., *Topographic and Spectroscopic Characterization of Electronic Edge States in CVD Grown Graphene Nanoribbons*, Nano Letters **12**, 1928–1933 (2012).

[49] Y. Li, D. Subramaniam, et al., *Absence of Edge States in Covalently Bonded Zigzag Edges of Graphene on Ir(111)*, Advanced Materials **25**, 1967–1972 (2013).

[50] J. V. Barth, G. Costantini, and K. Kern, *Engineering atomic and molecular nanostructures at surfaces*, Nature **437**, 671–679 (2005).

[51] R. M. Jacobberger, B. Kiraly, et al., *Direct oriented growth of armchair graphene nanoribbons on germanium*, Nature Communications **6**, 8006 (2015).

[52] Y. Zhang, Z. Li, P. Kim, L. Zhang, and C. Zhou, *Anisotropic Hydrogen Etching of Chemical Vapor Deposited Graphene*, ACS Nano **6**, 126–132 (2012).

[53] L. Chen, L. He, et al., *Oriented graphene nanoribbons embedded in hexagonal boron nitride trenches*, Nature Communications **8**, 14703 (2017).

[54] J. M. Tour, *Top-down versus bottom-up fabrication of graphene-based electronics*, Chemistry of Materials **26**, 163–171 (2014).

[55] J. V. Barth, *Molecular Architectonic on Metal Surfaces*, Annual Review of Physical Chemistry **58**, 375–407 (2007).

[56] J. Cai, P. Ruffieux, et al., *Atomically precise bottom-up fabrication of graphene nanoribbons.*, Nature **466**, 470–3 (2010).

[57] Y.-C. Chen, D. G. de Oteyza, et al., *Tuning the band gap of graphene nanoribbons synthesized from molecular precursors.*, ACS Nano **7**, 6123–8 (2013).

[58] J. Cai, C. A. Pignedoli, et al., *Graphene nanoribbon heterojunctions*, Nature Nanotechnology **9**, 896 (2014).

[59] S. Kawai, S. Saito, et al., *Atomically controlled substitutional boron-doping of graphene nanoribbons*, Nature Communications **6**, 8098 (2015).

[60] M. Bieri, M. Treier, et al., *Porous graphenes: two-dimensional polymer synthesis with atomic precision*, Chemical Communications, 6919 (2009).

[61] L. Lafferentz, V. Eberhardt, et al., *Controlling on-surface polymerization by hierarchical and substrate-directed growth*, Nature Chemistry **4**, 215–220 (2012).

[62] C. Moreno, M. Vilas-Varela, et al., *Bottom-up synthesis of multifunctional nanoporous graphene*, Science **360**, 199–203 (2018).

[63] K. Choy, *Chemical vapour deposition of coatings*, Progress in Materials Science **48**, 57–170 (2003).

[64] C.-M. Seah, S.-P. Chai, and A. R. Mohamed, *Mechanisms of graphene growth by chemical vapour deposition on transition metals*, Carbon **70**, 1–21 (2014).

[65] K. Yan, H. Peng, Y. Zhou, H. Li, and Z. Liu, *Formation of Bilayer Bernal Graphene: Layer-by-Layer Epitaxy via Chemical Vapor Deposition*, Nano Letters **11**, 1106–1110 (2011).

[66] V. I. Artyukhov, Y. Hao, R. S. Ruoff, and B. I. Yakobson, *Breaking of Symmetry in Graphene Growth on Metal Substrates*, Physical Review Letters **114**, 115502 (2015).

[67] D. Eom, D. Prezzi, et al., *Structure and electronic properties of graphene nanoislands on Co(0001).*, Nano letters **9**, 2844–8 (2009).

[68] D. Prezzi, D. Eom, et al., *Edge structures for nanoscale graphene Islands on Co(0001) surfaces*, ACS Nano **8**, 5765–5773 (2014).

[69] Z. Luo, S. Kim, N. Kawamoto, A. M. Rappe, and a. T. C. Johnson, *Growth mechanism of hexagonal-shape graphene flakes with zigzag edges*, ACS Nano **5**, 9154–9160 (2011).

[70] Q. Yu, L. a. Jauregui, et al., *Control and characterization of individual grains and grain boundaries in graphene grown by chemical vapour deposition.*, Nature materials **10**, 443–449 (2011).

[71] B. Wu, D. Geng, et al., *Equiangular hexagon-shape-controlled synthesis of graphene on copper surface*, Advanced Materials **23**, 3522–3525 (2011).

[72] X. Chen, S. Liu, et al., *Growth of triangle-shape graphene on Cu(111) surface*, Applied Physics Letters **100**, 98–101 (2012).

[73] L. Gao, W. Ren, et al., *Repeated growth and bubbling transfer of graphene with millimetre-size single-crystal grains using platinum*, Nature Communications **3**, 699 (2012).

[74] S.-H. Phark, J. Borme, et al., *Scanning tunneling spectroscopy of epitaxial graphene nanoisland on Ir(111).*, Nanoscale research letters **7**, 255 (2012).

[75] M. Olle, G. Ceballos, D. Serrate, and P. Gambardella, *Yield and shape selection of graphene nanoislands grown on Ni(111).*, Nano letters **12**, 4431–6 (2012).

[76] A. Garcia-Lekue, T. Balashov, et al., *Spin-Dependent Electron Scattering at Graphene Edges on Ni(111)*, Physical Review Letters **112**, 066802 (2014).

[77] V. Karpan, G. Giovannetti, et al., *Graphite and Graphene as Perfect Spin Filters*, Physical Review Letters **99**, 176602 (2007).

[78] M. Dresselhaus and G. Dresselhaus, *Intercalation compounds of graphite*, Advances in Physics **30**, 139–326 (1981).

[79] G. Giovannetti, P. Khomyakov, et al., *Doping Graphene with Metal Contacts*, Physical Review Letters **101**, 026803 (2008).

[80] C. Busse, P. Lazić, et al., *Graphene on Ir(111): Physisorption with Chemical Modulation*, Physical Review Letters **107**, 036101 (2011).

[81] P. A. Khomyakov, G. Giovannetti, et al., *First-principles study of the interaction and charge transfer between graphene and metals*, Physical Review B **79**, 195425 (2009).

[82] P. W. Sutter, J.-I. Flege, and E. A. Sutter, *Epitaxial graphene on ruthenium.*, Nature materials **7**, 406–11 (2008).

[83] A. Shikin, G. Prudnikova, V. Adamchuk, F. Moresco, and K. H. Rieder, *Surface intercalation of gold underneath a graphite monolayer on Ni(111) studied by angle-resolved photoemission and high-resolution electron-energy-loss spectroscopy*, Physical Review B **62**, 13202–13208 (2000).

[84] A. Varykhalov, J. Sánchez-Barriga, et al., *Electronic and Magnetic Properties of Quasifree-standing Graphene on Ni*, Physical Review Letters **101**, 157601 (2008).

[85] D. Farías, A. M. Shikin, K.-H. Rieder, and Y. S. Dedkov, *Synthesis of a weakly bonded graphite monolayer on Ni(111) by intercalation of silver*, Journal of Physics: Condensed Matter **11**, 8453–8458 (1999).

[86] A. M. Shikin, V. K. Adamchuk, and K. .-.-H. Rieder, *Formation of quasi-free graphene on the Ni(111) surface with intercalated Cu, Ag, and Au layers*, Physics of the Solid State **51**, 2390–2400 (2009).

[87] I. Gierz, T. Suzuki, et al., *Electronic decoupling of an epitaxial graphene monolayer by gold intercalation*, Physical Review B **81**, 235408 (2010).

[88] M. Papagno, P. Moras, et al., *Hybridization of graphene and a Ag monolayer supported on Re(0001)*, Physical Review B **88**, 235430 (2013).

[89] E. N. Voloshina, A. Generalov, et al., *Structural and electronic properties of the graphene/Al/Ni(111) intercalation system*, New Journal of Physics **13**, 113028 (2011).

[90] Y. Dedkov, A. Shikin, et al., *Intercalation of copper underneath a monolayer of graphite on Ni(111)*, Physical Review B **64**, 035405 (2001).

[91] Y. S. Park, J. H. Park, et al., *Quasi-free-standing graphene monolayer on a Ni crystal through spontaneous Na intercalation*, Physical Review X **4** (2014) 10.1103/PhysRevX.4.031016.

[92] M. Alattas and U. Schwingenschlögl, *Quasi-freestanding graphene on Ni(111) by Cs intercalation*, Scientific Reports **6**, 26753 (2016).

[93] N. I. Verbitskiy, A. V. Fedorov, et al., *Atomically precise semiconductor—graphene and hBN interfaces by Ge intercalation*, Scientific Reports **5**, 17700 (2015).

[94] E. Grånäs, J. Knudsen, et al., *Oxygen intercalation under graphene on Ir(111): energetics, kinetics, and the role of graphene edges.*, ACS Nano **6**, 9951–63 (2012).

[95] S. Ulstrup, M. Andersen, et al., *Sequential oxygen and alkali intercalation of epitaxial graphene on Ir(111): enhanced many-body effects and formation of pn -interfaces*, 2D Materials **1**, 025002 (2014).

[96] U. A. Schröder, M. Petrović, et al., *Core level shifts of intercalated graphene*, 2D Materials **4**, 015013 (2016).

[97] N. Ligato, L. Caputi, and A. Cupolillo, *Oxygen intercalation at the graphene/Ni(111) interface: Evidences of non-metal islands underneath graphene layer*, Carbon **100**, 258–264 (2016).

[98] C. Riedl, C. Coletti, T. Iwasaki, A. A. Zakharov, and U. Starke, *Quasi-Free-Standing Epitaxial Graphene on SiC Obtained by Hydrogen Intercalation*, Physical Review Letters **103**, 246804 (2009).

[99] B. Borca, F. Calleja, J. J. Hinarejos, A. L. Vzquez De Parga, and R. Miranda, *Reactivity of periodically rippled graphene grown on Ru(0001)*, Journal of Physics Condensed Matter **21** (2009) 10.1088/0953-8984/21/13/134002.

[100] B. Borca, S. Barja, et al., *Potential energy landscape for hot electrons in periodically nanostructured graphene*, Physical Review Letters **105**, 1–4 (2010).

[101] D. Pacilé, P. Leicht, et al., *Artificially lattice-mismatched graphene/metal interface: Graphene/Ni/Ir(111)*, Physical Review B **87**, 1–6 (2013).

[102] F. Calleja, H. Ochoa, et al., *Spatial variation of a giant spin–orbit effect induces electron confinement in graphene on Pb islands*, Nature Physics **11**, 43–47 (2015).

[103] D. Marchenko, A. Varykhalov, et al., *Giant Rashba splitting in graphene due to hybridization with gold*, Nature communications **3**, 1232 (2012).

[104] Y. Li, P. Tang, et al., *Topological insulators in transition-metal intercalated graphene: The role of d electrons in significantly increasing the spin-orbit gap*, Physical Review B **87**, 245127 (2013).

[105] R. Decker, J. Brede, et al., *Atomic-scale magnetism of cobalt-intercalated graphene*, Physical Review B **87**, 041403 (2013).

[106] S. Schumacher, F. Huttmann, et al., *Europium underneath graphene on Ir(111): Intercalation mechanism, magnetism, and band structure*, Physical Review B **90**, 235437 (2014).

[107] W. Q. Liu, W. Y. Wang, et al., *Atomic-Scale Interfacial Magnetism in Fe/Graphene Heterojunction.*, Scientific reports **5**, 11911 (2015).

[108] A. G. Rybkin, A. A. Rybkina, et al., *Magneto-Spin–Orbit Graphene: Interplay between Exchange and Spin–Orbit Couplings*, Nano Letters **18**, 1564–1574 (2018).

[109] Y. S. Dedkov, M. Fonin, U. Rüdiger, and C. Laubschat, *Graphene-protected iron layer on Ni(111)*, Applied Physics Letters **93**, 022509 (2008).

[110] W. Jolie, F. Craes, et al., *Confinement of Dirac electrons in graphene quantum dots*, Physical Review B **89**, 1–6 (2014).

[111] M. Morgenstern, N. Freitag, A. Vaid, M. Pratzer, and M. Liebmann, *Graphene quantum dots: Wave function mapping by scanning tunneling spectroscopy and transport spectroscopy of quantum dots prepared by local anodic oxidation*, Physica Status Solidi - Rapid Research Letters **10**, 24–38 (2016).

[112] P. Leicht, L. Zielke, et al., *In situ fabrication of quasi-free-standing epitaxial graphene nanoflakes on gold.*, ACS Nano **8**, 3735–42 (2014).

[113] J. Zhao, H. Liu, et al., *Rise of silicene: A competitive 2D material*, Progress in Materials Science **83**, 24–151 (2016).

[114] S. Beniwal, J. Hooper, et al., *Graphene-like Boron-Carbon-Nitrogen Monolayers*, ACS Nano **11**, 2486–2493 (2017).

[115] C. R. Dean, A. F. Young, et al., *Boron nitride substrates for high-quality graphene electronics*, Nature Nanotechnology **5**, 722–726 (2010).

[116] W. J. Yu, Z. Li, et al., *Vertically stacked multi-heterostructures of layered materials for logic transistors and complementary inverters*, Nature Materials **12**, 246–252 (2013).

[117] K. Roy, M. Padmanabhan, et al., *Graphene–MoS2 hybrid structures for multifunctional photoresponsive memory devices*, Nature Nanotechnology **8**, 826–830 (2013).

[118] L. Britnell, R. M. Ribeiro, et al., *Strong Light-Matter Interactions in Heterostructures of Atomically Thin Films*, Science **340**, 1311–1314 (2013).

[119] C. Huang, S. Wu, et al., *Lateral heterojunctions within monolayer MoSe2-WSe2 semiconductors.*, Nature materials **13**, 1096–101 (2014).

[120] X. Duan, C. Wang, et al., *Lateral epitaxial growth of two-dimensional layered semiconductor heterojunctions.*, Nature nanotechnology **9**, 1024–30 (2014).

[121] M.-Y. Li, Y. Shi, et al., *Epitaxial growth of a monolayer WSe2-MoS2 lateral p-n junction with an atomically sharp interface*, Science **349**, 524–528 (2015).

[122] S. Yang, C. Jiang, and S.-h. Wei, *Gas sensing in 2D materials*, Applied Physics Reviews **4**, 021304 (2017).

[123] X. Ling, Y. Lin, et al., *Parallel Stitching of 2D Materials.*, Advanced materials (Deerfield Beach, Fla.) **28**, 2322–9 (2016).

[124] E. Hernández, C. Goze, P. Bernier, and A. Rubio, *Elastic Properties of C and BxCyNz Composite Nanotubes*, Physical Review Letters **80**, 4502–4505 (1998).

[125] Y. Shi, C. Hamsen, et al., *Synthesis of few-layer hexagonal boron nitride thin film by chemical vapor deposition*, Nano Letters **10**, 4134–4139 (2010).

[126] A. Catellani, M. Posternak, A. Baldereschi, and A. J. Freeman, *Bulk and surface electronic structure of hexagonal boron nitride*, Physical Review B **36**, 6105–6111 (1987).

[127] K. Watanabe, T. Taniguchi, and H. Kanda, *Direct-bandgap properties and evidence for ultraviolet lasing of hexagonal boron nitride single crystal*, Nature Materials **3**, 404–409 (2004).

[128] C.-H. Park and S. G. Louie, *Energy gaps and stark effect in boron nitride nanoribbons.*, Nano letters **8**, 2200–3 (2008).

[129] V. Barone and J. E. Peralta, *Magnetic boron nitride nanoribbons with tunable electronic properties*, Nano Letters **8**, 2210–2214 (2008).

[130] F. Zheng, G. Zhou, et al., *Half metallicity along the edge of zigzag boron nitride nanoribbons*, Physical Review B **78**, 1–5 (2008).

[131] S. Okada, M. Igami, K. Nakada, and A. Oshiyama, *Border states in heterosheets with hexagonal symmetry*, Physical Review B **62**, 9896–9899 (2000).

[132] S. Dutta, A. K. Manna, and S. K. Pati, *Intrinsic Half-Metallicity in Modified Graphene Nanoribbons*, Physical Review Letters **102**, 6–9 (2009).

[133] Y. Ding, Y. Wang, and J. Ni, *Electronic properties of graphene nanoribbons embedded in boron nitride sheets*, Applied Physics Letters **95** (2009) 10.1063/1.3234374.

[134] S. Bhowmick, A. K. Singh, and B. I. Yakobson, *Quantum dots and nanoroads of graphene embedded in hexagonal boron nitride*, Journal of Physical Chemistry C **115**, 9889–9893 (2011).

[135] J. M. Pruneda, *Origin of half-semimetallicity induced at interfaces of C-BN heterostructures*, Physical Review B **81**, 8–11 (2010).

[136] L. Ci, L. Song, et al., *Atomic layers of hybridized boron nitride and graphene domains.*, Nature materials **9**, 430–435 (2010).

[137] M. Kan, J. Zhou, Q. Wang, Q. Sun, and P. Jena, *Tuning the band gap and magnetic properties of BN sheets impregnated with graphene flakes*, Physical Review B **84**, 1–5 (2011).

[138] R. Zhao, J. Wang, M. Yang, Z. Liu, and Z. Liu, *BN-embedded graphene with a ubiquitous gap opening*, Journal of Physical Chemistry C **116**, 21098–21103 (2012).

[139] Y. Zhou, Z. Wang, P. Yang, and F. Gao, *Novel Electronic and Magnetic Properties of Graphene Nanoflakes in a Boron Nitride Layer*, The Journal of Physical Chemistry C **116**, 7581–7586 (2012).

[140] J. Jung, Z. Qiao, Q. Niu, and A. H. MacDonald, *Transport properties of graphene nanoroads in boron nitride sheets*, Nano Letters **12**, 2936–2940 (2012).

[141] Y. Gong, G. Shi, et al., *Direct chemical conversion of graphene to boron- and nitrogen- and carbon-containing atomic layers.*, en, Nature communications **5**, 3193 (2014).

[142] M. Kan, Y. Li, and Q. Sun, *Recent advances in hybrid graphene-BN planar structures*, Wiley Interdisciplinary Reviews: Computational Molecular Science **6**, 65–82 (2016).

[143] W.-Q. Han, H.-G. Yu, and Z. Liu, *Convert graphene sheets to boron nitride and boron nitride–carbon sheets via a carbon-substitution reaction*, Applied Physics Letters **98**, 203112 (2011).

[144] X. Wei, M. S. Wang, Y. Bando, and D. Golberg, *Electron-beam-induced substitutional carbon doping of boron nitride nanosheets, nanoribbons, and nanotubes*, ACS Nano **5**, 2916–2922 (2011).

[145] M. P. Levendorf, C.-J. Kim, et al., *Graphene and boron nitride lateral heterostructures for atomically thin circuitry*, Nature **488**, 627–632 (2012).

[146] Z. Liu, L. Ma, et al., *In-plane heterostructures of graphene and hexagonal boron nitride with controlled domain sizes.*, Nature nanotechnology **8**, 119–24 (2013).

[147] Y. Gao, Y. Zhang, et al., *Toward single-layer uniform hexagonal boron nitride-graphene patchworks with zigzag linking edges*, Nano Letters **13**, 3439–3443 (2013).

[148] G. H. Han, J. a. Rodríguez-Manzo, et al., *Continuous growth of hexagonal graphene and boron nitride in-plane heterostructures by atmospheric pressure chemical vapor deposition*, ACS Nano **7**, 10129–10138 (2013).

[149] L. Liu, J. Park, et al., *Heteroepitaxial Growth of Two-Dimensional Hexagonal Boron Nitride Templated by Graphene Edges*, Science **343**, 163–167 (2014).

[150] M. Liu, Y. Li, et al., *Quasi-Freestanding Monolayer Heterostructure of Graphene and Hexagonal Boron Nitride on Ir(111) with a Zigzag Boundary*, Nano Letters **14**, 6342–6347 (2014).

[151] P. Sutter, R. Cortes, J. Lahiri, and E. Sutter, *Interface formation in monolayer graphene-boron nitride heterostructures*, Supporting information **12**, 4869–4874 (2012).

[152] R. Drost, S. Kezilebieke, et al., *Synthesis of Extended Atomically Perfect Zigzag Graphene - Boron Nitride Interfaces*, Scientific Reports **5**, 16741 (2015).

[153] R. Drost, A. Uppstu, et al., *Electronic states at the graphene - hexagonal boron nitride zigzag interface.*, Nano letters **9**, 5128–5132 (2014).

[154] M. Ollé, "Graphene nanoislands on Ni(111)", Doctoral Dissertation (Autonomous University of Barcelona (UAB), 2013), p. 135.

[155] Z. Fu and Y. An, *The growth modes of graphene in the initial stage of a chemical vapor-deposition process*, RSC Adv. **6**, 91157–91162 (2016).

[156] X. Li, W. Cai, L. Colombo, and R. S. Ruoff, *Evolution of graphene growth on Ni and Cu by carbon isotope labeling.*, Nano letters **9**, 4268–72 (2009).

[157] K. Wandelt, C. T. Campbell, J. Wintterlin, and M.-L. Bocquet, *Graphene on metal surfaces*, Surface Science **603**, 1841–1852 (2009).

[158] L. Baraton, Z. B. He, et al., *On the mechanisms of precipitation of graphene on nickel thin films*, en, EPL (Europhysics Letters) **96**, 46003 (2011).

[159] L. L. Patera, C. Africh, et al., *In situ observations of the atomistic mechanisms of Ni catalyzed low temperature graphene growth*, ACS Nano **7**, 7901–7912 (2013).

[160] C. Klink, I. Stensgaard, F. Besenbacher, and E. Lægsgaard, *An STM study of carbon-induced structures on Ni(111): evidence for a carbidic-phase clock reconstruction*, Surface Science **342**, 250–260 (1995).

[161] P. Jacobson, B. Stöger, et al., *Nickel carbide as a source of grain rotation in epitaxial graphene.*, ACS Nano **6**, 3564–72 (2012).

[162] C. Africh, C. Cepek, et al., *Switchable graphene-substrate coupling through formation/dissolution of an intercalated Ni-carbide layer*, Scientific Reports **6**, 19734 (2016).

[163] A. Reina, X. Jia, et al., *Large area, few-layer graphene films on arbitrary substrates by chemical vapor deposition.*, Nano letters **9**, 30–5 (2009).

[164] G. Mamantov and J. Margrave, *Decomposition of liquid borazine*, Journal of inorganic and nuclear chemistry **1337**, 348–351 (1961).

[165] W. Auwarter, "One Monolayer of Hexagonal Boron Nitride on Ni (111): an Atomically Sharp Interface", PhD thesis (2003), pp. 1–118.

[166] S. Liu, A. C. Van Duin, D. M. Van Duin, B. Liu, and J. H. Edgar, *Atomistic Insights into Nucleation and Formation of Hexagonal Boron Nitride on Nickel from First-Principles-Based Reactive Molecular Dynamics Simulations*, ACS Nano **11**, 3585–3596 (2017).

[167] V. Nehasil, K. Mašek, O. Moreau, and V. Matolín, *Miniature Electron Bombardment Evaporation Source: Evaporation Rate Measurement*, Czechoslovak Journal of Physics **47**, 261–268 (1997).

[168] V. N. Popok, I. Barke, E. E. Campbell, and K.-H. Meiwes-Broer, *Cluster–surface interaction: From soft landing to implantation*, Surface Science Reports **66**, 347–377 (2011).

[169] G. Binnig and H. Rohrer, *Scanning tunneling microscopy*, Surface Science **126**, 236–244 (1982).

[170] G. Binnig, H. Rohrer, C. Gerber, and E. Weibel, *Tunneling through a controllable vacuum gap*, Applied Physics Letters **40**, 178–180 (1982).

[171] G. Binnig and H. Rohrer, *Scanning Tunneling Microscopy*, Helvetica Physica Acta **55**, 726–735 (1982).

[172] G. Binnig, H. Rohrer, C. Gerber, and E. Weibel, *Surface Studies by Scanning Tunneling Microscopy*, Physical Review Letters **49**, 57–61 (1982).

[173] R. D. Young, *Surface microtopography*, Physics Today **24**, 42–49 (1971).

[174] J. Kim, S. Qin, et al., *Quantum size effects on the work function of metallic thin film nanostructures*, Proceedings of the National Academy of Sciences **107**, 12761–12765 (2010).

[175] J. Tersoff and D. Hamann, *Theory and application for the scanning tunneling microscope*, Physical review letters **50**, 1998 (1983).

[176] J. Tersoff and D. R. Hamann, *Theory of the scanning tunneling microscope*, Physical Review B **31**, 805–813 (1985).

[177] H. Eckardt, L. Fritsche, and J. Noffke, *Self-consistent relativistic band structure of the noble metals*, Journal of Physics F: Metal Physics **14**, 97 (1984).

[178] F. Esch, C. Dri, et al., *Publisher's Note: "The FAST module: An add-on unit for driving commercial scanning probe microscopes at video rate and beyond" [Rev. Sci. Instrum. 82, 053702 (2011)]*, Review of Scientific Instruments **82**, 089902 (2011).

[179] L. L. Patera, F. Bianchini, et al., *Real-time imaging of adatom-promoted graphene growth on nickel*, Science **359**, 1243–1246 (2018).

[180] R. S. Becker, J. A. Golovchenko, and B. S. Swartzentruber, *Electron Interferometry at Crystal Surfaces*, Physical Review Letters **55**, 987–990 (1985).

[181] C. J. Chen, *Introduction to Scanning Tunneling Microscopy* (1993), p. 412.

[182] R. J. Hamers, R. M. Tromp, and J. E. Demuth, *Surface electronic structure of Si (111)-(7x7) resolved in real space*, Physical Review Letters **56**, 1972–1975 (1986).

[183] M. F. Crommie, C. P. Lutz, and D. M. Eigler, *Imaging standing waves in a two-dimensional electron gas*, en, Nature **363**, 524–527 (1993).

[184] S. LaShell, B. McDougall, and E. Jensen, *Spin Splitting of an Au(111) Surface State Band Observed with Angle Resolved Photoelectron Spectroscopy*, Oct. 1996.

[185] P. Mallet, I. Brihuega, et al., *Role of pseudospin in quasiparticle interferences in epitaxial graphene probed by high-resolution scanning tunneling microscopy*, Physical Review B **86**, 045444 (2012).

[186] I. Brihuega, P. Mallet, et al., *Quasiparticle chirality in epitaxial graphene probed at the nanometer scale*, Physical Review Letters **101**, 1–4 (2008).

[187] P. Leicht, J. Tesch, et al., *Rashba splitting of graphene-covered Au(111) revealed by quasiparticle interference mapping*, Physical Review B **90**, 1–5 (2014).

[188] J. Lahiri, T. Miller, L. Adamska, I. I. Oleynik, and M. Batzill, *Graphene growth on Ni(111) by transformation of a surface carbide.*, Nano letters **11**, 518–22 (2011).

[189] J. Lahiri, T. S Miller, et al., *Graphene growth and stability at nickel surfaces*, en, New Journal of Physics **13**, 025001 (2011).

[190] A. Grüneis, K. Kummer, and D. V. Vyalikh, *Dynamics of graphene growth on a metal surface: a time-dependent photoemission study*, New Journal of Physics **11**, 073050 (2009).

[191] R. Addou, A. Dahal, P. Sutter, and M. Batzill, *Monolayer graphene growth on Ni(111) by low temperature chemical vapor deposition*, Applied Physics Letters **100**, 021601 (2012).

[192] J. Shelton, H. Patil, and J. Blakely, *Equilibrium segregation of carbon to a nickel (111) surface: A surface phase transition*, Surface Science **43**, 493–520 (1974).

[193] J. M. Blakely, J. S. Kim, and H. C. Potter, *Segregation of Carbon to the (100) Surface of Nickel*, Journal of Applied Physics **41**, 2693 (1970).

[194] Z. Chen, W. Ren, et al., *Bulk growth of mono- to few-layer graphene on nickel particles by chemical vapor deposition from methane*, Carbon **48**, 3543–3550 (2010).

[195] S. J. Chae, F. Güneş, et al., *Synthesis of Large-Area Graphene Layers on Poly-Nickel Substrate by Chemical Vapor Deposition: Wrinkle Formation*, Advanced Materials **21**, 2328–2333 (2009).

[196] H. J. Park, J. Meyer, S. Roth, and V. Skákalová, *Growth and properties of few-layer graphene prepared by chemical vapor deposition*, Carbon **48**, 1088–1094 (2010).

[197] Z.-Y. Juang, C.-Y. Wu, et al., *Graphene synthesis by chemical vapor deposition and transfer by a roll-to-roll process*, Carbon **48**, 3169–3174 (2010).

[198] A. Reina, X. Jia, et al., *Large Area, Few-Layer Graphene Films on Arbitrary Substrates by Chemical Vapor Deposition*, Nano Letters **9**, 30–35 (2009).

[199] J. Song, M. Bernien, C.-B. Wu, and W. Kuch, *Tuning the Electronic Properties of Rotated Graphene on Ni(111) by Nickel Carbide Intercalation*, The Journal of Physical Chemistry C **120**, 1546–1555 (2016).

[200] A. Dahal, R. Addou, P. Sutter, and M. Batzill, *Graphene monolayer rotation on Ni(111) facilitates bilayer graphene growth*, Applied Physics Letters **100**, 241602 (2012).

[201] R. Rameshan, V. Vonk, et al., *Role of precursor carbides for graphene growth on Ni(111)*, Scientific Reports **8**, 1–13 (2018).

[202] A. Garcia-Lekue, M. Ollé, et al., *Substrate-Induced Stabilization and Reconstruction of Zigzag Edges in Graphene Nanoislands on Ni(111)*, The Journal of Physical Chemistry C **119**, 1–19 (2015).

[203] S. Wang, L. Talirz, et al., *Giant edge state splitting at atomically precise graphene zigzag edges*, Nature Communications **7**, 11507 (2016).

[204] M. Eizenberg and J. M. Blakely, *Carbon interaction with nickel surfaces: Monolayer formation and structural stability*, The Journal of Chemical Physics **71**, 3467 (1979).

[205] S. H. Phark, J. Borme, et al., *Atomic structure and spectroscopy of graphene edges on Ir(111)*, Physical Review B **86**, 1–4 (2012).

[206] B. Wang, M. König, et al., *Ethene to Graphene: Surface Catalyzed Chemical Pathways, Intermediates, and Assembly*, The Journal of Physical Chemistry C **121**, 9413–9423 (2017).

[207] J. Lahiri, Y. Lin, P. Bozkurt, I. I. Oleynik, and M. Batzill, *An extended defect in graphene as a metallic wire.*, Nature nanotechnology **5**, 326–9 (2010).

[208] Y. Gamo, A. Nagashima, M. Wakabayashi, M. Terai, and C. Oshima, *Atomic structure of monolayer graphite formed on Ni(111)*, Surface Science **374**, 61–64 (1997).

[209] W. Zhao, S. M. Kozlov, et al., *Graphene on Ni(111): Coexistence of Different Surface Structures*, EN, The Journal of Physical Chemistry Letters **2**, 759–764 (2011).

[210] M. Fuentes-Cabrera, M. I. Baskes, A. V. Melechko, and M. L. Simpson, *Bridge structure for the graphene/Ni(111) system: A first principles study*, Physical Review B **77**, 1–5 (2008).

[211] F. Bianchini, L. L. Patera, M. Peressi, C. Africh, and G. Comelli, *Atomic scale identification of coexisting graphene structures on Ni(111)*, Journal of Physical Chemistry Letters **5**, 467–473 (2014).

[212] W. B. Zhang, C. Chen, and P. Y. Tang, *First-principles study for stability and binding mechanism of graphene/Ni(111) interface: Role of vdW interaction*, Journal of Chemical Physics **141** (2014) 10.1063/1.4890728.

[213] L. V. Dzemiantsova, M. Karolak, et al., *Multiscale magnetic study of Ni(111) and graphene on Ni(111)*, Physical Review B **84**, 1–11 (2011).

[214] L. L. Patera, F. Bianchini, et al., *Temperature-Driven Changes of the Graphene Edge Structure on Ni(111): Substrate vs Hydrogen Passivation*, Nano Letters **15**, 56–62 (2015).

[215] D. Van Tuan, J. Kotakoski, et al., *Scaling properties of charge transport in polycrystalline graphene*, Nano Letters **13**, 1730–1735 (2013).

[216] A. Luican-Mayer, J. E. Barrios-Vargas, et al., *Localized electronic states at grain boundaries on the surface of graphene and graphite*, 2D Materials **3**, 031005 (2016).

[217] H. I. Rasool, C. Ophus, W. S. Klug, A. Zettl, and J. K. Gimzewski, *Measurement of the intrinsic strength of crystalline and polycrystalline graphene*, Nature Communications **4**, 2811 (2013).

[218] Y. Wei, J. Wu, et al., *The nature of strength enhancement and weakening by pentagon–heptagon defects in graphene*, Nature Materials **11**, 759–763 (2012).

[219] P. Jacobson, B. Stöger, et al., *Disorder and Defect Healing in Graphene on Ni(111)*, The Journal of Physical Chemistry Letters **3**, 136–139 (2012).

[220] O. V. Yazyev and S. G. Louie, *Topological defects in graphene: Dislocations and grain boundaries*, Physical Review B **81**, 195420 (2010).

[221] O. V. Yazyev and S. G. Louie, *Electronic transport in polycrystalline graphene.*, Nature Materials **9**, 806–9 (2010).

[222] Y. Liu and B. I. Yakobson, *Cones, pringles, and grain boundary landscapes in graphene topology*, Nano Letters **10**, 2178–2183 (2010).

[223] T. H. Liu, G. Gajewski, C. W. Pao, and C. C. Chang, *Structure, energy, and structural transformations of graphene grain boundaries from atomistic simulations*, Carbon **49**, 2306–2317 (2011).

[224] Z.-L. Li, Z.-M. Li, et al., *What are grain boundary structures in graphene?*, Nanoscale **6**, 4309–4315 (2014).

[225] P. Y. Huang, C. S. Ruiz-Vargas, et al., *Grains and grain boundaries in single-layer graphene atomic patchwork quilts*, Nature **469**, 389–392 (2011).

[226] A. Ayuela, W. Jaskólski, H. Santos, and L. Chico, *Electronic properties of graphene grain boundaries*, New Journal of Physics **16**, 083018 (2014).

[227] E. Cockayne, G. M. Rutter, et al., *Grain boundary loops in graphene*, Physical Review B **83**, 1–7 (2011).

[228] J. Chen, T. Shi, et al., *Self healing of defected graphene*, Applied Physics Letters **102**, 103107 (2013).

[229] Z. J. Qi, C. Daniels, et al., *Electronic Transport of Recrystallized Freestanding Graphene Nanoribbons*, ACS Nano **9**, 3510–3520 (2015).

[230] E. A. Soares, G. J. P. Abreu, et al., *Graphene-protected Fe layers atop Ni(111): Evidence for strong Fe-graphene interaction and structural bistability*, Physical Review B **88**, 165410 (2013).

[231] Z. Wang, C. Tang, R. Sachs, Y. Barlas, and J. Shi, *Proximity-Induced Ferromagnetism in Graphene Revealed by the Anomalous Hall Effect*, Physical Review Letters **114**, 016603 (2015).

[232] M. Kralj, *Graphene spintronics: Intercalated boosters*, Nature Physics **11**, 11–12 (2014).

[233] D. Marchenko, A. Varykhalov, A. Rybkin, a. M. Shikin, and O. Rader, *Atmospheric stability and doping protection of noble-metal intercalated graphene on Ni(111)*, Applied Physics Letters **98**, 122111 (2011).

[234] A. Nagashima, N. Tejima, and C. Oshima, *Electronic states of the pristine and alkali-metal-intercalated monolayer graphite/Ni(111) systems*, Physical Review B **50**, 17487–17495 (1994).

[235] A. Grüneis and D. V. Vyalikh, *Tunable hybridization between electronic states of graphene and a metal surface*, Physical Review B **77**, 1–4 (2008).

[236] W.-B. Zhang and C. Chen, *Tuning metal–graphene interaction by non-metal intercalation: a case study of the graphene/oxygen/Ni (1 1 1) system*, Journal of Physics D: Applied Physics **48**, 015308 (2015).

[237] D. Haberer, D. V. Vyalikh, et al., *Tunable band gap in hydrogenated quasi-free-standing graphene.*, Nano letters **10**, 3360–6 (2010).

[238] M. H. Kang, S. C. Jung, and J. W. Park, *Density functional study of the Au-intercalated graphene/Ni(111) surface*, Physical Review B **82**, 085409 (2010).

[239] A. A. Rybkina, A. G. Rybkin, et al., *The graphene/Au/Ni interface and its application in the construction of a graphene spin filter.*, en, Nanotechnology **24**, 295201 (2013).

[240] M. Krivenkov, E. Golias, et al., *Nanostructural origin of giant Rashba effect in intercalated graphene*, 2D Materials **4**, 035010 (2017).

[241] Z. Qiao, S. a. Yang, et al., *Quantum anomalous Hall effect in graphene from Rashba and exchange effects*, Physical Review B **82**, 161414 (2010).

[242] J. Tesch, P. Leicht, et al., *Structural and electronic properties of graphene nanoflakes on Au(111) and Ag(111)*, Scientific Reports **6**, 23439 (2016).

[243] D. Nobis, M. Potenz, D. Niesner, and T. Fauster, *Image-potential states of graphene on noble-metal surfaces*, Physical Review B **88**, 195435 (2013).

[244] a. Herz, D. Wang, T. Kups, and P. Schaaf, *Solid-state dewetting of Au/Ni bilayers: The effect of alloying on morphology evolution*, Journal of Applied Physics **116**, 044307 (2014).

[245] J. Jacobsen, L. Nielsen, et al., *Atomic-Scale Determination of Misfit Dislocation Loops at Metal-Metal Interfaces*, Physical Review Letters **75**, 489–492 (1995).

[246] J. Barth, H. Brune, G. Ertl, and R. Behm, *Scanning tunneling microscopy observations on the reconstructed Au(111) surface: Atomic structure, long-range superstructure, rotational domains, and surface defects*, Physical Review B **42**, 9307–9318 (1990).

[247] S. Kawai, A. Benassi, et al., *Superlubricity of graphene nanoribbons on gold surfaces*, Science **351**, 957–961 (2016).

[248] M. Petrović, I. Šrut Rakić, et al., *The mechanism of caesium intercalation of graphene*, Nature Communications **4**, 2772 (2013).

[249] E. Starodub, N. C. Bartelt, and K. F. McCarty, *Oxidation of graphene on metals*, Journal of Physical Chemistry C **114**, 5134–5140 (2010).

[250] C. Xia, S. Watcharinyanon, et al., *Si intercalation/deintercalation of graphene on 6H-SiC(0001)*, Physical Review B **85**, 045418 (2012).

[251] L. Huang, Y. Pan, et al., *Intercalation of metal islands and films at the interface of epitaxially grown graphene and Ru(0001) surfaces*, Applied Physics Letters **99**, 163107 (2011).

[252] M. Sicot, P. Leicht, et al., *Size-selected epitaxial nanoislands underneath graphene moiré on Rh(111).*, ACS Nano **6**, 151–8 (2012).

[253] N. Levy, S. A. Burke, et al., *Strain-induced pseudo-magnetic fields greater than 300 tesla in graphene nanobubbles.*, Science (New York, N.Y.) **329**, 544–7 (2010).

[254] L. P. Nielsen, F. Besenbacher, et al., *Initial growth of Au on Ni(110): Surface alloying of immiscible metals.*, Physical Review Letters **71**, 754–757 (1993).

[255] I. Carlomagno, J. Drnec, et al., *Co film stretching induced by lattice mismatch and annealing: The role of Graphene*, Applied Surface Science **432**, 22–26 (2018).

[256] J. Drnec, S. Vlaic, et al., *Surface alloying upon Co intercalation between graphene and Ir(1 1 1)*, Carbon **94**, 554–559 (2015).

[257] P. M. Echenique and J. B. Pendry, *The existence and detection of Rydberg states at surfaces*, Journal of Physics C: Solid State Physics **11**, 2065–2075 (1978).

[258] G. Binnig, K. Frank, et al., *Tunneling Spectroscopy and Inverse Photoemission: Image and Field States*, Physical Review Letters **55**, 991–994 (1985).

[259] A. Hanuschkin, D. Wortmann, and S. Blügel, *Image potential and field states at Ag(100) and Fe(110) surfaces*, Physical Review B - Condensed Matter and Materials Physics **76**, 1–6 (2007).

[260] J. I. Pascual, C. Corriol, et al., *Role of the electric field in surface electron dynamics above the vacuum level*, Physical Review B - Condensed Matter and Materials Physics **75**, 1–7 (2007).

[261] A. Garcia-Lekue, D. Sánchez-Portal, A. Arnau, and L. W. Wang, *Plane-wave based electron tunneling through field emission resonance states*, Physical Review B - Condensed Matter and Materials Physics **88**, 1–9 (2013).

[262] S. Stepanow, A. Mugarza, et al., *Localization, splitting, and mixing of field emission resonances induced by alkali metal clusters on Cu(100)*, Physical Review B **83**, 115101 (2011).

[263] D. Niesner and T. Fauster, *Image-potential states and work function of graphene*, Journal of Physics: Condensed Matter **26**, 393001 (2014).

[264] S. Bose, V. M. Silkin, et al., *Image potential states as a quantum probe of graphene interfaces*, en, New Journal of Physics **12**, 023028 (2010).

[265] F. Craes, S. Runte, et al., *Mapping image potential states on graphene quantum dots*, Physical Review Letters **111**, 1–5 (2013).

[266] C. L. Lin, S. M. Lu, et al., *Manifestation of work function difference in high order gundlach oscillation*, Physical Review Letters **99**, 1–4 (2007).

[267] T. Miller, A. Samsavar, G. E. Franklin, and T. .-.-C. Chiang, *Quantum-Well States in a Metallic System: Ag on Au(111)*, Physical Review Letters **61**, 1404–1407 (1988).

[268] R. Fischer and T. Fauster, *Coupling of image states to quantum-well states for Au on Pd(111)*, Physical Review B **51**, 7112–7115 (1995).

[269] W. Jolie, F. Craes, and C. Busse, *Graphene on weakly interacting metals: Dirac states versus surface states*, Physical Review B **91**, 1–8 (2015).

[270] S. M. Hollen, G. A. Gambrel, et al., *Modification of electronic surface states by graphene islands on Cu(111)*, Physical Review B **91** (2015) 10.1103/PhysRevB.91.195425.

[271] J. Lobo-Checa, T. Okuda, et al., *Hidden surface states on pristine and H-passivated Ni(111): Angle-resolved photoemission and density-functional calculations*, Physical Review B - Condensed Matter and Materials Physics **77**, 1–8 (2008).

[272] A. Krönlein, J. Kemmer, P. J. Hsu, and M. Bode, *Quasiparticle interference scattering of spin-polarized Shockley-like surface state electrons: Ni(111)*, Physical Review B **89**, 1–7 (2014).

[273] K.-F. Braun and K.-H. Rieder, *Ni(111) surface state observed with scanning tunneling microscopy*, Physical Review B **77**, 245429 (2008).

[274] J. Kliewer, R. Berndt, et al., *Dimensionality effects in the lifetime of surface states*, Science **288**, 1399–1402 (2000).

[275] S. D. Kevan and R. H. Gaylord, *High-resolution photoemission study of the electronic structure of the noble-metal (111) surfaces*, Physical Review B **36**, 5809–5818 (1987).

[276] D. Malterre, B. Kierren, et al., *ARPES and STS investigation of Shockley states in thin metallic films and periodic nanostructures*, New Journal of Physics **9**, 391–391 (2007).

[277] P. Avouris, I.-W. Lyo, R. Walkup, and Y. Hasegawa, *Real space imaging of electron scattering phenomena at metal surfaces*, Journal of Vacuum Science & Technology B: Microelectronics and Nanometer Structures **12**, 1447 (1994).

[278] F. Reinert, G. Nicolay, S. Schmidt, D. Ehm, and S. Hüfner, *Direct measurements of the L-gap surface states on the (111) face of noble metals by photoelectron spectroscopy*, Physical Review B **63**, 115415 (2001).

[279] A. Bendounan, Y. Fagot Revurat, et al., *Surface state in epitaxial Ag ultrathin films on Cu()*, Surface Science **496**, L43–L49 (2002).

[280] F. Forster, E. Gergert, et al., *Electronic localization of quantum-well states in Ag/Au(111) metallic heterostructures*, Physical Review B **84**, 075412 (2011).

[281] T. Hsieh and T.-C. Chiang, *Spatial dependence and binding energy shift of surface states for epitaxial overlayers of Au on Ag(111) and Ag on Au(111)*, Surface Science **166**, 554–560 (1986).

[282] A. Bendounan, H. Cercellier, et al., *Modification of Shockley states induced by surface reconstruction in epitaxial Ag films on Cu(111)*, Physical Review B **67**, 1–10 (2003).

[283] A. Mugarza, "Electronic Structure of Low-Dimensional Systems Analyzed by Angle-Resolved Photoemission Spectroscopy", PhD thesis (University of the Basque Country (UPV/EHU), 2002), p. 204.

[284] R. Paniago, R. Matzdorf, G. Meister, and A. Goldmann, *Temperature dependence of Shockley-type surface energy bands on Cu(111), Ag(111) and Au(111)*, Surface Science **336**, 113–122 (1995).

[285] H. González-Herrero, P. Pou, et al., *Graphene Tunable Transparency to Tunneling Electrons: A Direct Tool To Measure the Local Coupling*, ACS Nano **10**, 5131–5144 (2016).

[286] E. H. Lieb, *Two theorems on the Hubbard model*, Physical Review Letters **62**, 1201–1204 (1989).

[287] T. Enoki and K. Takai, *The edge state of nanographene and the magnetism of the edge-state spins*, Solid State Communications **149**, 1144–1150 (2009).

[288] H. Lee, Y. W. Son, N. Park, S. Han, and J. Yu, *Magnetic ordering at the edges of graphitic fragments: Magnetic tail interactions between the edge-localized states*, Physical Review B - Condensed Matter and Materials Physics **72**, 1–8 (2005).

[289] K. Wakabayashi, K.-i. Sasaki, T. Nakanishi, and T. Enoki, *Electronic states of graphene nanoribbons and analytical solutions*, Science and Technology of Advanced Materials **11**, 054504 (2010).

[290] Y. Kobayashi, K.-i. Fukui, T. Enoki, and K. Kusakabe, *Edge state on hydrogen-terminated graphite edges investigated by scanning tunneling microscopy*, Physical Review B **73**, 125415 (2006).

[291] P. Merino, H. Santos, A. L. Pinardi, L. Chico, and J. A. Martin-Gago, *Atomically-resolved edge states on surface-nanotemplated graphene explored at room temperature*, Nanoscale **9**, 3905–3911 (2017).

[292] Y. Kobayashi, K. I. Fukui, T. Enoki, K. Kusakabe, and Y. Kaburagi, *Observation of zigzag and armchair edges of graphite using scanning tunneling microscopy and spectroscopy*, Physical Review B **71**, 2–5 (2005).

[293] P. P. Shinde, O. Gröning, et al., *Stability of edge magnetism in functionalized zigzag graphene nanoribbons*, Carbon (2017) 10.1016/j.carbon.2017.08.018.

[294] A. Politano, R. G. Agostino, E. Colavita, V. Formoso, and G. Chiarello, *Purely quadratic dispersion of surface plasmon in Ag/Ni(111): The influence of electron confinement*, Physica Status Solidi - Rapid Research Letters **2**, 86–88 (2008).

[295] K. Wakabayashi, S. Okada, R. Tomita, S. Fujimoto, and Y. Natsume, *Edge states and flat bands of graphene nanoribbons with edge modification*, Journal of the Physical Society of Japan **79**, 1–7 (2010).

[296] O. Voznyy, A. D. Güçlü, P. Potasz, and P. Hawrylak, *Effect of edge reconstruction and passivation on zero-energy states and magnetism in triangular graphene quantum dots with zigzag edges*, Physical Review B - Condensed Matter and Materials Physics **83**, 1–5 (2011).

[297] Y. Li, W. Zhang, M. Morgenstern, and R. Mazzarello, *Electronic and Magnetic Properties of Zigzag Graphene Nanoribbons on the (111) Surface of Cu, Ag, and Au*, Physical Review Letters **110**, 216804 (2013).

[298] G. Fiori, A. Betti, S. Bruzzone, and G. Iannaccone, *Lateral graphene-hBCN heterostructures as a platform for fully two-dimensional transistors*, ACS Nano **6**, 2642–2648 (2012).

[299] Y. Liu, S. Bhowmick, and B. I. Yakobson, *BN White Graphene with "Colorful" Edges: The Energies and Morphology*, Nano Letters **11**, 3113–3116 (2011).

[300] a. Nagashima, Y. Gamou, M. Terai, M. Wakabayashi, and C. Oshima, *Electronic states of the heteroepitaxial double-layer system: Graphite/monolayer hexagonal boron nitride/Ni(111)*, Physical Review B **54**, 13491–13494 (1996).

[301] L. a. Ponomarenko, a. K. Geim, et al., *Tunable metal-insulator transition in double-layer graphene heterostructures*, Nature Physics **7**, 958–961 (2011).

[302] V. O. Özçelik and S. Ciraci, *Nanoscale dielectric capacitors composed of graphene and boron nitride layers: A first-principles study of high capacitance at nanoscale*, Journal of Physical Chemistry C **117**, 15327–15334 (2013).

[303] B. Hwang, J. Hwang, et al., *Energy Bandgap and Edge States in an Epitaxially Grown Graphene/h-BN Heterostructure*, Scientific Reports **6**, 31160 (2016).

[304] Q. Peng and S. De, *Tunable band gaps of mono-layer hexagonal BNC heterostructures*, Physica E: Low-dimensional Systems and Nanostructures **44**, 1662–1666 (2012).

[305] A. Zhang, H. F. Teoh, Z. Dai, Y. P. Feng, and C. Zhang, *Band gap engineering in graphene and hexagonal BN antidot lattices: A first principles study*, Applied Physics Letters **98**, 023105 (2011).

[306] X. Fan, Z. Shen, a. Q. Liu, and J.-L. Kuo, *Band gap opening of graphene by doping small boron nitride domains*, Nanoscale **4**, 2157 (2012).

[307] B. Xu, Y. H. Lu, Y. P. Feng, and J. Y. Lin, *Density functional theory study of BN-doped graphene superlattice: Role of geometrical shape and size*, Journal of Applied Physics **108** (2010) 10.1063/1.3487959.

[308] A. Ramasubramaniam and D. Naveh, *Carrier-induced antiferromagnet of graphene islands embedded in hexagonal boron nitride*, Physical Review B **84**, 1–7 (2011).

[309] S. Gao, W. Lu, G. H. Zheng, Y. Jia, and S. H. Ke, *Spin-polarized electron transport in hybrid graphene-BN nanoribbons*, Journal of Physics: Conference Series **827** (2017) 10.1088/1742-6596/827/1/012012.

[310] N. C. Bristowe, M. Stengel, P. B. Littlewood, E. Artacho, and J. M. Pruneda, *One-dimensional half-metallic interfaces of two-dimensional honeycomb insulators*, Physical Review B **88**, 161411 (2013).

[311] a. Ohtomo and H. Y. Hwang, *A high-mobility electron gas at the LaAlO3/SrTiO3 heterointerface.*, Nature **427**, 423–426 (2004).

[312] A. Brinkman, M. Huijben, et al., *Magnetic effects at the interface between non-magnetic oxides*, Nature Materials **6**, 493–496 (2007).

[313] S. M. Kim, A. Hsu, et al., *Synthesis of patched or stacked graphene and hBN flakes: A route to hybrid structure discovery*, Nano Letters **13**, 933–941 (2013).

[314] J. Park, J. Lee, et al., *Spatially resolved one-dimensional boundary states in graphene–hexagonal boron nitride planar heterostructures*, Nature Communications **5**, 5403 (2014).

[315] A. Ismach, H. Chou, et al., *Toward the controlled synthesis of hexagonal boron nitride films*, ACS Nano **6**, 6378–6385 (2012).

[316] G. B. Grad, P. Blaha, K. Schwarz, W. Auwärter, and T. Greber, *Density functional theory investigation of the geometric and spintronic structure of h -BN/Ni(111) in view of photoemission and STM experiments*, Physical Review B **68**, 085404 (2003).

[317] M. N. Huda and L. Kleinman, *h-BN monolayer adsorption on the Ni(111) surface: A density functional study*, Physical Review B **74**, 075418 (2006).

[318] J. Gómez Díaz, Y. Ding, et al., *Hexagonal boron nitride on transition metal surfaces*, Theoretical Chemistry Accounts **132**, 1–17 (2013).

[319] W. Auwärter, T. Kreutz, T. Greber, and J. Osterwalder, *XPD and STM investigation of hexagonal boron nitride on Ni(111)*, Surface Science **429**, 229–236 (1999).

[320] W. Auwärter, M. Muntwiler, J. Osterwalder, and T. Greber, *Defect lines and two-domain structure of hexagonal boron nitride films on Ni(1 1 1)*, Surface Science **545** (2003) 10 . 1016/j.susc.2003.08.046.

[321] C. M. Orofeo, S. Suzuki, H. Kageshima, and H. Hibino, *Growth and low-energy electron microscopy characterization of monolayer hexagonal boron nitride on epitaxial cobalt*, Nano Research **6**, 335–347 (2013).

[322] Z. Zhang, Y. Liu, Y. Yang, and B. I. Yakobson, *Growth Mechanism and Morphology of Hexagonal Boron Nitride*, Nano Letters **16**, 1398–1403 (2016).

[323] C. Jin, F. Lin, K. Suenaga, and S. Iijima, *Fabrication of a freestanding boron nitride single layer and Its defect assignments*, Physical Review Letters **102**, 3–6 (2009).

[324] Y. Stehle, H. M. Meyer, et al., *Synthesis of Hexagonal Boron Nitride Monolayer: Control of Nucleation and Crystal Morphology*, Chemistry of Materials **27**, 8041–8047 (2015).

[325] J. C. Meyer, A. Chuvilin, G. Algara-Siller, J. Biskupek, and U. Kaiser, *Selective sputtering and atomic resolution imaging of atomically thin boron nitride membranes*, Nano Letters **9**, 2683–2689 (2009).

[326] X. Li, W. Hua, et al., *Effects of domain size on x-ray absorption spectra of boron nitride doped graphenes*, Applied Physics Letters **109**, 081601 (2016).

[327] A. K. Manna and S. K. Pati, *Tunable Electronic and Magnetic Properties in BxNyCz Nanohybrids: Effect of Domain Segregation.*, Journal of Physical Chemistry C **115**, 10842–10850 (2011).

[328] P. P. Shinde and V. Kumar, *Direct band gap opening in graphene by BN doping: Ab initio calculations*, Physical Review B - Condensed Matter and Materials Physics **84**, 1–6 (2011).

[329] a. Nagashima, N. Tejima, Y. Gamou, T. Kawai, and C. Oshima, *Electronic dispersion relations of monolayer hexagonal boron nitride formed on the Ni (111) surface*, Physical Review B **51**, 4606–4613 (1995).

[330] J. Zhu, S. Bhandary, B. Sanyal, and H. Ottosson, *Interpolation of atomically thin hexagonal boron nitride and graphene: Electronic structure and thermodynamic stability in terms of all-carbon conjugated paths and aromatic hexagons*, Journal of Physical Chemistry C **115**, 10264–10271 (2011).

[331] Z. Huang, V. H. Crespi, and J. R. Chelikowsky, *Electronic properties of mixed-phase graphene/h-BN sheets using real-space pseudopotentials*, Physical Review B **88**, 1–6 (2013).

[332] M. Petrović, M. Horn-von Hoegen, and F. J. Meyer zu Heringdorf, *Lateral heterostructures of hexagonal boron nitride and graphene: BCN alloy formation and microstructuring mechanism*, Applied Surface Science **455**, 1086–1094 (2018).

[333] N. Ding, Y. Lei, et al., *Structures and electronic properties of vacancies at the interface of hybrid graphene/hexagonal boron nitride sheet*, Computational Materials Science **117**, 172–179 (2016).

[334] N. Nakagawa, H. Y. Hwang, and D. a. Muller, *Why some interfaces cannot be sharp*, Nature Materials **5**, 204–209 (2006).

[335] R. Martinez-Gordillo and M. Pruneda, *Polar discontinuities and 1D interfaces in monolayered materials*, Progress in Surface Science **90**, 444–463 (2015).

[336] W. Harrison, E. Kraut, J. Waldrop, and R. Grant, *Polar heterojunction interfaces*, Physical Review B **18**, 4402–4410 (1978).

[337] J. Lu, L. C. Gomes, R. W. Nunes, a. H. Castro Neto, and K. P. Loh, *Lattice Relaxation at the Interface of Two-Dimensional Crystals: Graphene and Hexagonal Boron-Nitride*, Nano Letters **14**, 5133–5139 (2014).

[338] a. Catellani, M. Posternak, A. Baldereschi, H. J. F. Jansen, and a. J. Freeman, *Electronic interlayer states in hexagonal boron nitride*, Physical Review B **32**, 6997–6999 (1985).

[339] X. Blase, A. Rubio, S. G. Louie, and M. L. Cohen, *Quasiparticle band structure of bulk hexagonal boron nitride and related systems*, Physical Review B **51**, 6868–6875 (1995).

[340] P. C. Mende, Q. Gao, et al., *Characterization of hexagonal boron nitride layers on nickel surfaces by low-energy electron microscopy*, Surface Science **659**, 31–42 (2017).